

CRANFIELD UNIVERSITY

Daniele Quaglia

**Multidisciplinary Methods for  
Evaluation and Optimisation of  
Aircraft Flight Performance**

School of Aerospace, Transport and

Manufacturing

Centre for Aeronautics

Aerospace Engineering Division

PhD Thesis

Supervisor: Dr. Huamin Jia

October 2017

**CRANFIELD UNIVERSITY**

School of Aerospace, Transport and  
Manufacturing

PhD Thesis

Daniele Quaglia

**Multidisciplinary Methods for  
Evaluation and Optimisation of Aircraft  
Flight Performance**

Supervisor: Dr. Huamin Jia

October 2017

This thesis is submitted in partial fulfilment of the requirements for  
the degree of Doctor of Philosophy

© Cranfield University, 2017. All rights reserved. No part of this  
publication may be reproduced without the written permission of  
the copyright owner.

# Declaration of Authorship

I, Daniele Quaglia, declare that this thesis titled, ‘Multidisciplinary Methods for Evaluation and Optimisation of Aircraft Flight Performance’ and the work presented in it are my own. I confirm that:

- This work was done wholly or mainly while in candidature for a research degree at this University.
- Where any part of this thesis has previously been submitted for a degree or any other qualification at this University or any other institution, this has been clearly stated.
- Where I have consulted the published work of others, this is always clearly attributed.
- Where I have quoted from the work of others, the source is always given. With the exception of such quotations, this thesis is entirely my own work.
- I have acknowledged all main sources of help.
- Where the thesis is based on work done by myself jointly with others, I have made clear exactly what was done by others and what I have contributed myself.

Signed:

---

Date:

---

# Abstract

The aviation today is an increasing global market with 2.2 billion passengers travelling everyday due to the convenience that the air transportation has reached. Long term forecasts indicate that this growth will intensify and continue with a minimum of 2% passenger growth per year for the next two decades.

This traffic growth will push to the limit the actual air traffic management and airspace systems that cannot handle such volume of increase traffic. The air transportation growth not only affects the current global air transportation system, but also has both local and global impacts on the environment. In addition, aviation also generates significant noisy environmental effects to the population living in the vicinity of the terminal area.

Nowadays the aviation can use several procedures developed as first step for noise abatement and direct cost are managed by the on-board systems. The challenge is to introduce the future 4D trajectory management concept within on-board systems to manage the flight trajectory to optimize emissions, noise impact, contrails formation and also gate to gate flight time. Most of the previous studies have been focused on optimizing trajectories phases for a specific case only and without considering the operational level that need to be taken into account for a real gate to gate as described by the new Trajectory-Based Operations (TBO) concept.

This report shows the work that has been done to create a virtual flight environment where the flight management systems can be tested and evaluated respect to those new requirements requested for the future generation air traffic rules.

Trajectory optimization is implemented to calculate the optimal trajectory that minimize emissions and noise impact based on city pair air route in an operational level with realistic constraints and environment conditions. Multi-phase optimal control models the flight phases and control intermediate states of the aircraft.



The ultimate trajectories are tested within the simulation environment to assess 4D trajectory performance and conceptual aircraft flight performances. The feedbacks can be used by the aircraft designers to modify the conceptual aircraft in the case the performances are not met.

# Acknowledgements

I thank my parents for the support they gave me during my whole life which brought me to UK and to Cranfield.

This research would have not been possible if not for the opportunity that CleanSky project brought to me. I thank Dr. Huamin Jia for the opportunity he gave me. I thank him for his support and also freedom in let me doing my work in autonomy but with valuable advices which drove me to achieve my aims. I would like to thank Dr. Irfan Madani, Michael. Cooper, Ravinka and Ahmed Shinkafi for the valuable work done together for the CleanSky project and also during our personal research work and the endless discussion on the topics of simulation, trajectory optimisation, emission calculation, etc which were part in common in our works. Dr. Madani was extremely helpful when there were technical challenges that needed to be resolved and I thank him for his insight and patience during our long work done together during the CleanSky project and its many deliveries to be produced and the months spent in the laboratory checking the status of the simulations.

Academia aside I would like to thank my lovely fiance Ylfa for her support during these years. For the patience and endless support during my research work and as well during the thesis writing process. She has been an endless source of inspiration for myself and supported me during difficult times along the journey and she never let me give up.

# Contents

<b>Declaration of Authorship</b>	<b>i</b>
<b>Abstract</b>	<b>ii</b>
<b>Acknowledgements</b>	<b>iv</b>
<b>List of Figures</b>	<b>ix</b>
<b>List of Tables</b>	<b>xii</b>
<b>Abbreviations</b>	<b>xiii</b>
<b>Physical Constants</b>	<b>xvi</b>
<b>1 Introduction</b>	<b>1</b>
1.1 Aviation Enhancement . . . . .	1
1.2 The Need for 4D Trajectory-Based Operations . . . . .	4
1.3 Research Aims and Objectives . . . . .	8
1.4 Thesis Structure . . . . .	9
1.5 Publications . . . . .	10
<b>2 Literature study</b>	<b>13</b>
2.1 Trajectory Optimisation . . . . .	13
2.1.1 Parametric Optimisation Problems . . . . .	16
2.1.2 Trajectory as Optimal Control Problems . . . . .	17
2.2 Numerical Methods for solving Optimal Control Problems . . . . .	20
2.2.1 Indirect Methods . . . . .	20
2.2.2 Direct Methods . . . . .	22
2.2.2.1 Direct Shooting Methods . . . . .	23
2.2.2.2 Direct Multiple Shooting Methods . . . . .	24
2.2.2.3 Direct Collocation Methods . . . . .	24
2.2.2.4 Direct Pseudo-spectral Methods . . . . .	25
2.3 Nonlinear Programming Algorithms . . . . .	26
2.3.1 Gradient Algorithms . . . . .	28
2.3.2 Heuristic Algorithms . . . . .	29

2.4	Single and Multi-Objective Optimisation . . . . .	31
2.4.1	Weighted-sum Method . . . . .	32
2.4.2	$\varepsilon$ -constraint Method . . . . .	33
2.5	Environmental Objectives . . . . .	34
2.5.1	Noise annoyance . . . . .	34
2.5.1.1	Airframe Noise . . . . .	35
2.5.1.2	Engine Noise . . . . .	36
2.5.1.3	Noise measure . . . . .	36
2.5.1.4	Aircraft Noise Calculation Tools . . . . .	38
2.5.2	Engine emissions . . . . .	38
2.6	Summary . . . . .	40
<b>3</b>	<b>Greener Aircraft Trajectory Modelling</b>	<b>42</b>
3.1	Introduction . . . . .	42
3.2	Aircraft Motion . . . . .	42
3.2.1	Modelling Assumptions . . . . .	43
3.2.2	Reference Frames . . . . .	44
3.2.3	Equations of motion . . . . .	45
3.2.4	Aerodynamics and Propulsion Modelling . . . . .	46
3.2.5	Atmosphere Modelling . . . . .	52
3.2.6	Wind Modelling . . . . .	54
3.2.7	Flight Envelope Constraints . . . . .	55
3.3	Operational Constraints . . . . .	57
3.3.1	Constraints modelling . . . . .	57
3.3.1.1	Terminal Area Maximum Speed Constraint . . . . .	58
3.3.1.2	Terminal Area Minimum Climb Gradient Constraint . . . . .	59
3.4	Emissions Modelling . . . . .	60
3.5	Noise Modelling . . . . .	63
3.5.1	Integrated Noise Model (INM) . . . . .	64
3.5.2	Noise annoyance . . . . .	66
<b>4</b>	<b>Fundamental Theory of Optimisation</b>	<b>69</b>
4.1	Introduction . . . . .	69
4.2	Multiphase Optimal Control Problem . . . . .	69
4.3	Numerical Solution of Differential Equations . . . . .	71
4.3.1	Time Marching . . . . .	72
4.3.2	Collocation . . . . .	73
4.4	Radau Pseudospectral Method (RPM) . . . . .	77
4.5	Optimisation Criteria . . . . .	81
4.6	Multi-objective Optimisation . . . . .	82
4.6.1	The Pareto front . . . . .	83
4.7	Numerical Resolution . . . . .	83
<b>5</b>	<b>Simulation Environment</b>	<b>86</b>
5.1	Introduction . . . . .	86

5.2	Aircraft Dynamic Model . . . . .	87
5.2.1	Equations of Motion . . . . .	88
5.2.2	Gravitational Model . . . . .	89
5.2.3	Aerodynamic Model . . . . .	90
5.2.3.1	Aerodynamic coefficients estimation . . . . .	93
5.2.4	Propulsive Model . . . . .	95
5.3	Flight Controls Model . . . . .	97
5.3.1	Total Energy Control System (TECS) . . . . .	98
5.3.2	Total Heading Control System (THCS) . . . . .	102
5.4	Validation of the model . . . . .	106
<b>6</b>	<b>Case Studies</b>	<b>109</b>
6.1	Introduction . . . . .	109
6.2	London Heathrow - Amsterdam Schiphol . . . . .	109
6.2.1	Baseline Trajectory . . . . .	111
6.2.2	Departure Phase . . . . .	112
6.2.2.1	Current Procedure . . . . .	112
6.2.3	A new procedure . . . . .	114
6.2.3.1	Problem definition . . . . .	114
6.2.3.2	Results . . . . .	116
6.2.4	A 4D new procedure . . . . .	123
6.2.4.1	Problem definition . . . . .	123
6.2.4.2	Results . . . . .	124
6.2.5	En-Route Phase . . . . .	132
6.2.5.1	Current Procedure . . . . .	132
6.2.5.2	Problem definition . . . . .	132
6.2.5.3	Results . . . . .	134
6.2.6	Arrival Phase . . . . .	142
6.2.6.1	Problem definition . . . . .	143
6.2.6.2	Results . . . . .	144
<b>7</b>	<b>Conclusions and Future Work</b>	<b>149</b>
7.1	Conclusions . . . . .	149
7.2	Contribution to knowledge . . . . .	150
7.3	Milestones achieved . . . . .	151
7.4	Proposed Future Work . . . . .	152
<b>A</b>	<b>Flight Mechanics</b>	<b>154</b>
A.1	Reference Frames . . . . .	154
A.2	Angular relationships . . . . .	156
A.3	Angular Velocity . . . . .	157
A.3.1	Local horizon-Earth axes . . . . .	158
A.4	Kinematic Relationships . . . . .	158

---

A.5 Equations of Motion . . . . .	159
<b>B Aeronautical Information Publication (AIP) Charts</b>	<b>160</b>
<b>Bibliography</b>	<b>162</b>

# List of Figures

1.1	Average fuel burn 1960-2008 . . . . .	3
1.2	Progress in noise reduction . . . . .	4
1.3	Comparison between conventional routes, RNAV and RNAV-RNP operations . . . . .	5
1.4	ATM paradigm shift . . . . .	6
1.5	Environmental impact along flight trajectory . . . . .	7
1.6	Continuous Descent Approach (CDA) vs Step-down approach . . . . .	8
2.1	Altitude and speed profiles of minimum time to climb for a supersonic aircraft problem . . . . .	14
2.2	Different types of Direct Methods . . . . .	23
2.3	Rastrigin's function global minimum and local minimum points . . . . .	30
2.4	Example of a Pareto front for ZDT1 problem . . . . .	32
2.5	Example of Pareto front for two criteria multi-objective problem with non-convex region . . . . .	33
2.6	Airframe noise sources . . . . .	34
2.7	Engine noise pattern for Turbojet and Turbofan . . . . .	37
2.8	Relation between the overall sleep disturbance and indoor SEL . . . . .	39
3.1	Coordinate frames for a flight over a spherical Earth . . . . .	44
3.2	Forces applied to the aircraft . . . . .	45
3.3	Drag polar obtained using EUROCONTROL BADA dataset for Airbus A320 . . . . .	48
3.4	Airbus A320 drag polar corrected for compressibility . . . . .	49
3.5	Maximum Net Thrust and correspondent fuel flow for different flight levels of the modelled engine . . . . .	51
3.6	Wind Components at 200 hPa - forecast and multiple regression . . . . .	55
3.7	Airbus A320 flight envelope . . . . .	56
3.8	Step function and its continuous approximation . . . . .	58
3.9	Continuous approximation of maximum operational airspeed . . . . .	59
3.10	Continuous approximation of minimum climb gradient . . . . .	60
3.11	P3T3 Methodology . . . . .	62
3.12	Humidity Correction for Altitude NOx . . . . .	62
3.13	Geometric definition for INM model . . . . .	65
3.14	Relation between the overall sleep disturbance and indoor SEL . . . . .	67

---

4.1	Schematic of linkages for multiple phase OCP . . . . .	71
4.2	Comparison between Legendre-Gauss (LG), Legendre-Gauss-Radau (LGR) and Legendre-Gauss-Lobatto (LGL) collocation points . . . . .	76
4.3	Screenshot of a piece of Matlab code which defines the problem to be optimised . . . . .	84
4.4	Screenshot of a piece of Matlab code which defines the differential algebraic equations and path constraints . . . . .	85
4.5	Screenshot of Matlab command window at the end of the optimisation using GPOPS and INTLAB . . . . .	85
5.1	Simulink view of the simulation environment . . . . .	87
5.2	Simulink view of the aircraft dynamic model . . . . .	89
5.3	Simulink view of the aircraft aerodynamic model . . . . .	92
5.4	Adaptation of wing cranked profile into Datcom accepted profile . . . . .	94
5.5	Datcom+ 3D model of the studied aircraft, similar to Airbus A320 . . . . .	95
5.6	Simulink view of part of the Datcom model implement . . . . .	96
5.7	Coupling of aircraft longitudinal modes and controls . . . . .	99
5.8	TECS block diagram . . . . .	102
5.9	TECS block diagram . . . . .	104
5.10	Simulink view of the implemented Flight Control block . . . . .	105
5.11	TECS validation - Altitude and speed response to a controlled climb, descent and speed change . . . . .	107
5.12	THCS validation - Heading response to a coordinated turn . . . . .	108
6.1	Airbus A320 Aircraft . . . . .	110
6.2	London-Amsterdam routing . . . . .	111
6.3	EGLL-EHAM ground track profile of flight BAW440 on 8 Aug 2014 . . . . .	112
6.4	EGLL-EHAM altitude and speed profiles of flight BAW440 on 8 Aug 2014 . . . . .	113
6.5	Population density around EGLL and BPK 7G SID Trajectory . . . . .	114
6.6	Pareto front - Departure segment - Heathrow-Schiphol . . . . .	116
6.7	Latitude Longitude profile - Departure segment - Heathrow-Schiphol . . . . .	117
6.8	Altitude profile - Departure segment - Heathrow-Schiphol . . . . .	118
6.9	True airspeed profile - Departure segment - Heathrow-Schiphol . . . . .	118
6.10	Calibrated airspeed profile - Departure segment - Heathrow-Schiphol . . . . .	119
6.11	FPA profile - Departure segment - Heathrow-Schiphol . . . . .	120
6.12	Heading profile - Departure segment - Heathrow-Schiphol . . . . .	120
6.13	Aircraft mass profile - Departure segment - Heathrow-Schiphol . . . . .	121
6.14	Throttle profile - Departure segment - Heathrow-Schiphol . . . . .	122
6.15	Vertical load factor profile - Departure segment - Heathrow-Schiphol . . . . .	122
6.16	Pareto front - A new 4D Departure - Heathrow-Schiphol . . . . .	125
6.17	Pareto front - A new 4D Departure - Heathrow-Schiphol . . . . .	125
6.18	Footprint - 4D Departure segment - Heathrow-Schiphol . . . . .	126
6.19	Altitude profile - 4D Departure segment - Heathrow-Schiphol . . . . .	127
6.20	True airspeed profile - 4D Departure segment - Heathrow-Schiphol . . . . .	127



6.21	Calibrated airspeed profile - 4D Departure segment - Heathrow-Schiphol . . . . .	128
6.22	Flight path angle profile - 4D Departure segment - Heathrow-Schiphol	128
6.23	Heading profile - 4D Departure segment - Heathrow-Schiphol . . . . .	129
6.24	Mass profile - 4D Departure segment - Heathrow-Schiphol . . . . .	129
6.25	Throttle profile - 4D Departure segment - Heathrow-Schiphol . . . . .	130
6.26	Vertical load factor profile - 4D Departure segment - Heathrow-Schiphol . . . . .	130
6.27	Bank angle profile - 4D Departure segment - Heathrow-Schiphol . . . . .	131
6.28	Noise SEL contours for minimum noise objective function . . . . .	131
6.29	Pareto front fuel consumption vs flight time - EnRoute segment - Heathrow-Schiphol . . . . .	135
6.30	Pareto front fuel - NO <sub>x</sub> - EnRoute segment - Heathrow-Schiphol . . . . .	135
6.31	Latitude Longitude profile - EnRoute segment - Heathrow-Schiphol	136
6.32	Altitude profile - EnRoute segment - Heathrow-Schiphol . . . . .	137
6.33	True airspeed profile - EnRoute segment - Heathrow-Schiphol . . . . .	138
6.34	Calibrated airspeed profile - EnRoute segment - Heathrow-Schiphol	138
6.35	FPA profile - EnRoute segment - Heathrow-Schiphol . . . . .	139
6.36	Heading profile - EnRoute segment - Heathrow-Schiphol . . . . .	139
6.37	Aircraft mass profile - EnRoute segment - Heathrow-Schiphol . . . . .	140
6.38	Aircraft CO <sub>2</sub> emission profile - EnRoute segment - Heathrow-Schiphol	140
6.39	Aircraft NO <sub>x</sub> emission profile - EnRoute segment - Heathrow-Schiphol	141
6.40	RWY06 RNAV-Night Instrument Approach chart for EHAM . . . . .	142
6.41	Footprint - 4D Departure segment - Heathrow-Schiphol . . . . .	144
6.42	Altitude profile - 4D Arrival segment - Heathrow-Schiphol . . . . .	145
6.43	True airspeed profile - 4D Arrival segment - Heathrow-Schiphol . . . . .	145
6.44	Calibrated airspeed profile - 4D Arrival segment - Heathrow-Schiphol	146
6.45	Flight path angle profile - 4D Arrival segment - Heathrow-Schiphol	146
6.46	Heading profile - 4D Arrival segment - Heathrow-Schiphol . . . . .	147
6.47	Mass profile - 4D Arrival segment - Heathrow-Schiphol . . . . .	147
6.48	Throttle profile - 4D Arrival segment - Heathrow-Schiphol . . . . .	148
6.49	Vertical load factor profile - 4D Arrival segment - Heathrow-Schiphol	148
A.1	Coordinate systems for flight over spheric Earth . . . . .	155
B.1	London Heathrow (EGLL) - BPK SIDs . . . . .	160
B.2	Amsterdam Schiphol (EHAM) - RNAV Approach Chart . . . . .	161

# List of Tables

3.1	EUROCONTROL BADA dataset aerodynamic performance coefficients for Airbus A320 . . . . .	48
3.2	Operational engine conditions used to map the thrust and fuel consumption . . . . .	50
6.1	Phases definition for departure phase . . . . .	115
6.2	Problem setup for departure phase . . . . .	115
6.3	Phases definition for 4D departure phase . . . . .	123
6.4	Problem setup for 4D departure phase . . . . .	123
6.5	Problem setup for departure phase . . . . .	133
6.6	Phases definition for en-route phase . . . . .	133
6.7	Phases definition for arrival phase . . . . .	143
6.8	Problem setup for arrival phase . . . . .	143

# Abbreviations

<b>3-DOF</b>	<b>3-Degree Of Freedom</b>
<b>AGL</b>	<b>Above Ground Level</b>
<b>ACARE</b>	<b>Advisory Council for Aeronautics Research in Europe</b>
<b>AIP</b>	<b>Aeronautical Information Publication</b>
<b>AIRAC</b>	<b>Aeronautical Information Regulation and Control</b>
<b>AIRE</b>	<b>Atlantic Interoperability Initiative to Reduce Emission</b>
<b>ATC</b>	<b>Air Traffic Control</b>
<b>ASM</b>	<b>Air Space Management</b>
<b>ATFM</b>	<b>Air Traffic Flow Management</b>
<b>ATM</b>	<b>Air Traffic Management</b>
<b>ATS</b>	<b>Air Traffic Services</b>
<b>BADA</b>	<b>Base of Aircraft DAta</b>
<b>CAS</b>	<b>Calibrated AirSpeed</b>
<b>CCD</b>	<b>Continuous Climb Departure</b>
<b>CDA</b>	<b>Continuous Descent Approach</b>
<b>CFD</b>	<b>Computational Fluid Dynamics</b>
<b>CGL</b>	<b>Chebyshev-Gauss-Lobatto</b>
<b>DAE</b>	<b>Differential-Algebraic Equations</b>
<b>DOF</b>	<b>Degree Of Freedom</b>
<b>DP</b>	<b>Dynamic Programming</b>
<b>EEC</b>	<b>Eurocontrol Experimental Centre</b>
<b>FAA</b>	<b>Federal Aviation Administration</b>
<b>FIR</b>	<b>Flying Information Region</b>
<b>FSL</b>	<b>Forecasts System Laboratory</b>

---

<b>FMS</b>	<b>F</b> light <b>M</b> anagement <b>S</b> ystem
<b>GNSS</b>	<b>G</b> lobal <b>N</b> avigation <b>S</b> atellite <b>S</b> ystem
<b>GRIB</b>	<b>G</b> RIdded <b>B</b> inary
<b>HJB</b>	<b>H</b> amilton- <b>J</b> acobi- <b>B</b> ellman
<b>HLGL</b>	<b>H</b> ermite- <b>L</b> egendre- <b>G</b> auss- <b>L</b> obatto
<b>IAF</b>	<b>I</b> nitial <b>A</b> pproach <b>F</b> ix
<b>ICAO</b>	<b>I</b> nternational <b>C</b> ivil <b>A</b> viation <b>O</b> rganization
<b>ILS</b>	<b>I</b> nstrumental <b>L</b> anding <b>S</b> ystem
<b>IAS</b>	<b>I</b> ndicated <b>A</b> ir <b>S</b> peed
<b>ISA</b>	<b>I</b> nternational <b>S</b> tandard <b>A</b> tmosphere
<b>IPOPT</b>	<b>I</b> nterior <b>P</b> oint <b>O</b> P <b>T</b> imizer
<b>KKT</b>	<b>K</b> arush- <b>K</b> uhn- <b>T</b> ucker
<b>LG</b>	<b>L</b> egendre- <b>G</b> auss
<b>LGL</b>	<b>L</b> egendre- <b>G</b> auss- <b>L</b> obatto
<b>LGR</b>	<b>L</b> egendre- <b>G</b> auss- <b>R</b> adau
<b>NAP</b>	<b>N</b> oise <b>A</b> batement <b>P</b> rocedures
<b>NextGen</b>	<b>N</b> ext <b>G</b> eneration of air transportation system
<b>NLP</b>	<b>N</b> on- <b>L</b> inear <b>P</b> rogramming
<b>NOAA</b>	<b>N</b> ational <b>O</b> ceanic and <b>A</b> tmospheric <b>A</b> dministration
<b>MSL</b>	<b>M</b> ean <b>S</b> ea <b>L</b> evel
<b>MTOW</b>	<b>M</b> aximum <b>T</b> ake <b>O</b> ff <b>W</b> eight
<b>OC</b>	<b>O</b> perational <b>C</b> onstraints
<b>ODE</b>	<b>O</b> rdinary <b>D</b> ifferential <b>E</b> quation
<b>OEW</b>	<b>O</b> perating <b>E</b> mpy <b>W</b> eight
<b>PMM</b>	<b>P</b> oint <b>M</b> ass <b>M</b> odel
<b>RUC</b>	<b>R</b> apid <b>U</b> ppdate <b>C</b> ircle
<b>RWY</b>	<b>R</b> unway
<b>SESAR</b>	<b>S</b> ingle <b>E</b> uropean <b>S</b> ky <b>A</b> TM <b>R</b> esearch
<b>SID</b>	<b>S</b> tandard <b>I</b> nstrumental <b>D</b> eparture
<b>STAR</b>	<b>S</b> tandard <b>T</b> erminal <b>A</b> rrival <b>R</b> oute
<b>TBO</b>	<b>T</b> rajectory- <b>B</b> ased <b>O</b> perations

<b>TMA</b>	<b>T</b> erminal <b>M</b> aneuvering <b>A</b> rea
<b>TPBVP</b>	<b>T</b> wo <b>P</b> oint <b>B</b> oundary <b>V</b> alue <b>P</b> roblem
<b>USA</b>	<b>U</b> nited <b>S</b> tates of <b>A</b> merica

# Physical Constants

Air Pressure (MSL)	$p_0 = 1013.25 \text{ hPa}$
Air Density (MSL)	$\rho_0 = 1.225 \text{ kgm}^{-3}$
Air Temperature (MSL)	$T_0 = 288.15 \text{ K}$
Speed of Sound (MSL)	$a_0 = 340.294 \text{ ms}^{-1}$
Acceleration of gravity (MSL)	$g_0 = 9.80665 \text{ ms}^{-2}$

*What you get by achieving your goals  
is not as important as what you become  
by achieving your goals.*

*HENRY DAVID THOREAU*

# Chapter 1

## Introduction

### 1.1 Aviation Enhancement

Aviation has become an essential convenience in today's global society, with 3.1 billion passengers globally travelled in 2013 [1]. Last year annual passengers have increased 5% compared to 2012 and recent forecasts expect to exceed 6 billion by 2030 based on current projections. Likewise the number of aircraft departures reached 33 million globally during 2013, surpassing the old record established in 2012 of 32 million flights. This data shows that globally the Air Traffic Management (ATM) system handles more than 90 thousand flights per day. Only in the United States of America, the Federal Aviation Administration (FAA) has reported to have handled more than 30 million aircraft within En-Route flight phase in 2010 and presented forecasts showing 2% passenger growth rate per year between 2012 and 2030 [2]. Following the same trend, in Europe the European Organization for the Safety of Air Navigation (EUROCONTROL) reported a long-term forecast that indicates a growth of 1.8% per year as average for the same time interval [3].

The current ATM and airspace systems cannot handle such as great volume of increased traffic because it will reflect in a higher workload for air traffic controllers and flight crew and therefore the current ATM system will reach its limit capability. According to the prediction from EUROCONTROL, the air traffic expansion will have "most-likely" 14.4 million Instrumental Flight Rule (IFR) movements in Europe by 2035 which translates to an increase of 150% compared to 2012 [4]. Such air traffic growth imposes stringent requirements for flight safety, air traffic



management and airspace systems especially in a highly density traffic airspace. Furthermore the air transportation growth not only affects the current ATM system, but also has both local and global impacts on the environment.

Today air transport produces 2% of world's  $CO_2$  emissions through the burning of fossil fuels and it is expected to increase to 3% by 2050 with the continuous and steady forecast growth of traffic. With the aim to alleviate or reduce the environmental impact of air transportation growth, the Advisor Council for Aeronautics Research and Innovation in Europe (ACARE) has defined several targets to be achieved before 2020 [5]. The aim is to reach a reduction of carbon dioxide ( $CO_2$ ) emission by 50%, nitrogen oxide ( $NO_x$ ) emission by 80% and perceived external noise by 50%.

The European Commission has started two innovative Joint Technology Initiative (JTI) programmes: Single European Sky ATM Research (SESAR) [6] and Clean Sky [7] with the aim to improve the safety, capacity, efficiency, cost-effectiveness and environmental aspects of future aviation activity to handle with the predicted expansion. The SESAR programme was launched by the European Commission in 2004 to provide technological foundation to the architecture of the Single European Sky and provide the state-of-the-art technology for the creation of a uniform and high level of safety and efficiency over Europe's skies. Following that, the Clean Sky JTI programme was launched in 2008 with the ambitious aim to develop breakthrough technologies to significantly increase the environmental performances of air transport activities which would result in less noisy and more fuel efficient aircraft.

The efforts to reduce aircraft emissions and air pollution in the last 20 years have been mainly focused on the design and development of more efficient aircraft and engines. These have resulted in a new generation of engines and highly advanced wing designs. An evolution of averaged fuel burn for commercial aircraft is shown in FIGURE 1.1, which shows the trend of fuel burn along the years. A flat-line becomes visible after year 2000. Further improvements in reducing aircraft fuel consumption and therefore connected emissions can be achieved by modifying the current operational procedures. Everyday aircraft are restricted to follow procedures which in many cases are old and not updated considering the aircraft and engine performance but are convenient from an operational point of view. Future research efforts should focus on developing improved operational procedures customized for aircraft conditions and not only based on generic trajectories.

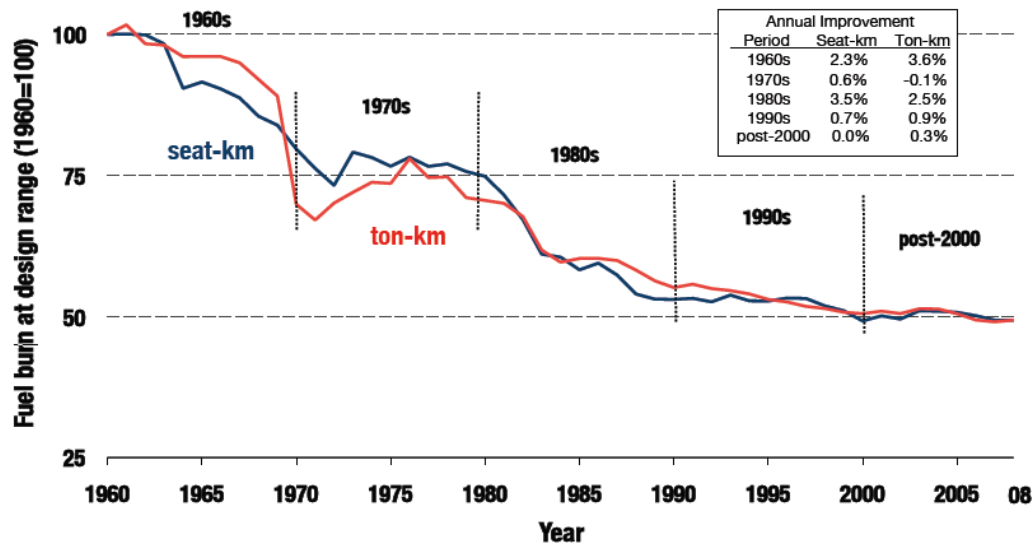


FIGURE 1.1: Average fuel burn for new aircraft, 1960-2008 [8].

In addition, aviation has also generated significant noisy environmental effects to residents, especially in the residential area in the vicinity of terminal areas. Aircraft noise is widely recognised to be one of the most objectionable impacts of aviation and an important environmental issue for those living close to airports as well as further field under the main arrival and departure tracks. Therefore, taking effective measures to control and mitigate the effect of aircraft noise is fundamental to achieving the sustainable development of the aviation industry.

With the improvement of engines and aircraft efficiencies, some effort was also made to reduce the noise generated by the aircraft (by engine and airframe) and consequently the noise impact on the population living around the airports as shown in FIGURE 1.2. However the trend of the noise exposure around the airport has flat-lined in the latest years in major airports [9].

Noise abatement procedures have been studied and developed as an initial step but are often designed manually by experts with the constraint to produce an unique procedure which then is applied to all the aircraft flying to and from the airport. The result procedure is obviously far from being considered optimal for every single aircraft. The same logic can be applied for pollutants, where the emission trends vary for each aircraft based on engines installed, and a standard procedure is far from being optimal.

In the last few years research has been carried out to create trajectories optimising the noise created by the aircraft activity in the terminal area and later on to the

noise impact on residential areas. However the problem definition was not complete and while the trajectories obtained were optimal from a theoretical point of view, they had to be translated to be accepted at an operational level.

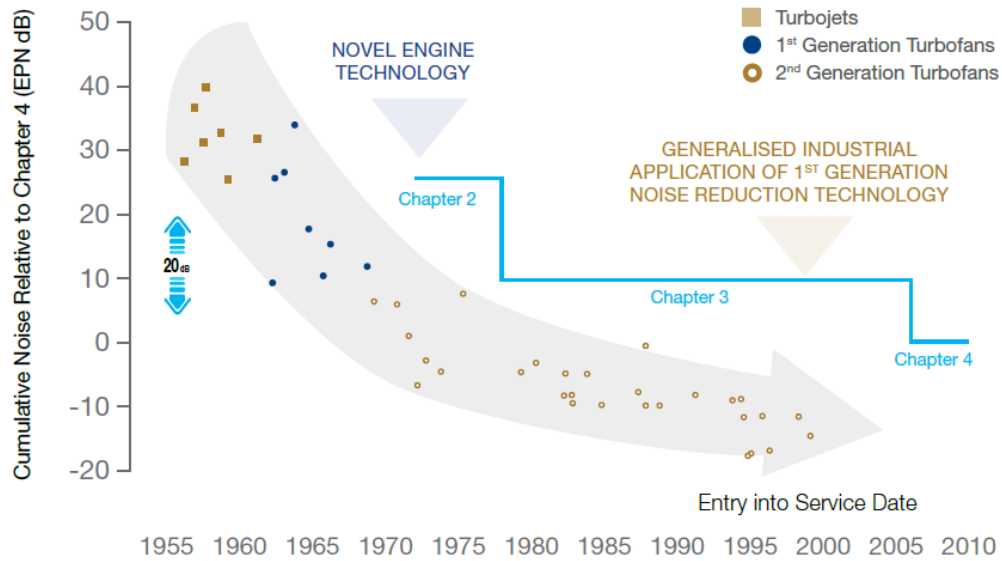


FIGURE 1.2: Progress in noise reduction [10].

It can be deduced then how complex it would be to optimise the general aircraft trajectory for greener operations because of so many contrasting objectives involved and the difference in the scenarios.

## 1.2 The Need for 4D Trajectory-Based Operations

The advent of satellite-based navigation technology has shifted the aircraft navigation system from traditional sensors-based design philosophy to the adoption of Performance-Based Navigation (PBN). The International Civil Aviation Organization (ICAO) has published its PBN Manual (DOC 9613) as an international standard. The PBN manual requests that future aircraft navigation and flight management system shall be based on Required Navigation Performance (RNP) systems. The RNP systems are capable of improving accuracy of the flown trajectory while maintaining the safety level and giving the aircraft the capability to follow the more complex and optimised procedures. The aircraft systems capability to follow with accuracy complex trajectories opens the door to the possibility to

leave the old idea of clearance-based operations to the new paradigm of Trajectory-Based Operations (TBO). The new procedures shall be constructed to better fit the user needs in terms of standard cost indexes (fuel and time) but also to reduce engine emissions, noise impact on the ground and avoid contrails formation.

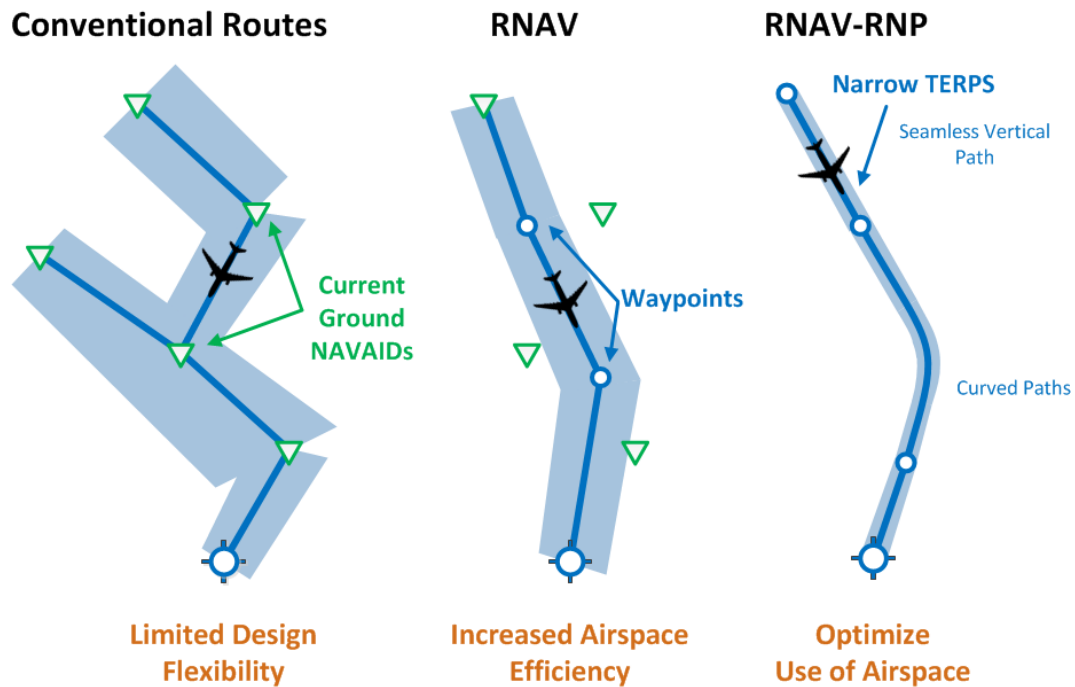


FIGURE 1.3: Comparison between conventional routes, RNAV and RNAV-RNP operations.

Both SESAR and NextGen have proposed 4D TBO as the fundamental cornerstone of future ATM systems [11]. The adoption of TBO makes increasing capacity and flexibility of the airspace possible and also the reduction of the aircraft impact on the environment. This is possible due by assigning to each aircraft the so called "Business/Mission Trajectory", tailor made according to user defined priorities while adhering to ATM constraints. The paradigm shift is well shown in FIGURE 1.4, where it is possible to see the procedural operations used in the past where the current and planned aircraft position are estimated; today with the help of radar it is possible to know exactly the aircraft position, and in the future with TBO the aircraft planned position and route intention will be known and shared between air traffic operators to better manage the air traffic and virtually let the aircraft fly in cylinders at specific times.

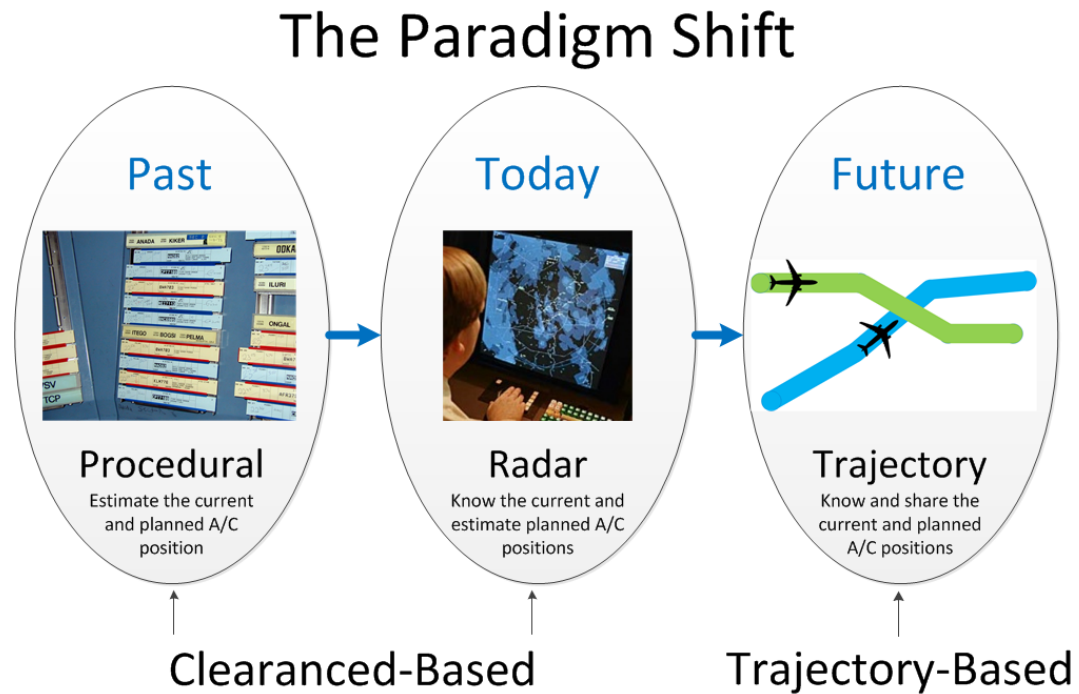


FIGURE 1.4: ATM paradigm shift.

An intermediate stage to the adoption of the fully negotiated TBO is the Time-Based Navigation (TBN), in which the aircraft are given Controlled-Time of Arrival (CTA) at specific waypoints along the flight trajectory, which is communicated to the aircrews by voice, and the aircrews are tasked to meet this time constraint. At present, the concept of CTA is implemented to meet a single time constraint, known as the metering fix, to reflect the Required Time of Arrival (RTA). The RTA functionality was first introduced into FMS in the early 1990's [12] and nowadays provides an effective time-based control method.

The current on-board Flight Management System (FMS) provides control system for flight planning, flight and fuel management tasks using atmospheric, navigation and engine data. The FMS build-in standard procedures are focused only in optimised direct operational costs (DOC) (i.e. time and fuel). The aforementioned SESAR core concept introduces the Reference Business Trajectories (RBT) principle in which Air Navigation Service Providers (ANSP), airport operators and the airspace users define together an optimal trajectory from gate to gate [11]. The RBT will be a 4D trajectory which will move beyond the DOC concept, considering emission and noise impact as well. The new generation of FMSs will have to manage the RBT in such a way to optimise all the factors, including fuel consumption, gate-to-gate flight time, contrails, emissions and noise. FIGURE 1.5 shows

some major factors the future FMS shall consider for the gate-to-gate mission.

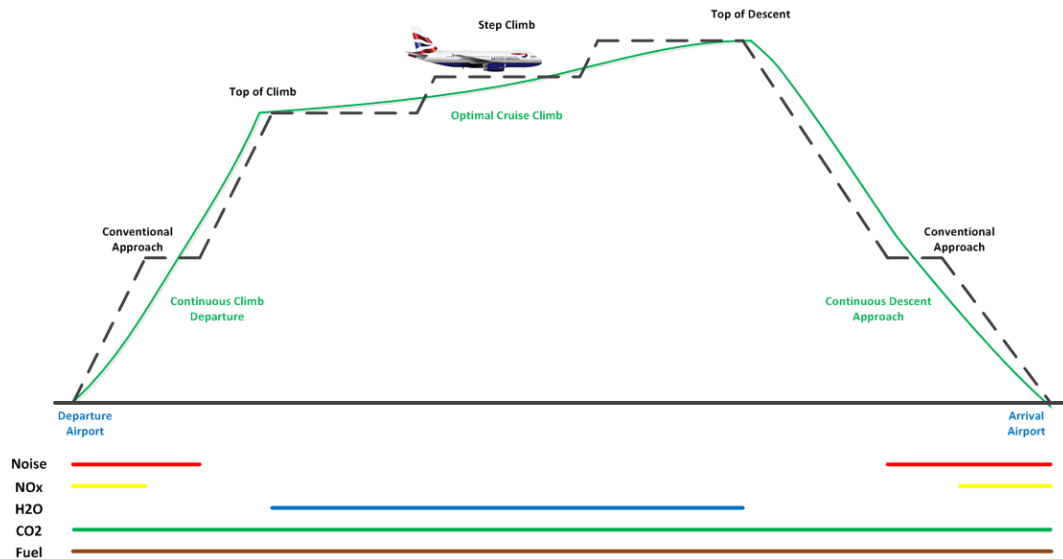


FIGURE 1.5: Environmental impact along flight trajectory.

Research activity in the previous years generated few concepts trying to achieve greener trajectories. One of the most important procedures designed and introduced to reduce noise and environmental effect created by traditional step-down approach was the so called Continuous Descent Approach (CDA). Step-down approach procedures often lead aircraft to descend to intermediate altitudes on the order of 2,000 to 3,000 feet above ground level, before transitioning onto the final approach path and final descent to the runway. The consequences of such procedures are the spread of noise and aircraft emissions onto nearby towns and cities, sometimes as far away as 30 NM from the runway threshold. The CDA principle is to delay descent beyond the regular Top Of Descent (TOD), and then to descend at idle or near idle thrust, while decelerating from the descent speed to the final approach speed without flying level as it is possible to see generally in FIGURE 1.5 and specifically in FIGURE 1.6.

Similarly to CDA, the same approach can be applied to the departure phase and is called Continuous Climb Departure (CCD). In CCD the aircraft climbs avoiding level flight with the aim to reduce noise and emissions, with a particular attention to  $NO_x$ . However the CCD approach has not received the same level of attention and implementation in operations. More attention instead has been received by Noise Abatement Departure Procedures (NADP) which aims to reduce noise nuisance in the terminal area during departure phase. The principle is to reduce the engine thrust immediately after take-off until the aircraft reaches a specified

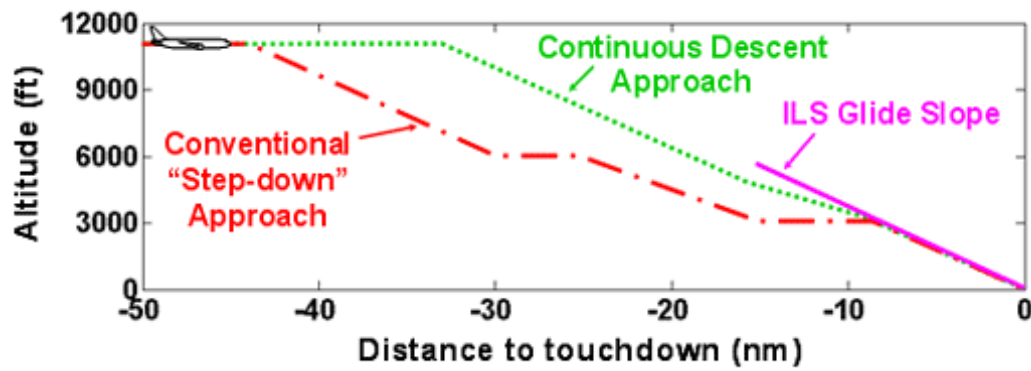


FIGURE 1.6: Continuous Descent Approach (CDA) vs Step-down approach.

altitude in clean configuration where it can continue climbing at normal engine settings. The reduced thrust generated by the engines generates less noise. The NADP procedure is applied mostly to airports which have big populations living in their terminal area.

The generated procedures previously introduced show that the research on optimising trajectories for operational procedures has been focused only on specific parts of the gate-to-gate mission. In a general view, each portion of the flight influences the overall mission in terms of time, fuel consumption, emissions and noise generated. In addition these studies considered only one aircraft flying the optimised procedure. However a more realistic study introducing different aircraft and generated scenarios should be considered in the future ATM system.

The aim of this Ph.D. research thesis is to advance from the old idea of portion of flights and to consider the overall trajectory from gate-to-gate as it is described by the new TBO concept. The concept considers the aircraft trajectory as a 4D where the tern of position components is combined with time to achieve greener trajectories which will be generated by the next generation FMS and applied in the future ATM system.

### 1.3 Research Aims and Objectives

The aim of this research is to develop an enhanced technique for optimal aircraft trajectory planning considering at the reduction of direct operating cost (i.e. fuel consumption and flight time) as well as environmental pollutants, noise perceived in the terminal area and contrails formation for a city pair mission. The ultimate

trajectories are used as greener procedures and have to respect the new requirements requested by future generation air traffic rules.

To achieve the aim of the research, several intermediate objectives are listed:

- Exhaustive literature review of methods used to optimise trajectories which include optimal control theory and associated numerical methods.
- To build all necessary components to model aircraft performance and wind forecasts as well as emissions, noise impact and contrails generation which affect city pair air routes and are required to be minimised in the future generation of air traffic rules.
- To develop a trajectory optimisation tool which calculates the optimal trajectory that minimises multi-objectives from the required ones listed in the previous point, based on city pair air route cases under air navigation constraints.
- Based on the enhanced techniques, design of more efficient trajectories for different haul length missions. Only the airborne phase of flight is considered which is defined from obstacle altitude for take-off to touch-down for landing.
- To develop a flight simulation system with a 4D guidance algorithm which is used to validate the ultimate trajectories by checking the feasibility of the optimal trajectory with the next-generation on-board systems.

## 1.4 Thesis Structure

The thesis is organized in the following structure:

- Chapter 2 presents current techniques for trajectory optimisation and related models which are used to describe noise annoyance and engine emissions.
- Chapter 3 contains the mathematical description of the models developed for this work. First the equations of motion which describe the aircraft dynamics are described then, the emission and noise computation methodology is given.



- Chapter 4 defines formally the optimisation problem and the way to resolve it is described.
- Chapter 5 shows the result of applying the proposed methodology to an optimal control problem in a hypothetical scenario with only noise or emission as cost function. This chapter allows the proof of the proposed optimisation framework.
- Chapter 6 shows the result of applying the methodology for a more real and complex scenario based on real cases such as a short haul flight between London Heathrow airport to Amsterdam Schiphol airport.
- Chapter 7 gives conclusions that are obtained from this work and a summary of possible future work is presented.
- Appendix A gives a more detailed explanation of how the equations of motion used to describe the greener aircraft model were obtained.

## 1.5 Publications

The list of publications resulting from this work is below listed:

### Conference Proceedings

- W. Gu, R. Navaratne, D. Quaglia, Towards the Development of a Multi-Disciplinary Flight Trajectory Optimization Tool GATAC, ASME Turbo Expo 2012.
- M. Cooper, C. Lawson, D. Quaglia, Towards Trajectory Prediction and Optimization for Energy Efficiency of an Aircraft with Electrical and Hydraulic Actuation Systems, ICAS 2012.
- R. Sabatini, A. Gardi, S. Ramasamy, Y. Liu, D. Zammit-Mangion and Daniele Quaglia, Novel Avionics and Air Traffic Management Systems for Intent Based Operations, Tenth USA/Europe Air Traffic Management Research and Development Seminar (ATM2013).
- R. Seresinhe, C. Lawson, A. Shinkafi, D. Quaglia and I. Madani, Airframe systems power off-take modelling in more-electric large aircraft for use in

trajectory optimisation; 29th Congress of the International Council of Aeronautical Sciences, 2014, St Petersburg, Russia, ICAS 2014

- A. Shinkafi, C. Lawson, R. Seresinhe, D. Quaglia and I. Madani, An intelligent ice protection system for next generation aircraft trajectory optimisation; 29th Congress of the International Council of Aeronautical Sciences, 2014, St Petersburg, Russia, ICAS 2014

### **CleanSky Technical Reports**

- D. Quaglia, I. Madani, H. Jia, D. Zammit-Mangion. Optimal Trajectories Concepts for Cycle 1. Document number: SGO-WP 3.2-C-U-OUT-0143.
- D. Quaglia, I. Madani, H. Jia, D. Zammit-Mangion. Performance Comparison between the SPOT and APM-Turbomatch Models. Document number: SGO-WP 3.2-C-U-RPT-0221.
- S. Hartjes, D. Quaglia, I. Madani, D. Nalianda, M. Sammut, R. Muscat, D. Visser, H. Jia, R. Sabatini, D. Zammit-Mangion, E. Stenzel. Report on the Performance Analysis of the Trajectories Cycle 1. Document number: SGO-WP 3.2.2-C-U-DEL-0039.
- D. Quaglia, I. Madani, H. Jia, R. Sabatini, D. Zammit-Mangion. Feedback to GATAC Tool Design from Lessons of Cycle 2. Document number: SGO-WP 3.2-C-U-OUT-0253.
- S. Hartjes, D. Quaglia, I. Madani, M. Sammut, D. Visser, H. Jia, R. Sabatini, D. Zammit-Mangion, E. Stenzel. Report on the Performance Analysis of the Trajectories Cycle 2. Document number: SGO-WP 3.2.2-C-U-DEL-0280.
- D. Quaglia, I. Madani, A. Gardi, H. Jia, R. Sabatini, D. Zammit-Mangion. Optimal Trajectory Concepts for Cycle 2. Document number: SGO-WP 3.2.2-C-U-OUT-0303.
- D. Quaglia, S. Ramasamy, A. Gardi, I. Madani, H. Jia, R. Sabatini, D. Zammit-Mangion. Software Design Description - Aircraft Dynamics Model (ADM) for 3D/4D Trajectories. Document number: SGO-WP 3.1-C-U-OUT-0327.

- D. Quaglia, S. Ramasamy, A. Gardi, I. Madani, H. Jia, R. Sabatini, D. Zammit-Mangion. Software Requirements Description - Aircraft Dynamics Model (ADM) for 3D Trajectories. Document number: SGO-WP 3.1-C-U-OUT-0328.
- A. Gardi, S. Ramasamy, D. Quaglia, I. Madani, H. Jia, R. Sabatini, D. Zammit-Mangion. Software Design Description - Air Traffic Management Model. Document number: SGO-WP3.1-C-U-OUT-0341.
- S. Ramasamy, A. Gardi, D. Quaglia, I. Madani, H. Jia, R. Sabatini, D. Zammit-Mangion. Software Design Description - Demographic Distribution Database (D3) Exploitation and Integration in GATAC. Document number: SGO-WP 3.1-C-U-OUT-0333.
- S. Ramasamy, A. Gardi, D. Quaglia, I. Madani, H. Jia, R. Sabatini, D. Zammit-Mangion. Software Design Description - Digital Terrain Elevation Database (DTED) Exploitation and Integration in GATAC. Document number: SGO-WP 3.1-C-U-OUT-0334.
- A. Gardi, S. Ramasamy, D. Quaglia, I. Madani, H. Jia, R. Sabatini, D. Zammit-Mangion. Software Requirements Description - Air Traffic Management Model. Document number: SGO-WP3.1-C-U-OUT-0336.
- S. Ramasamy, A. Gardi, D. Quaglia, I. Madani, H. Jia, R. Sabatini, D. Zammit-Mangion. Trajectories Generated by GATAC v3 Beta. Document number: SGO-WP 3.3.2-C-U-RPT-0329.
- D. Quaglia, A. Gardi, I. Madani, H. Jia, R. Sabatini, D. Zammit-Mangion. Review of the environmental gains from the Optimal Trajectories Regional Specificities. Document number: SGO-WP 3.2.2-C-U-RPT-0313.
- A. Gardi, S. Ramasamy, D. Quaglia, I. Madani, H. Jia, R. Sabatini, D. Zammit-Mangion. Air Traffic Management Models and Constraints for GATAC Integration. Document number: SGO-WP 3.2.3-C-U-OUT-0335.
- G. Poussin (Thales Avionics), GSAF (Cranfield University). Intermediate Models and Tools Assessment Report for Cycle 2.
- R. Seresinhe, D. Quaglia, M. Pelletier de Chambure, L. Virgili, S. Yunos. Report on the Performance Analysis of Trajectories Using GATAC Version 3. Document number: D-3.2.2-7, Clean Sky, 2014

# Chapter 2

## Literature study

The literature review carried out during the research period is divided into three main sections. The first section introduces and discusses trajectory optimisation problems which other researchers have encountered with particular attention on reduction of pollutants and noise annoyance due to air traffic. The second section gives an understanding of optimal control problems applied as trajectory optimisation which allows to achieve the objectives introduced in the previous chapter. Finally the third section introduces the optimisation techniques available that were used to optimise the formed trajectory problem.

### 2.1 Trajectory Optimisation

Trajectory optimisation is a wide and important area in atmospheric and space flights which includes planning, guidance, navigation and control. Initial work on trajectory optimisation was driven primarily by the space exploration during the middle of the last century which provided challenging technical problems. In parallel the continuous and fast improvement in digital computers provided the tools to solve numerically those problems [13–15].

Probably the most famous problem where trajectory optimisation was applied and allowed to achieve an extraordinary result is the so called *Minimum time to climb of a supersonic aircraft* problem [16]. It simply poses that a supersonic aircraft has to climb from mean sea level to 20 km minimizing the overall flight time. For many years, this problem was considered one of the most challenging problems

in the trajectory optimisation field. Intuitively a minimum-time path would be a direct and shortest route to the target. Instead the solution turned out to be very counter-intuitive. The supersonic aircraft initially climbs to approximately 10 km, then it performs a rapid dive where at the end of it the aircraft becomes supersonic, then a phase of acceleration during a slow climb and finally the rapid climb with deceleration to target speed. The optimal climb would take 320 s against over 600 s following a normal direct path approach. The optimised altitude profile is shown in FIGURE 2.1

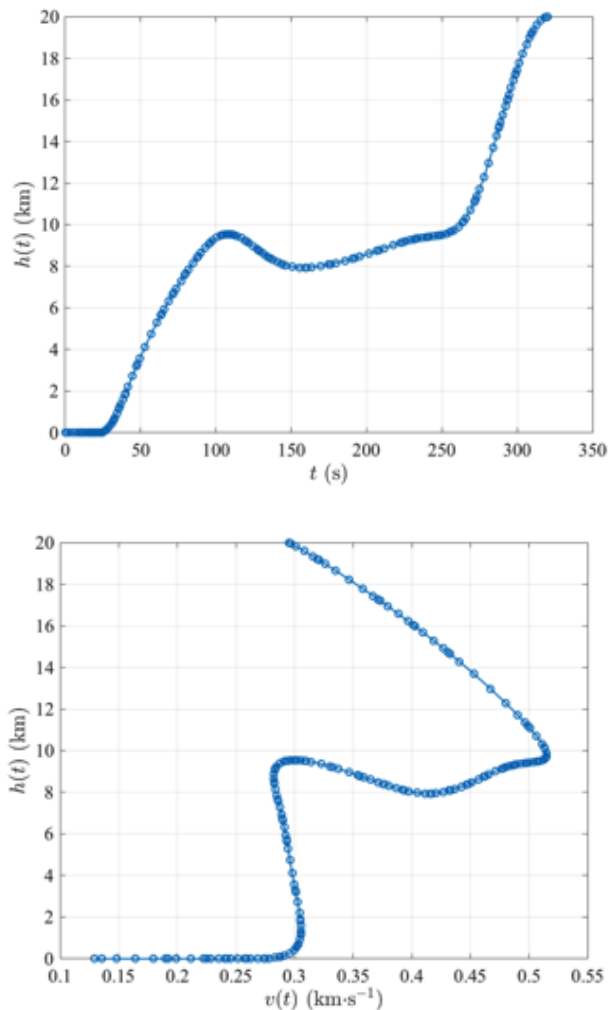


FIGURE 2.1: Altitude and speed profiles of minimum time to climb for a supersonic aircraft problem [17]

Nowadays, trajectory optimisation has expanded into a wide range of aerospace applications. More complex problems are solved including orbital transfer of spacecraft, trajectory planning of commercial aircraft and unmanned aerial vehicles (UAV).

However, trajectory optimisation problems are a branch of the more generic optimisation problems which can be classified in several ways. According to Hull[18], problems set to be optimised can be classified as per nature of equations used and resulting unknowns to be optimised. Optimisation of systems defined by algebraic equations where the unknowns are points are called Parametric Optimisation Problems (POP). Optimisation of systems defined by algebraic equations and ordinary differential equations where the unknowns are points and curves are called Optimal Control Problems (OCP).

In order to describe the different methods available for solving optimisation problems, the following classification as per relevant criteria may be defined as follows:

- **The nature of the object function and constraints involved** (linear, nonlinear, geometric, quadratic).
- **The presence of constraints** (equality or inequality constrained or unconstrained problems).
- **The deterministic nature of the variables** (deterministic or stochastic programming problems).
- **The number of objective functions** (single and multi-objective programming problems).
- **The value permitted for the decision variables** (Integer or real-valued programming problems).

According to the classification provided, the aircraft trajectory optimisation problem can be classified as constrained, dynamic, optimal control, nonlinear, real-valued, deterministic, multi-objective, and multi-parameter problem.

Each problem type has its own resolution technique which are going to be discussed in details in section 2.2. The strategy of most of the techniques however is to obtain an approximated solution of the given problem by applying mathematical tools obtaining auxiliary problems of another type. For example, OCP problems are solved numerically by discretisation of the continuous variables and then solving the approximated problem as a parametric optimisation problem.

### 2.1.1 Parametric Optimisation Problems

A generic parametric optimisation problem is defined formally as follows:

$$\begin{aligned}
 & \text{minimize} && J(\mathbf{x}) && \mathbf{x} \in \mathfrak{R}^n \\
 & \text{subject to} && \mathbf{f}(\mathbf{x}) = 0 \\
 & && \mathbf{g}(\mathbf{x}) \leq 0
 \end{aligned} \tag{2.1}$$

where  $\mathbf{x}$  is the  $n$ -dimension vector of the decision variables,  $J(\mathbf{x})$  is the cost-function and  $\mathbf{f}(\mathbf{x})$  and  $\mathbf{g}(\mathbf{x})$  define the equality and inequality constraints respectively. One main advantage of the parametric optimisation problem is that it can be solved straight away using non-linear optimisation techniques which will be discussed later.

The trajectory optimisation if approached as a parametric problem needs to be described without ambiguities with a set of parameters. A commercial aircraft generally follows a sequence of flight procedures (e.g. climbing maintaining a constant indicated airspeed, cruise at a fixed altitude and Mach number, descending maintaining a constant Mach number with idle throttle, etc.) where each procedure may vary due to certain state of flight. For example an aircraft can perform the climbing phase at different indicated airspeed and a cruise phase can happen at different altitudes and Mach number. Hence the trajectory seems be parametrized naturally into a set of parameters.

Trajectory optimisation as parametric problem has been already used by other researchers. In 2006, Vormer optimised continuous descents for arrival traffic scenarios at Amsterdam Airport Schiphol in The Netherlands where the flight path was represented as sets of straight and curved segments, and parametrized using aircraft accelerations, path lengths, turn radii and path angles [19]. In 2009, Wu represented the trajectory by series of paths parametrized by set of speeds, altitudes and throttle settings [20]. Also in 2009, Torres parametrized the trajectory using only two sets of variables: aircraft speed and engine thrust setting to describe trajectory along the defined segment [21]. In 2012, Valenzuela parametrized the aircraft flight in trajectory patterns where horizontal and vertical profiles were considered uncoupled and adapted for each flight application. For example for a descending phase, the vertical profile pattern was modelled using flown distance till deceleration for descend is needed, a target descent Mach speed and a target

descent calibrated airspeed. In addition the cruise Mach number and altitude were added into the optimisation. The overall 5 parameters of the decision variables were enhanced to 13 including 4 waypoints (4 latitude and 4 longitude parameters) describing the aircraft horizontal pattern. The lower number of parameters was also possible because the aircraft flight phases were modelled by flying at constant Mach or Calibrated airspeed, constant altitude and constant path angle or by given engine rating (e.g. Take-Off full throttle or idle). The modelling results were too simplistic for Trajectory Based Operation (TBO) applications and in addition the turning was considered instantaneous which could be accepted in cruise phase but not at lower altitudes close-by the airport where the speeds are low and turning could mean several seconds where the plane is banking. In 2012, Vaddi[22] proposed a 4D green trajectory design for Terminal Area (TMA) operations and approached as parametric optimisation and solved using nonlinear optimisation techniques. In his research, Vaddi added the engine emissions and aircraft noise onto the trajectory optimisation problem for a B757 aircraft entering terminal airspace for landing. Flap deployment for the aircraft were limited to aircraft maximum airspeed, however, they were not introduced as decision variables in the optimisation but indirectly associated with scheduled time discretisation of the problem. A similar approach was used for the gear extraction. In this research, it is not possible to know a priori when the aircraft extract the different flaps and/or the gear but it is very important to directly connect it to the aircraft states especially due to the high impact to overall noise generation and perception on the ground.

### 2.1.2 Trajectory as Optimal Control Problems

Trajectory optimisation problems have been translated as optimal control problems since 1960 in the field of aerospace engineering, in particular in the field of space flight mission planning. The aim of the optimal control theory is to determine the controls to a dynamic system which optimise (i.e. minimise or maximise) a defined performance index while the dynamic system satisfies imposed constraints.

Intuitively, Rao [23] pointed out the importance to distinguish between trajectory optimisation and optimal control concept. In brief, Rao suggests it is more appropriate to use *trajectory optimisation* to describe problems where the inputs to



the system are static parameters and it is desired to determine the values of these parameters which optimise the given performance index (i.e. a function optimisation problem). On the hand using the term *optimal control* to describe problems where the inputs to the system are themselves functions and it is desired to determine the ultimate input function which minimise the given performance index (i.e. a functional optimisation problem). Therefore the modelling of the problem defines how it is going to be called. If the trajectory optimisation problem we want to optimise has inputs which are function of time (e.g. throttle and roll history controls are functions of time), function of states (e.g. path constraints) and also presence of static parameters, the problem will be called Optimal Control Problem. Otherwise if the problem is modelled in such a way where the inputs are summarised as static parameters (e.g. a list containing aircraft route waypoints location, climbing and descending scheduled airspeed values, initial cruise altitude and initial cruise airspeed) then the problem will be called trajectory optimisation problem.

A generic continuous optimal control problem is posed formally as follows:

Determine the control history  $u(t) \in \mathfrak{R}^m$ , the state history  $x(t) \in \mathfrak{R}^n$ , the parameters  $q \in \mathfrak{R}^r$ , the initial time  $t_0 \in \mathfrak{R}$  and the final time  $t_f \in \mathfrak{R}$  that optimises the performance index

$$J = \Phi[\mathbf{x}(t_0), t_0, \mathbf{x}(t_f), t_f; \mathbf{q}] + \int_{t_0}^{t_f} \Gamma[\mathbf{x}(t), \mathbf{u}(t), t; \mathbf{q}] dt \quad (2.2)$$

subject to the system dynamics

$$\dot{\mathbf{x}} = \mathbf{f}[\mathbf{x}(t), \mathbf{u}(t), t; \mathbf{q}] \quad (2.3)$$

the path constraints

$$\mathbf{C}_{min} \leq \mathbf{C}[\mathbf{x}(t), \mathbf{u}(t), t; \mathbf{q}] \leq \mathbf{C}_{max} \quad (2.4)$$

and the boundary conditions

$$\phi_{min} \leq \phi[\mathbf{x}(t_0), \mathbf{x}(t_f), t; \mathbf{q}] \leq \phi_{max} \quad (2.5)$$

where  $t \in [t_0, t_f]$  is the independent variable.

The differential equation Eq. 2.3 describes the dynamics of the considered system while the Eq. 2.2 measures the quality of the resulting trajectory. If the interest is to minimise the performance index, then a combination of states and control which return a lower value of  $J$  is preferred. Historically the optimisation control problem was known as the Bolza problem. If  $\Phi = 0$  the problem is called a Lagrange problem and if  $\Gamma = 0$  the problem is called a Mayer problem. In addition a trajectory optimisation problem could use static parameters, which have to be considered in the performance index and in extreme cases also more than one phase. For example the trajectory optimisation of a space rocket would involve more than one phase, describing different dynamic systems due to instantaneous lose of masses between the rocket stages. In that circumstance additional equations need to be added which provide the continuous of the states and controls or link them between the phases.

The application of optimal control to commercial aircraft trajectory optimisation started at the beginning using energy state approximations [16] and singular arcs [24]. Betts in [25] introduced first time realistic path constraints imposed at that time by FAA flight regulations. Those path constraints (i.e. flight at constant Mach number, constant flight rate and constant calibrated airspeed) were used because it was simple to translate the results obtained by the optimisation process to operational procedures to be followed by the pilot.

More recently, Soler [26] described the commercial aircraft trajectory in a sum of different flight phases and operational procedures combined together into a hybrid system. Giving the phase sequence as climbing, cruising and descending, the hybrid system had the characteristic of a controlled switched dynamic system where the switching times between the phases need to be determined to optimize fuel consumption and time.

With the new flight guidance proposed in SESAR and Clean Sky programmes, the flight mission is defined as a free-flight trajectory with more freedom to define the best trajectory without being bounded to current operational approach. Therefore it is appropriate to generate these optimal trajectories for specified goals (e.g. economical or environmental-friendly, etc.) with only concerning the aircraft performance capabilities and constraints at the same time.

With more attention to work focused on environmental objectives, in 2009 Hartjes [27] used optimal control to optimise noise and emissions along SID procedures

at Amsterdam (EHAM) airport. The number of phases of the OCP were reduced introducing switch functions which allowed replacing discrete transitions using a continuous smooth function. Houacine in 2010 [28] analysed the benefits of optimal control problem used as a tool of flight trajectory design to reduce noise generated along and fuel consumed for take-off and landing segments. Minimization of noise and emission have been introduced in the optimal control problem also by Oliveira in 2011 [29] for an on-board trajectory optimisation of RNAV departure and arrival procedures for a generic flight from a Amsterdam (EHAM) to Munich (EDDM). Both departure and arrival segments were optimised for time and fuel consumption. Noise annoyance was used in the optimisation of the departure phase and emissions with flight time objectives were considered in a multi-objective optimisation for the arrival segment.

In other contexts, Sridhar [30] used optimal control to obtain wind-optimal trajectories for a fixed selected altitude during cruise phase avoiding regions of airspace that facilitate persistent contrails formation. The same approach of constant altitude during the cruise phase was used by [31] to optimise DOC with the addition of arrival error cost associated to unexpected wind conditions.

## 2.2 Numerical Methods for solving Optimal Control Problems

Optimal Control Problems (OCP) must be resolved numerically with the exception of simple problems. In the past years several numerical approaches have been developed and today those numerical methods are principally divided into two categories: indirect and direct methods.

### 2.2.1 Indirect Methods

Indirect methods were the first kind of methods developed in solving optimal control problems and they apply the calculus of variations, also called Pontryagin's minimum principle [32]. In optimal control theory is well-known that the state of the system can be adjoined to the objective function and to path constraints forming the Hamiltonian. With reference to equations of the generic optimal

control problem from 2.2 to 2.5, the first order optimal conditions are derived using the augmented Hamiltonian, defined as:

$$\mathcal{H}(\mathbf{x}, \lambda, \mu, \mathbf{u}, t) = \Gamma + \lambda^T \mathbf{f} + \mu^T \mathbf{C} \quad (2.6)$$

where  $\lambda(t) \in \mathfrak{R}^n$  is the costate and  $\mu(t) \in \mathfrak{R}^c$  is the Lagrange multiplier associated with the path constraint. Deriving the Hamiltonian is sufficient to obtain the first order optimality conditions of the problem and obtaining the *Hamiltonian system* as follows:

$$\dot{\mathbf{x}} = \left[ \frac{\partial \mathcal{H}}{\partial \lambda} \right]^T, \quad \dot{\lambda} = - \left[ \frac{\partial \mathcal{H}}{\partial \mathbf{x}} \right]^T \quad (2.7)$$

The conditions as then stated. Initially by *Pontryagin's Minimum Principle*, then boundary conditions, then costate initial and final conditions or so called *transversality conditions* and concluding by the Lagrange multipliers for the path constraints conditions called *complementary slackness conditions* as follows:

$$\mathbf{u}^* = \arg \min_{\mathbf{u} \in \mathcal{U}} \mathcal{H} \quad (2.8)$$

$$\phi(\mathbf{x}(t_0), t_0, \mathbf{x}(t_f), t_f) = 0 \quad (2.9)$$

$$\lambda(t_0) = - \frac{\partial \Phi}{\partial \mathbf{x}(t_0)} + \boldsymbol{\nu}^T \frac{\partial \phi}{\partial \mathbf{x}(t_0)}, \quad \lambda(t_f) = - \frac{\partial \Phi}{\partial \mathbf{x}(t_f)} - \boldsymbol{\nu}^T \frac{\partial \phi}{\partial \mathbf{x}(t_f)} \quad (2.10)$$

$$\mathcal{H}(t_0) = - \frac{\partial \Phi}{\partial t_0} + \boldsymbol{\nu}^T \frac{\partial \phi}{\partial t_0}, \quad \mathcal{H}(t_f) = - \frac{\partial \Phi}{\partial t_f} - \boldsymbol{\nu}^T \frac{\partial \phi}{\partial t_f} \quad (2.11)$$

The Hamiltonian system, the boundary conditions, transversality conditions and complementary slackness conditions form the so called Hamiltonian Boundary Value Problem (HBVP) which can be solved as a two-point boundary value problem. However HBVP analytical solution is only possible for special cases and therefore not feasible for most practical problems. Numerical methods are necessary to transform the optimality, path and boundary conditions into an Non-Linear Problem (NLP). Betts published a complete description of shooting and collocation methods used for trajectory optimisation problems [33].

Shooting methods use numerical integration schemes, such as Runge-Kutta 4th order, and treat the two boundary value problems into a series of initial value problems. This produced sensitivity issues of the initial guess: a poor initial guess can lead to divergence due to instability of the integration of the equations, which were summarized by Bryson and Ho [34]. Difference techniques were developed

trying to resolve the sensitivity issue of the shooting methods. An approach was to solve a sequence of problems instead of the main problem, where the solution of one problem was used as the initial guess for a slightly modified one, till the main problem was solved.

Collocation indirect methods have been applied to problems since 1970. Collocation methods do not use numerical integration schemes which are computationally expensive as later will explain for the direct collocation methods. However a good initial guess for the costates and path is still required.

In summary the main complications of the indirect methods are the creation of a good initial guess for the problem which includes also the costates. The costate conditions also increase the dimension of the problem to solve.

## 2.2.2 Direct Methods

Direct methods seek to minimise the objective function directly by parametrising using specified function forms (e.g. polynomials) and therefore approximating the state and/or the control of the OCP problem and solving it without adding optimality conditions. The approximation of the state and/or control of the OCP allows *transcribing* the infinite-dimensional OCP problem into a finite-dimensional optimisation problem with algebraic constraints known as Non-Linear Programming (NLP) problem. One of the cons is the possible inaccuracy in the solution introduced due to approximation but as pro the overall system size is smaller and therefore the direct methods are computationally simpler than the indirect methods.

First Hull [18], then Rao [23] categorized direct methods in the following way: In the case where only the control functions are approximated, the resulting method is called *control parametrization method* and time-stepping numerical integration is required for state equations. These methods are called "shooting methods", named obtained by the analogy of controlling a shooting cannon to hit the target. When both the state and control are approximated the resulting method is called *state and control parametrization method* and time-stepping numerical integration is not required. These methods are further subdivided into *local* and *global* methods. Local methods break the problem dynamics into sub-intervals and the state and control at the sub-interval node is obtained by quadrature approximation and

not by integration. Global methods or so called Pseudospectral methods go even further. They span the entire problem interval. They approximate the solution of the problem by a finite sum of the form  $\mathbf{x}(t) = \sum_{k=1}^N a_k \phi_k(t)$ . The pseudospectral methods differ then in based of which function class to be used  $\phi_k(t)$  and how to determine the parameters of the coefficients  $a_k$ . Control parameterization methods include direct shooting shooting methods and direct multiple shooting method. State and control parameterization method include direct collocation methods and pseudo-spectral methods. The different types of direct methods can be seen in FIGURE 2.2.

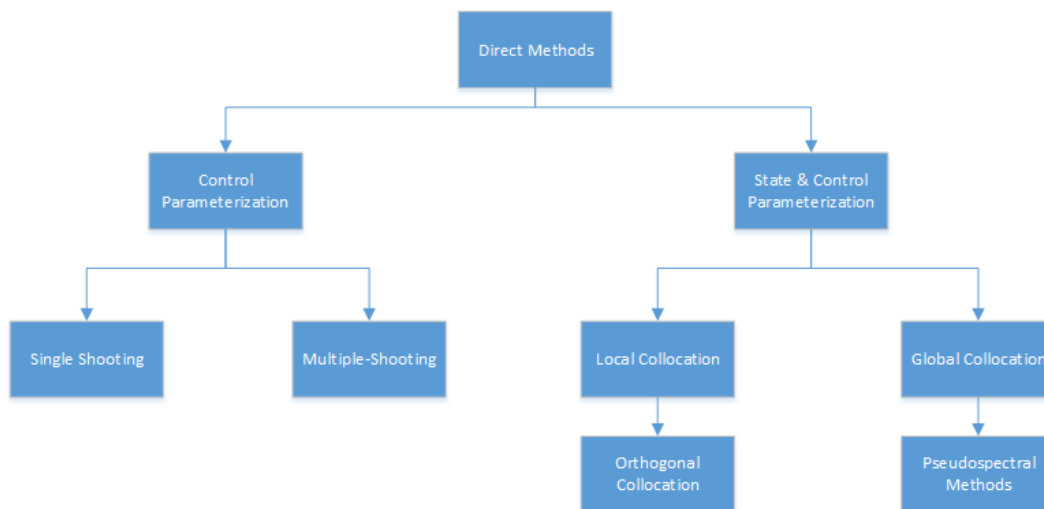


FIGURE 2.2: Different types of Direct Methods

### 2.2.2.1 Direct Shooting Methods

Direct shooting methods are part of control parametrization methods and is the most basic direct method for solving optimal control problems. The system control is parametrized using an approximated function such as:

$$\mathbf{u}(t) \approx \sum_{i=1}^m \mathbf{a}_i \psi_i(t) \quad (2.12)$$

where  $\mathbf{a}_i, i = 1, \dots, m$  are the parameters which have to be obtained by the NLP solver and  $\psi_i(t), i = 1, \dots, m$  are the selected approximation functions (e.g. polynomials). Time-stepping numerical integration algorithms are then used to solve

differential equations. Cost function is similarly determined by a quadrature approximation. Direct shooting method results very simple in numerical implementations however it suffers of sensitivity errors, especially due to numerical integration performed over long time intervals.

### 2.2.2.2 Direct Multiple Shooting Methods

Direct multiple shooting method is the other type of control parametrization methods. In multiple shooting methods the time interval  $[t_0, t_f]$  is divided into  $S+1$  sub-intervals. The direct shooting method previously described in 2.2.2.1 is used for each sub-intervals using initial conditions the values of states at the beginning of each sub-intervals and optimising the parametrized control coefficients. Continuity between sub-intervals is introduced by the following condition:

$$\mathbf{x}(t_i^-) - \mathbf{x}(t_i^+) = 0 \quad (2.13)$$

The overall optimisation problem is increased due to including values of the state for each sub-interval as parameters, however the direct multiple shooting method result in an improvement due to smaller time intervals and therefore integration errors. Direct multiple shooting method still results simple in numerical implementations however it suffers of sensitivity errors like the corresponding indirect methods (divergence and instability). Numerical integration also results a slow computation which will be seen solved in direct collocation methods. Betts[33] and Rao [23] describe more in details the direct shooting methods and their implementations used to solve OCPs.

### 2.2.2.3 Direct Collocation Methods

In the direct collocation methods the states and controls are both approximated by functional form and have been shown to be more powerful in solving OCP problems. In the direct collocation methods the independent variable interval (i.e. time) is divided into  $S$  subintervals  $[t_{s-1}, t_s], (s = 1, \dots, S)$  and final time  $t_f = t_S$ .

The approximation for the controls and the states are described as follow:

$$\mathbf{u}(t) \approx \sum_{n=1}^N \mathbf{a}_n \Psi_n(t) \quad (2.14)$$

$$\mathbf{x}(t) \approx \sum_{n=1}^N \mathbf{b}_n \Psi_n(t) \quad (2.15)$$

where  $\mathbf{a}_n$  and  $\mathbf{b}_n$  are the coefficients respectively for control and states to be optimised and  $\Psi_n$  the trial function to be used. The trial functions are commonly trigonometric functions or orthogonal polynomials such as Legendre polynomials. For these methods the state is therefore not integrated explicitly using a normal integration scheme but implicitly using quadrature at specific nodes:

$$\mathbf{x}(t_{i+1}) \approx \mathbf{x}(t_i) + \sum_{q=1}^Q \beta_{iq} \mathbf{f}[\mathbf{x}(\tau_q), \mathbf{u}(\tau_q), \tau_q] \quad (2.16)$$

where  $\tau_q (q = 1, \dots, Q)$  are the nodes of the quadrature approximation. The quadrature approximation is also used to approximate the integral part of the the cost function resulting in:

$$J \approx \Phi[\mathbf{x}(t_0), \mathbf{t}_f, t_f] + \sum_{q=1}^Q \beta_{iq} \Gamma[\mathbf{x}(\tau_q), \mathbf{u}(\tau_q), \tau_q] \quad (2.17)$$

At the end the continuity between subintervals is enforced by the compatibility condition defined as follows:

$$\mathbf{x}(t_s^-) = \mathbf{x}(t_s^+), (s = 2, \dots, S - 1) \quad (2.18)$$

A local collocation method is similar to the algorithm used for direct multiple shooting method previously described in 2.2.2.2. The time interval is divided into sub-intervals and continuity between sub-intervals is ensured by adding compatibility constraint at each sub-interval interface.

An example of global collocation method is the recently grown pseudo-spectral method. In pseudospectral method the state is approximated using a global polynomial form and collocation is performed at chosen points.

#### 2.2.2.4 Direct Pseudo-spectral Methods

Direct pseudo-spectral methods are the most recent methods developed to solve ordinary and partial differential equations. Most work has been started in fluid



dynamics research and particularity of the methods is that global form of orthogonal collocation is used at chosen points. Therefore the degree of the polynomial form used is varied while the chosen points are fixed. The term pseudospectral methods was first introduced by Orszag in 1972 [35] however only in 1988 it was first used to solve nonlinear OCP problems where Chebyshev polynomial were used [36]. Rao pointed out that Chebyshev polynomials lead to more complicated conditions because do not satisfy the isolation condition [23]. The Lagrange polynomials were therefore most used as form function in pseudospectral methods. The collocation points which were used with Legendre polynomials are known as Gauss, Gauss-Radau and Gauss-Lobatto.

In the direct pseudospectral method the independent variable interval is  $\tau \in [-1, 1]$  and the controls and states are approximated as follow:

$$\mathbf{x}(\tau) = \sum_{i=1}^N \mathbf{x}(\tau_i) L_i(\tau) \quad (2.19)$$

$$\mathbf{u}(\tau) = \sum_{i=1}^M \mathbf{u}(\tau_i) L_i(\tau) \quad (2.20)$$

where  $L$  is the Legendre polynomials used as form function and controls and states are interpolated respectably for  $N$  and  $M$  nodes. The states can be differentiated easily as follow:

$$\dot{\mathbf{x}}(\tau) = \sum_{i=1}^N \mathbf{x}(\tau_i) \dot{L}_i(\tau) \quad (2.21)$$

## 2.3 Nonlinear Programming Algorithms

As shown in the previous sections, Optimal Control Problems or Parametric Optimization Problems lay on the ability to solve nonlinear optimisation problems also called nonlinear programming (NLP). The choice of NLP algorithm is very important to achieve robustness of the selected method to solve the problem.

A generic NLP is described as follow:

$$\begin{aligned}
& \text{minimize} && J(\mathbf{x}) \\
& \text{subject to} && \mathbf{f}(\mathbf{x}) = 0 \\
& && \mathbf{g}(\mathbf{x}) \leq 0 \\
& && \mathbf{x}_L \leq \mathbf{x} \leq \mathbf{x}_U
\end{aligned} \tag{2.22}$$

where  $\mathbf{x} \in \Re^n$  is the  $n$ -dimension vector of the problem decision variables which has to satisfy lower and upper boundaries respectively  $\mathbf{x}_L$  and  $\mathbf{x}_U$ ;  $J(\mathbf{x})$  is the cost-function and  $\mathbf{f}(\mathbf{x}) \in \Re^m$  and  $\mathbf{g}(\mathbf{x}) \in \Re^p$  define respectively the equality and inequality constraints to the problem.

First order optimality conditions are known as Karush-Kuhn-Tucker conditions (KKT) and are described as follows:

$$f_i(\mathbf{x}) = 0, \quad (i = 1, \dots, m) \tag{2.23}$$

$$g_i(\mathbf{x}) \leq 0, \quad (i = 1, \dots, p) \tag{2.24}$$

$$\tau_i \geq 0, \quad (i = 1, \dots, p) \tag{2.25}$$

$$\tau_i g_i \geq 0, \quad (i = 1, \dots, p) \tag{2.26}$$

$$\nabla J(\mathbf{x}) + \sum_{i=1}^m \lambda_i \nabla f_i(\mathbf{x}) + \sum_{i=1}^p \tau_i \nabla g_i(\mathbf{x}) = 0 \tag{2.27}$$

The equation 2.27 shows how important is to have information about derivatives of the objective function and the constraint functions with respect of the decision variables. Nonlinear problems may be *sparse* or *dense* based on the nature of those derivatives. When the majority of the derivatives are non-zero, the NLP problem is called dense. When the majority of the derivatives are instead zero, the NLP problem is called sparse. Rao describes how normally dense problems typically have only few hundreds variables and constraints, and instead sparse problems could have up to millions of variables and constraints [23].

Numerically techniques to solve NLP are mainly divided in gradient-based and heuristic-based. The main difference between gradient-based and heuristic-based techniques can be reduced to whether or not they require the computation of derivatives in the resolution of the problem. Gradient-based which are based on computation of derivatives provides a faster resolution of the problem but could

end up in a local minimum of the problem (this is to be taken into account for problems which its nature is not well known). Another disadvantage or limitation of gradient-based techniques is that the system functions has to be continuous, otherwise derivatives can not be computed; this is a big limitation for example in discontinuous systems, e.g. with integers decision variables. Heuristic-based instead allow the solver to obtain the global solution but the resolution time increases a lot.

### 2.3.1 Gradient Algorithms

Gradient-based algorithms are used to solve NLPs problems using derivatives of the objective function and constraint functions. All the gradient algorithms are iterative. First an initial guess of the unknown decision variables is required. From the known decision variables a "direction" and a "step length" are determined which are used to update the decision variables for the next iteration.

The iterative process of the gradient algorithms which follow the line search approach [Powell][Gill] can be summarized as follow:

$$\mathbf{x}_{k+1} = \mathbf{x}_k + \alpha_k \mathbf{p}_k \quad (2.28)$$

where  $k$  is the iteration index during the process of optimisation,  $\alpha_k$  is the search direction and  $\mathbf{p}$  the search step length estimated at the  $k$  iteration to compute the  $k + 1$  iteration decision variables. For example, for an unconstrained problem, the direction  $\mathbf{p}$  is defined as follow:

$$\mathbf{p}_k = -\mathbf{g}_k(\mathbf{G}_k)^{-1} = -\nabla J(\mathbf{x})(\nabla^2 J(\mathbf{x}))^{-1} \quad (2.29)$$

where  $\mathbf{g}_k$  is the Gradient and  $\mathbf{G}_k$  is the Hessian of the cost function  $J(\mathbf{x})$ . The first necessary condition is that  $g(x) = 0$  but it is not sufficient. The second sufficient condition is that  $G(x) \geq 0$  which means be defined positive. These conditions clearly require that the cost function  $J(x)$  be at least twice continuously differentiable.

The Newton's method as just defined may still be slow to converge or may even diverge. [Nocedal and Wright] modified the Newton's method and stabilize it

introducing line searches and thrust regions. The resulting method is called quasi-Newton.

The most diffuse quasi-netwon method is the Sequential Quadratic Programming (SQP) method. During a major iteration the cost function is approximated by a quadratic function and linearised constraint functions are also estimated. The solution of this problem (approximated problem) is used to generate step length and direction for the next major iteration. The BFGS update is done at each major iteration where a constant Hessian is assumed.

SQP method is defined as global convergence due to these advantages: - Use an approximation of the Hessian - Satisfaction of the KKT conditions - Direct handling of equality and inequality constraints

One of the most diffuse SQP method is SNOPT which has been successfully implemented in many direct methods in solving OCP problems such as...

### 2.3.2 Heuristic Algorithms

Heuristic methods differs mainly from gradient method in sense than heuristic method is a *global* technique while a gradient algorithm is a *local* technique. Gradient algorithms as explained in the previous section rely on the convexity and smoothness of the cost function and constraint functions. A solution produced by gradient algorithm may not be a global minimum and depends on the location of the initial guess. For example the Rastringin's function[37], poses a challenge for Heuristic algorithms such as Genetic Algorithms(GA). MATLAB software suite provides examble of this function and how to obtain the global optimal solution and not local solution. From FIGURE 2.3 it is possible to see how it is important for some functions to provide a good initial point when solving the problem.

It is difficult to graphically know the shape of trajectory optimisation cost functions and therefore understand if a gradient based algorithm is well suited or not. In the research community there have been cases where optimal control problems presented more than one local minima. Hence the need is real to consider other kind of algorithms which can provide a global technique and be used for at least validation in case the optimisation time becomes too high.

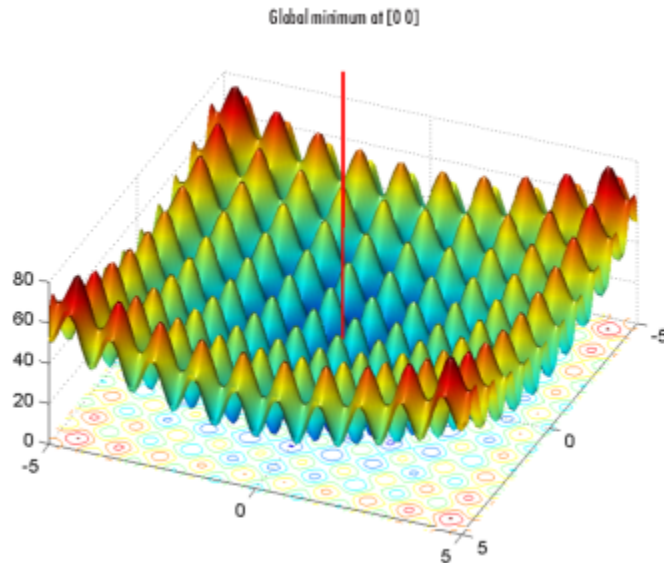


FIGURE 2.3: Rastrigin's function global minimum and local minimum points

In an heuristic algorithm the search in the decision space is performed in a stochastic manner instead of in a deterministic manner as performed by the gradient algorithms. Rao during his research work[38] describes the Genetic Algorithms methods composed of a sequence of 5 processes: encoding, fitness, selection, crossover and mutation. The optimisation decision variables are represented in the encoding phase, such as using binary encoding. The fitness phase is like the object function which is wanted to be optimised. The selection phase determines the "survival" of the fitness, meaning the decision variables which produce the fitness objective value are selected for the next process which is the crossover and mutation. The crossover and mutation processes introduce the stochastic of the heuristic optimisation process. Different decision variables set which form the "population" of the problem are paired randomly and in addition there also a random mutation in the set resulting in new formed set of population to evaluate its fitness against the selected objectives. This one cycle of process involving encoding, fitness, selection, crossover and mutation is called a generation. Many generations are required to obtain solutions which are close to the optimal, infact heuristic methods are really computationally slow due to their randomness of producing results. One of the disadvantages of the heuristic methods is that there is not a clear way to understand if a problem has reached the global minimum or not. It is just a matter of keep generating new results and evaluate their fitness against the previous generation. Betts[33] believes GA and other heuristic methods are not suitable for trajectory optimisation problems. McEnteggart and Whidborne

[39] adopted GA to solve multi-objective trajectory optimisation problem for the planning of environmentally-friendly trajectories. GA optimiser was used in parallel to an inverse dynamic model which was used to model the aircraft dynamics. The concept was rather interesting, however, the aircraft dynamic had to result simplistic to allow its inversion. In the end the computational heaviness of GA and most importantly, the challenges faced to integrate GA and the pseudospectral method, especially when an off-the-shelf optimisation solver is adopted, GA was not appeared to be suitable for this study.

## 2.4 Single and Multi-Objective Optimisation

Single-objective optimisation aims at finding the control variables that drives a set of system states satisfying trajectory constraints with the purpose to minimize a single cost function as described before. However for problems that involves more than one objective and especially with contrasting objectives (such as for this work), multi-objective optimisation can be used to have a better view of the solutions trade-off.

Multi-Objective Optimization (MOO) involves more than one objective into the optimisation problem at the same time and achieve a Pareto optimality. Its name is due to Vilfredo Pareto during his study of distributional efficiency between social welfare and resource allocation [40]. Because of the presence of more than one objective, the optimal solution is not a single point in the domain but a trade-off of optimal solutions. The set of ultimate trade-off solutions is known as the Pareto frontier. In case of two objective problem the Pareto frontier is a curve that traces the optimal solutions minimising both objective functions. In one point of the curve, one of the solution's objective can not be improved any further without deteriorating the other objective. For example, let's consider the problem known as ZDT1 [41] and the formulation is as follow in EQ. 2.30.

$$\begin{aligned} f_1 &= z_1 \\ f_2 &= g(1.0 - \sqrt{\frac{f_1}{g}}) \\ g(z_2, \dots, z_n) &= 1.0 + \frac{9}{n-1} \sum_{i=2}^n z_i \end{aligned} \tag{2.30}$$

where  $f_1$  and  $f_2$  are the objective which want to be optimised and  $z$  is the decision vector for the ZDT1 problem and  $0 \leq z_i \leq 1, i = 1, \dots, n$  and  $n$  is the a parameter

to scale the problem. The pareto front obtained for the ZDT1 problem is shown in FIGURE 2.4.

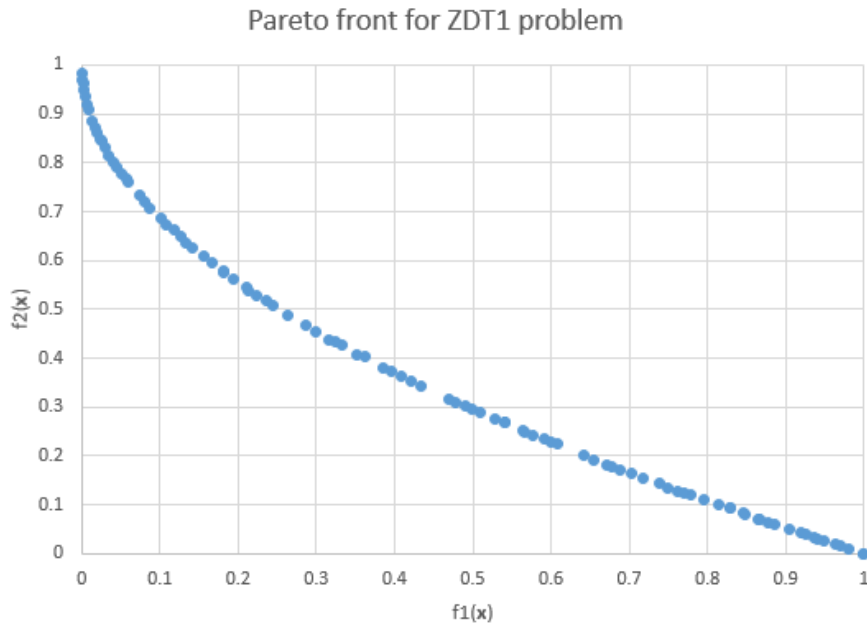


FIGURE 2.4: Example of a Pareto front for ZDT1 problem

Several methods have been developed during the years to perform MOO and are now being described.

### 2.4.1 Weighted-sum Method

The weighted-sum method is the most widely used to solving multi-objective optimisation problems and allows to combine several objective (MOO) functions into one using different weight values per objective function. The relative value of the weights reflect the relative importance of the objective functions. The weighted-sum method is shown in mathematical form as follows:

$$\min_{\mathbf{z}} [J_1(\mathbf{z}), J_2(\mathbf{z}), \dots, J_n(\mathbf{z})] = \min_{\mathbf{z}} \sum_{i=1}^n w_i J_i(\mathbf{z}) \quad (2.31)$$

where  $J_i$  is the  $i$ -th objective function and  $w_i$  is the  $i$ -th weight. If all the weights are positive ( $w_i \geq 0$ ) the obtained minimum is Pareto optimal[42]. The weights are generally normalised (i.e.  $\sum_{i=1}^n w_i = 1$ ), providing that the MOO objective functions are also normalised.

Multiple optimisation runs conducted with different weights following the rules just explained allow to obtain multiple points on the Pareto front. However, this simple approach could not ensure evenly spread points on the Pareto front[43]. If part of the Pareto front is non-convex, then the weighted-sum method can not obtain solutions on the Pareto front. This problem arise during Deb's work in 2001 [44]. Figure 2.5 shows a non-convex region of the Pareto front.

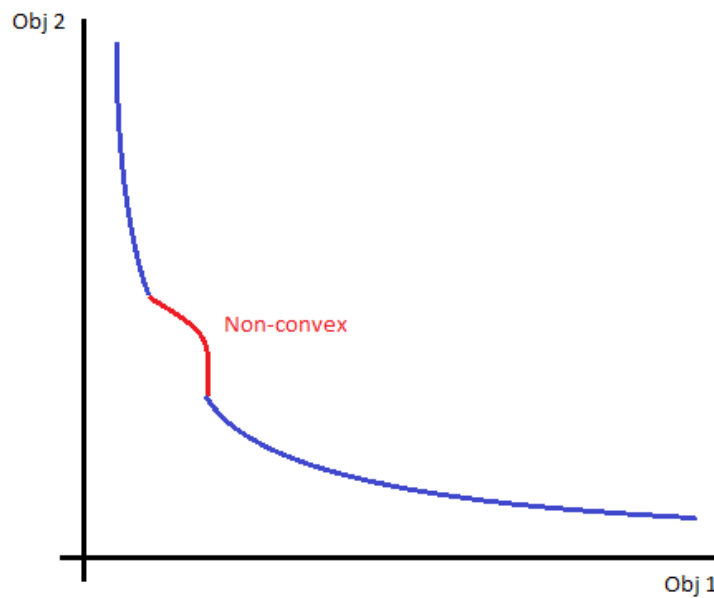


FIGURE 2.5: Example of a Pareto front for two criteria multi-objective problem with non-convex region

## 2.4.2 $\varepsilon$ -constraint Method

The  $\varepsilon$ -constraint method is introduced to tackle the difficulties of the weighted sum method in order to obtain intermediate optimal solution when a non-convex optimisation case occurs. The  $\varepsilon$ -constraint method consist in optimising the problem only for the  $i$ -th objective at a time while the others are reformulated as constraints. The  $\varepsilon$ -constraint formulation is the following

$$\begin{aligned} \min_{\mathbf{z}} J_i(\mathbf{z}) \\ J_j \leq e_j, \quad i \neq j, \quad j = 1, \dots, n_J \end{aligned} \quad (2.32)$$

This is also a simple approach. By progressively changing the constraint value  $e_j$ , different point on the Pareto front are obtained. Andersson [43] explains well this



methodology: first the extremes of the Pareto front are obtained, then the range of the different objective functions are calculated and constraint values selected accordingly. The method works well in obtaining an even spread Pareto front, only if the Pareto front is continuous.

## 2.5 Environmental Objectives

### 2.5.1 Noise annoyance

Aircraft noise is part of the pollution produced by an aircraft during the flight. The aircraft global noise is a combination of many sources. The noise sources are engine, wing, control surfaces, auxiliary power generator, hydraulic system, etc. The most contribution to the noise produced by aircraft is generated by airframe (i.e. fixed and moveable surfaces) and engine. In Figure 2.6 these contributions are identified.



FIGURE 2.6: Airframe noise sources

The departure and approach phases are the noisiest in the mission profile of civil aircraft as initially shown in Figure 1.5 for the city pair mission. The reason is because during the departure phase, engines are at the maximum throttle position but the high-lift surfaces are not fully extended. During the approach phase, in the ideal condition of engines in idle condition, the high-lift surfaces are full extracted

and they generate a lot of noise due to aerodynamic turbulence. In addition during the final approach phase, the extraction of the landing gear increase this aerodynamic noise component. For last extremely noisy reverse thrust procedure may be applied immediately after touch down. In 2001 the FAA had measurement campaign and published noise level data for certified airplanes [45].

Noise is something that can be different from person by person and therefore initially only surveys were used to analyse noise annoyance. Verkeyn in 2004 explained that Schultz in 1978 was the first who started modelling noise annoyance during his surveys on the produced noise of airway, railway and road traffic. In his work, the noise annoyance levels were function of the sound exposure. In addition he started studying the percentage of the people who were highly annoyed for each noise event.

In 1982, Fidell[46] went through three different telephonic surveys before and after three noise abatement procedure which were been tested at John Wayne airport, California. The analysis of the three different procedures showed significant drop of noise exposure levels, although the response of the surveyed people was in contrast with the exposure levels measured and manifested still high annoyance due to the airport activities.

#### **2.5.1.1 Airframe Noise**

Airframe noise is often called Aerodynamic noise. It is generated by iteration of air flow with the airframe. The airframe configuration is disturbed by control surfaces deflections which increase the noise. This statement is cleared by ESDU [47] that shows how a landing configuration aircraft generates much more noise for all the audio spectral frequencies than in clean configuration. It is possible to say that everything that modifies the flow around the airframe generates more noise than it is already generated. The list of aircraft components that are responsible of airframe noise are:

- Main wing
- Slats
- Flaps
- Spoilers

- Horizontal and vertical tails
- Control surfaces
- Landing gears

The order of noise level generated by these devices may change according to the specific design and configuration of the aircraft. For a typical wide-body aircraft such as Airbus A320, the highest level of airframe noise comes from the extracted landing gear during landing phase.

### **2.5.1.2 Engine Noise**

Engine noise is the main noise source for the aircraft [48] and its contribution can be split in several components related to engine activity. These components are:

- Jet streams noise
- Turbine noise
- Noise related with the combustion
- Fan and compressor noise

The percentage of noise generated by each component varies between engine types and also as function of bypass ratio [48]. Examples of noise radiation patterns are shown in Figure 2.7.

The engine noise that covers also the noise generated by engine jets should be covered to produce an acceptable engine noise propagation model.

### **2.5.1.3 Noise measure**

It is now explained the different noise measure which describe the noise generated by the aircraft. The reason because there isnt one single measure is because noise is something that can be different from person by person. The most important noise indexes used with the models are listed and explained below:

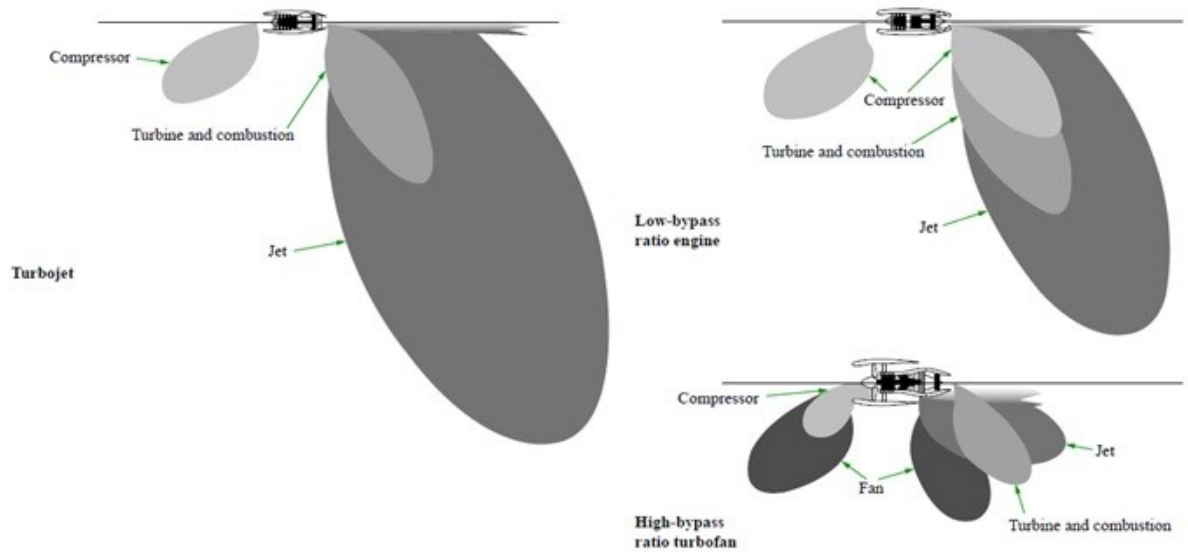


FIGURE 2.7: Engine noise pattern for Turbojet and Turbofan [49]

- Decibel (dB) is the oldest but important sound pressure measure index used to compare the sound pressure of a sound source to a reference pressure ( $L_{REF} = 20\mu Pa$ ). Normally dB is expressed in logarithmic scale.

$$L_P = 10 \log_{10} \frac{p^2}{L_{REF}^2} \quad (2.33)$$

- A-weighted Sound Exposure Level (SEL/ $L_{AE}$ ) is the most common measure of overall noise exposure for airplane flying over a certain area and it is the sum of the sound energy over the duration of a noise event.

$$L_{AE} = 10 \log_{10} \int_{t_i}^{t_f} \frac{p^2(t)}{L_{REF}^2} dt \quad (2.34)$$

- A-Weighted Maximum Sound Level (L<sub>MAX</sub>/ $L_{Amax}$ ) is the single event maximum sound level metric.
- Effective Perceived Noise Level (EPNL/ $L_{EPN}$ ) is often used in certification procedures. It is an index of the subjective effects of aircraft activity on human beings. It takes into account the pure sound pressure but also the duration of the noisy event. The sound band of analysis is from 50Hz to 10kHz and the detailed explanation of this index is reported in [50].

#### 2.5.1.4 Aircraft Noise Calculation Tools

Aircraft noise calculation tools have been developed in the years based on the noise measure methods described earlier. Noise contour is one of the most diffuse for its simplicity and easy read characteristics. The most important tool widely used to generate the contour is Integrated Noise Model (INM). INM was developed by FAA and the algorithm used can be found on [51]. It uses experimental Noise-Power-Distance (NPD) data to calculate the noise generated by the aircraft given the engine settings and control configuration, geometrical position of the aircraft respect to the measure source and other environmental factors. Doc 29 was developed by European Civil Aviation Conference (ECAC) and the algorithm to compute the noise can be found on Volume 2 of the report [52]. Doc 29 algorithm is very similar to the one used by INM. They both use NPD dataset and both take into account geometrical position of the aircraft respect to a measurement location and atmospheric attenuations as well.

Many reports use the INM model as noise model to calculate noise exposure and maximum exposure level and study the noise impact along the trajectory. Therefore the INM algorithm was selected to be implemented within the optimisation process in this work.

In 1997, the Federal Interagency Committee on Aviation Noise (FICAN) published a research which lasted several years, as a result a dose-response curve for predicting nocturnal awakenings was presented [53]. In Figure 2.8 it is possible to see the relation between indoor sound exposure level and the awakened people in percentage. This function represents the worst case as it is possible to see by the red circle which shows the analysed data.

#### 2.5.2 Engine emissions

Aircraft engine emissions are divided into categories of CO<sub>2</sub> and non-CO<sub>2</sub>. The Carbon dioxide can be related with the contribution to the climate change. The latter contains water vapour, methane, NO<sub>x</sub>, etc. CO<sub>2</sub> and NO<sub>x</sub> are closely related to the engine fuel consumption along the flight mission. To give an example, 1 Kg of kerosene fuel burn in flight produces around 3.16 Kg of CO<sub>2</sub> due to its proportionality to engine fuel flow[54]. A short description of the most important pollutants is now provided:

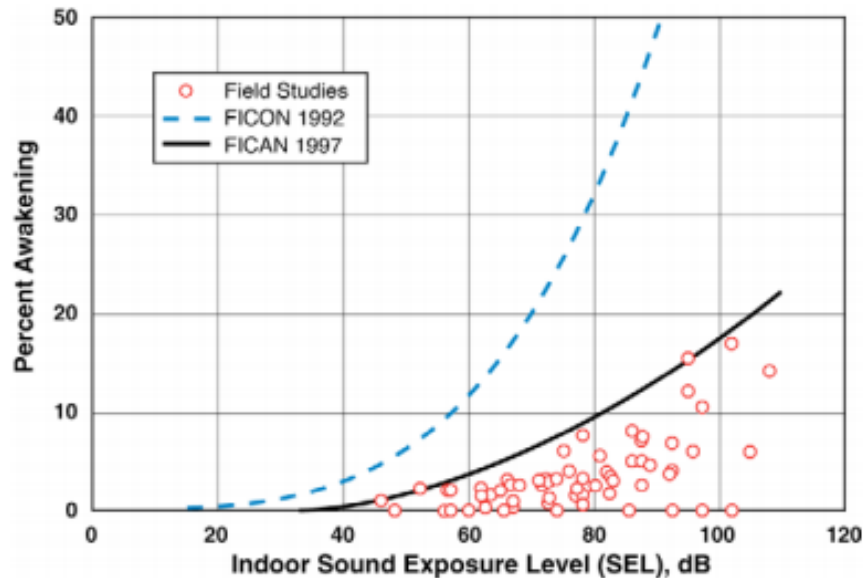


FIGURE 2.8: Relation between the overall sleep disturbance and indoor SEL[53]

CO<sub>2</sub> - The carbon dioxide generation is attributed to the complete chemical reaction of the fuel-air mixture. The common way to reduce the CO<sub>2</sub> in the exhaust gas is to reduce the overall fuel burned, increasing the efficiency of the gas turbine cycle or modifying the trajectory flown by the aircraft.

CO - The carbon monoxide generation is attributed to the non-complete combustion of the fuel-air mixture. This phenomenon happens when the gas turbine cycle is at low power setting resulting in low combustion temperature.

NO<sub>x</sub> - The oxides of nitrogen are NO<sub>2</sub>, NO and N<sub>2</sub>O. They are produced by oxidation of the nitrogen which is contained in the inlet air at high temperatures in the combustion chamber. The NO<sub>x</sub> generation is the main causes of smog and acid rain.

H<sub>2</sub>O - The water vapour is generated by the combustion of the engine and causes condensation and contrails. The cirrus clouds created can be visible from seconds to hours depending of atmospheric conditions and may affect climate [55]. Recently study show that cirrus clouds cover 1% of European sky and 4% of US sky and a reduction of water emission is only possible by reducing the fuel burnt[56] or to avoid regions which support contrail formation modifying the aircraft trajectory.

For engine exhaust emissions emitted below 3000 ft AGL, regulatory requirements are imposed by ICAO [57]. Therefore each engine must be tested and certified to fulfil those requirements. The ICAO requirements are based on idealised landing

and take-off cycles. For these cycles the ICAO provides an emission databank with the typical Emission Index (EI) that gives the amount of the respective emission in [g] per [kg] fuel burnt. This emission databank is used in this work to estimate the engine emissions along the trajectory.

## 2.6 Summary

The results of the literature study showed that the trajectory optimisation problem can be tackled using two main approaches. The parametric optimisation approach is a natural translation of the pilot procedures such as performing climb and descent at constant indicated airspeed. However if this approach was used, the domain of possible trajectories would be limited. Instead, the optimal control approach guarantees a full domain of possible trajectories achievable and only limited by the aircraft performance and it fits perfectly the new Trajectory Based Operation (TBO) paradigm. Unfortunately the decision of using optimal control problem forced the use of gradient-based Non-Linear Programming (NLP) algorithms to solve the problem. Heuristic algorithms were found not appealing in the optimal control methodology as concluded first by Betts[33] and later by Rao[38]. Therefore in this work the trajectory problem is tackled as optimal control problem and gradient-based NLP is going to be used.

Most of the work studied which used optimal control approach relied on a pure single objective or on use of the sum weighting methodology for more objectives. Only few works, such as [73] did not use the sum weighting methodology but opted for alternative methodologies. These methodologies introduce complexity in the overall optimisation with the aim to provide solutions in non-convex region of the Pareto. Therefore these methodology will be considered only if non-convex Pareto regions are encountered. Unfortunately, these works were only focused on noise optimisation around terminal areas and therefore considering only departure and arrival phases of flight. This work wants to consider the city pair problem when possible. However it is understandable that noise optimisation have to be constricted to terminal areas.

Another point to be mentioned is that only little work was done in apply the optimised trajectories to on-board FMS and validate the optimal trajectory against

the real environment. This work is trying to reduce this gap and push further for the application of greener trajectories.



# Chapter 3

## Greener Aircraft Trajectory Modelling

### 3.1 Introduction

This chapter describes the different models needed to set up the optimisation framework. First the model for the aircraft dynamics with relative constraints are presented. In addition the engine emission and aircraft noise model adopted for this research are described.

### 3.2 Aircraft Motion

Commercial aircraft trajectory between take-off and landing involves the study of aircraft centre of mass along the whole period of time involved between take-off and landing which in some cases is up to more than 10 hours for long haul flights. The nominal aircraft trajectory describing the motion of the aircraft's CG is obtained using the 3 Degree Of Freedom (3-DOF) Point Mass Model (PMM) with variable mass modelling. The 3-DOF model is widely used for trajectory generation and optimisation as shown in several research works, such as from Bousson[58], Soler[26], Rivas[59], de Oliveira[60] and many more.

The system of differential equations is formed by kinematic, dynamic and aircraft mass relations. The kinematic equations describe the aircraft position in the inertial system due to aircraft speed, attitude and wind contribution. The dynamic

equations describe the aircraft acceleration and attitude rate due to the forces applied to the aircraft which can be divided in aerodynamic, propulsive and gravitational. The aircraft mass equation simply takes into account the engines fuel burning due to flying. Appendix A describes more into details the flight mechanics theory and the modelling methodology which leads to the final aircraft equations of motion used in this research.

### 3.2.1 Modelling Assumptions

To describe the general aircraft trajectory problem several assumptions have to be introduced. The hypotheses used are listed as follow:

- 3-Degrees of Freedom (DOF): The aircraft rotations around the centre of gravity (CG) are considered smaller than aircraft translational motion and therefore are neglected. This leads to describe the aircraft motion by using 3-DOF point mass dynamic model applied to aircraft CG. This assumption has been widely used in aircraft performance optimisation studies such as [Roskam], [Stevens&Lewis]. The guidance system on board of the aircraft is going to control the fast dynamics such as body attitude, engine regimes and turn manoeuvres are assumed to be achieved in a coordinated way.
- WGS-84: The Earth is considered defined by the WGS-84 ellipsoid and non-rotating. This is expected since we are not focusing in a specific flight phase such as departure and arrival but in the overall mission from take-off to landing. The flat Earth which many literatures implied is only accurate to up to 200 NM [61] and can not be applying in this work.
- Variable mass: The aircraft mass is reduced by fuel burn along the trajectory.
- Constant gravity: The Earth acceleration due to gravity in the atmospheric flight of the aircraft is considered perpendicular to Earths surface and equal to  $9.81 [m/s^2]$ .
- Symmetric flight: The aircraft is assumed to have plane of symmetry and to fly symmetric (i.e. forces lie on the plane of symmetry).
- Thrust force lies on the longitudinal body axis: The aircrafts engine thrust is assumed to have a small angle of attack.

### 3.2.2 Reference Frames

The reference frames used in describing the aircraft motion over non-rotating spherical Earth are the Earth axes frame  $F_e(O_e, x_e, y_e, z_e)$ , the curvilinear ground frame  $F_c(O_c, x_c, y_c, z_c)$ , the local horizon frame  $F_h(O_h, x_h, y_h, z_h)$ , the wind axes frame  $F_w(O_w, x_w, y_w, z_w)$  and the body axes frame  $F_b(O_b, x_b, y_b, z_b)$ .

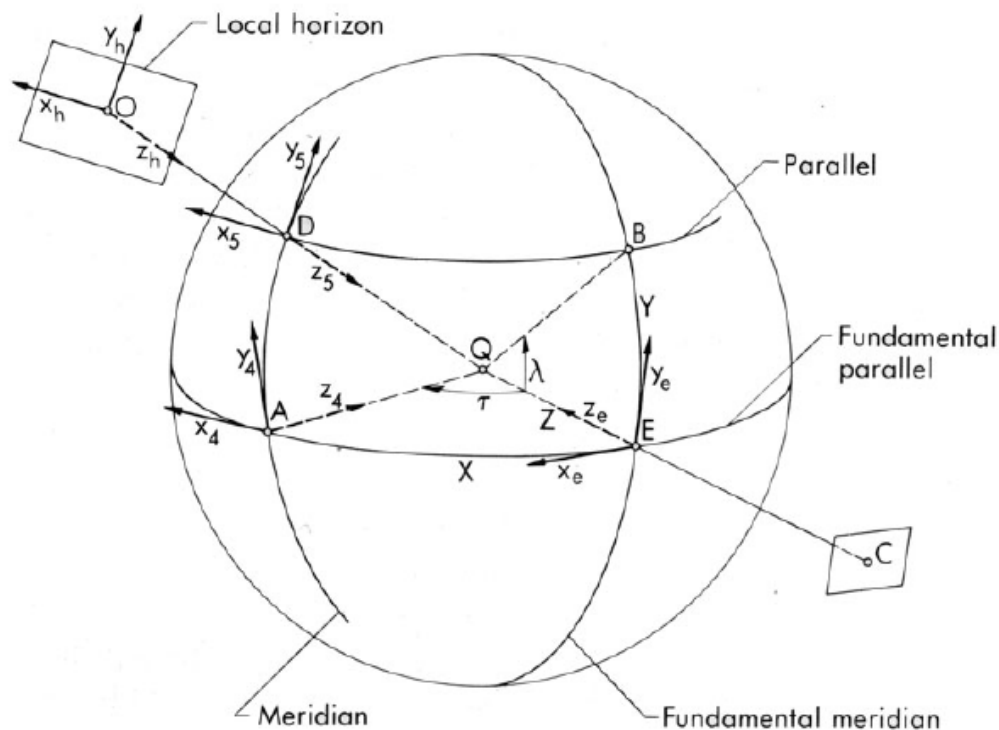


FIGURE 3.1: Coordinate frames for a flight over a spherical Earth [62]

The Earth axes frame  $F_e$  is a Cartesian right-handed reference frame which is fixed to the Earth. Its origin  $O_e$  is a point on the Earth's surface at mean sea level and is defined by its geodetic latitude  $\varphi_e$  and longitude  $\lambda_e$ . X-axis  $x_e$  and Y-axis  $y_e$  lie in the tangent plane and the main axes points respectively towards north and east. Z-axis  $z_e$  points toward the centre of the Earth.

The curvilinear ground frame  $F_c$  is an orthogonal right-handed reference frame which is also fixed to the Earth at mean sea level. The X-axis is measured along the fundamental parallel; the Y-axis along the fundamental meridian and Z-coordinate radially as shown in the picture.

The local horizon frame  $F_h$  is a Cartesian right-handed reference frame which is fixed to the aircraft centre of gravity and its axes are parallel to the curvilinear ground system's axes.

The wind axes frame  $F_w$  is a Cartesian right-handed reference frame and its origin is fixed to the aircraft centre of gravity but the X-axis is coincident with the aircraft velocity vector and the Z-axis is perpendicular with the X-axis, contained in the plane of symmetry and positive downward.

The body axes frame  $F_b$  is a Cartesian right-handed reference frame and its origin is fixed to the aircraft centre of gravity but the X-axis lies in the symmetric plane of the aircraft and is directed towards the aircraft's nose. The Z-axis is perpendicular to the X-axis and also lies in the symmetric plane and directed below. The Y-axis results perpendicular to the X-Z plane and directed out to the right wing.

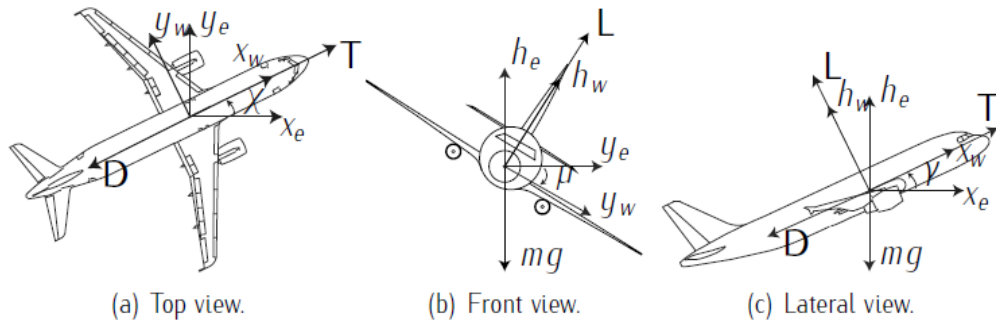


FIGURE 3.2: Forces applied to the aircraft [63]

### 3.2.3 Equations of motion

Under the assumptions previously introduced and references to the frames just discussed is possible to define 3-DOF equations of motion for the greener aircraft which are constructed by dynamic, kinematic and variable mass equations.

The equations of motion are described by the following Differential Algebraic Equations (DAE) system:

$$\begin{aligned}
 \dot{V} &= \frac{N_e \cdot T_e(\eta, V, h) - D(L, V, h)}{m} - g \sin(\gamma) + \dot{w}_V \\
 \dot{\gamma} &= \frac{g(n \cos \mu - \cos \gamma)}{V} + \dot{w}_\gamma \\
 \dot{\chi} &= n \cdot \frac{g \sin \mu}{V \cos \gamma} + \dot{w}_\chi \\
 \dot{\varphi} &= \frac{V \cos \gamma \sin \chi + w_\varphi}{R_E + h} \\
 \dot{\lambda} &= \frac{V \cos \gamma \cos \chi + w_\lambda}{(R_E + h) \cos \varphi} \\
 \dot{h} &= V \sin \gamma + w_h \\
 \dot{m} &= -c \cdot N_e \cdot T_e
 \end{aligned} \tag{3.1}$$

where:

$V$	= Aircraft true airspeed [ $m/s$ ]
$m$	= Aircraft mass [ $kg$ ]
$T_e$	= Aircraft's engine net thrust [ $N$ ]
$N_e$	= Number of engines installed on the aircraft (non-dimensional)
$n$	= Aircraft's load factor (non-dimensional)
$w_\lambda$	= Wind speed component towards east [ $m/s$ ]
$w_\varphi$	= Wind speed component towards north [ $m/s$ ]
$w_h$	= Wind speed component upward [ $m/s$ ]
$\gamma$	= Flight path angle [ $rad$ ]
$\chi$	= Heading angle [ $rad$ ]
$\lambda$	= Longitude [ $rad$ ]
$\varphi$	= Latitude [ $rad$ ]
$h$	= Altitude [ $m$ ]
$L$	= Aircraft overall lift force [ $N$ ]
$D$	= Aircraft overall drag force [ $N$ ]
$c$	= Engine fuel consumption [ $kg/s$ ]
$g$	= Earth's gravitational acceleration constant [ $m/s^2$ ]
$\mu$	= Aircraft bank angle [ $rad$ ]
$R_E$	= Earth's average radius [ $m$ ]

The system described by EQ. 3.1 is a general system of equations and have 7 states ( $V, \chi, \gamma, \phi, \lambda, h$  and  $m$ ), 3 controls ( $T, L$  and  $\mu$ ) and  $t$  is the independent variable. The system can be particularized, for example to describe cruise flight at constant speed the following are applied ( $\dot{V} = 0, \dot{\gamma} = 0$  and  $\mu = 0$ ) which consequently provides the well know system of equations for cruise condition  $L = mg$  and  $T = D$ .

Additional equations involving existing variables need to be added to close the system. Atmosphere, aircraft aerodynamics and propulsion modelling are going to be described in the next sections.

### 3.2.4 Aerodynamics and Propulsion Modelling

The aircraft performance modelling is essential to be able to describe the aerodynamic and propulsive forces as function of aircraft states. The aerodynamic forces

are generated due to the motion of the aircraft in the atmospheric environment while the propulsive forces are generated by the installed engines.

The lift  $L$  and drag  $D$  forces described in the EOM are defined as the product of the correspondent force coefficient and the dynamic pressure and are expressed as follow:

$$L = \frac{1}{2}\rho V^2 S C_L \quad (3.2)$$

$$D = \frac{1}{2}\rho V^2 S C_D \quad (3.3)$$

where  $C_L$  and  $C_D$  are the overall lift and drag coefficients and  $S$  is the wing reference area of the generic aircraft.

The relation between drag and lift forces and therefore coefficients is also called *drag polar*. In general, for each aerodynamic configuration, the drag polar of an aircraft has the following form:

$$C_D = C_D(C_L, M) \quad (3.4)$$

In the assumption that lift coefficient is linear to the aircraft angle of attach and that the aircraft autopilot is keeping the angle of attach below the stall conditions. Hence the drag coefficient can be assumed to be a parabolic function of the lift coefficient.

$$C_D = C_{D0}(M) + k(M)C_L^2 \quad (3.5)$$

where  $C_{D0}$  is the zero-lift drag coefficient and  $kC_L^2$  is the induced drag factor. The two components are unique for each aerodynamic configuration of the aircraft. EUROCONTROL in cooperation with aircraft manufacturers and operating airlines has created and maintains an aircraft performance database called Base of Aircraft Data (BADA). The aerodynamic coefficients collected in BADA are also different for each aerodynamic configuration. For example, for Airbus A320 aircraft there are a total of 5 aerodynamic available, named: take-off, initial climb, cruise, approach and landing. During these phases the aerodynamic configuration changes, such as slats and flaps extraction. Maximum speed and altitude threshold are normally associated with these set of parameters. Almost all the research work studied uses BADA data, in addition only the CleanSky project relied on BADA dataset for their simulation, therefore the decision to use BADA dataset also for this study was made. The BADA dataset contains performance coefficients for more than 300 aircraft and its validity is accepted by international community for

trajectory generation purpose. This allows the optimisation process to be applied to more than one aircraft and have more future applications.

AircraftConfiguration	$C_{D0}$	$C_{D2}$	$C_{L_{max}}$
Clean (Cruise)	0.0267	0.0387	1.5998
1 (Initial climb)	0.0230	0.0440	2.2681
1+F (Take-off)	0.0330	0.0410	2.5131
2 (Approach)	0.0380	0.0419	2.8591545
FULL (Landing)	0.0960	0.0371	3.0776

TABLE 3.1: EUROCONTROL BADA dataset aerodynamic performance coefficients for Airbus A320

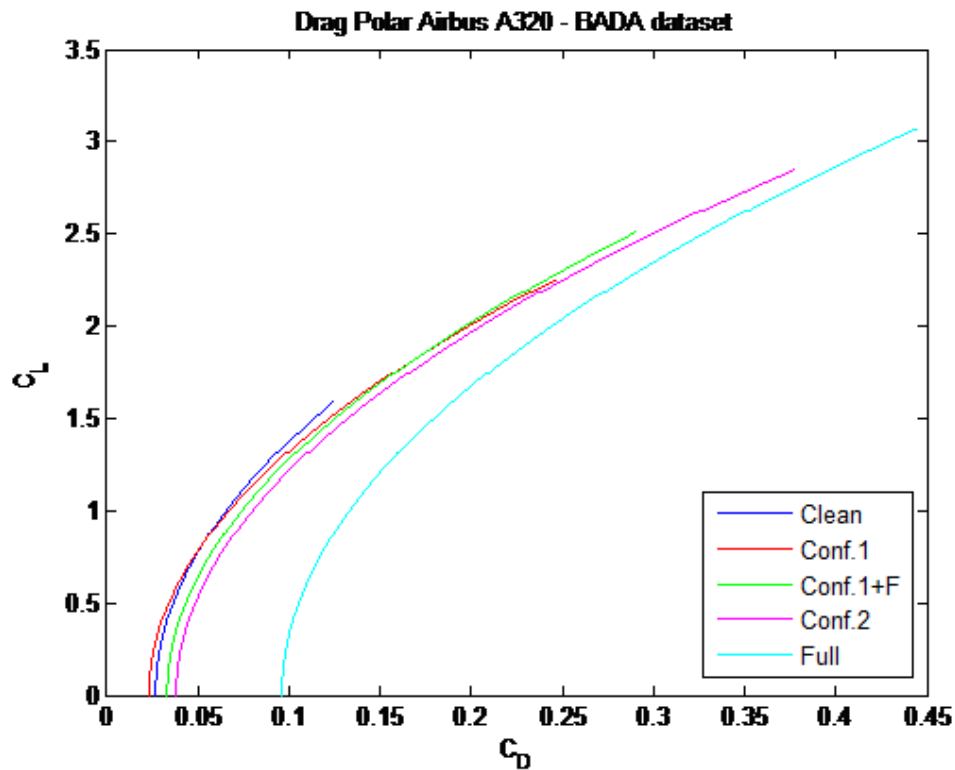


FIGURE 3.3: Drag polar obtained using EUROCONTROL BADA dataset for Airbus A320

However it is well known that the drag polar described by BADA coefficients are only function of lift coefficient. The drag coefficient is not function of Mach. This has to be corrected to obtain realistic results. The Mach contribution in the equation allows the aircraft drag to rise to when the aircraft enters drag rise conditions. Without the modelling of this condition the optimisation algorithm results in pushing the aircraft to the highest altitude possible and to the fastest speed allowed. Klima[64] required a proper modelling of the aircraft off-cruise

conditions and studied the BADA model applied to jet aircraft around their Mach critical conditions. Klima concluded that the cruise Mach number given in BADA could be assumed to the Mach critical for the aircraft and used it to compute the compressibility effects. The following equations describe the empirical method used and validated by Klima to correct the BADA data adding the compressibility effect.

$$Y = \frac{Mach}{M_{CC}} - 1 \quad (3.6)$$

$$C_{DC} = \begin{cases} 0.001000 + 0.02727Y - 0.1952Y^2 + 19.09Y^3 & X \geq 1.0 \\ 0.001000 + 0.02727Y + 0.4920Y^2 + 3.573Y^3 & 1.0 > X \geq 0.95 \\ 0.0007093 + 0.006733Y + 0.01956Y^2 + 0.01185Y^3 & 0.95 > X \geq 0.8 \\ 0.00013889 + 0.00055556Y + 0.00055556Y^2 & 0.8 > X \geq 0.5 \\ 0 & 0.5 > X \end{cases} \quad (3.7)$$

The result of applying this empirical method to the A320 drag polar is shown in FIGURE 3.4.

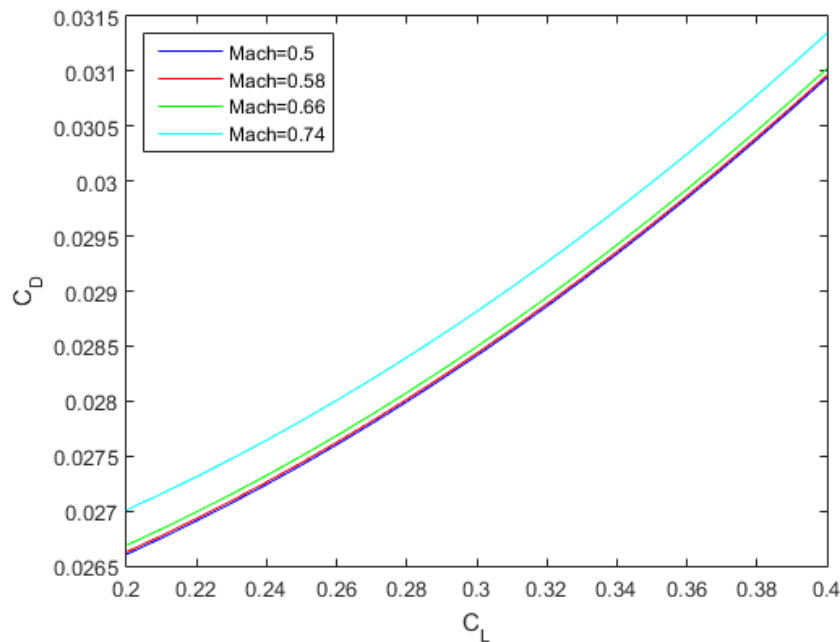


FIGURE 3.4: Airbus A320 drag polar corrected for compressibility

BADA dataset also provides engine performance data in addition to the aerodynamic performance data. In the specific, it is possible to obtain both the maximum



thrust available for different flight levels and the correspondent fuel consumption for the same condition. However the engine performance model used in BADA looked like too simplistic because the total thrust of the aircraft was only related to altitude and the specific fuel consumption was only related to thrust and speed. Clearly this solution would not be applicable to an optimisation case. Therefore, to obtain a more fidelity in the engine performance characteristics, in this work it was used data obtained by turbine performance simulation software called TURBOMATCH developed by Cranfield University.

TURBOMATCH is gas turbine performance software developed to simulate engine performance and fault diagnostics. For these reasons the engine is modelled to a very high detail. This kind of detail results in high accuracy but has a significant computational penalty which does not make it a candidate for optimisation calculation applications. However, it is possible to simulate a modelled engine that was similar to the CFM-56-5B4, which is installed on the Airbus A320, over a vast envelope domain and the resulting database used with polynomial techniques to create a continuous and differentiable performance model of the engine. The engine performance for a generic turbofan engine can be mainly modelled as function of altitude, flight speed and throttle applied. However the engine involves several control systems which regulate the Turbine Entry Temperature (TET) as function of the throttle. Those controls laws are not available, therefore the thrust and related engine performance characteristics are modelled as function of altitude, aircraft flight speed expressed in Mach and TET. It is assumed to be a linear relation between the throttle and the TET since this research is not about the correctness of the relation between the throttle and the TET.

The engine operational conditions used to map the engine characteristics are collected in the following table:

Variable	Range
Altitude	From 0 to 12,000 ft
Mach	From 0 to 0.9
TET	From 900 to 1,500 K

TABLE 3.2: Operational engine conditions used to map the thrust and fuel consumption

The obtained engine performance are shown in FIGURE 3.5.

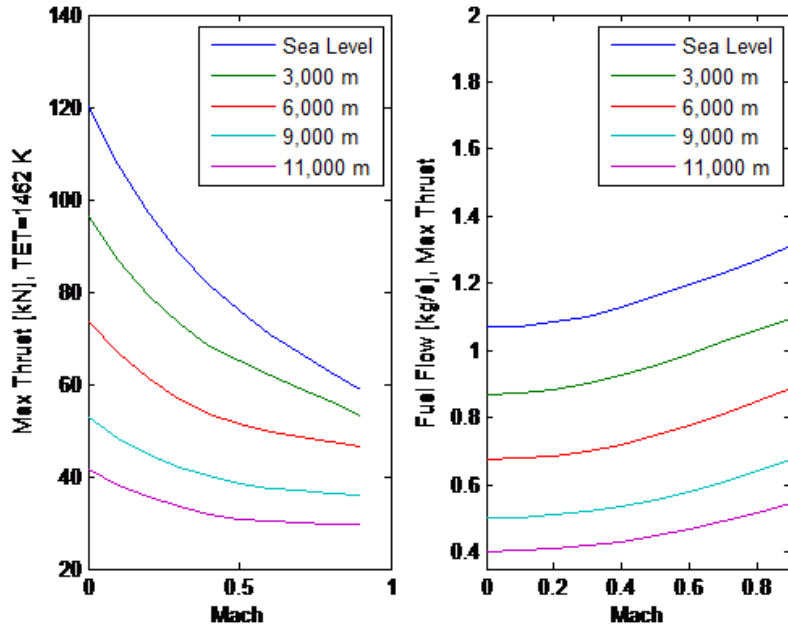


FIGURE 3.5: Maximum Net Thrust and correspondent fuel flow for different flight levels of the modelled engine

From FIGURE 3.5 it is possible to see that the modelled engine is capable of producing 121 kN of thrust at sea level in ISA conditions at the maximum static take-off setting with Turbine Entry Temperature (TET) of 1462 K. The idle conditions for the same engine are obtained with a TET of 906 K. The TET for the engine is driven by the engine throttle  $\delta$  by the following relation.

$$TET = \delta(1492 - 906) + 906 \quad (3.8)$$

And the overall thrust force  $T$  and fuel flow  $FF$  to be considered together with the EOM are summarized as follow:

$$T = N_e(p_{000}^T + p_{010}^T \cdot h + p_{100}^T \cdot M + p_{020}^T \cdot h^2 + p_{110}^T \cdot h \cdot M + p_{200}^T \cdot M + p_{001}^T \cdot T_{ET} + p_{011}^T \cdot h \cdot T_{ET} + p_{101}^T \cdot M \cdot T_{ET} + p_{002}^T \cdot T_{ET}^2) \quad (3.9)$$

$$FF = N_e(p_{000}^F F + p_{010}^F F \cdot h + p_{100}^F F \cdot M + p_{020}^F F \cdot h^2 + p_{110}^F F \cdot h \cdot M + p_{200}^F F \cdot M + p_{001}^F F \cdot T_{ET} + p_{011}^F F \cdot h \cdot T_{ET} + p_{101}^F F \cdot M \cdot T_{ET} + p_{002}^F F \cdot T_{ET}^2) \quad (3.10)$$

where  $N_e$  is equals to 2 for the Airbus A320 aircraft and the polynomial coefficients were obtained from multiple regression analysis where the coefficients of

determination  $R^2$  for the thrust and fuel flow functions obtained have achieved  $R_T^2 = 0.9915$  and  $R_{FF}^2 = 0.9970$  indicating a very high quality of the regression meaning the high accuracy of the engine performance data is almost maintained with a great advantage in computational term.

### 3.2.5 Atmosphere Modelling

Standard atmosphere model used in aviation has being used to describe the atmosphere properties. The air density  $\rho$ , air pressure  $p$  and air temperature  $T$  are defined by International Standard Atmosphere (ISA) as a function of geopotential pressure altitude. Air density is directly involved in the computation of aircraft lift and drag forces. Atmosphere properties are also used to relate different aircraft speed types to each other (i.e. True Airspeed, Calibrated Airspeed, Mach) and ISA model relates them as function of altitude.

Geopotential pressure altitude  $h_P$  and geometric altitude  $h$  are related by the following relation:

$$h_P = \frac{h \cdot R_E}{h + R_E} \quad (3.11)$$

Atmosphere properties at Mean Sea Level (MSL) conditions occur in the ISA model at the point where geopotential pressure altitude  $h_P = 0$  and are listed as follow:

$$\begin{aligned} T_0 &= 288.15 & [K] \\ p_0 &= 101325 & [Pa] \\ \rho_0 &= 1.225 & [\frac{kg}{m^3}] \\ a_0 &= 340.294 & [\frac{m}{s}] \end{aligned} \quad (3.12)$$

The ISA model relies on the assumption that the atmosphere follows the behaviour of a perfect gas and that the temperature is constant in the tropopause. In reality the atmosphere deviates from the ISA conditions and non-ISA atmosphere needs to be used. The non-ISA atmosphere follows the same hypotheses as the ISA atmosphere but with the introduction of temperature deviation at MSL and expressed as  $\Delta T$ . The Temperature deviation can be either be positive or negative. For more details about the ISA and non-ISA models, the reader can find more information in Section 3.1 of BADA User Manual [65].

The air temperature at a generic altitude  $T(\Delta T, h)$  is expressed as follows:

$$\begin{aligned} T(\Delta T, h) &= T_0 + \Delta T - 0.0065 \cdot h & (0 \leq h < 11000) \\ T(\Delta T, h) &= 216.65 + \Delta T & (h \geq 11000) \end{aligned} \quad (3.13)$$

where  $\Delta T$  is the difference in atmospheric temperature at MSL between a given non-standard and ISA atmosphere.

The air pressure at a generic altitude  $p(\Delta T, h)$  is expressed as follows:

$$\begin{aligned} p(\Delta T, h) &= p_0 \left( \frac{T(\Delta T, h) - \Delta T}{T_0} \right)^{5.2561} & (0 \leq h < 11000) \\ p(\Delta T, h) &= p_0 \left( \frac{T(\Delta T, h=11000) - \Delta T}{T_0} \right)^{5.2561} \cdot e^{-\frac{g}{R \cdot 216.65} (h - 11000)} & (h \geq 11000) \end{aligned} \quad (3.14)$$

where  $R$  is the universal gas constant and  $R = 287.05 \frac{J}{Kg \cdot K}$ .

The air density at a given altitude  $\rho(\Delta T, h)$  is expressed as follows:

$$\rho(\Delta T, h) = \frac{p(\Delta T, h)}{R \cdot T(\Delta T, h)} \quad (3.15)$$

The speed of sound at a given altitude  $a(\Delta T, h)$  is expressed as follows:

$$a(\Delta T, h) = \sqrt{1.4 \cdot R \cdot T(\Delta T, h)} \quad (3.16)$$

The speed of sound is directly related to the computation of the aircraft Mach number  $M(V, h, \Delta T)$  by the following relation:

$$M(V, h, \Delta T) = \frac{V}{a(\Delta T, h)} \quad (3.17)$$

The above additional equations provide the atmospheric parameters necessary for the calculation of aircraft performance and the trajectory modelling. It is possible to see that the temperature deviation from ISA condition has impact on all the atmospheric parameters needed to the trajectory computation and can not be neglected when simulating real cases scenarios.

### 3.2.6 Wind Modelling

The wind is present in the atmosphere and it has great impact on resulting aircraft ground speed and therefore time constraints introduced along the trajectory. In this research the wind modelling is defined only by its deterministic component which represent the past meteorological condition or a forecast one. Hence, the stochastic component is neglected. Wind information for past and/or forecast is generally obtained from MET offices. National Oceanic and Atmospheric Administration (NOAA) runs numerical models based on measurements obtained by ground stations, meteorological balloons and satellite images and published results via GRIdded Binary (GRIB) structured files. For Europe the data are provided 4 times per day (0, 06, 12, 18) hours with a maximum horizontal grid of 0.25deg x 0.25deg and 14 different barometric levels from sea level up to 70,000 feet. Even if the data are published every 6 hours, each publication has weather information for each hour for the next 172 hours based on each computation time. The GRIB binary structured files can be extracted into readable format like CSV files. However the data need extra manipulation to be integrated into the optimisation process. Regression analysis is introduced.

The meteorological data is translated into an analytical function by multiple regression analysis. In details, the wind model is composed by two wind components (i.e. South-North and West-East components) because the Earth's perpendicular component is neglected. The two wind components are functions of global position or the aircraft by the tern latitude  $\lambda$ , longitude  $\varphi$  and altitude  $h$  as follow:

$$\begin{aligned} V_{w\lambda} &= f(\lambda, \varphi, h) \\ V_{w\varphi} &= g(\lambda, \varphi, h) \\ V_{wh} &= 0 \end{aligned} \tag{3.18}$$

In FIGURE 3.6 it is possible to see the real data extracted by GRIB file for the 11th July 2012 at the altitude of 220 HPa and the analytical function obtained by the multiple regression. The R2 coefficient called coefficient of determination, which indicates the goodness of fit for the two wind components was reported as .0.639 for east component and 0.691 for the north component which indicate not a great fit but it is acceptable at this level of work.

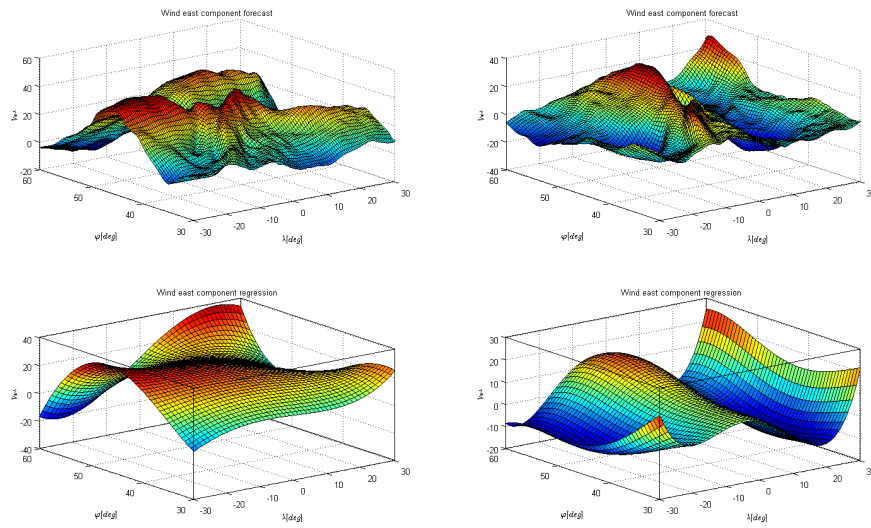


FIGURE 3.6: Wind Components at 200 HPa - forecast and multiple regression

### 3.2.7 Flight Envelope Constraints

The flight envelope defines the maximum altitude (i.e. ceiling) and the minimum and maximum airspeed at which the aircraft can operate. The ceiling altitude is defined by regulation as the altitude the aircraft can fly while still be able to climb with a rate of 300 ft/min. And of course this value is function of the aircraft weight and atmospheric conditions. BADA user manual[65] defines the ceiling altitude as follows:

$$h_{max} = \min \begin{cases} h_{MO} \\ h_{max} + G_t \cdot (\Delta T - C_{Tc,4}) + G_w \cdot (m_{MTOW} - m) \end{cases} \quad (3.19)$$

where  $h_{MO}$  is the max. operating altitude,  $h_{max}$  is the max. altitude at MTOW and ISA conditions,  $G_t$  temperature gradient on max. altitude,  $G_w$  weight gradient on max. altitude,  $C_{Tc,4}$  thrust temperature coefficient and  $m_{MTOW}$  is the max. take-off weight and all are provided by the BADA dataset for the aircraft;  $m$  is the aircraft mass at a given condition. The minimum aircraft speed is function of the stall speed related to the aerodynamic configuration in use and is described as follow:

$$V_{min} = 1.2 \cdot (V_{stall})_{configuration} \quad (3.20)$$

The maximum aircraft speed for a jet airliner is usually provided by two different parameters. One specifies the calibrated airspeed (i.e. VMO) and the other

specifies the Mach number (i.e. MMO). For the Airbus A320 type are defined as follows:

$$V_{MO} = 350kts \quad (3.21)$$

$$M_{MO} = 0.82 \quad (3.22)$$

The aircraft mass is also constrained to a maximum value already introduced (i.e. MTOW) and defined as  $m_{MTOW}$  and a minimum value  $m_{min}$ . Both values are provided by BADA dataset.

$$m_{min} < m < m_{MTOW} \quad (3.23)$$

The aircraft flight envelope assures that the optimised trajectory is feasible under a physical point of view and also for safe and efficient operations. Hence, the performance constraints are applied to the state and control variables in the EOM. The aircraft flight envelope for Airbus A320 series aircraft is shown in FIGURE 3.7.

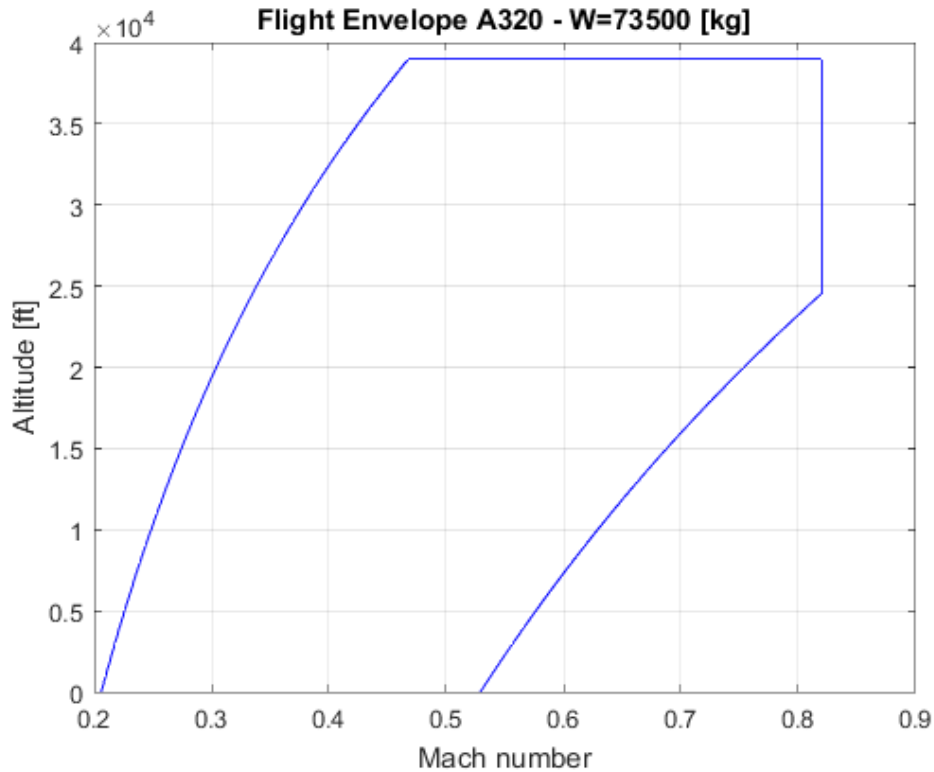


FIGURE 3.7: Airbus A320 flight envelope

### 3.3 Operational Constraints

with a reduced climb rate of 100 feet per minute. In addition the flight envelope defines the minimum and maximum speed that the aircraft can fly. Several operational constraints are defined for a selected flight plan. Normally the operational constraints can be obtained from Aircraft Operational Manual or from the Air Traffic Control (ATC). Those constraints must be followed by the plane and therefore need to be taken into account within the optimal control problem. Three different operational constraints were collected regarding the Airbus A320 aircraft. The first limits the aircraft calibrated airspeed to 250 knots when the altitude of the aircraft is below flight level FL100 (i.e. 10,000 feet).

$$V \leq 250KCAS \quad \text{below } 10000ft \quad (3.24)$$

The second limits the aircraft rate of climb as function of aircraft flight level as follow:

$$\dot{h} \leq \begin{cases} 2400ft/min & h \leq 20000ft \\ 1800ft/min & 20000 < h \leq 30000ft \\ 2400ft/min & h > 30000ft \end{cases} \quad (3.25)$$

The third constraint limits the aircraft roll rate to a maximum of 15 degrees.

$$-15 \text{ deg}/s \leq \mu \leq +15 \text{ deg}/s \quad (3.26)$$

#### 3.3.1 Constraints modelling

The trajectory optimisation approach chosen for this research requires to have gradient information easily available for the NPL solver. Black-box models or stepwise functions can be used in the optimisation loop but require the use of Automatic Differentiation (AD) which use numerical derivatives algorithm to supply the gradient information needed by the solve. This process adds extra computational cost and inaccuracies the overall optimisation process that could cause infeasibility of the results and therefore should be avoided. In order to ensure convergence, the NPL solver requires at least one time continuous differentiable for every function present in the NPL problem. This requires special care for the constraints introduced before which are stepwise functions. To transform these



discrete step constraints into continuous differentiable switch function the use of arc-tangent function is selected as successfully introduced in other optimisation processes[66]. The basic switch function is defined as follow:

$$f_{step}(t) = \begin{cases} f_l, & t \leq t_{step} \\ f_r, & t > t_{step} \end{cases} \quad (3.27)$$

$$f_{step}^{approx}(t) = \left\{ \frac{\arctan [\beta(t - t_{step})]}{\pi} + \frac{1}{2} \right\} (f_r - f_l) + f_l \quad (3.28)$$

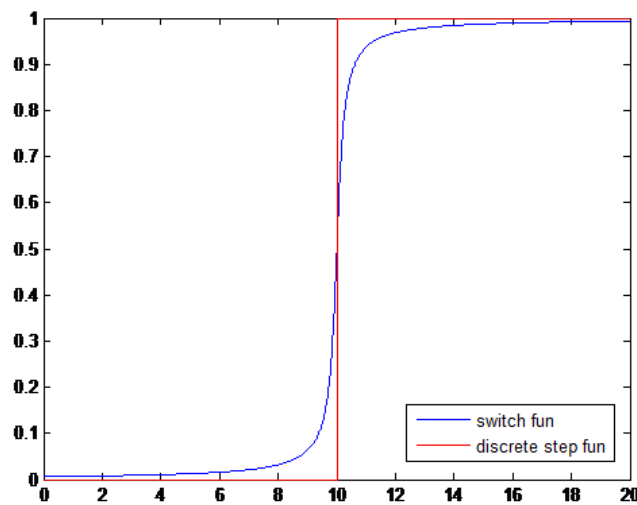


FIGURE 3.8: Step function and its continuous approximation

The parameter  $\beta$  is used to control the smoothness of the resulted approximation of the step function. For example, in the figure, it is possible to see the step function which changes from 0 to 1 at  $x_{sw} = 10$  and the approximation with  $\beta = 0.5$ . The higher  $\beta$  value is used and better approximation of the step function is obtained with cost of maybe occurring in a failure by the NLP solver to find a solution.

### 3.3.1.1 Terminal Area Maximum Speed Constraint

ICAO introduced for all flight in Terminal Area (TMA) below 10,000 ft a constraint for the airspeed to be maximum to 250 kts Calibrated Airspeed (CAS)[67]. Also NATS (the UK Air Navigation Service Provider) states in the published flight charts which restrict each flight below 10,000 ft to a maximum calibrated airspeed of 250 kts. Above 10,000 ft or cleared otherwise by the ATC controller the aircraft

can use any airspeed which is suitable to the mission. In case of the Airbus A320, the constructor indicates 350 kts as maximum calibrated airspeed to be used during normal operations. This kind of constraint can be implemented and modelled using the step function approximation introduced before. The resulting continuous approximation is shown in FIGURE 3.9.

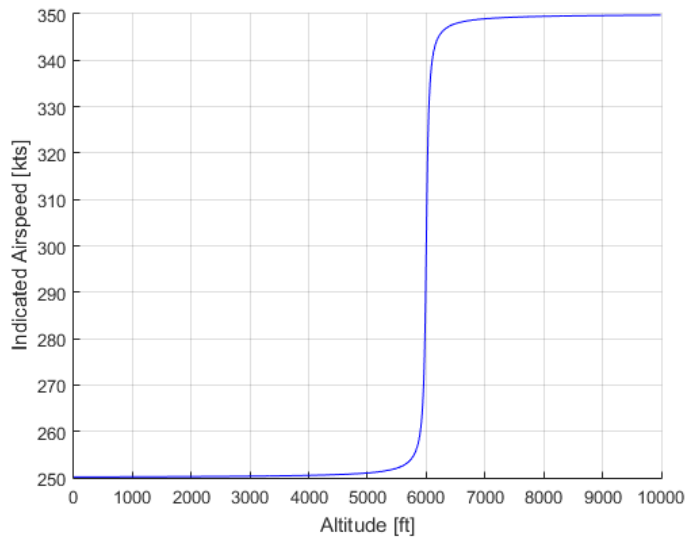


FIGURE 3.9: Continuous approximation of maximum operational airspeed

The resulting constraint is introduced into the optimisation problem by adding a path constraint as function of the interested states true airspeed  $V$  and altitude  $h$ .

$$C_{maxOpSpd}^{approx}(V, h) - V_{CAS}(V, h) \geq 0 \quad (3.29)$$

### 3.3.1.2 Terminal Area Minimum Climb Gradient Constraint

Noise Abatement procedures for London Heathrow airport impose to maintain a minimum of 4% climb gradient till reaching 4,000 ft during take-off phase. After 4,000 ft the aircraft is allowed to reduce the climb gradient and usually it is done to allow the aircraft to increase its airspeed while the engine setting is still in Take-off setting (TOGA). In the same matter the minimum climb gradient constraint can be modelled and approximated by the step function approximation introduced before and the result is shown in FIGURE 3.10.

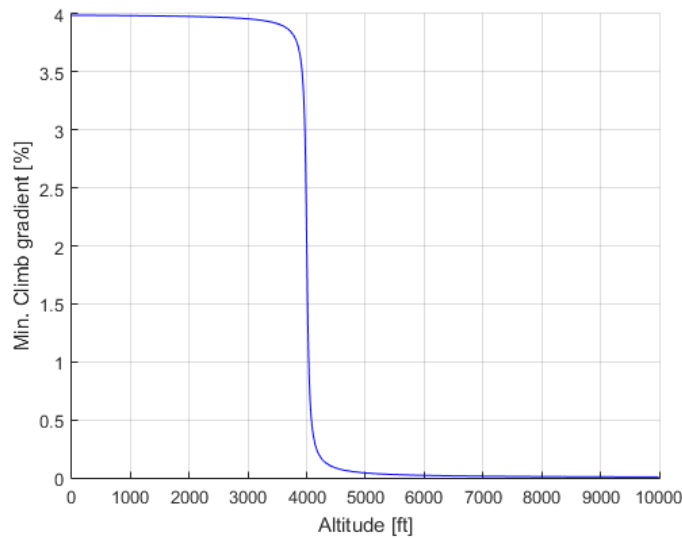


FIGURE 3.10: Continuous approximation of minimum climb gradient

The resulting constraint is introduced into the optimisation problem by adding a path constraint as function of the interested states flight path angle  $\gamma$  and altitude  $h$ .

$$ClimbGradient(V, h, \gamma) - C_{minCG}^{approx}(V, h, \gamma) \geq 0 \quad (3.30)$$

### 3.4 Emissions Modelling

During the literature study, several methods were encountered to model engine emissions. The most important ones were: The Boeing-2 fuel flow method [68], the DLR fuel flow method [54], the EUROCONTROL Advanced Emission Model 3 (AEM3) method [69] and the P3T3 method [70]. The AEM3 is a modified version of the original Boeing Method 2 (BM2) that was initially used to estimate NO<sub>x</sub>, CO and HC pollutants. In the AEM3 method, the fuel flow is corrected for temperature and pressure and then straight used to compute emission indices. More detailed into its modelling is the P3T3 method. It relies upon the pressure and temperatures at the combustion stage. These engine specific parameters are not widely available, however due to the use of Turbomatch engine performance model to obtain the engine performance data, it is possible to extract these parameters and use them to compute the emission indices using the P3T3 methodology. For

more information about the P3T3 methodology, the reader is advised to check the document [54] and [70].

From the ICAO databank [71] it is possible to obtain tables for each engine tested that contains the reference emission index for each pollutant just mentioned as function of fuel flow and for four different engine thrust settings (i.e. 100%, 85%, 30% and Idle condition 7%). The ground level reference emissions indices were taken from the ICAO databank for aircraft engine in use.

The P3T3 methodology is presented in terms of EINO<sub>x</sub> calculations, but it can also be applied to EICO and EITHC. The process for calculating EINO<sub>x</sub> is illustrated in Figure 3.11. First, EINO<sub>x</sub>, P3, and FAR from ground level measurements at reference conditions (e.g., ISA conditions at sea level) are plotted against combustor inlet temperature. The relationships provided by these plots are used to determine the reference EINO<sub>x</sub>, reference combustor inlet pressure, and reference FAR corresponding to the inlet temperature at the flight condition. The reference EINO<sub>x</sub> is then corrected for the difference in combustor inlet pressure and FAR between the ground level reference condition (REF) and the flight condition (FLT) using the following relationship:

$$EINOx_{FLT} = EINOx_{REF} \left( \frac{P3_{FLT}}{P3_{REF}} \right)^a \left( \frac{FAR_{FLT}}{FAR_{REF}} \right)^b e^{19(h_{REF} - h_{FLT})} \quad (3.31)$$

The values for the pressure and FAR exponents,  $a$  and  $b$ , are determined by conducting parametric tests either in a combustor test rig or an engine altitude facility. In addition to the P3 and FAR corrections, a humidity correction is also required as indicated by the exponential term. This is necessary as air cannot hold as much water due to the lower ambient temperatures with increasing altitudes. Certification data in the ICAO Databank are corrected to a humidity of .00634 g water per kg dry air (60% relative humidity, ISA day). Figure 3.12 shows how the humidity correction from ISA, sea level varies with altitude; the correction becoming larger at higher altitudes.

Thus, any ground level EINO<sub>x</sub> measurements, obtained at relatively high humidity, will increase by around 12 or 13% for an equivalent high altitude condition. Standard ISO 5878 defines specific humidity (kg water to kg dry air) with varying altitude and relative humidity. It is clear from Figure 3.12 that at typical cruise altitudes, the error by choosing different relative humidity curves to describe the

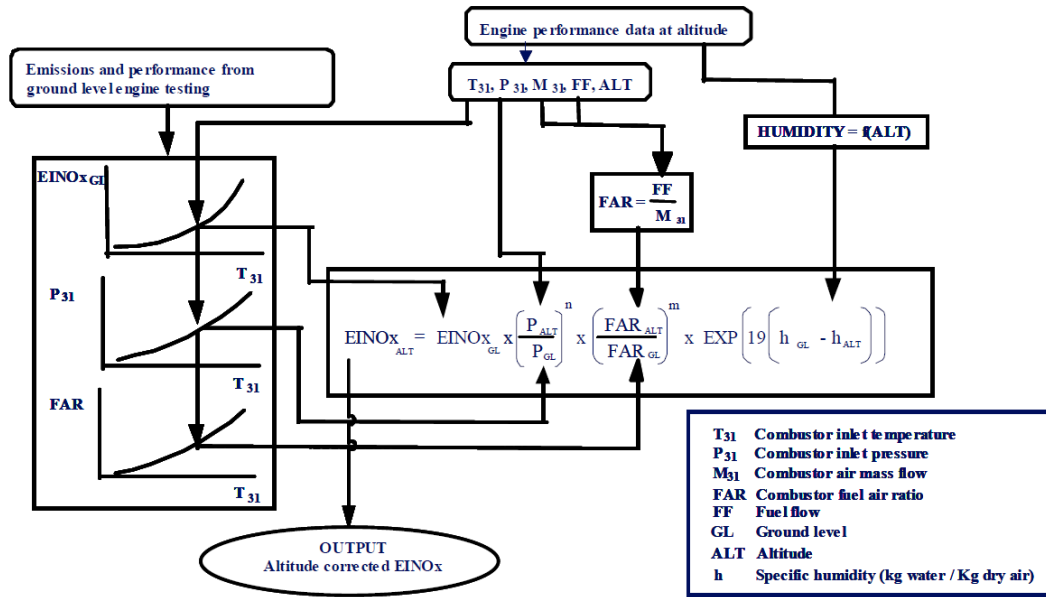


FIGURE 3.11: P3T3 Methodology [70]

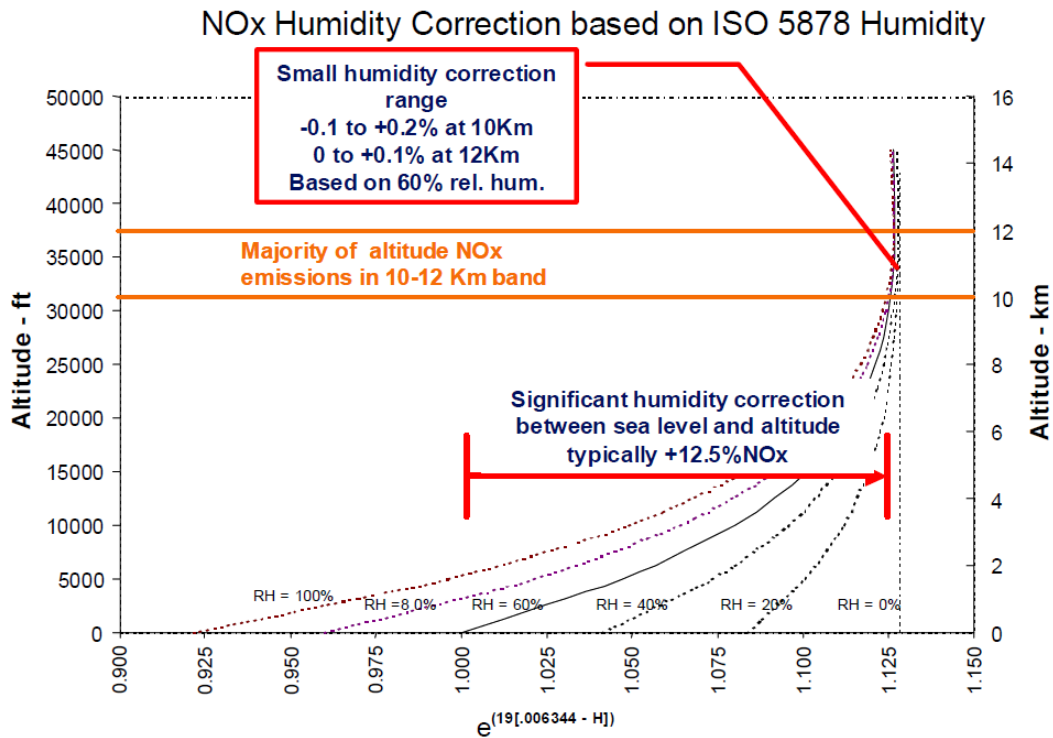


FIGURE 3.12: Humidity Correction for Altitude NOx [70]

altitude condition is small because the air is so dry. 60% relative humidity should therefore be used if actual humidity is not available (as in the current ICAO Annex 16 procedure).

To summarize, the calculation of emission indexes (EI) corrected for altitude using the P3T3 method are shown as follows

$$\begin{aligned} EINO_x &= EINO_x^{GL} \frac{P_3}{P_3^{GL}}{}^a \frac{FAR}{FAR^{GL}}{}^b RH_{corrected} \\ EICO &= EICO^{GL} \frac{P_3}{P_3^{GL}}{}^a \frac{FAR}{FAR^{GL}}{}^b RH_{corrected} \\ EIHC_x &= EIHC_x^{GL} \frac{P_3}{P_3^{GL}}{}^a \frac{FAR}{FAR^{GL}}{}^b RH_{corrected} \end{aligned} \quad (3.32)$$

where FAR is combustor Fuel Air Ratio which is given as  $FAR = FuelFlow/M3$ , M3 is the combustor air mass flow, P3 is the combustor inlet pressure Finally the total emission of each pollutant can be calculated as integral of instant emission per engine as follow:

$$\begin{aligned} HC &= N_e \cdot \int_{t_0}^{t_f} EIHC(t) \cdot ff_{engine}(t) dt \\ CO &= N_e \cdot \int_{t_0}^{t_f} EICO(t) \cdot ff_{engine}(t) dt \\ NO_x &= N_e \cdot \int_{t_0}^{t_f} EINO_x(t) \cdot ff_{engine}(t) dt \end{aligned} \quad (3.33)$$

More simplified is the modelling of CO<sub>2</sub>, H<sub>2</sub>O and SO<sub>x</sub> because these pollutants are strictly related to the amount of fuel burnt, therefore the formula to calculate the pollutants is expressed as follow:

$$\begin{aligned} CO_2 &= N_e \cdot \int_{t_0}^{t_f} EICO_2(t) \cdot ff_{engine}(t) dt \\ H_2O &= N_e \cdot \int_{t_0}^{t_f} EIH_2O(t) \cdot ff_{engine}(t) dt \\ SO_x &= N_e \cdot \int_{t_0}^{t_f} EISO_x(t) \cdot ff_{engine}(t) dt \end{aligned} \quad (3.34)$$

where EICO<sub>2</sub> is constant to 3155 [g/kg]; EIH<sub>2</sub>O is constant to 1237 [g/kg] and EISO<sub>x</sub> is constant to 0.8 [g/kg].

### 3.5 Noise Modelling

Since the beginning of noise studies, several metrics were created as discovered during the literature study for this research. Human sensitivity to different acoustic frequencies lead the experts to move from a pure sound pressure and to develop weighted scales to have a more accurate modelling. The most diffuse noise metric is the maximum A-weighted sound level ( $L_{Amax}$  or  $LAMAX$ ) and it is expressed

in dB(A). The maximum A-weighted sound level at any given location is defined as follow:

$$L_i = \max_t L_{pi}(t) \quad (3.35)$$

where  $L_{pi}(t)$  is the sound pressure level at the location  $i$  also expressed in dB(A).

Because the research is focused in reducing noise generated by the aircraft during its flight, the selection of noise metrics is fundamental. The noise model implemented is based on the methodology developed by the Integrated Noise Model (INM) research [51].

### 3.5.1 Integrated Noise Model (INM)

The Integrated Noise Model (INM) is developed by the Federal Aviation Administration (FAA) and is adopted as standard software for noise studies along departure and arrival procedures all over the world. INM provides a database with four different noise metrics (i.e.  $L_{AE}$ ,  $L_{ASmx}$ ,  $L_{EPN}$  and  $L_{PNTSmx}$ ) called Noise-Power/Thrust-Distance (NPD/NTP) where experimental data obtained from measurements at some specific reference conditions for each aircraft type and reference engine are collected and are used as reference dataset for the algorithm.

The NPD/NTP database consists of a list of A-weighted sound levels recorded at different distance from the measure point, and for different aircraft engine power/thrust setting. The distances of the measure points are: 200,400,630, 1000, 2000, 4000, 6300, 10000,16000, 25000 feet. The power/throttle settings for CFM56-5x engines are: 1500, 3000, 5000, 12000, 15500, 19000, 22500 corrected net thrust. A further attribute specifies if the measurement was for a departure or arrival aircraft due to engine and surface control differences. The NPD/NTP database is referenced to a standard day conditions, which means measuring points situated at mean sea level, air temperature of 70-80 Fahrenheit degrees and 70% relative humidity. In addition the NPD/NTP database refers to the noise impact to due to an infinite-length aircraft segment. Interpolation or extrapolation is imposed to obtain noise levels between or outside power/thrust and distance values. Using NPD/NTP data with the INM algorithm which is explained in [51] it is possible to calculate the average noise exposure and the maximum noise levels for a datum aircraft trajectory.

In Figure 3.13 it is possible to see the geometric definition used by INM algorithm. The noise-exposure level  $L_{e,\infty}$  is obtained by interpolation/extrapolation of NPD data. Several corrections need to be added to obtain the value of noise for the finite segment length because NPD data is referred to an infinite flight segment. These adjustments are summarised as follows:

- Segment duration correction: To adjust the noise calculation for non-reference aircraft speeds.
- Segment length correction: To adjust the noise calculation for finite-length flight segment.
- Installation effect correction: To adjust the noise calculation for lateral directivity due to shielding, refraction and reflection caused by airframe and engines installation.
- Lateral attenuation correction: To adjust the noise calculation for iteration between sound propagating from the aircraft to the ground.

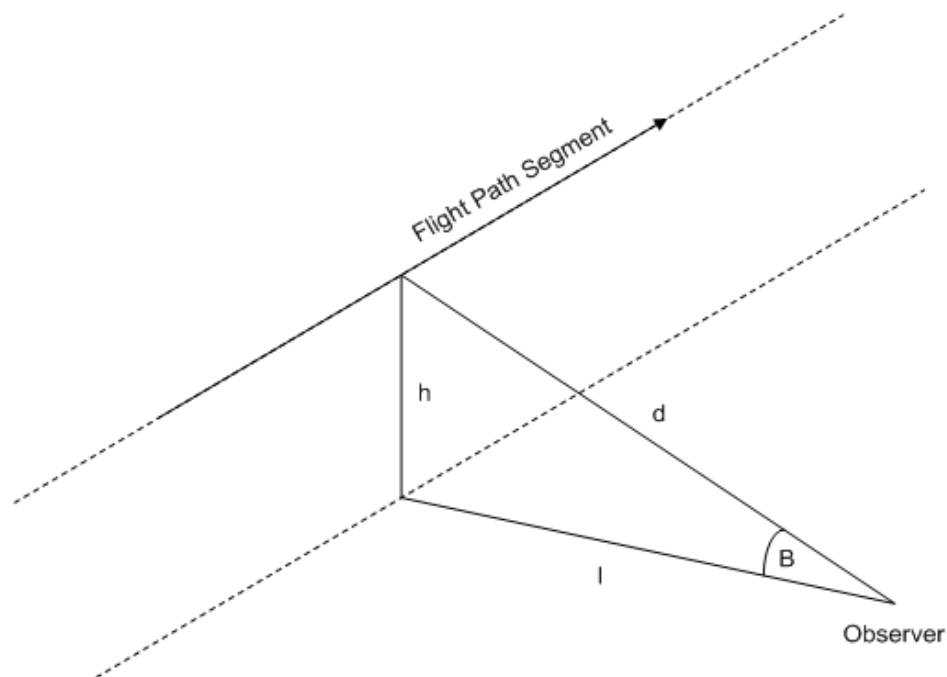


FIGURE 3.13: Geometric definition for INM model



The equation that shows the corrections to be added to obtain the noise-exposure level for a finite segment length is expressed as follow:

$$L_{e,seg} = L_{e,\infty}(P/T, d) + LA_{ADJ}(l, \beta) + DUR_{ADJ} + LEN_{ADJ} + INS_{ADJ}(\varphi_{en}) \quad (3.36)$$

where  $L_{e,seg}$  is the Noise exposure level for infinite length segment,  $LA_{ADJ}$  is the adjustment for lateral attenuation,  $DUR_{ADJ}$  is the adjustment for segment duration,  $LEN_{ADJ}$  is the adjustment for finite segment length,  $INS_{ADJ}$  is the adjustment for engine installation effects, function of depression angle  $\varphi_{en}$ .

The INM algorithm can therefore be applied to the total trajectory segments and the noise exposure level for the whole trajectory is expressed as follow:

$$L_e = 10 \cdot \log_1 0 \sum_{i=1}^{n_{seg}} 10^{0.1 \cdot L_{e,seg_i}} \quad (3.37)$$

The maximum noise exposure level for a single segment and for the whole trajectory is expressed as follows

$$L_{max}^{seg} = L_{max,\infty}(P/T, d) + LA_{ADJ}(l, \beta) + INS_{ADJ}(\varphi_{en}) \quad (3.38)$$

$$L_{max} = \max_{i=1,seg} L_{max}^{seg} \quad (3.39)$$

### 3.5.2 Noise annoyance

The noise exposure level does not assess the real impact of the aircraft activity on the ground and the impact on the population. Information regarding population density and location around the airport is a better way to estimate if the noise produced by the aircraft activity is really perceived by the population.

The study performed by the Federal Interagency Committee on Aviation Noise (FICAN) in 1997 defined a way to model the overall sleep disturbance as function of the sound exposure level measured inside the house [53]. This relation can be merged with the population distribution to obtain the rate of awakened people expected by the aircraft activity when the indoor SEL is above 30dB. In [72] the typical house insulation is estimated to be a factor of 20.5 dB and the SEL obtained by INM model is corrected by that value to calculate the indoor noise as follow:

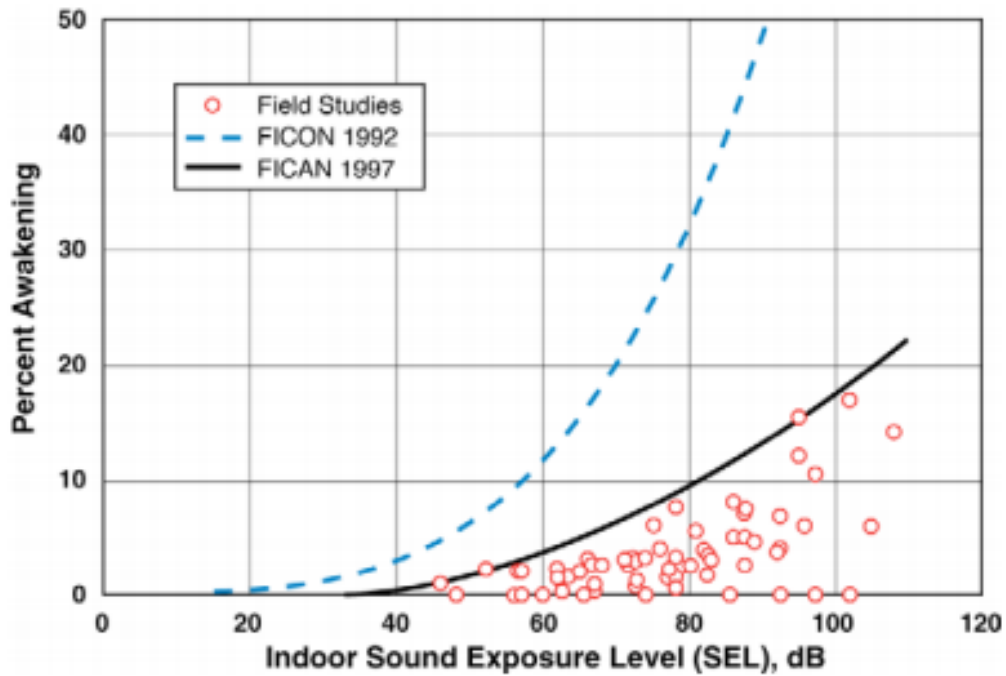


FIGURE 3.14: Relation between the overall sleep disturbance and indoor SEL[53]

$$SEL_{indoor} = SEL_{outdoor} - 20.5dB \quad (3.40)$$

$$Awakening[\%] = 0.0087 \cdot (SEL_{indoor} - 30dB)^{1.79} \quad (3.41)$$

From the percentage of awakened people is straightforward to obtain the number of people awakened by population distribution data.

Other approaches to model the noise annoyance exist. The noise event measured in its magnitude and location is not enough to determine the precise annoyance produced. For example, FICAN does not take into account the duration of the noise event, nor the spectra distribution. Xavier Prats during his research takes into account non-acoustic elements to obtain a more global annoyance model. The factors taken into account are as follow:

- Existing background noise which is already perceived by the population.
- The time of the day when the noise event occurs.

- The type of day when the noise event occurs (working day, weekend, holiday period, etc).
- A distinction of the type of zones which are affected by the noise event (rural, residential, industrial, hospitals, schools, etc).
- Socio-economic aspects (age, education level, economic level, etc).

This way of thinking the noise annoyance is more detailed and requires more information and extensive surveys which are not only limited to terminal area. Xavier introduces fuzzy logic to be able to deal with this kind of modelling. More information regarding this approach of noise annoyance can be found here[\[73\]](#).

# Chapter 4

## Fundamental Theory of Optimisation

### 4.1 Introduction

This chapter describes the methodology which is proposed to solve the greener aircraft trajectory problem modelled in Chapter 3. It can be formally written as multi-objective constrained optimisation problem. The problem is not feasible analytically due to its non-linearity and hence resolved numerically using numerical methodologies described in Chapter 2. First, the Optimal Control Problem is introduced as a more generic multiphase case where many optimal control problems are linked between them. Mathematical tools are then introduced to describe the numerical methodology that is used to solve the problem. Towards the end of the chapter, the transformation between single-objective into multi-objective problem is described.

### 4.2 Multiphase Optimal Control Problem

Rao and Benson [17] defined a multi-phase optimal control problem which is in summary as follows:

Given a set of  $P$  phases where the generic phase  $p \in [1, \dots, P]$ . Determine the control history  $\mathbf{u}^{(p)}(t) \in \mathfrak{R}^{m_p}$ , the state history  $\mathbf{x}^{(p)}(t) \in \mathfrak{R}^{n_p}$ , the static parameters

$\mathbf{q}^{(p)} \in \Re^{q_p}$  in phase  $p$ , that optimises the performance index or optimisation criteria which has the following form:

$$J = \sum_{p=1}^P [\Phi^{(p)}(\mathbf{x}^{(p)}(t_0), t_0, \mathbf{x}^{(p)}(t_f), t_f; \mathbf{q}^{(p)}) + \int_{t_0}^{t_f} \Gamma^{(p)}(\mathbf{x}^{(p)}(t), \mathbf{u}^{(p)}(t), t; \mathbf{q}^{(p)}) dt] \quad (4.1)$$

which is subject to dynamic constraints of:

$$\dot{\mathbf{x}}^{(p)} = \mathbf{f}^{(p)}[\mathbf{x}^{(p)}(t), \mathbf{u}^{(p)}(t), t; \mathbf{q}^{(p)}] \quad (4.2)$$

where the inequality path constraints are:

$$\mathbf{C}^{(p)}(\mathbf{x}^{(p)}(t), \mathbf{u}^{(p)}(t), t; \mathbf{q}^{(p)}) \leq 0 \quad (4.3)$$

with the boundary conditions:

$$\phi_{min} \leq \phi^{(p)}(\mathbf{x}^{(p)}(t_0), \mathbf{x}^{(p)}(t_f), t; \mathbf{q}^{(p)}) \leq \phi_{max} \quad (4.4)$$

and if more than one phase is considered (i.e.  $P > 1$ ), the phase continuity conditions will be defined as:

$$\mathbf{P}^{(s)}(\mathbf{x}^{p_i^s}(t_f), t_f^{p_i^s}; \mathbf{q}^{p_i^s}, \mathbf{x}^{p_u^s}(t_0), t_0^{p_u^s}; \mathbf{q}^{p_u^s}) = 0 \quad (4.5)$$

where  $t \in \Re$  and  $L$  is the number of phases to be linked,  $p_i^s$  the "left" phase numbers and  $p_u^s$  the "right" phase numbers. In general the phases can not be sequential. A schematic of how phases can potentially be linked is shown in Figure 4.1 where five phases are considered and the end of phase 1, 2 and 3 are respectively linked to the starts of phases 2, 3 and 4, while the end of phase 2 is linked to the start of phase 5 [17]. Figure 4.1 shows the multiphase OCP capabilities of phase linking, however the use of phase linking applied to aircraft trajectory problem is restricted to a sequential way only in this work.

To solve the multiphase optimal control problem described by eqs 4.1-4.5, Rao and Benson [17] use General Pseudospectral Optimisation Software (GPOPS) toolbox. GPOPS toolbox is software written in MATLAB that allows the user to solve OCP problems using pseudo-spectral numeric algorithm to transcribe the Optimal Control Problems (OCPs) into the non-linear problem (NLP). The formed NLP problem can be solved using various solvers (e.g. IPOPT, SNOPT, etc) as

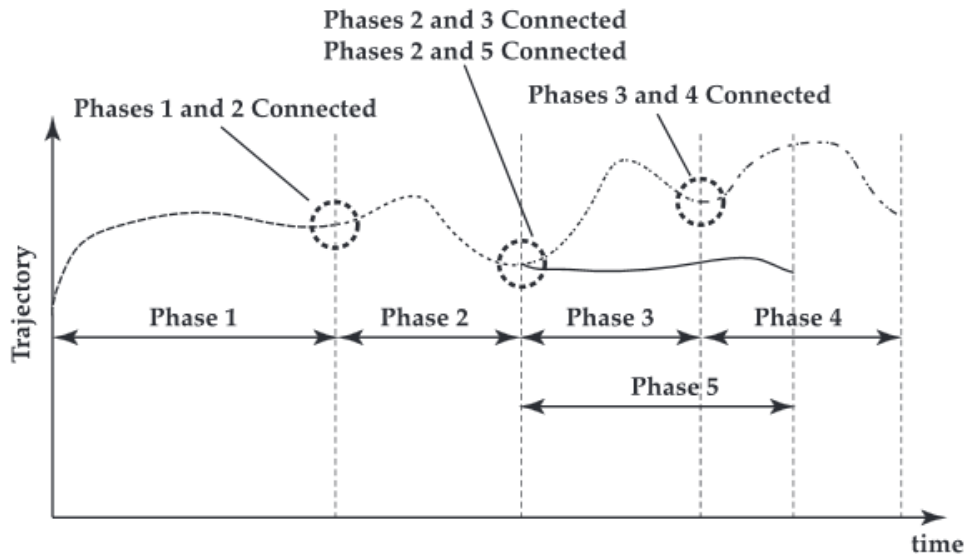


FIGURE 4.1: Schematic of linkages for multiple phase OCP [17]

previously described. In this thesis, the solver SNOPT[74] is used to solve the formed NLP problem.

In addition, INTLAB[75] toolbox is also used to obtain the derivatives of the problem states against control variables in a faster way than using the SNOPT in-built finite difference method. INTLAB is, therefore, not necessary for the quality of the result as it is, just to improve the performance of the overall optimisation framework. All of these toolboxes: GPOPS and INTLAB are software open source publicly downloadable from the provider website and require licenses if they are used for commercial applications. GPOPS toolbox has had lots of changes during the recent years and nowadays they have released GPOPS-II which is no longer opensource and uses different MATLAB function-type (e.g. m-files) to prevent the user to see how the implementation is done which results in more difficult to use especially when errors occur during the problem setup.

### 4.3 Numerical Solution of Differential Equations

Rao[38] describes the ability to solve differential equations (i.e. integrate of differential equations 4.2) as fundamental part to numerically solve the OCP problem. If we consider the following first order differential equation:

$$\dot{x}(t) = f(t), \quad x(t_0) = x_0 \quad (4.6)$$

The solution at the time  $t_{i+1}$  known as  $x(t_{i+1}) = x_{i+1}$  is written in the equivalent integral form knowing the solution at  $t_i$  as:

$$x_{i+1} = x_i + \int_{t_i}^{t_{i+1}} \dot{x}(t) dt = x_i + \int_{t_i}^{t_{i+1}} f(t) dt \quad (4.7)$$

The equation 4.7 describes the so called Initial Value Problem (IVP) and can be solved by two different approaches [76]. The first approach uses explicit numerical integration scheme which are known as "time marching" and a second approach uses implicit numerical integration schemes which are known as "collocation".

### 4.3.1 Time Marching

In time marching schemes (or methods) the integral of equation 4.7 is approximated by discretising the time interval by simpling time  $h_i = t_{i+1} - t_i$  and where the solution at the time  $t_{i+1}$  is obtained sequentially using current solution, and in some cases also the solution of previous step. Time marching schemes are further divided into two categories: multi-step and multi-stage.

Euler forward, Euler backward, trapezoidal, also known as Crank-Nicolson, Adams-Bashforth and Adams-Moulton are single and multi-step schemes which were developed along the years. Hermite-Simpson and Runge-Kutta are instead multi stage schemes and are more complicated and were developed after the multi-step schemes as improvements of them.

Euler schemes are the most simple and most known single step schemes used in solving ODEs. The Euler scheme general form is described as follows [38]:

$$\int_{t_i}^{t_{i+1}} f(t)dt \approx h_i[\theta f_i + (1 - \theta)f_{i+1}] \quad (4.8)$$

where  $f_i$  and  $f_{i+1}$  are respectively the integrand at the instant  $i$  and  $i + 1$  and  $\theta \in [0, 0.5, 1]$  defines respectively the Euler forward, trapezoidal or Euler backward scheme. Both Euler schemes (i.e.  $\theta = 0$  and  $\theta = 1$ ) are 1st-order which results in accuracy of  $O(h^2)$  local truncation error. Trapezoidal scheme instead is a 2nd-order scheme which results having an accuracy of  $O(h^3)$ .

Higher accuracy integration schemes are obtained by increasing the number of steps involved. Two-step schemes such as for Adams-Bashforth and Adams-Moulton require the evaluation of the integrand  $f$  at time step  $t_{i-1}$  and  $t_i$ . Adams-Bashforth scheme general form is described as follow:

$$\int_{t_i}^{t_{i+1}} f(t) dt \approx h_i \left[ f_i + \frac{1}{2}(f_i - f_{i-1}) + \frac{5}{2}(f_i - f_{i-1})^2 + \frac{3}{8}(f_i - f_{i-1})^3 + \dots \right] \quad (4.9)$$

which is also a 2nd-order scheme resulting in having an accuracy of  $O(h^3)$ .

Multi stage schemes, such as Hermite-Simpson and Runge-Kutta schemes, divide the time interval  $[t_i, t_{i+1}]$  into  $N$  sub-intervals and the time at each sub-interval is called  $j$ -stage and has the following form:

$$\tau_j = t_i + h_i \alpha_j, \quad (j = 1, \dots, N), \quad (h_i = t_{i+1} - t_i) \quad (4.10)$$

and where  $\alpha_j \in [0, +1]$  and the values determines the degree and the name of the scheme. Hermite-Simpson scheme is a 3rd-order which results in having  $N = 3$  and its general form is:

$$\int_{t_i}^{t_{i+1}} f(t) dt \approx \frac{h_i}{6} [f_i + 4f_{\frac{i}{2}} + f_{i+1}] \quad (4.11)$$

It is possible to see that the integral is approximated using a quadratic polynomial form. The integrand values at the endpoints ( $i$  and  $i + 1$ ) plus at the midpoint ( $i/2$ ) of the interval determines the solution. Runge-Kutta classical scheme is a 4th-order scheme, hence sometimes it is referred as RK4, and its general form is:

$$\int_{t_i}^{t_{i+1}} f(t) dt \approx \frac{h_i}{6} [k_1 + 2k_2 + 2k_3 + k_4] \quad (4.12)$$

Comparing the RK4 form against Hermite-Simpson and it is possible to see some similarities, infact Runge-Kutta scheme is a more general version of Hermite-Simpson. All the time machine schemes are better represented by the Butcher array.

### 4.3.2 Collocation

The collocation scheme is another way of solving differential equations and it was first introduced by Crandall in 1956[77] before the finite element schemes came



into existence and hence before collocation schemes massively became known. The collocation scheme was used to solve boundary value problems such as in structural and computational fluid dynamics (CFD) fields. An initial guess of the solution was forced to satisfy the differential equation and the boundary constraints. The collocation scheme implies the weighted residuals method, where the trial function constructs the trial solution and the weight function provides the criteria to minimize the residual.

A subset of collocation schemes which have caught most attention in OCP is the so-called orthogonal collocation. In an orthogonal collocation scheme the polynomial used is chosen from the family of orthogonal polynomials and the collocation points used are the roots of the chosen polynomial. The most diffuse collocation points in orthogonal collocation schemes are those which are obtained from the roots of Legendre polynomials family and in other cases from the roots of Chebyshev polynomial family [33][38].

Collocation schemes are divided into three main categories, differentiated based on the nature of the end points used:

- Gauss collocation scheme: neither of the endpoints are collocation points.
- Radau collocation scheme: only one of the endpoints is a collocation point.
- Labatto collocation scheme: both of the endpoints are collocation points.

In the collocation schemes, the trial functions used are Dirac delta functions centered at a set of collocation points. This implies that the differential equation must be satisfied exactly at the collocation points. Considering a generic differential equation for  $x(\tau) \in \mathfrak{R}^n$ , so that

$$F[\dot{x}(\tau), x(\tau), \tau] = 0, \quad \tau \in [-1, 1] \quad (4.13)$$

The boundary conditions are defined at the extreme points as follows

$$\beta[x(-1), x(1)] = 0 \quad (4.14)$$

The solution  $x(t)$  is approximated using a basis of orthogonal polynomials  $\phi_k(\tau)$  as trial functions and is expressed as follows

$$x(\tau) \approx X(\tau) = \sum_{k=1}^N a_k \phi_k(\tau) \quad (4.15)$$

The objective is then to determine the coefficients  $a_k$  so that the boundary conditions are satisfied and the residual is null at a set of collocation points.

The pseudospectral schemes can be used with the basis of Lagrange polynomial as trial functions, formed from the collocation points, in this case the function that approximates the state functions becomes as follows

$$\mathbf{x}(\tau) \approx \mathbf{X}(\tau) = \sum_{k=1}^N \mathbf{c}_k L_k(\tau) \quad (4.16)$$

where  $L_k(\tau)$  are Lagrange polynomials. Lagrange polynomials are used because they have the following characteristic:

$$L_k(\tau_i) = \begin{cases} 1, & k = j \\ 0, & k \neq j \end{cases} \quad (4.17)$$

which is known as isolation property. The isolation property of the Lagrange polynomials applied to the state approximation leads to the following:

$$\mathbf{c}_k = \mathbf{x}(\tau_k) \quad (4.18)$$

The advantage of the collocation approach is that the coefficients of the Lagrange polynomials  $\mathbf{c}_k$  result equal to the value approximating the polynomial at the collocation points.

The orthogonal collocation scheme was first in solving differential equations by Boor in 1973 [78]. The use of orthogonal collocation in quadrature approximation of integrals produce extremely accurate solutions, much more accurate than using standard collocation.

Let's consider the approximation of the integral of a function  $g(\tau)$  using Legendre-Gauss (LG) collocation technique of  $N$  points, the quadrature approximation is

expresses as follows:

$$\int_{-1}^1 g(\tau) d\tau \approx \sum_{k=1}^N w_k g(\tau_k) \quad (4.19)$$

where  $\tau_k$  are the Legendre-Gauss (LG) collocation points which are the roots of the  $N$ th degree Legendre polynomial  $P_n(\tau)$ , and  $w_k$  are the Legendre-Gauss weights. The approximation becomes an equality if the function  $g(\tau)$  is a polynomial of degree  $2N - 1$ . Therefore the accuracy obtained by using the quadrature collocation is higher than the number of collocation points used, which instead was the condition of time marching schemes.

Other quadrature schemes include the Legendre-Gauss-Radau (LGR) which results exact for a polynomial of degree  $2N - 2$  where  $N$  is the number of LGR collocation points which are the  $N$  roots of the polynomial  $P_{N-1}(\tau) + P_N(\tau)$ ; Legendre-Gauss-Lobatto (LGL) which results exact for polynomial of degree  $2N - 3$  where  $N$  is the number of LGL collocation points which are the  $N$  roots of the polynomial  $\dot{P}_N(\tau)$  together with the endpoints. A comparison between Legendre-Gauss (LG), Legendre-Gauss-Radau (LGR) and Legendre-Gauss-Lobatto (LGL) collocation points for  $N = 5$  is shown in Figure 4.2.

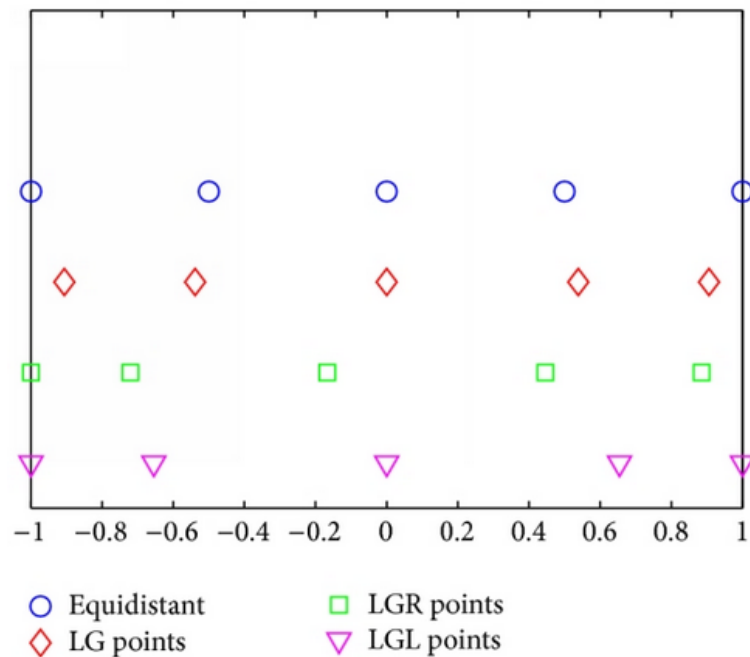


FIGURE 4.2: Comparison between Legendre-Gauss (LG), Legendre-Gauss-Radau (LGR) and Legendre-Gauss-Lobatto (LGL) collocation points [79]

## 4.4 Radau Pseudospectral Method (RPM)

The Radau Pseudospectral Method (RPM) is a global orthogonal collocation scheme, also known as pseudospectral scheme which implies the Legendre-Gauss-Radau points as collocation points. It has been developed by Garg [80] in the attempt of using Legendre-Gauss-Radau collocation points to solve either finite-horizon or infinite-horizon problems. The RPM was later implemented in the Matlab toolbox GPOPS [17]. To describe the RPM scheme as clear as possible, in this section the general OCP problem is considered formed by one phase only. The reader is referred to [81] for a more detailed explanation of the RPM pseudospectral scheme.

In RPM scheme, the time interval  $t \in [t_0, t_f]$  is transformed in a new independent variable  $\tau \in [-1, +1]$ . The relation between  $t$  and  $\tau$  is defined as follow:

$$t = \frac{t_f - t_0}{2}\tau + \frac{t_f + t_0}{2} \quad (4.20)$$

The OCP problem is therefore defined in term of the new independent variable. Determine the control  $\mathbf{u}(\tau)$ , the state  $\mathbf{x}(\tau)$ , the integral, the initial time  $t_0$  and the final time  $t_f$  on the interval  $\tau \in [-1, +1]$  that minimize the cost function, subject to the dynamic constraints, the path constraints, the integral constraints and the event constraints.

The interval  $\tau \in [-1, +1]$  is divided into a mesh of  $K$  mesh intervals  $[T_{k-1}, T_k]$ ,  $k = 1, \dots, K$  where  $T_0, \dots, T_K$  are the mesh points and where  $T_0 = -1$  and  $T_K = +1$ . In each interval  $k$  the control and state are defined respectively as  $\mathbf{u}^{(k)}(\tau)$  and  $\mathbf{x}^{(k)}(\tau)$  and the overall OCP problem is now defined as:

$$J = \Phi(\mathbf{x}^{(1)}(-1), t_0, \mathbf{x}^{(K)}(+1), t_f) + \frac{t_f - t_0}{2} \sum_{k=1}^K \int_{T_{k-1}}^{T_k} \Gamma[\mathbf{x}^{(k)}(\tau^{(k)}), \mathbf{u}^{(k)}(\tau^{(k)}), \tau^{(k)}; t_0, t_f] d\tau \quad (4.21)$$

the dynamic constraints

$$\frac{2}{t_f - t_0} \frac{d\mathbf{x}^{(k)}(\tau^{(k)})}{d\tau^{(k)}} = \mathbf{f}[\mathbf{x}^{(k)}(\tau^{(k)}), \mathbf{u}^{(k)}(\tau^{(k)}), \tau^{(k)}; t_0, t_f] \quad (4.22)$$

the path constraints

$$\mathbf{C}_{min} \leq \mathbf{C}[\mathbf{x}^{(k)}(\tau^{(k)}), \mathbf{u}^{(k)}(\tau^{(k)}), \tau^{(k)}; t_0, t_f] \leq \mathbf{C}_{max} \quad (4.23)$$

and the boundary conditions

$$\phi_{min} \leq \phi[\mathbf{x}^{(1)}(-1), t_0, \mathbf{x}^{(K)}(+1), t_f, \mathbf{q}] \leq \phi_{max} \quad (4.24)$$

Now the OCP for  $K$  mesh intervals is defined and it is possible to apply the RPM transcription as follow: The state  $\mathbf{x}^{(k)}$  and the control  $\mathbf{u}^{(k)}$  are approximated using a set of Lagrange interpolating polynomials at the LGR collocation points as previously introduced.

$$\mathbf{x}^{(k)}(\tau) \approx \mathbf{X}^{(k)}(\tau) = \sum_{j=1}^{N_k+1} \mathbf{X}_j^{(k)} l_j^{(k)}(\tau) \quad (4.25)$$

$$\mathbf{u}^{(k)}(\tau) \approx \mathbf{U}^{(k)}(\tau) = \sum_{j=1}^{N_k} \mathbf{U}_j^{(k)} l_j^{(k)}(\tau) \quad (4.26)$$

where  $\tau \in [-1, +1]$ ,  $\mathbf{X}^{(k)}$  and  $\mathbf{U}^{(k)}$  are the approximation of the state and control respectively at  $N_k+1$  and  $N_k$  collocation points, and  $l_j^{(k)}(\tau)$  is the triac of Lagrange polynomials,  $\tau_1^{(k)}, \dots, \tau_{N_k}^{(k)}$  are the LGR collocation points in the sub-interval  $k$ . To be able to apply the transformation to the dynamic equations constraints there is the need to differentiate the approximated state with respect to the new time variable.

$$\frac{d\mathbf{X}^{(k)}(\tau)}{d\tau} = \sum_{j=1}^{N_k+1} \mathbf{X}_j^{(k)} \frac{dl_j^{(k)}(\tau)}{d\tau} \quad (4.27)$$

It is possible now to transcript the differential equations at the LGR collocation points and obtaining:

$$\sum_{j=1}^{N_k+1} D_{ij}^{(k)} \mathbf{X}_j^{(k)} - \frac{t_f - t_0}{2} \mathbf{f}[\mathbf{X}_i^{(k)}, \mathbf{U}_i^{(k)}, \tau_i^{(k)}, t_0, t_f] = 0, \quad i = 1, \dots, N_k \quad (4.28)$$

where  $\mathbf{U}_i^{(k)}$ ,  $i = 1, \dots, N_k$  are the approximations of the control at the LGR collocation points for the  $k$  mesh interval; and  $\mathbf{D}_{ij}^{(k)}$  is the differentiation matrix of the LGR points for  $k$ -mesh interval.

$$\mathbf{D}_{ij}^{(k)} = \left[ \frac{dl_j^{(k)}(\tau)}{d\tau} \right]_{\tau_i^{(k)}} \quad i = 1, \dots, N_k, j = 1, \dots, N_k + 1, k = 1, \dots, K \quad (4.29)$$

It is also possible to collocate the dynamic equations by implicit integral form. This method is part of the RPM scheme and is described in [80]. The implicit

integral form of the RPM allows to obtain:

$$\mathbf{X}_{i+1}^{(k)} - \mathbf{X}_i^{(k)} = \frac{t_f - t_0}{2} \sum_{j=1}^{N_k} \mathbf{I}_{ij}^{(k)} \mathbf{f}[\mathbf{X}_i^{(k)}, \mathbf{U}_i^{(k)}, \tau_i^{(k)}, t_0, t_f], \quad i = 1, \dots, N_k \quad (4.30)$$

where  $\mathbf{I}_{ij}^{(k)}$  is the integration matrix of the LGR points for  $k$ -mesh interval and can be obtained from the differentiation matrix [80] as follow:

$$\mathbf{I}^{(k)} \equiv [\mathbf{D}_{2:N_k+1}^{(k)}]^{-1} \quad (4.31)$$

Now the path constraints are transcribed at the LGR collocation points as follow:

$$\mathbf{C}_{min} \leq \mathbf{C}[\mathbf{X}^{(k)}, \mathbf{U}^{(k)}, \tau_i^{(k)}; t_0, t_f] \leq \mathbf{C}_{max}, \quad i = 1, \dots, N_k \quad (4.32)$$

And to conclude the boundary conditions are transcribed at the LGR points as follow:

$$\phi_{min} \leq \phi[\mathbf{X}_1^{(1)}, t_0, \mathbf{X}_{N_k+1}^{(K)}, t_f, \mathbf{q}] \leq \phi_{max} \quad (4.33)$$

In the RPM scheme there is no need of the continuity condition to provide continuity in the state at the mesh points  $k$  because it is already taken into account explicitly. The Eq. cost function subject to the algebraic constraints of Eqs. - compose the NonLinear Problem (NLP) which is going to be optimised by the NLP optimiser.

The set of decision variables obtained by RPM method are formed by considering the states, controls, static parameters and initial and final time for all the phases considered in the problem. The decision vector  $\mathbf{Z}$  is expressed as follows:

$$\mathbf{Z} = \begin{bmatrix} \mathbf{z}^{(1)} \\ \mathbf{z}^{(2)} \\ \vdots \\ \mathbf{z}^{(P)} \end{bmatrix} \quad (4.34)$$

where  $\mathbf{z}^{(p)}$  is a vector that contains all the variables of  $p$ -phase, such as coefficients approximating the states, controls and static parameters and initial and final time.

These phase-based variables are expressed as follows:

$$\mathbf{z}^{(p)} = \begin{bmatrix} \mathbf{V}_1^{(p)} \\ \vdots \\ \mathbf{V}_{n_x^{(p)}}^{(p)} \\ \mathbf{W}_1^{(p)} \\ \vdots \\ \mathbf{W}_{n_u^{(p)}}^{(p)} \\ \mathbf{q}^{(p)} \\ t_0^{(p)} \\ t_f^{(p)} \end{bmatrix}, \quad p = 1, \dots, P \quad (4.35)$$

where the matrix  $\mathbf{V}_i^{(p)}$  contains the coefficients approximating the  $i$ -state at phase  $p$  and  $\mathbf{W}_i^{(p)}$  contains the coefficients approximating the  $i$ -control at phase  $p$ , and  $n_x^{(p)}$  and  $n_u^{(p)}$  are the number of states and control for phase  $p$ .

The dynamic equations of the aircraft were shown in section 3.2 and according to equation 3.1 the states are chosen to be:

$$\mathbf{x}(t) = [V(t), \gamma(t), \chi(t), \varphi(t), \lambda(t), h(t), m(t)] \quad (4.36)$$

And the controls are chosen to be:

$$\mathbf{u}(t) = [n_z(t), \eta(t), \mu(t)] \quad (4.37)$$

Then, the nonlinear programming problem (NLP) obtained by the RPM method is formed as follow. Obtain the decision variables of vector  $\mathbf{Z}$  that

$$\min_{\mathbf{Z}} J(\mathbf{Z}) \quad (4.38)$$

subject to the constraints

$$\mathbf{F}_{min} \leq \mathbf{F}(\mathbf{Z}) \leq \mathbf{F}_{max} \quad (4.39)$$

with the following boundary limit

$$\mathbf{Z}_{min} \leq \mathbf{Z} \leq \mathbf{Z}_{max} \quad (4.40)$$

where  $J$  is the objective function to be minimized. The possible objective functions are going to be shown in the next section. The introduced NLP problem is solved using SNOPT solver [74].

## 4.5 Optimisation Criteria

Nowadays commercial aircraft operations concern mostly on overall fuel consumed and flying time resulting from a trajectory. If  $t_0$  and  $t_f$  are the initial and final time of a generic trajectory, the objective function which describes the fuel cost associated is defined as:

$$J_{fuel} = Price_{fuel} \cdot \int_{t_0}^{t_f} FF(t)dt \quad (4.41)$$

where  $Price_{fuel}$  is the fuel price and  $FF(t)$  the fuel flow which was defined in Eq. 3.10 and is function of the throttle used along the trajectory and relative SFC. Because the fuel price is constant during the flight, it can be considered as a constant. Therefore the same kind of ultimate trajectories obtained using  $C_f$  can also be obtained as difference between the initial and final aircraft mass. This approach is preferred because it doesn't involve a further integral calculation. The aircraft mass, which is a state, is already integrated because of its presence in the differential equation constraints. As a result the fuel cost is defined by Mayer component as:

$$J_{fuel} = Price_{fuel} \cdot (m_0 - m_f) = Price_{fuel} \cdot Fuel_{burnt} \quad (4.42)$$

Time cost involves many commercial operations such as insurance, air traffic control fees, crew salaries, turn around time, etc. The objective function which describes the time cost is defined as:

$$J_{time} = Price_{time} \cdot \int_{t_0}^{t_f} dt = Price_{time}(t_f - t_0) \quad (4.43)$$

Nowadays Flight Management Systems (FMS) allow the pilot to modify these costs which results in autopilot to fly a different trajectory (e.g. different computed climbing speed, cruising speed, cruising altitude, etc). A cost index (CI) is defined



which relates the cost of a time delay to the price of the fuel as follows:

$$CI = \frac{Price_{time}}{Price_{fuel}} \quad (4.44)$$

The CI is carefully calculated and may vary everyday due to fuel cost variations. Therefore pilots receive Cost Index update from the Airline Operational Centre (AOC) prior each flight to be entered into the FMS computers. The the objective function which allows to optimise the overall flight time can be simplified, considering that  $t_0 = 0$  and the price of time considered as constant.

$$J_{time} = \int_{t_0}^{t_f} dt = t_f \quad (4.45)$$

Regarding the environmental pollutants, the objective function which allows to optimise a specific emission component can be defined as follows. For example for the  $NO_x$ :

$$J_{NO_x} = \int_{t_0}^{t_f} EINO_x \cdot FF(t) dt \quad (4.46)$$

where  $EINO_x$  is defined by Eq. 3.33. Other emission criteria are obtained in the following way, just replace the EI with the appropriate one.

The impact of sound exposure level of a flight can be described by the following objective function.

$$J_{noise} = 0.0087 \cdot (SEL - 30)^{(1.97)} \quad (4.47)$$

where  $SEL$  is the overall sound exposure level for the considered trajectory measured on the ground and computed by the noise method explained in 3.

## 4.6 Multi-objective Optimisation

The optimisation of the greener aircraft trajectory involves several objectives at the same time, such as flight time, fuel consumption, engine emissions and noise generated. Hence, the aim of the optimisation process is to obtain the ultimate trajectory which minimises a set of  $N_J$  objectives and it can be formed as follows.

$$\min_{z \in Z} (J_1, J_2, \dots, J_{N_J}) \quad (4.48)$$

The process of minimization means that all the objective functions are minimised at the same time. If the considered objectives are not in conflict between each others, then the found solution is constituted by every object function at its optimum. Unfortunately the greener aircraft trajectory problem and its objective functions are in general conflicting which means that an obtained trajectory ( solution of the problem ) produces a certain value for one object function but produces a non acceptable one for another; and so on if more than two objectives are considered. Therefore it is not possible to find a solution which is optimal for all the objective functions simultaneously. The list of ultimate trajectories obtained for more than two objective functions can not be improved for one object function without degrading at least another objective function. The ultimate trajectories compose the well known Pareto optimality. Its name is due to Vilfredo Pareto during his study of distributional efficiency between social welfare and resource allocation [40].

### 4.6.1 The Pareto front

A solution of the problem  $z_{opt}$  is defined to be part of the pareto front if there is not another one  $z$  such that  $J_i(z) < J_i(z_{opt})$  for all the  $i$ -objective functions and  $J_j(z) < J_j(z_{opt})$  for at least one  $j$ -objective function. The shape of the pareto front is in general curved

## 4.7 Numerical Resolution

A direct transcription scheme is used in this research. Then the transcribed optimal control problem containing differential and algebraic constraints is solved as a NLP problem with only algebraic constraints. To better understand a series of screenshots are added. In Figure 4.3 it is possible to see a piece of Matlab code which defines the trajectory problem. In specific a list of waypoints which defines different phases and initial and final conditions used and bounds for the problem variables. In Figure 4.4 the differential algebraic equations and path constraints are implemented and they differ in the phases. In addition it is possible to see the engine and emissions implemented by using regression analysis using altitude, Mach and engine turbine temperature which is linear related to the throttle control. Finally in Figure 4.5 it is possible to see the output provided by the numerical

NLP algorithm which succeeded in optimising the problem. The ultimate trajectory can be re-constructed from the different phases and plotted. See Chapter 6 where results are shown.

```
56 -     SECTIONS = 1;
57
58 -     %% Segmentation
59 -     % BPK
60 -     Lat(1) = dms2degrees([51 44 59.00]);
61 -     Lon(1) = dms2degrees([0 -06 24.00]);
62 -     % DIGSU N52 01 26 E000 38 05
63 -     Lat(2) = dms2degrees([52 01 26.00]);
64 -     Lon(2) = dms2degrees([0 38 05.00]);
65 -     % SONDO
66 -     Lat(3) = dms2degrees([52 05 06.00]);
67 -     Lon(3) = dms2degrees([01 48 42.00]);
68 -     % SULUT % N 52 26.8755 E 3 25.26384
69 -     Lat(4) = dm2degrees([52 26.8755]);
70 -     Lon(4) = dm2degrees([03 25.26384]);
71 -     % SUGOL % N 52 31.53066 E 3 58.041
72 -     Lat(5) = dm2degrees([52 31.53066]);
73 -     Lon(5) = dm2degrees([03 58.041]);
74 -     % Convert LAT and Lon to Radians
75 -     Lat = deg2rad(Lat);
76 -     Lon = deg2rad(Lon);
77
78 -     %% Initial and final conditions
79 -     % INITIAL CONDITIONS
80 -     t0 = 0; % [s]
81 -     h0 = 6000; % [ft]
82 -     v0 = 250; % [KCAS]
83 -     fpa0 = 0; % [deg]
84 -     psi0 = 22; % [deg]
85 -     m0 = 66e+3; % [kg]
86 -     % FINAL CONDITIONS
87 -     hf = 10000; % [ft]
88 -     vf = 250; % [KCAS]
89 -     fpaf = 0; % [rad]
90 -     psif = 0; % [rad]
91 -     phif = 0; % [rad]
92
93 -     %% Bounds on variables
94 -     tfmin = 10; % [s]
95 -     tfmax = 10000; % [s]
96 -     latmin = dms2degrees([51 00 00]); % [deg]
97 -     latmax = dms2degrees([53 00 00]); % [deg]
98 -     longmin = dms2degrees([0 -50 00]); % [deg]
99 -     longmax = dms2degrees([5 00 00]); % [deg]
```

FIGURE 4.3: Screenshot of a piece of Matlab code which defines the problem to be optimised

```

45 - invmu = 1./mu;
46 - vCAS = sqrt(((2.*p0)./(mu.*rho0)).*((1+(P./p0).*((1+(mu.*rho.*v.*v)./(2.*P)).^invmu)-1).^mu)-1));
47
48 % Calculated parameters as function of variables
49 - CL = (2.*m.*g.*N)./(rho.*S.*v.*v.*cos(fpa));
50 - CD = CDO + K.*CL.^2;
51 - q = 0.5.*rho.*v.*v;
52 - D = q.*S.*CD;
53
54 %% Turbomatch Engine Performance
55 % TET [K]
56 - TET = (dT * (1462-906)) + 906; %dT should be between 0 and 1. 0 means IDLE and 1 TOGA
57 % NetThrust [N]
58 - NetThrust = 2.*(- (643539622444933.*Mach.^3)./274877906944 + (2572942706693193.*Mach.^2.*TET)./7036
59 %FuelFlow [kg/s]
60 - FuelFlow = 2.*(- (1829973047648471.*Mach.^3)./36028797018963968 + (371684735431191.*Mach.^2.*TET)./
61 %NOx [kg/s]
62 - NOx = 2.*( (1993412871596689.*Mach.^3)./9223372036854775808 + (35659182704573.*Mach.^2.*TET)./
63 %CO2 [kg/s]
64 - CO2 = FuelFlow.*3.16;
65
66 %% DAE
67 - vdot = g.*(NetThrust-D)./(m.*g.-sin(fpa));
68 - fpadot = (g.*(N.*cos(phi)-cos(fpa)))./v;
69 - psidot = (g./v).*(N.*(sin(phi)./cos(fpa)));
70 - latdot = v.*cos(fpa).*sin(psi)./(R0+h);
71 - longdot = v.*cos(fpa).*cos(psi).*sec(lat)./(R0+h);
72 - hdot = v.*sin(fpa);
73 - mdot = -FuelFlow;
74 - phidot = phicom;
75 - NOxdot = NOx;
76 - CO2dot = CO2;
77
78 %% PATH
79 - if sol.phase == 1
80 - path = [Mach vCAS hdot];
81 - elseif sol.phase == 2
82 - path = [Mach vCAS];
83 - elseif sol.phase == 3
84 - path = [Mach vCAS];
85 - elseif sol.phase == 4
86 - path = [Mach vCAS hdot];
87 - end

```

FIGURE 4.4: Screenshot of a piece of Matlab code which defines the differential algebraic equations and path constraints

```

Command Window
Major Minors Step nCon Feasible Optimal MeritFunction nS Penalty
90 1 4.1E-01 102 1.7E-06 1.2E-06 1.2997855E+03 197 9.9E+01 s
91 1 1.0E+00 103 (5.5E-08) 2.7E-06 1.2997854E+03 197 9.9E+01
92 1 1.0E+00 104 1.4E-06 1.5E-06 1.2997852E+03 197 9.9E+01
93 1 1.0E+00 105 1.8E-06 1.9E-06 1.2997850E+03 197 9.9E+01
94 1 1.0E+00 106 7.5E-06 2.9E-06 1.2997846E+03 197 9.9E+01
95 2 1.0E+00 107 2.4E-05 4.7E-06 1.2997841E+03 196 9.9E+01
96 1 1.0E+00 108 4.4E-05 1.4E-05 1.2997832E+03 196 9.9E+01
97 1 1.0E+00 109 (4.1E-07) 4.4E-06 1.2997827E+03 196 9.9E+01
98 1 1.0E+00 110 1.1E-06 2.5E-06 1.2997821E+03 196 9.9E+01
99 1 1.0E+00 111 (9.1E-07) 5.6E-06 1.2997818E+03 196 9.9E+01
Major Minors Step nCon Feasible Optimal MeritFunction nS Penalty
100 1 1.0E+00 112 1.6E-05 3.3E-06 1.2997811E+03 196 9.9E+01 R
101 1 1.0E+00 113 (1.8E-07) 3.5E-06 1.2997808E+03 196 9.9E+01 s
102 1 1.0E+00 114 5.2E-06 3.4E-06 1.2997805E+03 196 9.9E+01
103 1 1.0E+00 115 1.2E-06 4.1E-06 1.2997802E+03 196 9.9E+01
104 1 1.0E+00 116 (4.4E-07) 2.9E-06 1.2997799E+03 196 9.9E+01
105 1 1.0E+00 117 1.3E-06 5.4E-06 1.2997795E+03 196 9.9E+01
106 2 1.0E+00 118 3.3E-05 4.1E-06 1.2997786E+03 195 9.9E+01
107 2 1.0E+00 119 1.4E-05 3.7E-06 1.2997780E+03 194 9.9E+01
108 3 1.0E+00 120 5.2E-06 2.7E-06 1.2997776E+03 194 9.9E+01
109 2 1.0E+00 121 9.1E-06 4.9E-06 1.2997772E+03 193 9.9E+01
Major Minors Step nCon Feasible Optimal MeritFunction nS Penalty
110 1 1.0E+00 122 (6.7E-07) 2.3E-06 1.2997769E+03 193 9.9E+01
111 1 1.0E+00 123 2.9E-06 1.7E-06 1.2997767E+03 193 9.9E+01 R
112 1 4.4E-01 125 1.6E-06 (9.2E-07) 1.2997767E+03 193 9.9E+01 s
113 2 1.0E+00 126 (4.8E-08) (9.6E-07) 1.2997766E+03 192 9.9E+01

SNOPTA EXIT 0 -- finished successfully
SNOPTA INFO 1 -- optimality conditions satisfied
Problem name
No. of iterations 4668 Objective value 1.2997766245E+03
No. of major iterations 113 Linear objective 0.0000000000E+00
Penalty parameter 9.924E+01 Nonlinear objective 1.2997766245E+03
No. of calls to funobj 126 No. of calls to funcon 126
No. of superbasics 192 No. of basic nonlinears 2756
No. of degenerate steps 1882 Percentage 40.32
Max x 1 1.0E+00 Max pi 123 9.9E+03
Max Primal infeas 0 0.0E+00 Max Dual infeas 532 9.8E-03
Nonlinear constraint violn 1.2E-06

Solution printed on file 9
Elapsed time is 37.347031 seconds.
ft >>

```

FIGURE 4.5: Screenshot of Matlab command window at the end of the optimisation using GPOPS and INTLAB

# Chapter 5

## Simulation Environment

### 5.1 Introduction

This chapter describes the simulation environment which was created to test and evaluate the greener trajectories generated by the optimisation process which was described in Chapter 4. The aim of the simulation environment is to provide a test bed for the coupling of the optimised trajectories generated and the aircraft on-board systems which are in charge of flying the aircraft to achieve a greener flight.

The simulation environment has been developed in Matlab/Simulink tool in collaboration with Michael Cooper [82] during his research about actuator energy consumption during aircraft flight. The simulation environment is composed of several blocks.

- The aircraft dynamic model, which describes the 6-DOF motion of the aircraft. This is a more complete aircraft dynamic model than was used in the optimisation process due to introduction of rotational around aircraft x, y and z axis.
- The atmospheric model, which provides information about the atmosphere and wind components at the position of the fighting aircraft.
- The navigational model simulates the measurement of the physical properties that the aircraft needs to fly and provides the information to the other systems

- The autopilot and actuation models contains the control laws used to fly the aircraft and maintain it stable

The overall block diagram as seen from the top level of the Matlab Simulink software is shown in 5.1.

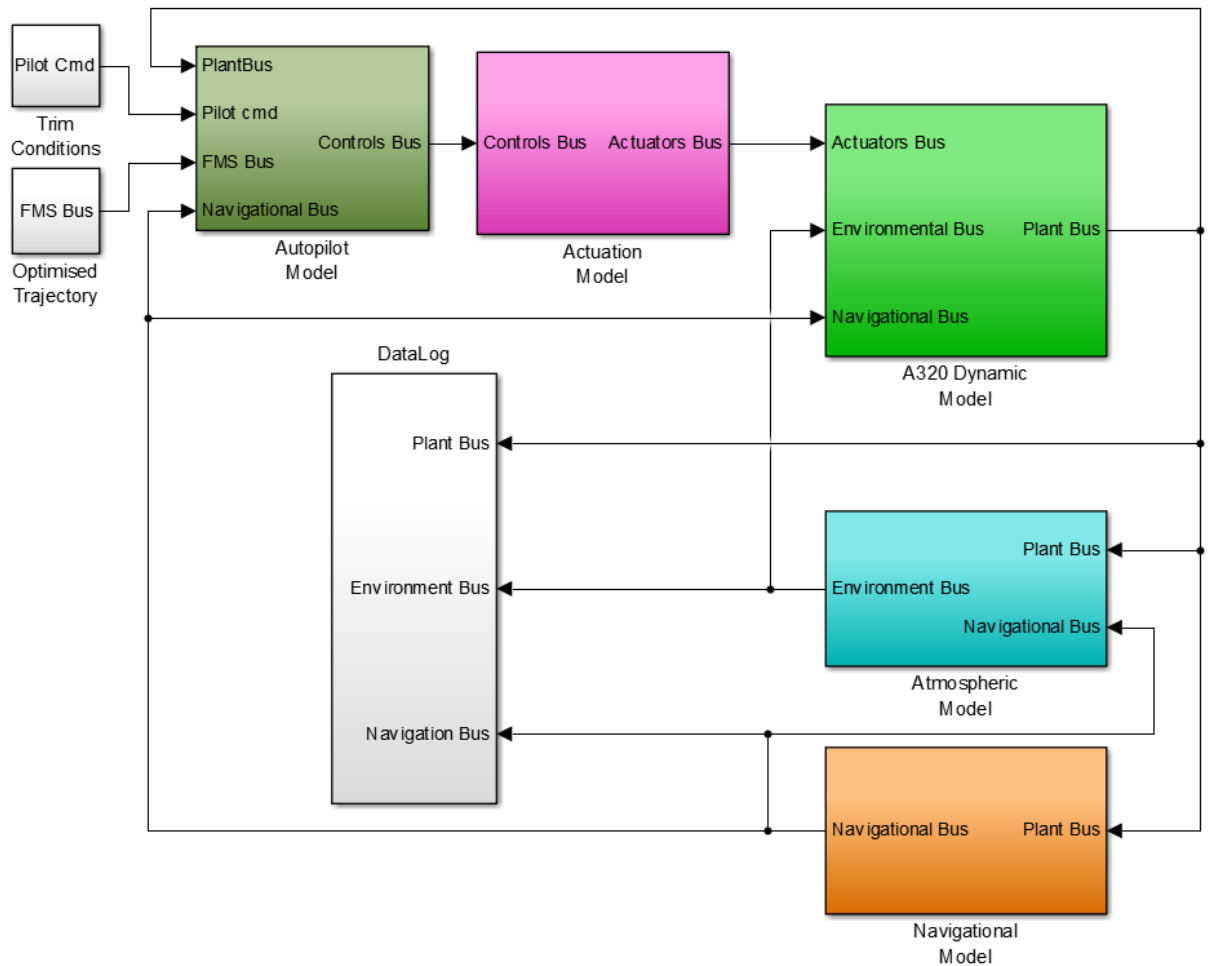


FIGURE 5.1: Simulink view of the simulation environment

## 5.2 Aircraft Dynamic Model

To be able to test and validate the greener trajectories a high fidelity aircraft dynamic model is required. The 6 degree of freedom (6-DOF) is able to describe completely the aircraft motion during its mission and therefore is selected for this purpose. Its complexity does not allow its use in optimisation environment or when fast computations are needed, such as in on-board systems when instead a reduced 3-DOF model was used.

### 5.2.1 Equations of Motion

The aircraft dynamic model used in the environment simulation is based on a 6 degree of freedom (6-DOF) rigid body model which relies on Newton's second law of motion. The 6-DOF model is not novel and have been applied into many aircraft simulators cores since decades. For the full derivation of the 6-DOF model the reader can refer to textbooks which cover the complete derivation [83]. The 6-DOF equations of motion are implemented using the Simulink block "6DOF (Euler angles)" which implies vector form for the variables involved to obtain the most efficient computational results.

$$\begin{bmatrix} \dot{p}_n \\ \dot{p}_e \\ \dot{p}_d \end{bmatrix} = \begin{bmatrix} c_\theta c_\psi & s_\phi s_\theta c_\psi - c_\phi s_\psi & c_\phi s_\theta c_\psi + s_\phi s_\psi \\ c_\theta s_\psi & s_\phi s_\theta s_\psi - c_\phi c_\psi & c_\phi s_\theta s_\psi + s_\phi c_\psi \\ -s_\theta & s_\phi c_\theta & c_\phi c_\theta \end{bmatrix} \begin{bmatrix} u \\ v \\ w \end{bmatrix} \quad (5.1)$$

$$\begin{bmatrix} \dot{u} \\ \dot{v} \\ \dot{w} \end{bmatrix} = \begin{bmatrix} rv - qw \\ pw - ru \\ qu - pv \end{bmatrix} + \frac{1}{m} \begin{bmatrix} F_x \\ F_y \\ F_z \end{bmatrix} \quad (5.2)$$

$$\begin{bmatrix} \dot{\phi} \\ \dot{\theta} \\ \dot{\psi} \end{bmatrix} = \begin{bmatrix} 1 & s_\phi t_\theta & c_\phi t_\theta \\ 0 & c_\phi & -s_\phi \\ 0 & s_\phi \sec\theta & c_\phi \sec\theta \end{bmatrix} \begin{bmatrix} p \\ q \\ r \end{bmatrix} \quad (5.3)$$

$$\begin{bmatrix} \dot{p} \\ \dot{q} \\ \dot{r} \end{bmatrix} = \begin{bmatrix} \Gamma_1 pq - \Gamma_2 qr \\ \Gamma_5 pr - \Gamma_6 (p^2 - r^2) \\ \Gamma_7 pq - \Gamma_1 qr \end{bmatrix} + \begin{bmatrix} \Gamma_3 L + \Gamma_4 N \\ \frac{1}{I_y} M \\ \Gamma_4 L + \Gamma_8 N \end{bmatrix} \quad (5.4)$$

The 6-DOF equations of motion represented by Eqs 5.1-5.4 the requires external forces and moments to obtain the trajectory of the aircraft in the 3D space. The main forces and moments applied to the aircraft centre of gravity (CG) are described as follow:

$$\mathbf{F} = \mathbf{F}_g + \mathbf{F}_a + \mathbf{F}_p \quad (5.5)$$

$$\mathbf{M} = \mathbf{M}_a + \mathbf{M}_p \quad (5.6)$$

where the subscript  $g$  denotes the force applied to the CG due to gravitational force and  $a$  and  $p$  denotes the force and moment due to aerodynamic and propulsion

effects respectively. The overall diagram of the aircraft dynamic model is shown in Figure 5.2.

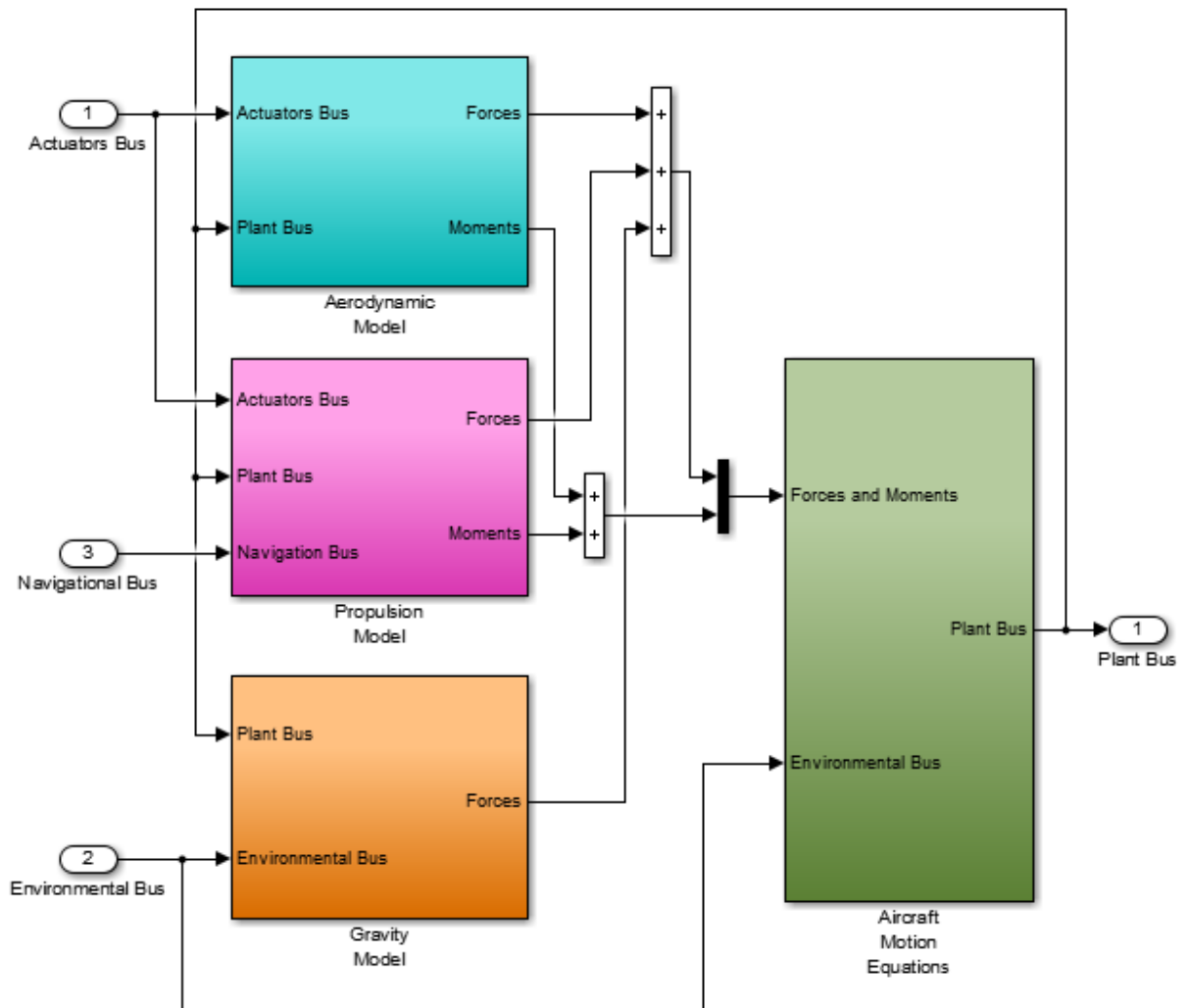


FIGURE 5.2: Simulink view of the aircraft dynamic model

### 5.2.2 Gravitational Model

The gravitational force is applied to the aircraft Centre of Gravity (CG) and is directed to the centre of the Earth. Because the force is applied to the aircraft CG, there is no rotational moment applied by the gravitational force. In terms of body axis system of reference, the gravity vector, which has magnitude of  $mg$  needs to be rotated due to the aircraft attitude (i.e. pitch and roll angles). The



gravitational model is expressed by the following:

$$\mathbf{F}_g^b = \begin{bmatrix} -mg & \sin\theta \\ mg & \cos\theta\sin\phi \\ mg & \cos\theta\cos\phi \end{bmatrix} \quad (5.7)$$

### 5.2.3 Aerodynamic Model

The aerodynamic forces and moments are generated by the air flow around the aircraft body. The main airframe component are the wings. In addition the fuselage, the aerodynamic appendixes and the engine nacelles also produce forces and moments. In general terms, the aerodynamic forces can be described as follow:

$$F_{drag} = F_x = \frac{1}{2}\rho V^2 S C_D \quad (5.8)$$

$$F_{side} = F_y = \frac{1}{2}\rho V^2 S C_Y \quad (5.9)$$

$$F_{lift} = F_z = \frac{1}{2}\rho V^2 S C_L \quad (5.10)$$

where  $\rho$  is the density of the air which surrounds aircraft body,  $V$  is the aircraft true airspeed,  $S$  is the aircraft planform wing surface,  $C_D$ ,  $C_Y$  and  $C_L$  are respectively the drag, the side and the lift nondimensional coefficients which define the aerodynamic characteristics of the aircraft. They are function of many variables and generally they are obtained by wind tunnels exhaustive tests for aircraft different attitude, control surfaces positions and aircraft rotational movements.

The overall non-dimensional coefficients  $C_D$ ,  $C_Y$  and  $C_L$  can be described by the linear combination of static and dynamic coefficients as follow:

$$C_D = C_{D_0} + \frac{\partial C_D}{\partial \alpha} \alpha + \frac{\partial C_D}{\partial q} q + \frac{\partial C_D}{\partial \delta_e} \delta_e \quad (5.11)$$

$$C_Y = C_{Y_0} + \frac{\partial C_Y}{\partial \beta} \beta + \frac{\partial C_Y}{\partial p} p + \frac{\partial C_Y}{\partial r} r + \frac{\partial C_Y}{\partial \delta_a} \delta_a + \frac{\partial C_Y}{\partial \delta_r} \delta_r \quad (5.12)$$

$$C_L = C_{L_0} + \frac{\partial C_L}{\partial \alpha} \alpha + \frac{\partial C_L}{\partial q} q + \frac{\partial C_L}{\partial \delta_e} \delta_e \quad (5.13)$$

The derivatives of the coefficients against the rotational moments  $p$ ,  $q$  and  $r$  must be non-dimensional and therefore the mean wing chord  $\bar{c}$ , wingspan  $b$  and airspeed  $V$  are taken into account. The aerodynamic derivatives use a special notation: for

example the notation  $C_{D_\alpha}$  is the derivative of the drag coefficient per angle of attack variation. Using the following notation and introducing the non-dimensional for rotational moments we obtain the following:

$$C_D = C_{D_0} + C_{D_\alpha} \alpha + C_{D_q} \frac{\bar{c}}{2V} q + C_{D_{\delta_e}} \delta_e \quad (5.14)$$

$$C_D = C_{Y_0} + C_{Y_\beta} \beta + C_{Y_p} \frac{b}{2V} p + C_{Y_r} \frac{b}{2V} r + C_{Y_{\delta_a}} \delta_a + C_{Y_{\delta_r}} \delta_r \quad (5.15)$$

$$C_D = C_{L_0} + C_{L_\alpha} \alpha + C_{L_q} \frac{\bar{c}}{2V} q + C_{L_{\delta_e}} \delta_e \quad (5.16)$$

Like for the gravitational force, the aircraft body axis are used to describe the aerodynamic forces. Therefore the aerodynamic forces can be written in vector form as follow:

$$\mathbf{F}_a^b = \begin{bmatrix} F_x \\ F_y \\ F_z \end{bmatrix} \quad (5.17)$$

The aerodynamic forces are not applied to the aircraft CG but instead to the centre of pressure (CP). In addition the aerodynamic control appendixes generate moments around the  $xyz$  axis which need to be modelled. The aerodynamic moments applied to the aircraft body are described as follows:

$$L = \frac{1}{2} \rho V^2 S b C_l \quad (5.18)$$

$$M = \frac{1}{2} \rho V^2 S \bar{c} C_m \quad (5.19)$$

$$N = \frac{1}{2} \rho V^2 S b C_n \quad (5.20)$$

where  $\rho$  is the density of the air which surrounds aircraft body,  $V$  is the aircraft true airspeed,  $S$  is the aircraft planform wing surface,  $\bar{c}$  is the wing mean chord,  $b$  the wingspan and  $C_l$ ,  $C_m$  and  $C_n$  are respectively the x-axes, y-axes and z-axes nondimensional coefficients which define the aerodynamic characteristics of the aircraft. Like for the aerodynamic forces coefficients they are function of many variables and generally they are obtained by wind tunnels exhaustive tests for aircraft different attitude, control surfaces positions and aircraft rotational movements. Using the same notation applied to the aerodynamic force derivatives we can express the rotational moments coefficients as follows:

$$C_l = C_{l_0} + C_{l_\beta} \beta + C_{l_p} \frac{b}{2V} p + C_{l_r} \frac{b}{2V} r + C_{l_{\delta_a}} \delta_a + C_{l_{\delta_r}} \delta_r \quad (5.21)$$

$$C_m = C_{m_0} + C_{m_\alpha} \alpha + C_{m_q} \frac{\bar{c}}{2V} q + C_{m_{\delta_e}} \delta_e \quad (5.22)$$

$$C_n = C_{n_0} + C_{n_\beta} \beta + C_{n_p} \frac{b}{2V} p + C_{n_r} \frac{b}{2V} r + C_{n_{\delta_a}} \delta_a + C_{n_{\delta_r}} \delta_r \quad (5.23)$$

The aerodynamic moments can be written in vector form as follow:

$$\mathbf{M}_a^b = \begin{bmatrix} L \\ M \\ N \end{bmatrix} \quad (5.24)$$

The overall diagram of the aircraft aerodynamic model is shown in Figure 5.3.

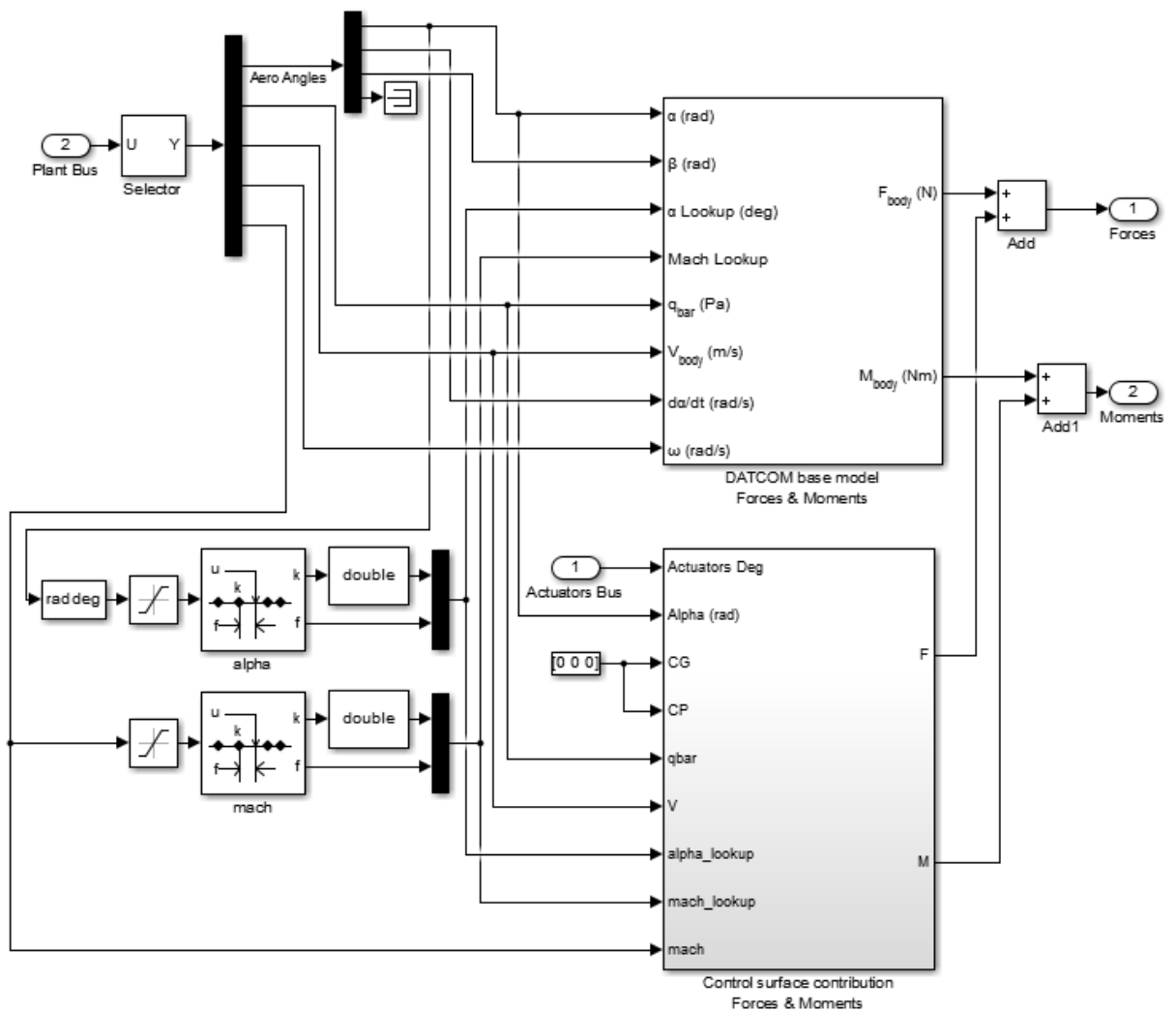


FIGURE 5.3: Simulink view of the aircraft aerodynamic model

### 5.2.3.1 Aerodynamic coefficients estimation

The aerodynamic coefficients estimation can come from exhaustive and complex Computational Fluid Dynamic (CFD) simulations, or from expensive wind tunnel measurements campaigns where a scaled model of the aircraft is mounted at the end of a probe and the forces and moments can be measured for different flying conditions and aircraft attitudes. In addition, other analytical methods can be applied, which are often used during the aircraft design phase. Few software allow to obtain aerodynamic derivatives. The most diffuse and known are Datcom[84] and the Vortice Lattice method[85].

The Datcom software provides rapid and economical estimations of the aerodynamic characteristics of the aircraft. The program is based on the USAF Stability and Control DATCOM [84], a comprehensive handbook of semi-empirical methods for the determination of static and dynamic as well as control and high-lift derivatives of preliminary aircraft geometries. The digital version of the program is called DATCOM+[86] that uses the old fortran language code which was made available many years later by the USAF and introduced few functionalities for visualizing the overall model which in input using text files.

The main advantage in using Datcom is its component build-up capability for the aircraft configuration. The user can estimate the aerodynamic stability and control characteristic contributions for each geometrical component individually or for the whole aircraft configuration. Another feature of Datcom is the capability to use pre-obtained data (i.e. wind-tunnel test, flight test, computational) for simpler configurations to improve the prediction accuracy for the full configuration as considered[87]. There is a negative aspect about Datcom: it provides a complete set of data only on straight-tapered wings configuration. Unfortunately the Airbus A320 aircraft has a cranked wing configuration. Therefore to obtain the aerodynamic data the wing must be adapted to a straight-tapered wing. This has been done modifying only the trailing edge angle and the root chord for the central line, all the other parameters like the sweep angle and the surface wing area were kept fixed to avoid a big gap from the real A320 wing response to this configuration. The Figure 5.4 shows this modification.

Datcom allows the user to define the airfoil for the main wing, tail wing and vertical surface. Airbus like every other bigger aircraft manufacturer does not release the airfoil characteristics, therefore an estimation of the airfoil to be used has to be

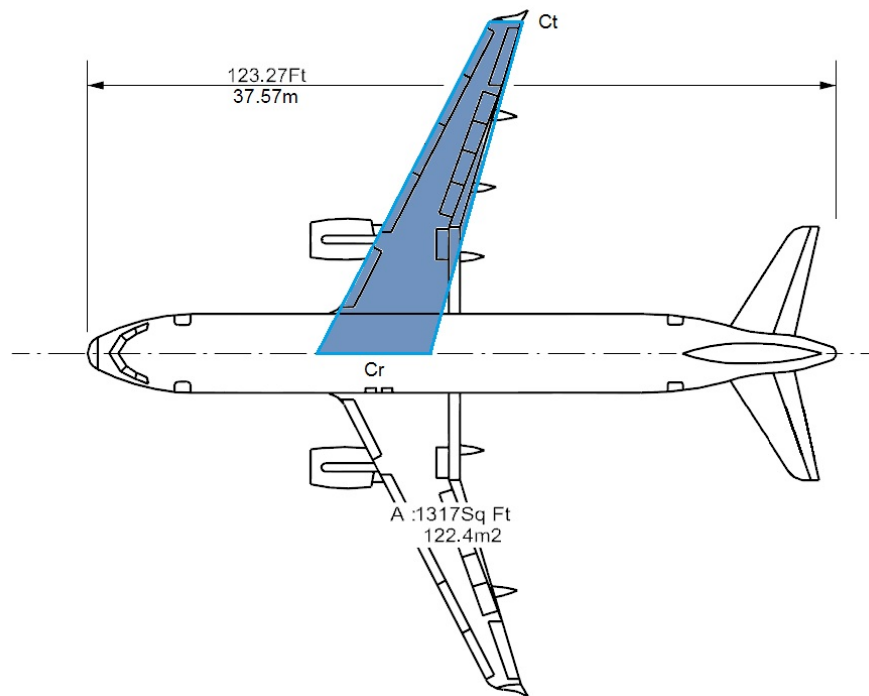


FIGURE 5.4: Adaptation of wing cranked profile into Datcom accepted profile

done. Considering that the main wing of the A320 is twisted along span, the main wing was assumed un-twisted and the profile was assumed to be a NACA 23012. This assumption was made based on a parametric analysis as explained by Helldor in his final M.Sc. thesis [88].

The Datcom input file can be created based on the Datcom manual[84]. There is no GUI within the program; therefore the creation of the aircraft model file could be immensely confusing. There are only points in space that the user can place to obtain the fuselage and to set the reference for the aircraft control surfaces. Only from the input file is difficult to understand if the user has made mistakes writing down the aircraft model configuration input file. DATCOM+ has a 3D visualisation feature which makes possible visualizing the aircraft and rotates the view all around the aircraft. This feature avoids macro-mistakes before obtain any kind of data from the output file. The 3D view of the A320 generated from the input file within DATCOM+ is shown in Figure 5.5. Figure 5.5 also shows that there is no engine nacelles into the model. DATCOM+ does not model engine nacelles or engine pylons. Since the nacelles and pylons introduce a significance drag component to the whole drag, this cant be neglected. The Drag generated externally the engine nacelles is calculated later on and added as propulsive forces components. To obtain data from Digital Datcom the user has to prepare several input file

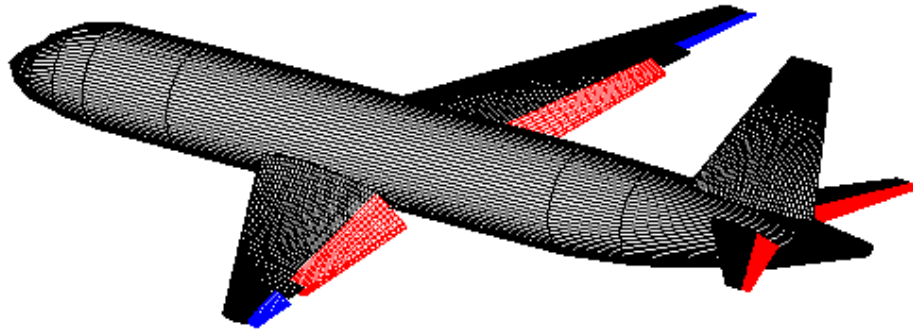


FIGURE 5.5: Datcom+ 3D model of the studied aircraft, similar to Airbus A320

that the software reads before processing the static and dynamic coefficients for the configuration selected and save it into an output file. Therefore there is not only one input file but many, with different velocity and altitude set and also with the presence of surface deflections or clean configuration only. The aerodynamic derivatives obtained by analysis done in Datcom+ software were saved and imported into Matlab environment and look-up tables used to allow the simulation to extract the appropriate coefficient per flight condition. Figure 5.6 shows the static contribution of coefficients obtained by Datcom+ analysis implemented into the Simulink model.

#### 5.2.4 Propulsive Model

The propulsive model models the forces and moments applied to the aircraft generated by the engines which are installed. The engine thrust is only one component. In addition the engine nacelles produce drag force which results in an additional pitching down moment which need to be taken into account in the modelling. The level of fidelity depends on the quality of the engine model available. The

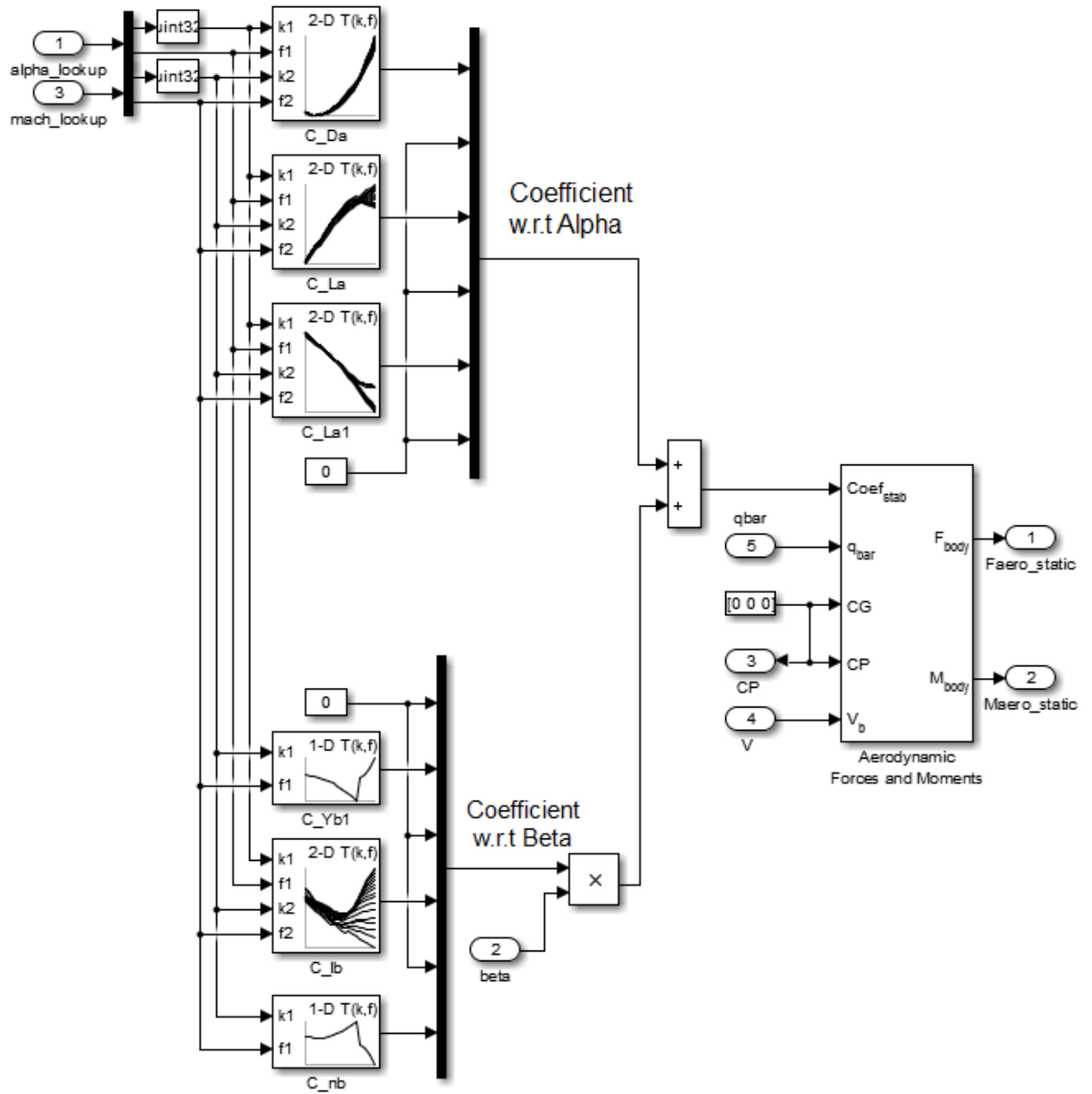


FIGURE 5.6: Simulink view of part of the Datcom model implement

propulsive forces and moments can be written in vector form as follow:

$$\mathbf{F}_p^b = \begin{bmatrix} F_x^p \\ F_y^p \\ F_z^p N \end{bmatrix} \quad (5.25)$$

$$\mathbf{M}_p^b = \begin{bmatrix} L_p \\ M_p \\ N_p \end{bmatrix} \quad (5.26)$$

The values of the forces and rotational moments are obtained by the look-up table data obtained from Chapter 3 where the engine for the aircraft Airbus A320 was modelled.

### 5.3 Flight Controls Model

Flight Control System (FCS) is an essential part in the aircraft simulation environment. It is needed to be able to close the loop between the kinematic and dynamic block which simulates the aircraft and the request of manoeuvring which are performed in a gate-to-gate mission, such as increase and decrease flight level, acceleration or deceleration and turning to a target heading. The aircraft control inputs are grouped as follows:

$$\text{Control Inputs} = \begin{bmatrix} \delta_e \\ \delta_t \\ \delta_a \\ \delta_r \end{bmatrix} = \begin{array}{l} \text{Elevator angle} \\ \text{Throttle position} \\ \text{Aileron angle} \\ \text{Rudder angle} \end{array} \quad (5.27)$$

The aircraft output states are grouped as follows:

$$\text{Output States} = \begin{bmatrix} u \\ v \\ w \\ p \\ q \\ r \\ \phi \\ \theta \\ \psi \\ p_n \\ p_e \\ p_d \end{bmatrix} = \begin{array}{l} \text{velocity along } x\text{-axes} \\ \text{velocity along } y\text{-axes} \\ \text{velocity along } z\text{-axes} \\ \text{Roll rate} \\ \text{Pitch rate} \\ \text{Yaw rate} \\ \text{Euler roll angle} \\ \text{Euler pitch angle} \\ \text{Euler yaw angle} \\ \text{Inertial } n \text{ position} \\ \text{Inertial } e \text{ position} \\ \text{Inertial } d \text{ position} \end{array} \quad (5.28)$$

Many different architecture of aircraft flight control systems are present in the literature, hence it would be too extensive to cover and it is not really the aim of this thesis, therefore only the essential material for this work is added. The



typical commercial aircraft. such as the study aircraft, is considered stable along the flight and therefore does not require really stability augmentation. This assumption would not be possible for military fighters or such as modern jumbo aircraft like Airbus A380. The imposed constraint for stabilizer area resulted in low stability margin which needed design of stability augmentation systems to obtain safe operations.

The Flight Control System (FCS) model implemented in the simulation environment was selected in collaboration with Michael Cooper's research work [82]. In his research the needed for a FCS which would reduce the oscillation of the system under controls for different flight conditions was a main requirement. The classic FCS architecture is the so called Single-Input-Single-Output (SISO) controller. A main disadvantage in using a SISO controller is the amount of work in tuning the SISO controller architecture for all the flight conditions (all possible airspeed, altitude and aircraft mass the aircraft can flight at) for different manoeuvres. The classic SISO control works very well when the controller is tuned for a single flight condition. When the point is changed along the aircraft envelope then gain scheduling for the different controllers is the only solution which would have resulted in long controller gains tuning campaigns. In addition, this approach would have resulted in the Simulink solver to reduce the time step of the solver to deal with the discontinuities of the controller gains causing an increase in the overall simulation time needed. For these reasons the attention was shifted to more sophisticated control architectures. One candidate is the so called Total Energy Control System (TECS).

### 5.3.1 Total Energy Control System (TECS)

The Total Energy Control System (TECS) was first introduced by Lambregts in 1983 [89]. In it's first concept, the TECS was focusing only in the aircraft longitudinal axes. The controller uses throttle and elevator deflector to control the aircraft's total energy which is the sum between kinetic and potential energies.

The coordination of throttle and elevator deflector in TECS is radically different than the SISO architectures. In Figure 5.7 the coupling between the longitudinal controls (i.e. throttle and elevator control) and the aircraft longitudinal states (i.e. altitude and airspeed) for TECS autopilot is shown. It is understandable for an aircraft that an increase in throttle command results in an acceleration and

also an increase in flying altitude. Therefore if a level acceleration is required, an elevator control is required to null the altitude gain. The elevator control command modifies the overall aircraft drag which results in altering the expected acceleration.

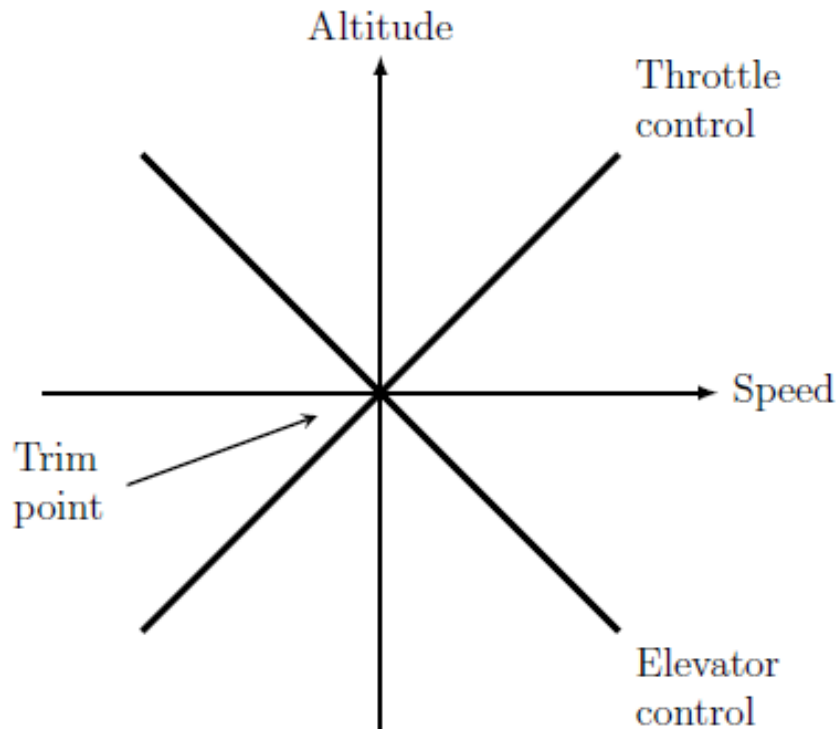


FIGURE 5.7: Coupling of aircraft longitudinal modes and controls [90]

The TECS architecture have been validated[91] and also implemented and tested on board of a Boeing 737 aircraft [92] and on board as other general aviation aircraft[93]. A benefit which was discovered of the TECS architecture is that little adjustments are required in adapting the controller to another aircraft [94]. This is possible due to different control loops which work are different bandwidth between each others. The inner loop controllers which drive the elevators, ailerons, rudder and engine throttles, are more dependent to the aircraft dynamics and they can provide also augmented stability if needed. The other loop controllers control the aircraft energy states and the aircraft can be represented as a point mass at these levels. The outer loop controllers handle the top level aircraft functionality such as navigation, path following, altitude intercept and hold, ground speed hold, indicated airspeed and Mach hold, ILS, etc.

One of the main advantage of the TECS architecture is the reduced control oscillation in comparison with SISO architecture. Bruce in his integration work observed

a reduction of elevator activity under turbulence conditions from  $0.81^\circ$  Root Mean Square (RMS) to  $0.16^\circ$  RMS on board of a Boeing 737 aircraft maintaining alternated target airspeed and altitude. This aspect is important and is what we want to obtain if the desired 4D trajectory resulting from the optimisation process has to be used as input to the FCS. Unnecessary control oscillations, especially regarding the throttle control could result in losing the meeting condition at the final waypoint where the Requested Time of Arrival (RTA) was imposed.

As it was introduced before, the concept at the origin of the TECS is the control of the aircraft total energy. The aircraft total energy is composed from kinetic and from potential components which can be shown as follows:

$$E = mgh + \frac{1}{2}mV^2 \quad (5.29)$$

where  $m$  is the aircraft mass,  $g$  is the acceleration due to the Earth's gravity,  $h$  is the flying altitude and  $V$  is the aircraft true airspeed. Under the hypothesis that the aircraft mass dynamic is very slow, due to fuel burnt it is possible to differentiate the energy equation and obtaining the following:

$$\dot{E} = mg\dot{h} + mV\dot{V} \quad (5.30)$$

Normalising the resulted energy rate by aircraft mass a specific energy rate is obtained:

$$\dot{E}_s = \frac{\dot{E}}{mg} = \dot{h} + \frac{1}{g}V\dot{V} \quad (5.31)$$

Introducing a further normalisation for aircraft airspeed and the final form of specific energy rate formulation is obtained and shown in the following:

$$\frac{\dot{E}_s}{V} = \frac{\dot{h}}{V} + \frac{\dot{V}}{g} = \gamma + \frac{\dot{V}}{g} \quad (5.32)$$

where  $\gamma$  is the aircraft Flight Path Angle (FPA) which measures the angle between the aircraft airspeed vector and the horizontal reference plane. Equation 5.32 shows how the specific energy rate is the sum of two contributions, the FPA and the airspeed rate normalized by Earth's acceleration constant.

Analysing the aircraft longitudinal steady-state equilibrium it is possible to obtain the following relations, see [82] for a more detailed explanation:

$$\Delta T_c = mg\left(\gamma_e + \frac{\dot{V}_e}{g}\right) \quad (5.33)$$

where  $T_c$  is the thrust command and  $\gamma_e$  and  $V_e$  are the error at the steady-state condition. Hence it is possible to notice how a change in aircraft thrust level will result in a proportional change in total energy. This shows that the aircraft total energy is controlled only by controlling the engine throttle.

The control law to control the engine throttle involves the use of a Proportional and Integral (PI) controller and can be shown in Laplace form as function of  $s$  as follows:

$$\delta_t(s) = K_p^t \frac{\dot{E}_s}{V} + \frac{K_i^t}{s} \frac{\dot{E}_s}{V} \quad (5.34)$$

where  $K_p^t$  and  $K_i^t$  are the proportional and integral controller gains for the throttle controller.

The control law to control the amount of energy to flow between kinetic and potential form.

$$\delta_e(s) = K_p^e \dot{E}_s + \frac{K_i^e}{s} \dot{E}_s + \text{damping terms} \quad (5.35)$$

where  $K_p^e$  and  $K_i^e$  are the proportional and integral controller gains for the elevator controller. The resulting block diagram for the two controllers used is shown in 5.8. The Multi Input Multi Output (MIMO) structure of the TECS architecture is clearly visible.

The engine and pitch inner loop controllers are implemented using PI scheme with pitch rate feedback for the pitch loop and thrust feedback for the engine loop. In reality, thrust measurement is not available and engine pressure ratio is normally used instead. However this kind of details should be used only if designing the engine control system which is not the scope of this research work and therefore thrust measurement is used without problems.

The tune of the two controllers were done manually, using the gains published for the Boeing 737 as initial guess. This is considered acceptable since the purpose is to show the ability to fly ultimate trajectories and not to design control systems to be used in real aircraft which should instead follow a deeper process using eigenstructure analysis and more to achieve flightworthy.

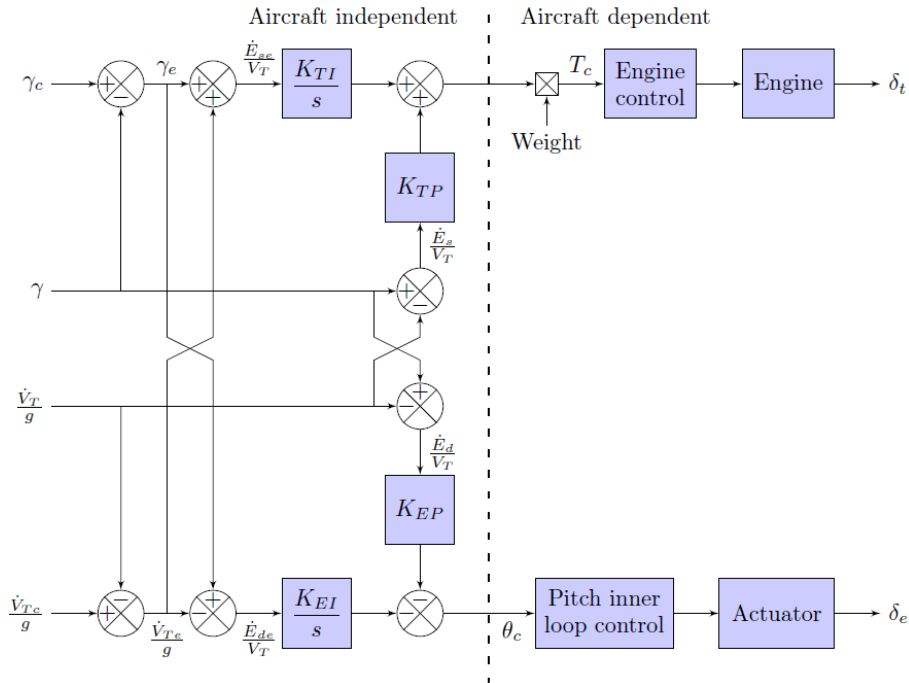


FIGURE 5.8: TECS block diagram. Taken from [82]

### 5.3.2 Total Heading Control System (THCS)

The Total Heading Control System (THCS) is a natural extension of the TECS architecture described in the previous section. The THCS applies the energy balanced control technique to control the aircraft roll and yaw motions using ailerons and rudder control surfaces. The THCS architecture was initially published by Bruzzini[95] and it was applied in the simulation of a McDonnell Douglas F-15 Eagle aircraft in achieving coordinate turns. Since THCS is a natural evolution of TECS, the description of THCS will not be repeated as in details as for TECS. However the reader can find a more detailed explanation about THCS in the following documents [95] and [96].

From the body axis equations of motion Eq. 5.2, the aircraft lateral force expressed in body axis is shown again as follows

$$\dot{v} = \frac{F_y}{m} + g \sin(\phi) \cos(\theta) + pw - ru \quad (5.36)$$

where  $F_y$  is the lateral force,  $m$  is the aircraft mass,  $g$  the Earth acceleration,  $\phi$  and  $\theta$  respectively the pitch and roll angles. Under the hypothesis of aircraft in stable conditions, hence pitch and roll angles are small; and that the aircraft is in a steady coordinated turn ( $F_y = 0$ ) and ( $p = 0$ ), the equation can be simplified as

follows:

$$\dot{v} = g\phi - ru \quad (5.37)$$

Applying normalisation by true airspeed, as done for the total energy in the TECS, allows to obtain the side slip angle rate  $\dot{\beta}$ . In a steady coordinated turn  $\dot{\beta} = 0$ , therefore we can express the following

$$\frac{\dot{v}}{V} = \dot{\beta} = \frac{g\phi}{V} - \frac{ru}{V} = 0 \quad (5.38)$$

The aircraft airspeed  $u$  component magnitude can be considered of the same order of the aircraft true airspeed  $V$  magnitude and therefore removed in the equation. This simplification allows to obtain the following which is valid in steady state condition

$$\phi = \frac{V}{g}r \quad (5.39)$$

Analysing the aircraft lateral steady-state equilibrium for incremental steps, it is possible to obtain the following relation

$$\Delta\phi = \frac{V}{g}(\dot{\beta} + \Delta r) \quad (5.40)$$

The previous equation shows how bank angle increment, produced by ailerons deflection, also produces a pure yaw rotation if the side slip angle is held at zero. Using the same principle, the yaw rate produced by rudder deflection can be used to roll the aircraft if the side slip angle rate is held at zero.

The control law to control the aircraft heading and side slip angle involves a roll angle command proportional to  $(\psi_{error} + \beta_{error})$  for control by the ailerons. In the same way, aircraft heading and side slip angle can be controlled by the rudder by commanding a yaw rate proportional to  $(\psi_{error} - \beta_{error})$ . Decoupled coordinated control is achieved only if the dynamics of  $(\psi_{error} + \beta_{error})$  is identical to the dynamics of  $(\psi_{error} - \beta_{error})$ . The heading and side slip angle errors are simply computed by subtraction between the target and measured values as follows

$$\dot{\psi}_{error} = \dot{\psi}_{target} - \dot{\psi}_{measured} \quad (5.41)$$

$$\dot{\beta}_{error} = \dot{\beta}_{target} - \dot{\beta}_{measured} \quad (5.42)$$

The heading and side slip angle rates are obtained by a proportional gain of the target and actual heading angle and side slip angle.

$$\dot{\psi}_{target} = K_{\psi}(\psi_{target} - \psi_{measured}) \quad (5.43)$$

$$\dot{\beta}_{target} = K_{\beta}(\beta_{target} - \beta_{measured}) \quad (5.44)$$

It is mandatory that the gain pairs have the same value to ensure matched dynamics between the two energy transfers. Both control laws involve the use of a Proportional and Integral (PI) controller, as was used for the TECS, and can be shown in Laplace form as function of  $s$  as follows:

$$\delta_a(s) = \frac{V}{g} K_a (K_p^a (\dot{\psi}_e + \dot{\beta}_e) + \frac{K_i^a}{s} (\psi_e + \beta_e)) \quad (5.45)$$

$$\delta_r(s) = K_r (K_p^r (\dot{\psi}_e - \dot{\beta}_e) + \frac{K_i^r}{s} (\psi_e - \beta_e)) \quad (5.46)$$

where  $K_p^a$  and  $K_i^a$  are the proportional and integral controller gains for the ailerons controller and  $K_p^r$  and  $K_i^r$  are the proportional and integral controller gains for the rudder controller.

The resulting block diagram for the two controllers used is shown in 5.9. The Multi Input Multi Output (MIMO) structure of the TECS architecture is clearly visible.

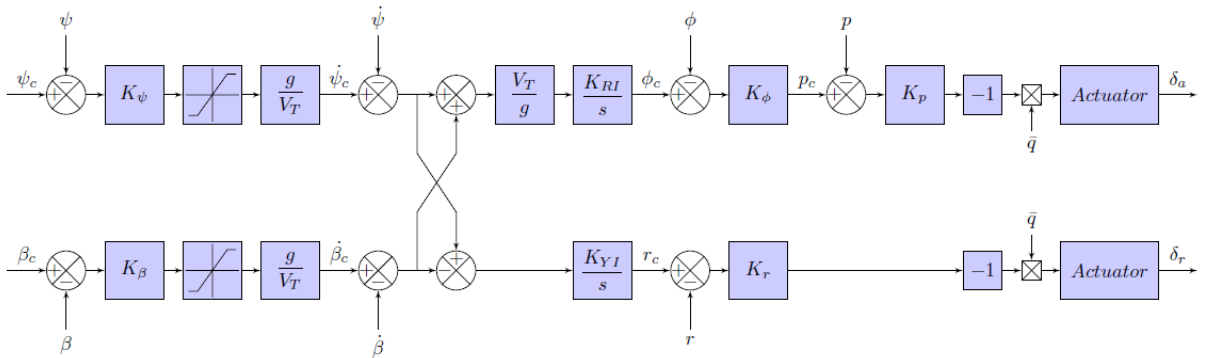


FIGURE 5.9: TECS block diagram. Taken from [82]

The overall diagram of the implemented FCS using TECS and THCS just described is shown in Figure 5.10.

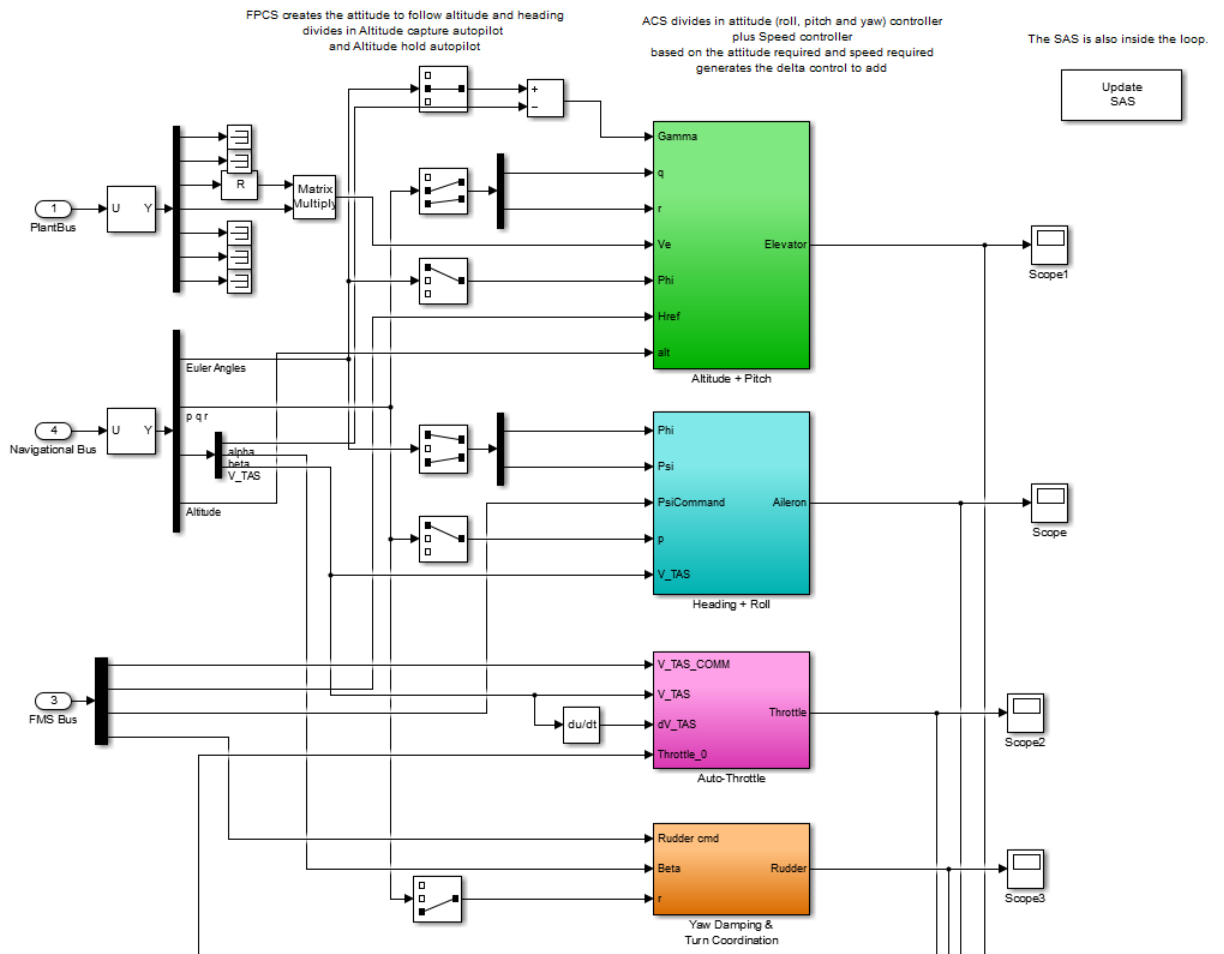


FIGURE 5.10: Simulink view of the implemented Flight Control block



## 5.4 Validation of the model

This section is intended to demonstrate the operational behaviour of the TECS while it executes a series of manoeuvres. 5.11 shows the A320 aircraft starting from a trimmed operating point in cruise at an altitude of 10,000 m and with a true airspeed of 233 m/s which results around of 0.78 Mach. Trimming is achieved using the Matlab function `trim`, which acts to find a steady state operating point of a system which satisfy constraints. The function is given the commanded altitude and airspeed while having the throttle, elevator and angle of attack as free variables which are optimised to satisfy the constraints.

There is an initial step command to climb to 10200 m, while maintaining a constant airspeed, once the commanded altitude has been reached there is a demanded speed increase by 5 m/s to 238 m/s at constant altitude. Lastly, both variables are commanded to return to initial values but timed such that the speed decrease command is initiated during the descent. The aim of the plot is to show the good accuracy of TECS at handling coupled elevator plus throttle manoeuvres.

One weakness in the current FCS tuning can be seen in the throttle position plot which shows evidence of damped oscillatory behaviour. This is due to a poorly tuned engine inner control loop, but has been left in the figure to demonstrate that throttle oscillations do not induce major elevator oscillations. This justifies the decision to use a TECS controller. The TECS loop operates at a lower bandwidth than the inner control loops, therefore a oscillatory behaviour like this does not get transmitted to the commands for the coupled controller. With a regular SISO FCS the oscillation of the throttle would induce pitch oscillations in the aircraft which the elevator would then try to cancel out.

In addition, to demonstrate the behaviour of THCS in controlling lateral motion a heading change command is imposed and a controlled turn is expected. The manoeuvres of interest are shown in 5.12 and include an initial heading change of 45 degrees with zero commanded sideslip. This is exactly the condition described as coordinated banked turn.

The results show that THCS provides smooth control over both heading angle and sideslip angle in a coordinated fashion. here are no significant oscillatory motions induced in the control surface demands. The control surface plot demonstrates the

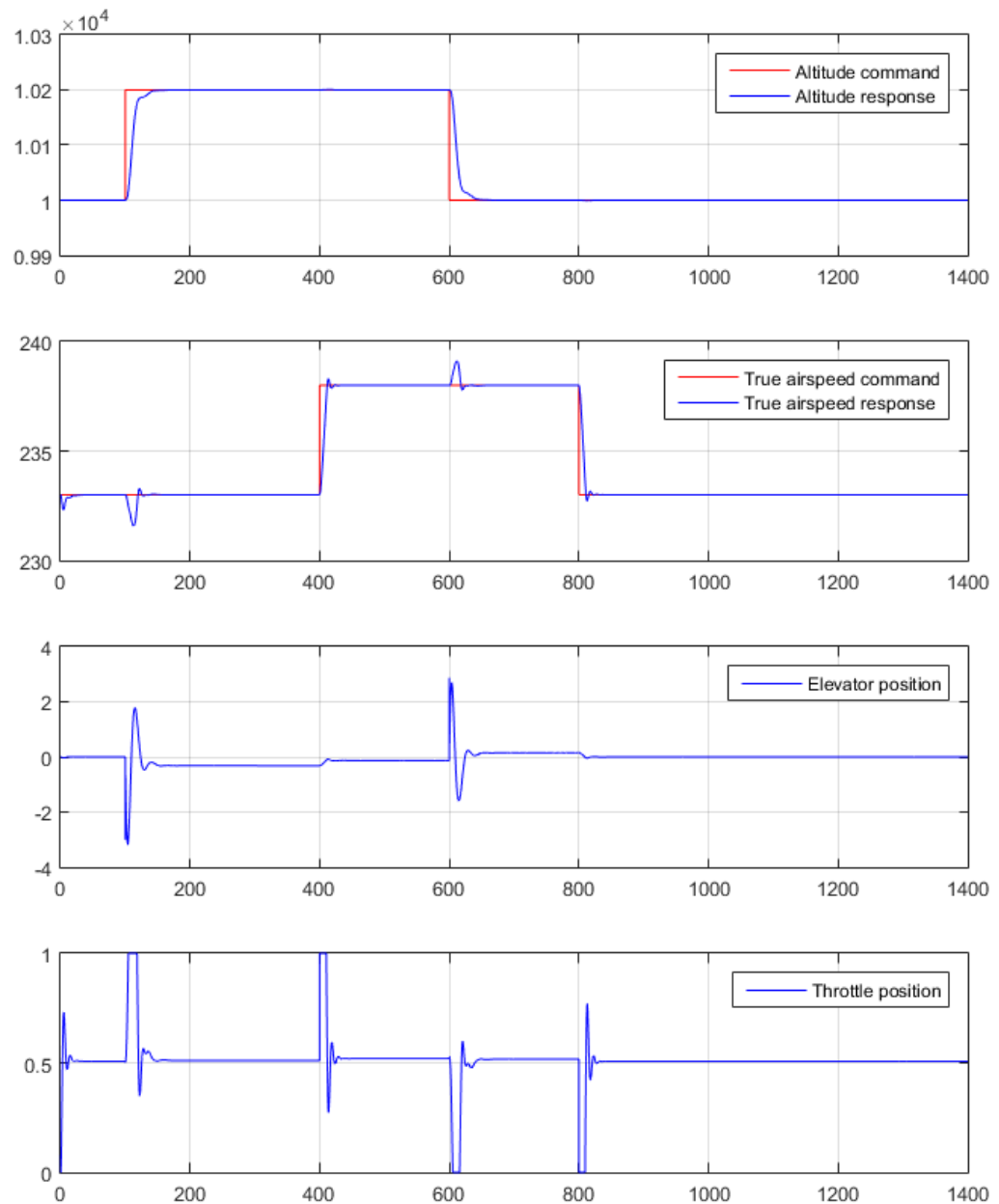


FIGURE 5.11: TECS validation - Altitude and speed response to a controlled climb, descent and speed change

synchronisation between aileron and rudder movements used to distribute energy between the roll and yaw axes of motion.

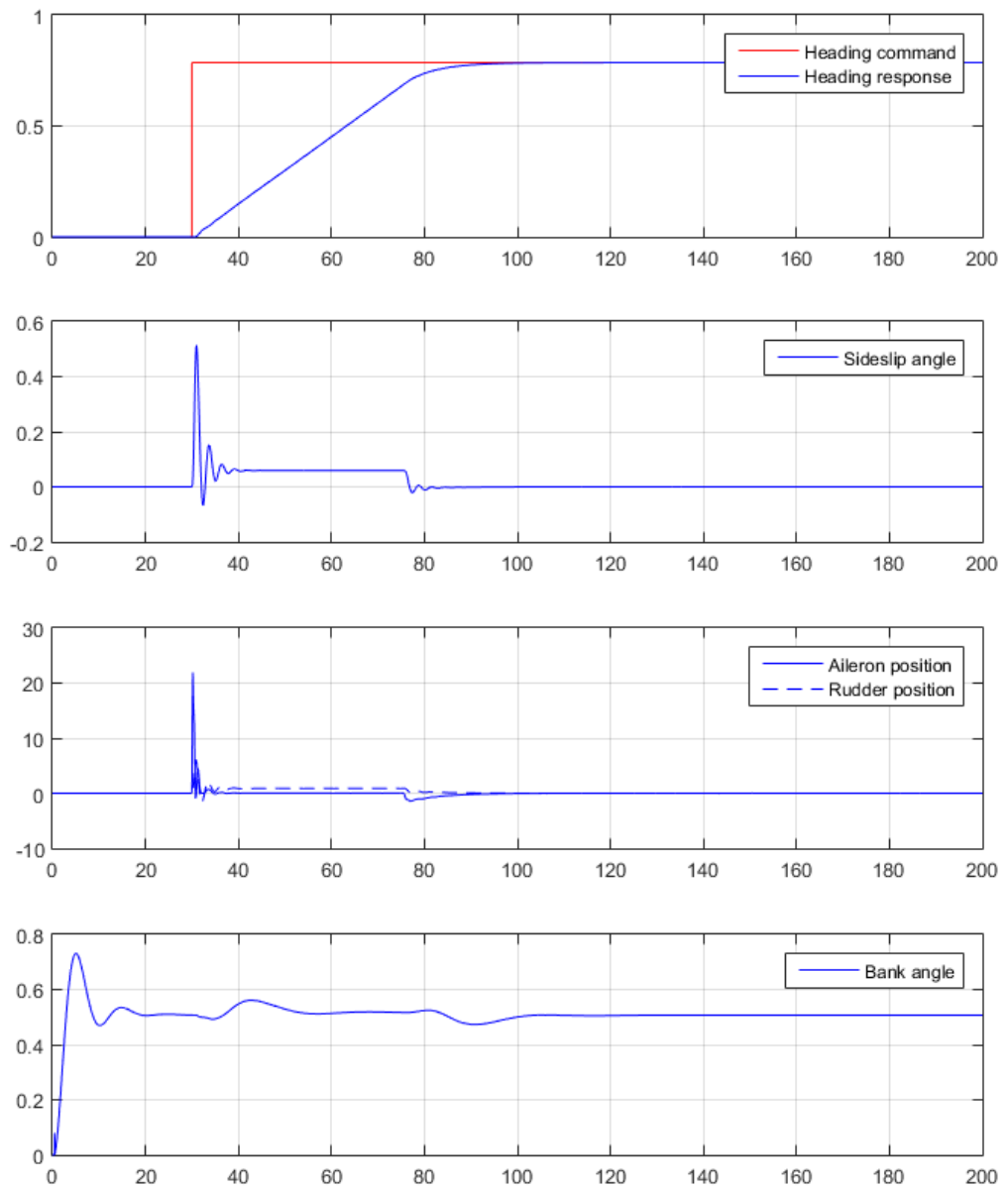


FIGURE 5.12: THCS validation - Heading response to a coordinated turn

# Chapter 6

## Case Studies

### 6.1 Introduction

This chapter presents the result of the application of the optimisation methodology, presented in the Chapter 4 to real flight missions. The optimised trajectory is then feed to the simulation environment presented in Chapter 5. The gains that are achieved by including noise and emission within the optimisation loop and compares the optimal flight operations for conventional aircraft in terms of fuel burn, flight time and emissions.

### 6.2 London Heathrow - Amsterdam Schiphol

The case study presented here reflects numerical examples based on a complete flight from London Heathrow (EGLL/LHR) airport to Amsterdam Schiphol (EHAM/AMS) airport. The aircraft for the mission is the Airbus A320 type (shown in Figure 6.1), a twin turbofan, single aisle, medium range jet airliner. The Airbus A320 can accommodate up to 150 passengers in a 2-class typical configuration and is used by several airlines for the same mission every day, such as British Airways (BA) and Royal Dutch Airlines (KLM). The Airbus A320 type is a proven design aircraft and is used as a baseline aircraft in many research projects, such as CleanSky. The Airbus A320 can be equipped with different engines by request of the airline. The most diffuse engine installed on A320 is the CFM-56-5B type.



FIGURE 6.1: Airbus A320 Aircraft [97]

This flight mission is considered a short-haul mission. The flight time is normally around 50 minutes. There is not an unique flight plan for this flight. Even though UK airspace is at the border with the Dutch airspace, several entry/exit waypoints are normally used and airlines can modify the flight plan prior departure and also during flight to adjust their needs. The selected flight plan for this mission includes several procedures, a Standard Instrument Departure (SID), a Standard Terminal Arrival Route (STAR) and an RNAV-based Instrument Approach (IA). A Google Earth projection of this short-haul mission trajectory can be seen in Figure 6.2.

The mission is composed of three phases indicated with different colours in Figure 6.2, and they have the following meaning:

- The departure phase, begins at 83ft Above Ground Level (AGL) with an airspeed circa of 140 kts and terminates at the end of the SID for the departure airport. The selected SID is the BPK7G, see Appendix B for the complete chart.
- The en-route phase, begins after the aircraft has reached the BPK VOR waypoint and terminates when the aircraft enters the Amsterdam Schiphol STAR procedure which is defined by the SUGOL way-point. See Appendix B for the complete charts.



FIGURE 6.2: London-Amsterdam routing

- The arrival segment, begins after the aircraft has reached the SUGOL way-point and terminates at a screen height of 50 ft AGL at the runway threshold. The STAR used in this phase for Amsterdam Schiphol airport is RNAV-Night RWY06. See Appendix B for the complete chart.

The total flying distance is of approximately 427.65 km.

### 6.2.1 Baseline Trajectory

A baseline trajectory is needed to be able to provide a benchmark for comparison and assess the environmental gains introduced. A regular commercial flight based on an Airbus A320 aircraft flying the corresponding route was selected to represent typical commercial flights from Heathrow airport to Schiphol airport. One flight track log from FlightAware [98] for this flight, departed at 15:41 GMT on Friday, 8 August 2014, was simulated to estimate the fuel consumption and the noise level during departure using the same SID procedure as previously introduced.

The flight arrived at Schiphol airport at 16:25 GMT (17:25 local time) with estimated flight duration of 44 minutes and the flown distance is approximately 437 km. The weather condition reported at Heathrow airport on 8 August 2014 15:40 GMT is considered normal with the wind speed of 16.7 km/h (4.6 m/s) in



westerly direction, the visibility of 9.8 km and temperature of 15 C. Under these weather conditions where the temperature and the wind speed are within the average conditions, the simulation assumes that the effect of these two parameters are negligible, hence the ISA condition are used during the simulation.

Figure 6.3 shows Google Earth screenshot of this commercial flight trajectory data, the ground speed and altitude profiles during for the overall mission are shown instead in Figure 6.4.

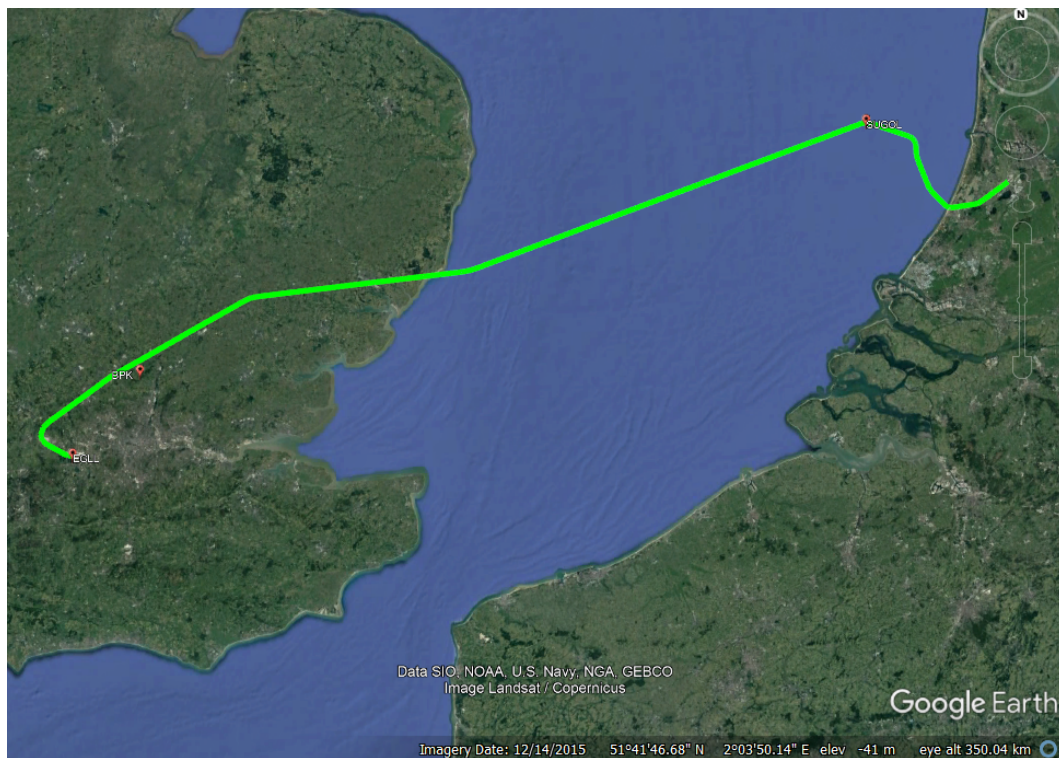


FIGURE 6.3: EGLL-EHAM ground track profile of flight BAW440 on 8 Aug 2014 [98]

## 6.2.2 Departure Phase

### 6.2.2.1 Current Procedure

For the departure at Heathrow Airport (EGLL), the Runway 27 Left (RWY27L) is used and the BPK 7G SID is used as shown in Appendix B in Figure B.1. This westerly departure is preferable and has been one of the highest percentage loadings compared to other SIDs [99].

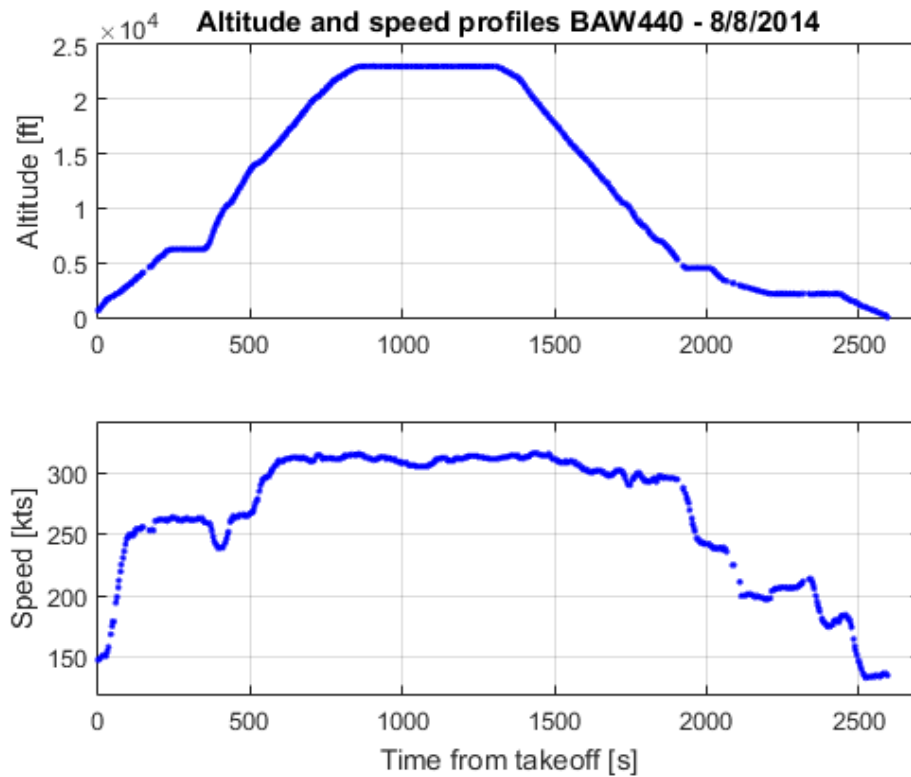


FIGURE 6.4: EGLL-EHAM altitude and speed profiles of flight BAW440 on 8 Aug 2014 [98]

This departure starts at Runway 27L and climbs directly after take-off towards Burnham (BUR) NDB at QDM 300 degrees and then turns right to align with Chilterns (CHT) NDB and Brooksman Park (BPK) VOR, consecutively. These departure procedures avoid inhabited areas such as Greater London, Slough and Maidenhead. After this turning manoeuvre, a straight segment follows to BPK VOR at which the BPK 7G SID ends and the en-route phase of the trajectory starts.

All SIDs in Figure B.1 reflect Noise Preferential Routeings applied on Heathrow airport departing for Brooksman Park. Current Noise Abatement Procedures in London Heathrow airport are described in UK AIP London Heathrow Aerodrome Document (EG AD 2-EGLL, Section EGLL AD 2.21 [100]). These procedures are intended to provide noise reduction for noise sensitive areas in close proximity to the departure runway end (resemblance of ICAOs NADP-1). The EGLL Noise Abatement Procedures also impose an airspeed restriction of 250 KCAS and a final altitude of FL60 at BPK VOR. A climb beyond this flight level is only permitted upon a clearance and instructions by the ATC.



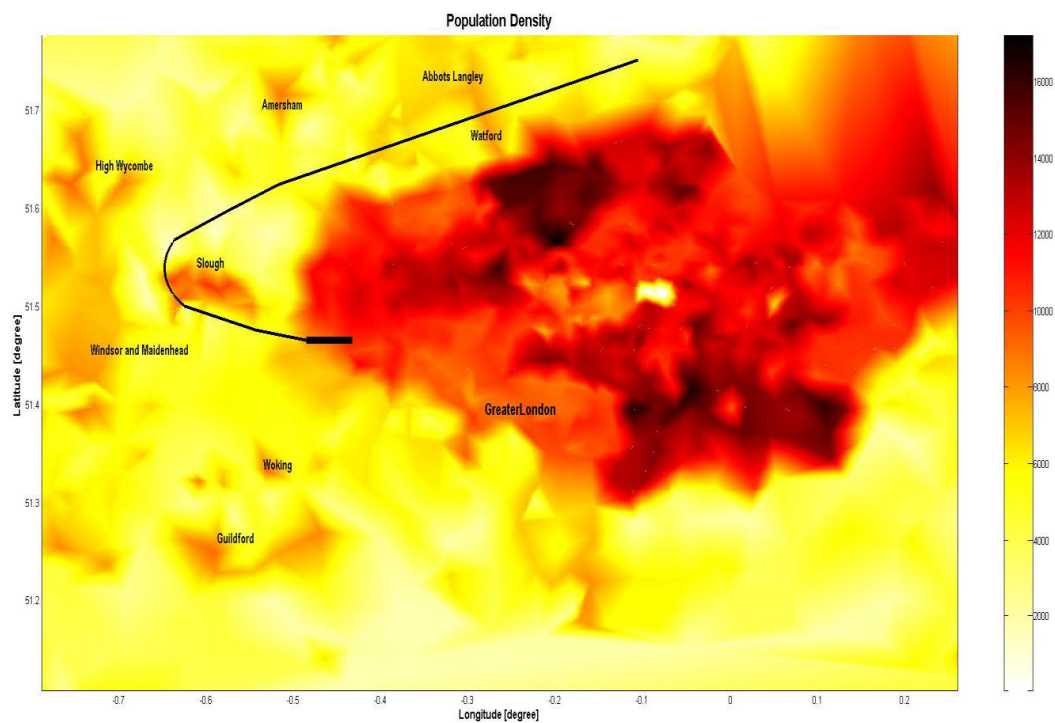


FIGURE 6.5: Population density around EGLL and BPK 7G SID Trajectory

### 6.2.3 A new procedure

To allow the optimisation algorithm to optimise the procedure while maintaining ATC constraints, the problem is set up in the way to leave the optimiser to optimise both vertical and horizontal profiles; however several waypoints are introduced between phases with altitude restrictions as described in the SID procedure as is shown in Figure B.1.

#### 6.2.3.1 Problem definition

The departure problem is considered to be composed by 4 phases and they are summarised in Table 6.1. The first phase of the departure is discretised by 10 intervals with 4 nodes per interval for a total of 40 nodes. The remaining 3 phases were discretised by 5 intervals each and all using 4 nodes per interval for a total of 20 nodes per phase. The overall problem uses a total of 100 nodes. The decision to use only 5 intervals for the last phase is due to the fact that the aircraft is flying straight due to altitude constraints so there is no need to introduce additional variables to describe a level flight phase. The airspeed on the other hand could

Phase	Start at	End at	Restrictions
P1	RWY27R	LON R306	Aircraft needs to fly over LON R306 at or above 4,000 ft Aircraft needs to maintain minimum 4% climb gradient to 4,000 ft
P2	LON R306	LON R327	Aircraft needs to fly over LON R327 at or above 5,000 ft No descent allowed
P3	LON R327	CHT	Aircraft needs to fly over CHT at 6,000 ft No descent allowed
P4	CHT	BPK	Aircraft needs to fly over BPK at 6,000 ft No descent allowed

TABLE 6.1: Phases definition for departure phase

require more nodes to be described but this can not be known a priori, it will be evaluated later on.

The overall states and control with initial, final and boundaries conditions are listed in the following table: The aircraft final mass is not specified because it is

Variable name	Initial condition	Final condition	Min. boundary	Max. boundary
Altitude	83 ft	6,000 ft	83 ft	6,000 ft
FPA	0	0	0	25 deg
Heading	270 deg	66 deg	0 deg	360 deg
CAS	150 kts	250 kts	150 kts	250 kts
Latitude	51 27 53.25 N	51 44 59.00 N	51 00 00.00 N	52 00 00.00 N
Longitude	000 28 54.99 W	000 06 24.00 W	001 00 00.00 W	000 00 00.00 N
Mass	66,000 kg	-	60,000 kg	66,000 kg
Throttle	-	-	0.0	1.0
Vertical Load factor	-	-	0.0	2.0
Bank angle	-	-	-15 deg	+15 deg

TABLE 6.2: Problem setup for departure phase

going to be determined along the optimisation. The aircraft minimum boundary for the departure phase was set to 60,000 kg even though a less fuel consumption is expected. The FPA can only be greater than zero because we are considering a departure phase only.

The transcribed problem obtained from RPM method has 1348 objective variables and 1298 constraints which contain also the linkage between the 4 phases. The results are shown in the next section.

### 6.2.3.2 Results

Figure 6.6 shows the pareto front obtained at the end of the MMO optimisation for the departure phase for two objectives (flight time and fuel consumption) using weighted-sum method. It is possible to see that many optimal conditions are grouped to the left-top part of the figure. This shows that improving the departure flight time of a fraction of second results in burning kg of fuel. Instead the right-bottom of the pareto front, shows more distributed optimal conditions. However the same discussion can be done here as well. Saving half a kg of fuel (from 468.5 to 468) results in increasing the flight time of departure phase by almost 10 seconds.

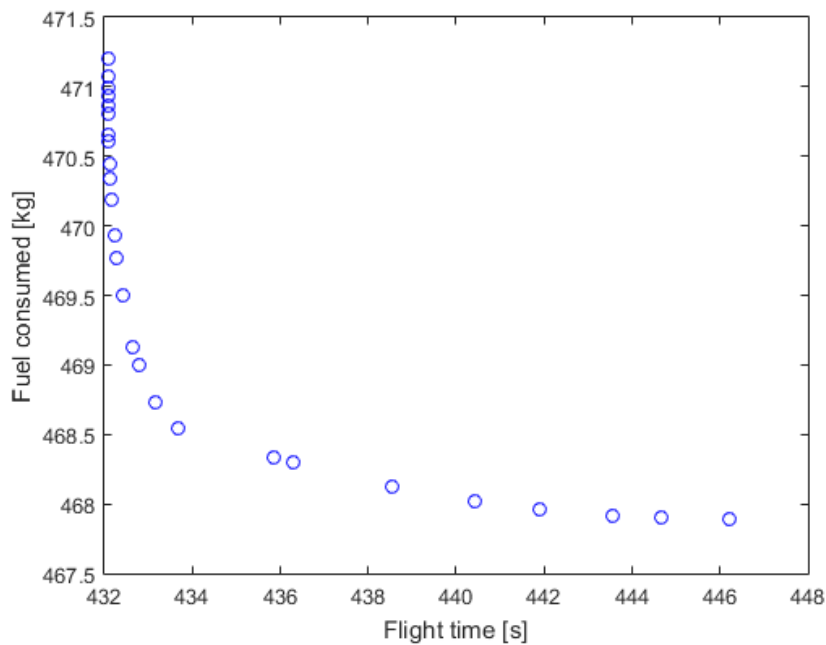


FIGURE 6.6: Pareto front - Departure segment - Heathrow-Schiphol

If the extreme point of the pareto are considered (minimum time and minimum fuel consumption cases), the trajectories are plotted in the next figures.

Figure 6.7 shows the longitude-latitude profile for the two Pareto extreme-points and both trajectories are almost identical under this point of view.

Figure 6.8 shows the altitude profile for the two trajectories and some differences are started appearing. It is possible to see how the trajectory that minimise the flight time objective initially follows the same climb rate, which is due to aircraft

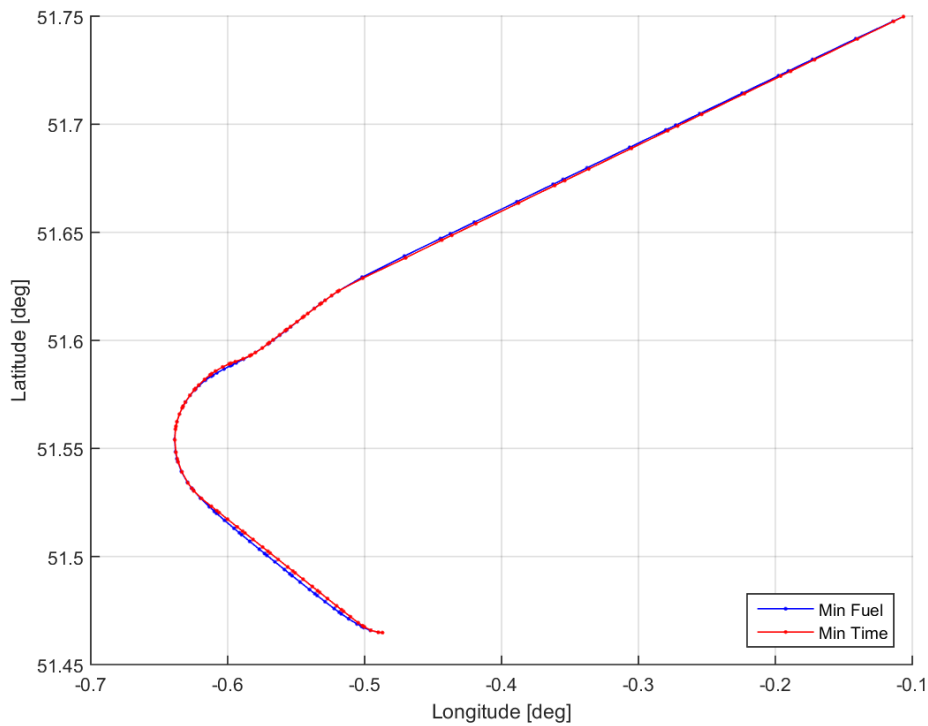


FIGURE 6.7: Latitude Longitude profile - Departure segment - Heathrow-Schiphol

performance limitations, then increasing the climb rate to reach the altitude constraint as soon as possible, then reduce it for a little while, then to the maximum climb rate possible till 6,000 ft is reached. Instead the trajectory that minimise the fuel consumption objective, after the initial climb which reflects the minimum time trajectory, it applies a lower climb rate almost constant to the 4,000 ft, then an increase of climb rate to meet the altitude constraint posed at 5,000 ft, and then finally a more gentle climb to meet the final altitude of 6,000 ft.

Figure 6.9 and Figure 6.10 show true airspeed and calibrated airspeed profiles respectively for the minimum time and minimum fuel consumption trajectories. It is possible to notice how the minimum time trajectory accelerates to the maximum calibrated airspeed and maintains it till the end of departure phase. The minimum fuel consumption trajectory, instead, accelerates initially to the same calibrated airspeed value, but then maintained almost a constant true airspeed during the climb, which resulted in a reduction of calibrated airspeed till 240 KCAS. Prior reach of the BPK waypoint, and termination of the departure phase, the aircraft accelerates to meet the airspeed condition of 250 KCAS.

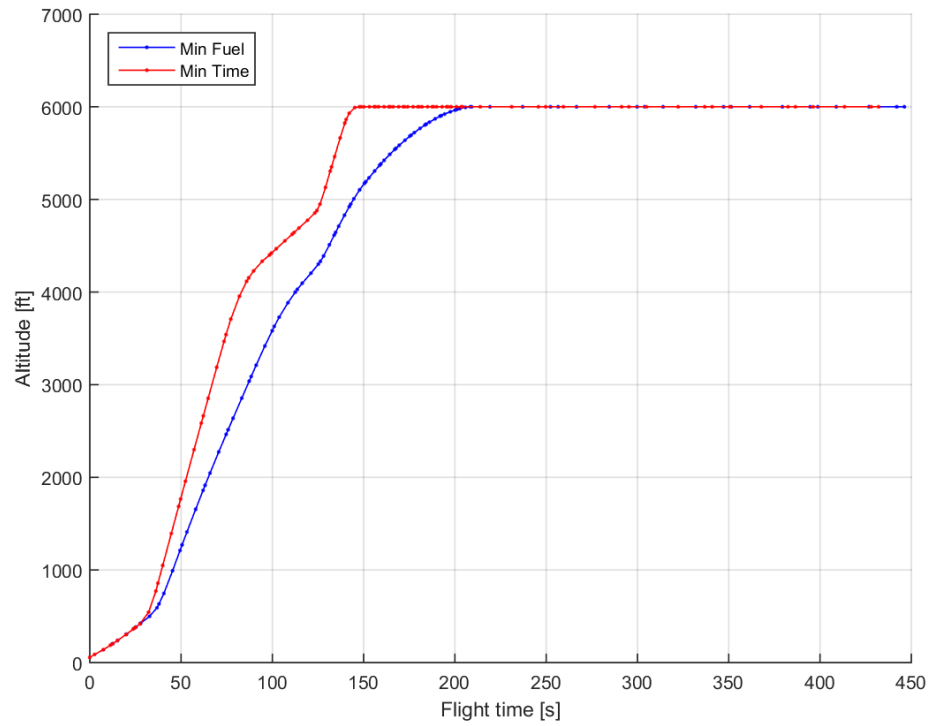


FIGURE 6.8: Altitude profile - Departure segment - Heathrow-Schiphol

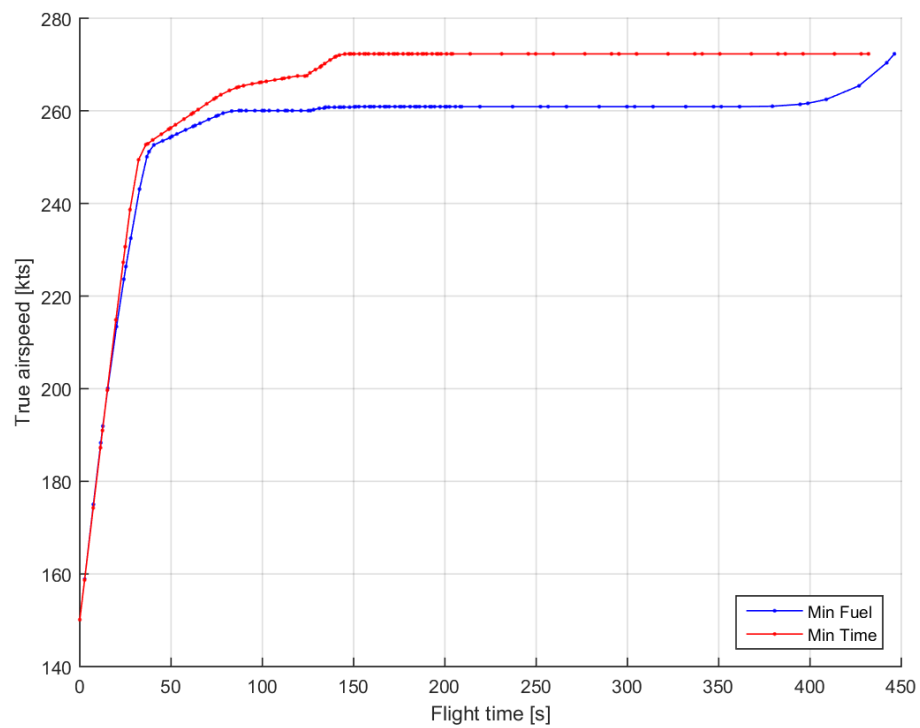


FIGURE 6.9: True airspeed profile - Departure segment - Heathrow-Schiphol

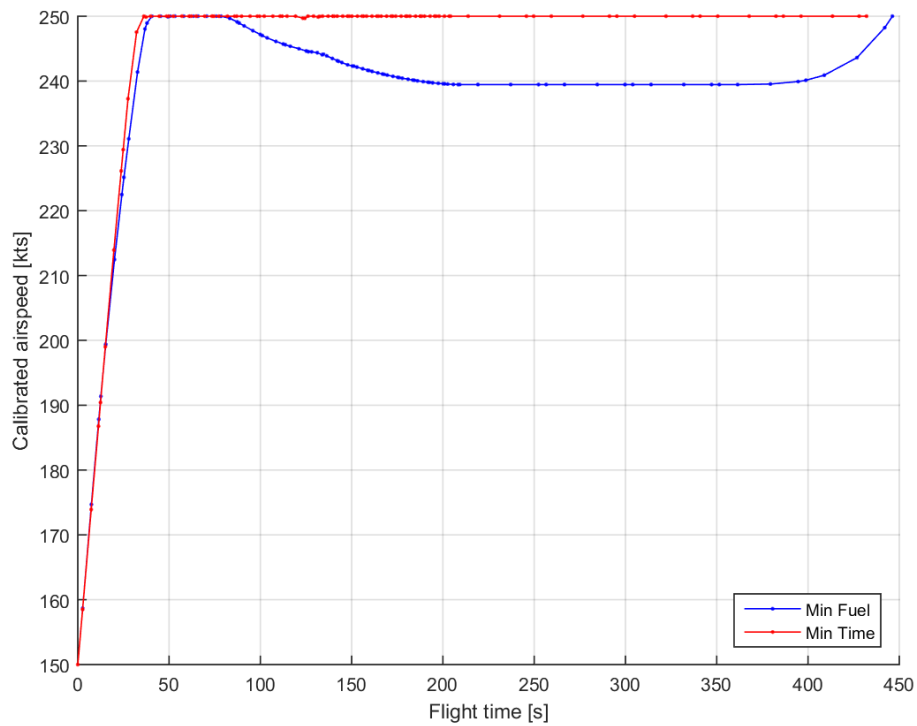


FIGURE 6.10: Calibrated airspeed profile - Departure segment - Heathrow-Schiphol

Figure 6.11 shows the flight path angle (FPA) for both trajectories and here it is possible to see better the conditions which result in the altitude profile described before. Initially both trajectories are limited to a minimum climb gradient of 4% which result in a FPA of just above 2 degrees angle. This condition is met again for the minimum time trajectory at around 100 seconds after departure when the aircraft has to meet the altitude constraint of 5,000 ft and has therefore the need to reduce its climb rate. Once climbed above 4,000 ft this FPA restriction is removed and allows the aircraft to level off.

Figure 6.12 shows the heading angle for both trajectories and it is possible to see that they are almost the same. They both cross the zero degree North at the same time.

Figure 6.13 shows the aircraft mass profile for both trajectories. The minimum time trajectory burn more fuel at the beginning of the departure and this can also be seen later in the throttle profile. The minimum fuel trajectory shows the save of fuel at the beginning of the departure due to a more smooth use of throttle and increases its saving by flying at a lower speed once reached the 6,000 ft. The final

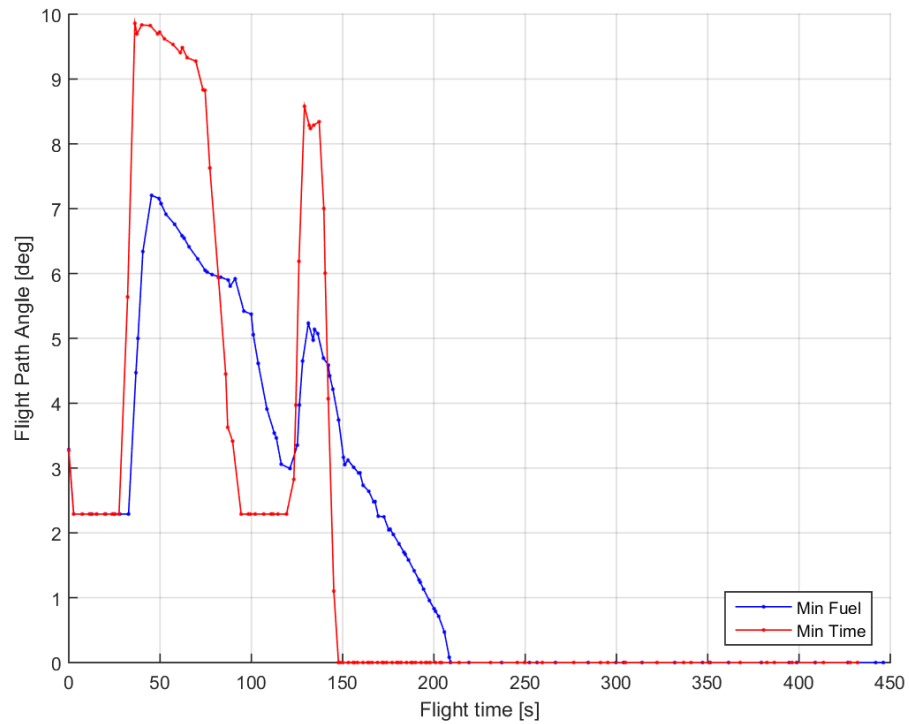


FIGURE 6.11: FPA profile - Departure segment - Heathrow-Schiphol

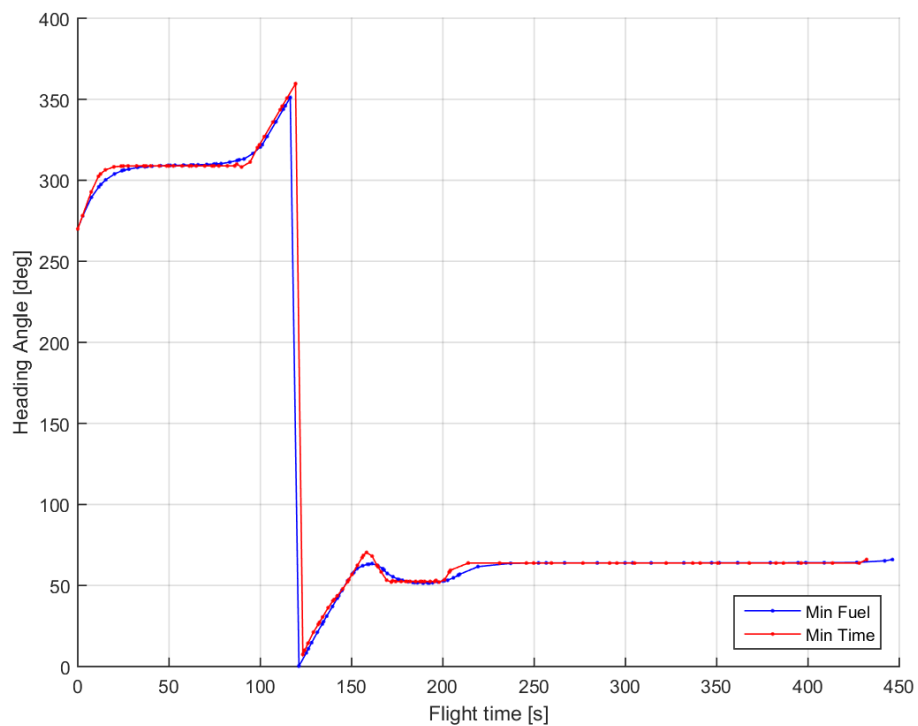


FIGURE 6.12: Heading profile - Departure segment - Heathrow-Schiphol

acceleration to meet the final speed condition increases at the end the mass rate reduction though.

Figure 6.14 shows the throttle profile for both trajectories. It is possible to see how the minimum time trajectory pretends more from the engine, using full throttle for a longer time, especially during the climbing phase. Once the final altitude is reached, the throttle is adjusted to maintain the final speed and reach the end of the departure phase as fast as possible. The minimum fuel consumption trajectory instead manages the engine throttle during the climb and acceleration phase and uses a lower airspeed during the level flight at 6,000 ft. Only at the end, a higher throttle is required to meet the final speed condition.

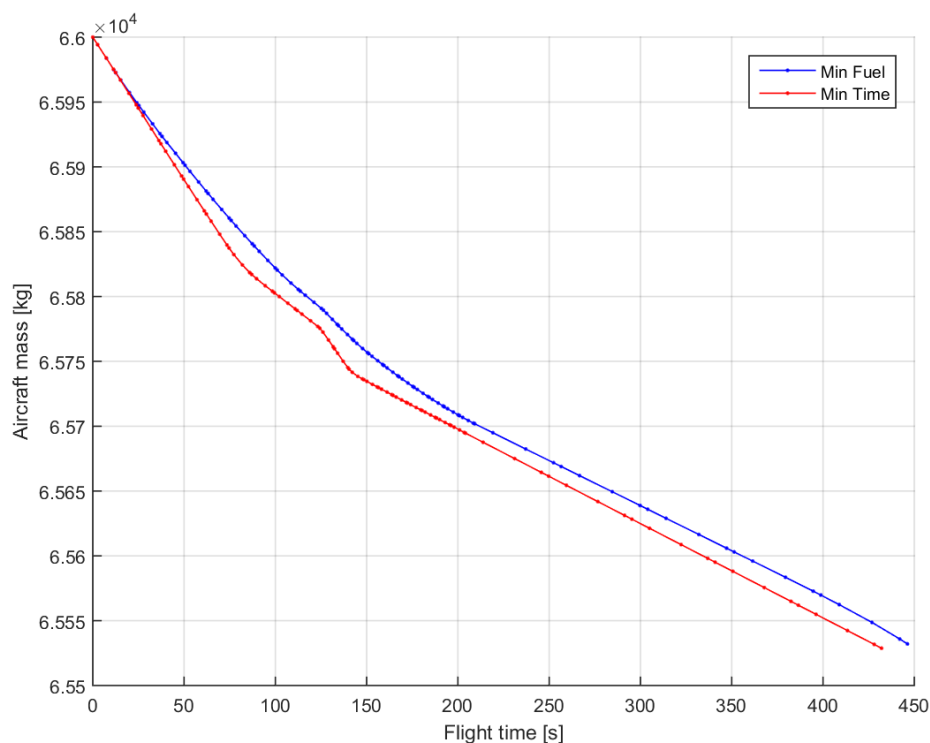


FIGURE 6.13: Aircraft mass profile - Departure segment - Heathrow-Schiphol

Figure 6.15 shows the aircraft vertical load factor during the departure phase for both trajectories. It is possible to see how the minimum time trajectory uses more extreme vertical acceleration values to achieve the objective. This indeed results in a less comfortable flight for the on-board passengers and therefore could be considered in design phase. The minimum fuel consumption trajectory uses a more comfortable approach and only exceed 1.2 g once to meet the imposed altitude condition. The rest of the time is contained between plus and minus 1.1 g.



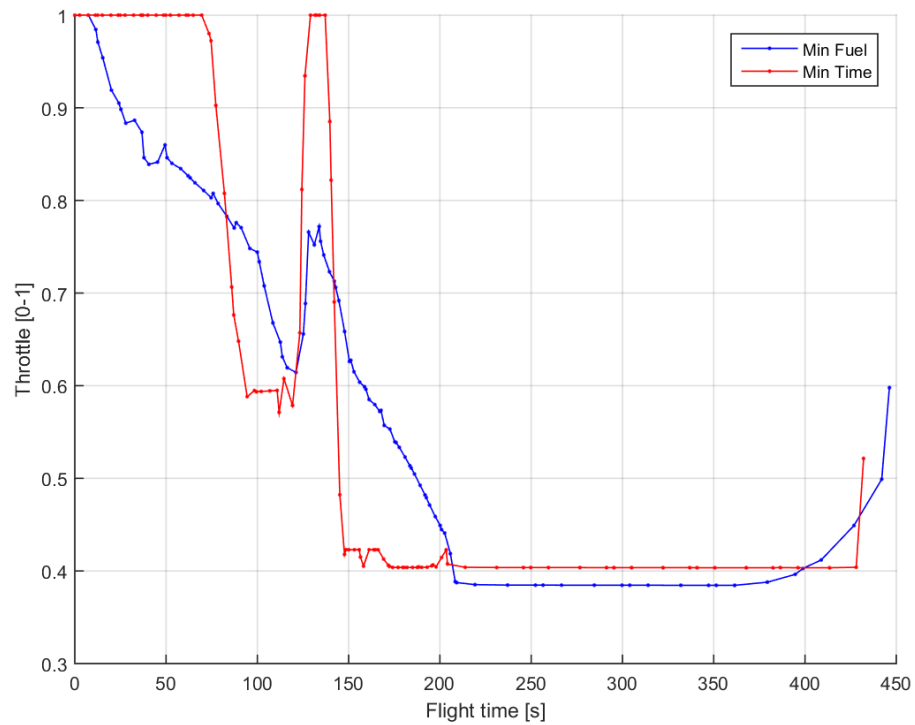


FIGURE 6.14: Throttle profile - Departure segment - Heathrow-Schiphol

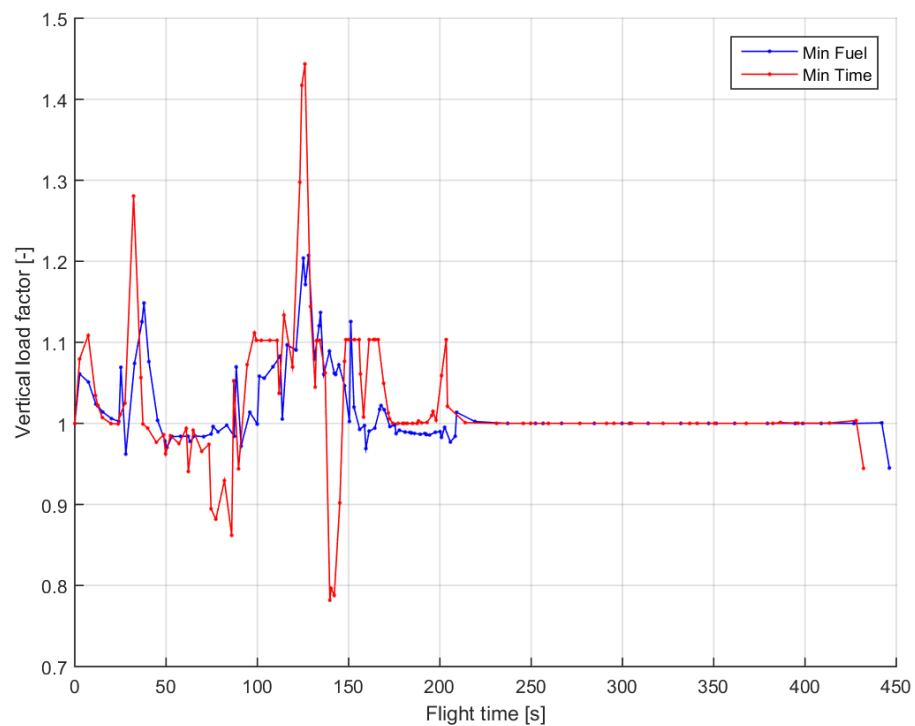


FIGURE 6.15: Vertical load factor profile - Departure segment - Heathrow-Schiphol

## 6.2.4 A 4D new procedure

The previous section considered the departure phase of EGLL-EHAM flight under ATC constraints. Now let consider the same departure phase but without way-point restrictions, nor altitude and speed restrictions that were designed for many aircraft and let only the performance and operational constraints drive to more optimised results. To allow the optimisation algorithm to satisfy this request, the problem is set up in the way to leave the optimiser to optimise both vertical and horizontal profiles in one phase only: from take-off to end of SID at BPK waypoint with only altitude and speed final conditions as is shown in Figure B.1.

### 6.2.4.1 Problem definition

The departure problem is considered to be composed by one phase and they are summarised in Table 6.3.

Phase	Start at	End at	Restrictions
P1	RWY27R	BPK	Aircraft needs to fly over BPK at 6,000 ft and at 250 KCAS No descent allowed

TABLE 6.3: Phases definition for 4D departure phase

The 4D departure is discretized by 10 intervals with four nodes per interval for a total of 40 nodes. The overall states and control with initial, final and boundaries conditions are listed in the following table.

Variable name	Initial condition	Final condition	Min. boundary	Max. boundary
Altitude	83 ft	6,000 ft	83 ft	6,000 ft
FPA	0	0	0	25 deg
Heading	270 deg	66 deg	0 deg	360 deg
CAS	150 kts	250 kts	150 kts	250 kts
Latitude	51 27 53.25 N	51 44 59.00 N	51 00 00.00 N	52 00 00.00 N
Longitude	000 28 54.99 W	000 06 24.00 W	001 00 00.00 W	000 00 00.00 N
Mass	66,000 kg	-	60,000 kg	66,000 kg
Throttle	-	-	0.0	1.0
Vertical Load factor	-	-	0.0	2.0
Bank angle	-	-	-15 deg	+15 deg

TABLE 6.4: Problem setup for 4D departure phase

The aircraft final mass is not specified because it is going to be determined along the optimisation. The aircraft minimum boundary for the departure phase was set to 60,000 kg even though a less fuel consumption is expected. The FPA can only be greater than zero because we are considering a departure phase only.

The transcribed problem obtained from RPM method has 1348 objective variables and 1298 constraints which contain also the linkage between the 4 phases. The problem for the minimum noise, described by cost function from Eq. 4.47 resulted in having the presence of numerical noise in the results. To reduce the numerical noise it was necessary to limit the rate of change of the control inputs to the optimiser. This was performed by using throttle rate, vertical load factor rate and bank angle rate as control variables and adding the throttle rate, vertical load factor and bank angle in the list of state variables in the optimisation.

The obtained results are shown in the next section.

#### 6.2.4.2 Results

Figure 6.16 shows the Pareto front obtained at the end of the MMO optimisation for the this case for two objectives (flight time and fuel consumption) using  $\epsilon$ -constrained method. Comparing the pareto obtained in the previous case, it is possible to see that removing the waypoint constraints allows to reach the final departure point conditions in the range of 347-353 seconds instead of in the range of 432-446. It is possible to see that there is a rapid increase of fuel consumption if we are looking to perform the departure phase in 350 s.

In addition to the Pareto obtained for flight time and fuel consumed we introduced the noise objective as awakenings of the population. Figure 6.17 shows the Pareto front obtained at the end of the MMO optimisation for the this case for two objectives (fuel consumption and awakenings due to noise emission) using  $\epsilon$ -constrained method. The constraint for fuel burn have been applied using values from min fuel solution and min noise solution with a step of 1 kg of fuel consumed from one simulation to the other. The obtained Pareto does not have presence of non-convex regions.

We are now considering the extreme points of both Paretos (i.e. minimum time, minimum fuel consumption and minimum awakening due to noise received on the ground), the trajectories are plotted in the next figures.

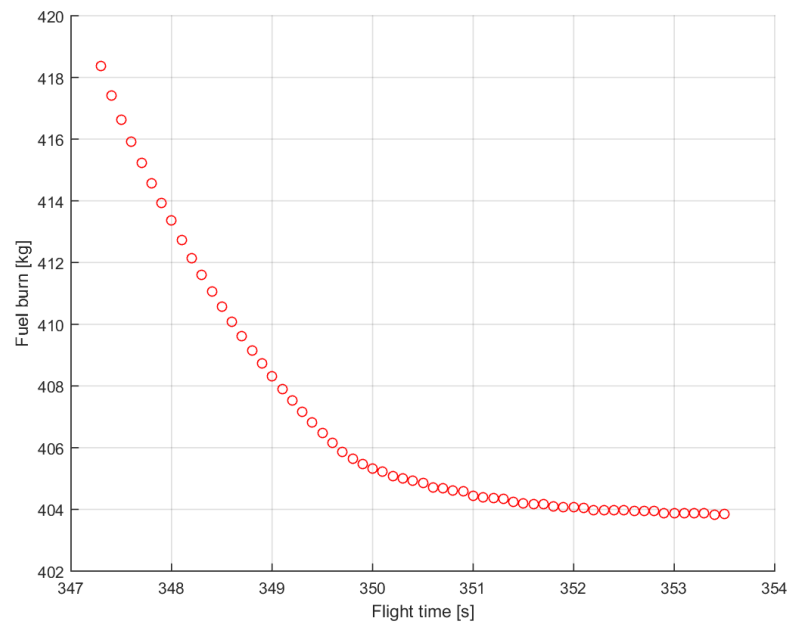


FIGURE 6.16: Pareto front - A new 4D Departure - Heathrow-Schiphol

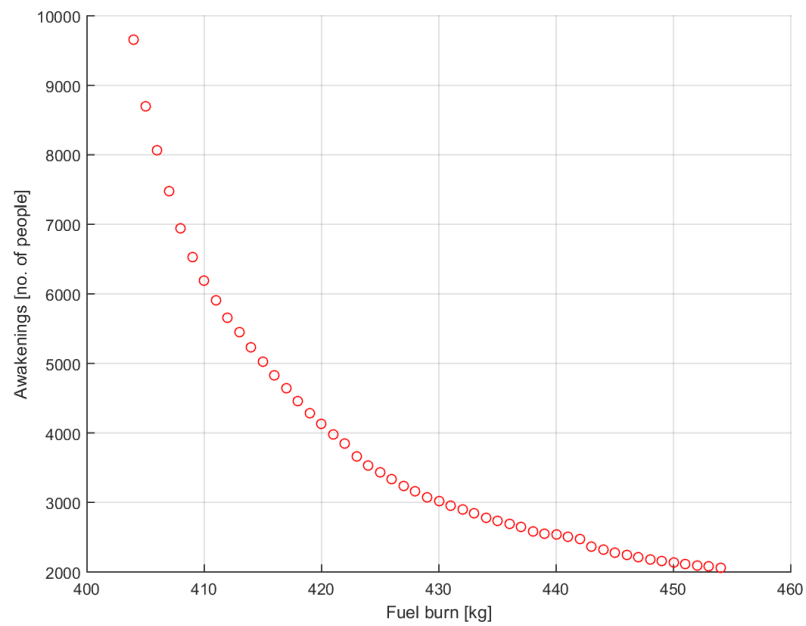


FIGURE 6.17: Pareto front - A new 4D Departure - Heathrow-Schiphol

Figure 6.18 shows the footprint of the three ultimate trajectories to minimize time, fuel consumption and awakenings due to the aircraft departure. Figures 6.19-6.27 show the altitude, true and calibrated airspeed, flight path and heading angles, aircraft mass, throttle, vertical load factor and bank angle profiles respectively.

As it can be seen in Figure 6.18, both ultimate solutions for minimise fuel consumption and flight time are obtaining the shortest footprint, turning immediately right after take-off and heading straight to the final point of the departure procedure. The solution for minimum noise, instead, results a more smooth footprint to go through the population areas of greater London minimizing the awakenings people.

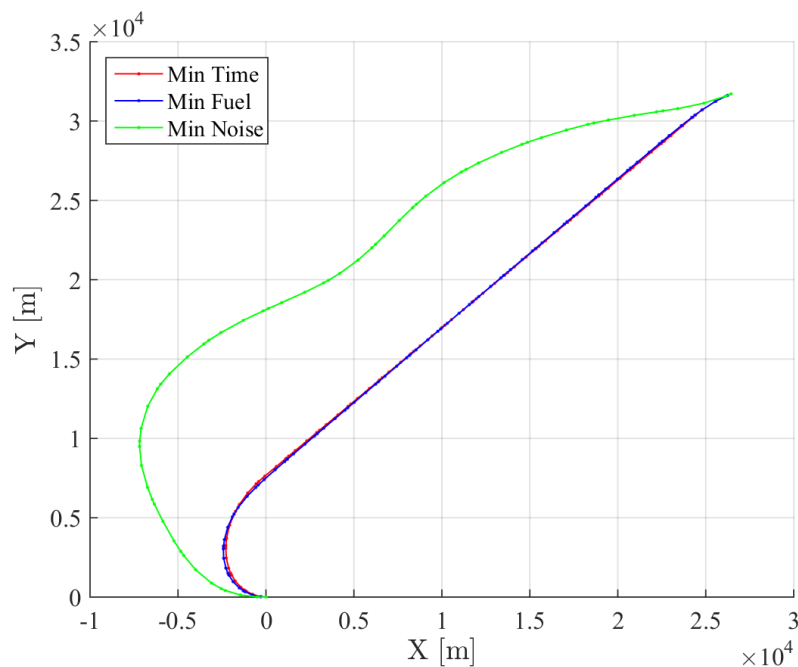


FIGURE 6.18: Footprint - 4D Departure segment - Heathrow-Schiphol

From Figures 6.19-6.21 is possible to see the different approach in the vertical and airspeed profiles. The minimum time solution climbs with the maximum climb rate allowed by the performance, reducing the climb rate only to accelerate but maintaining the minimum climb gradient constraint and then continue climbing till reaching the final altitude. The minimum fuel solution, instead, climbs with the minimum climb gradient allowed till the maximum calibrated airspeed allowed is achieved (i.e. 250 KCAS) and then continues climbing with a less rate of climb than the minimum time solution, to save fuel. The minimum noise solution initially follows the same patten than the minimum fuel, it continues climbing with a slightly less and not constant airspeed, then it levels off while reduces the airspeed, to

lower the number of people awakened by passing over their populated areas. Once the most populated areas are passed, the aircraft accelerates again and continues climbing again to reach the phase final conditions.

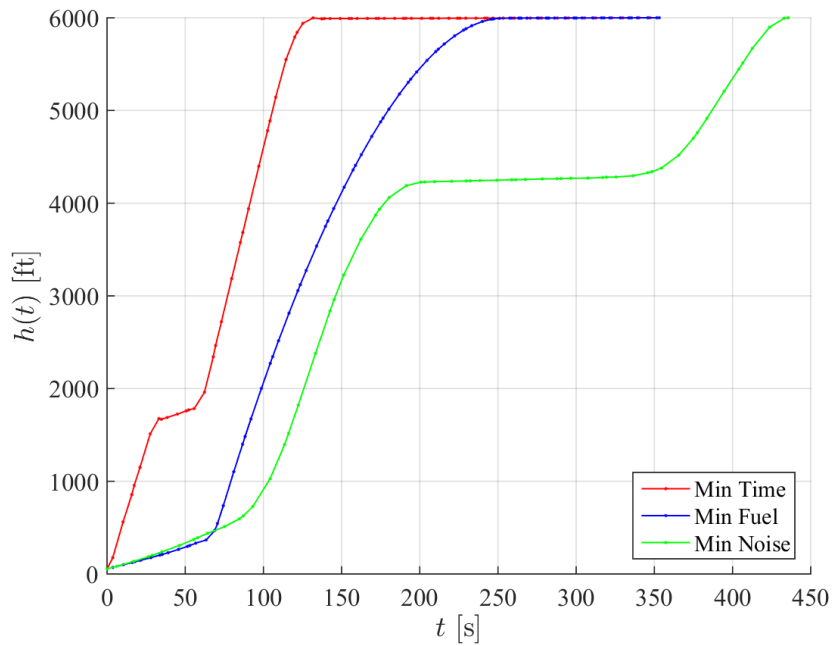


FIGURE 6.19: Altitude profile - 4D Departure segment - Heathrow-Schiphol

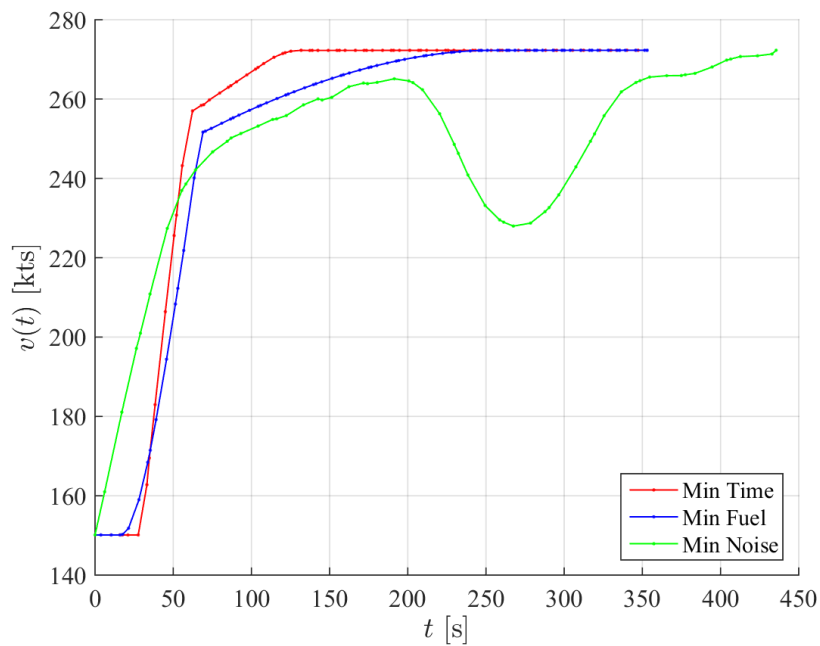


FIGURE 6.20: True airspeed profile - 4D Departure segment - Heathrow-Schiphol

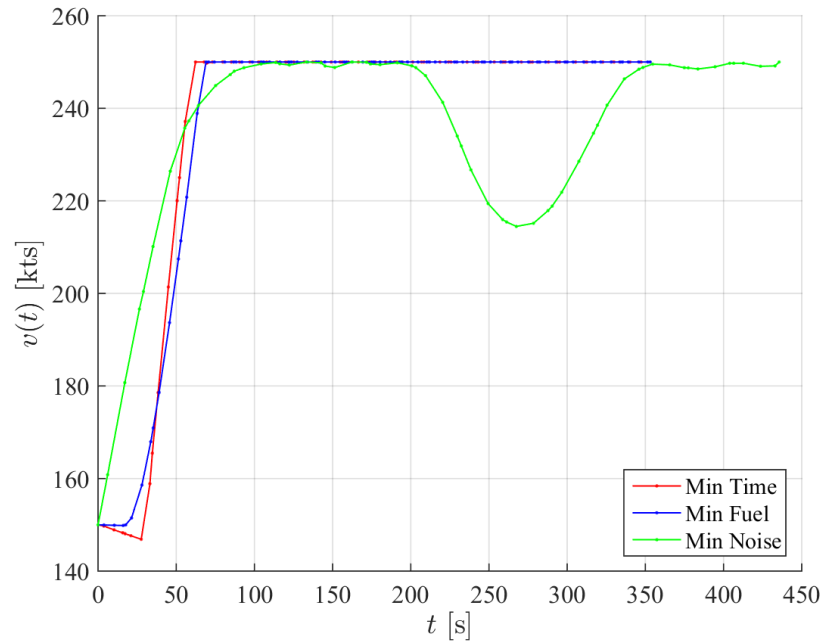


FIGURE 6.21: Calibrated airspeed profile - 4D Departure segment - Heathrow-Schiphol

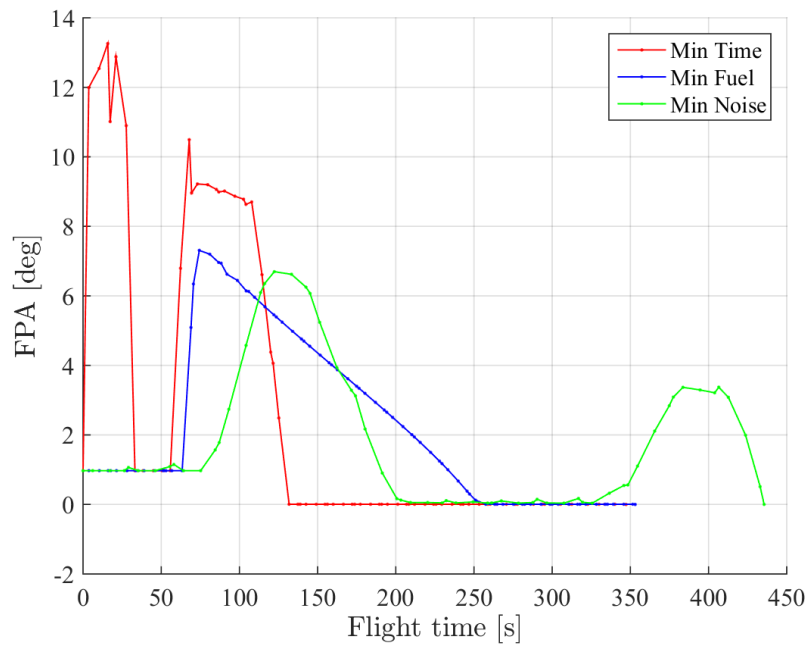


FIGURE 6.22: Flight path angle profile - 4D Departure segment - Heathrow-Schiphol

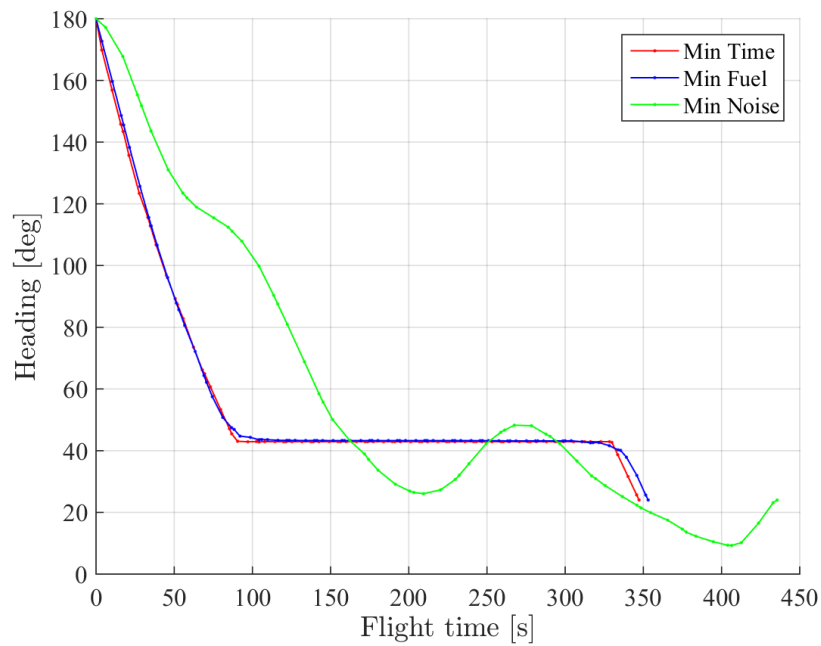


FIGURE 6.23: Heading profile - 4D Departure segment - Heathrow-Schiphol

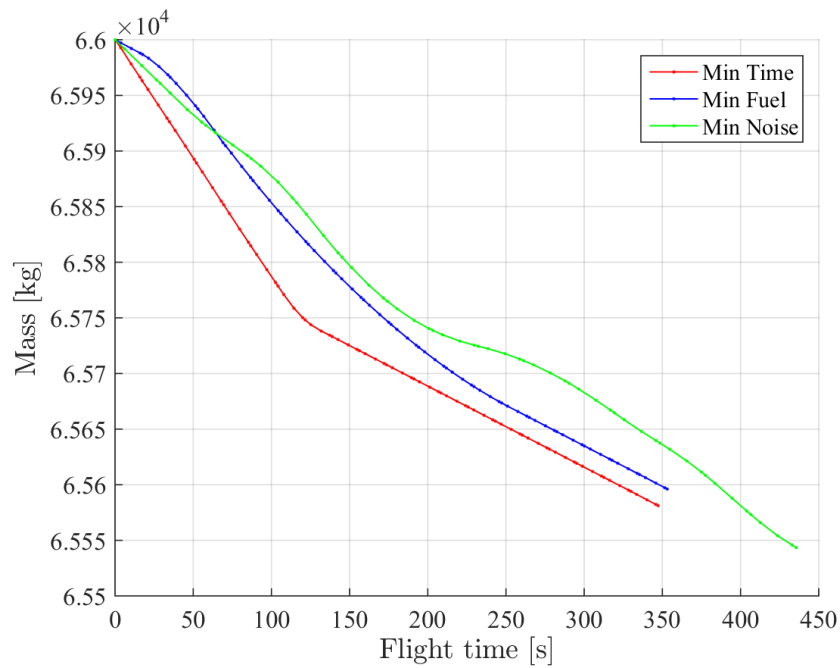


FIGURE 6.24: Mass profile - 4D Departure segment - Heathrow-Schiphol



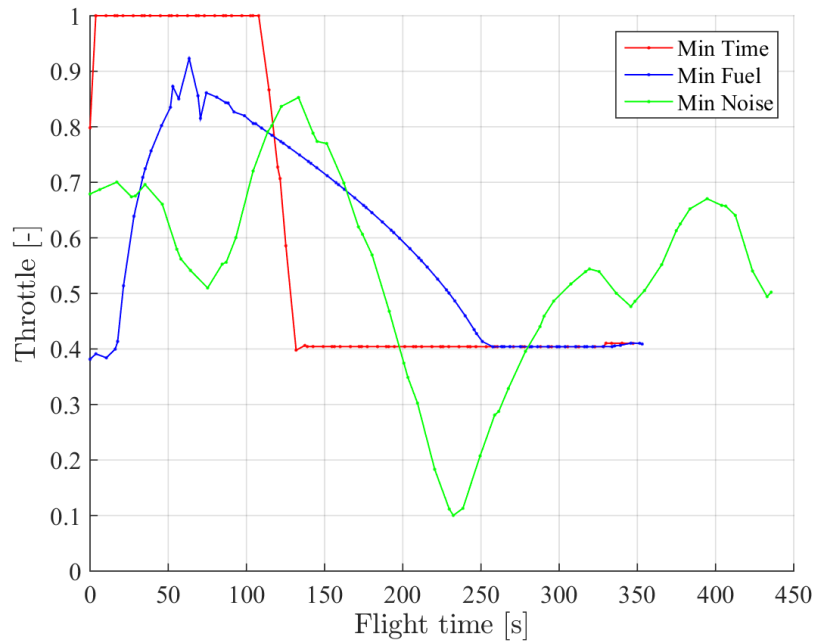


FIGURE 6.25: Throttle profile - 4D Departure segment - Heathrow-Schiphol

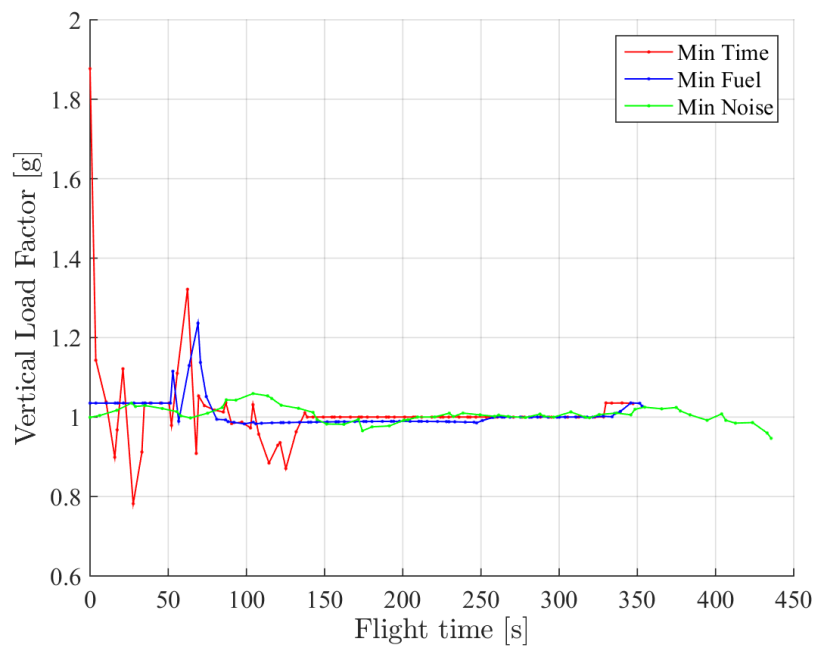


FIGURE 6.26: Vertical load factor profile - 4D Departure segment - Heathrow-Schiphol

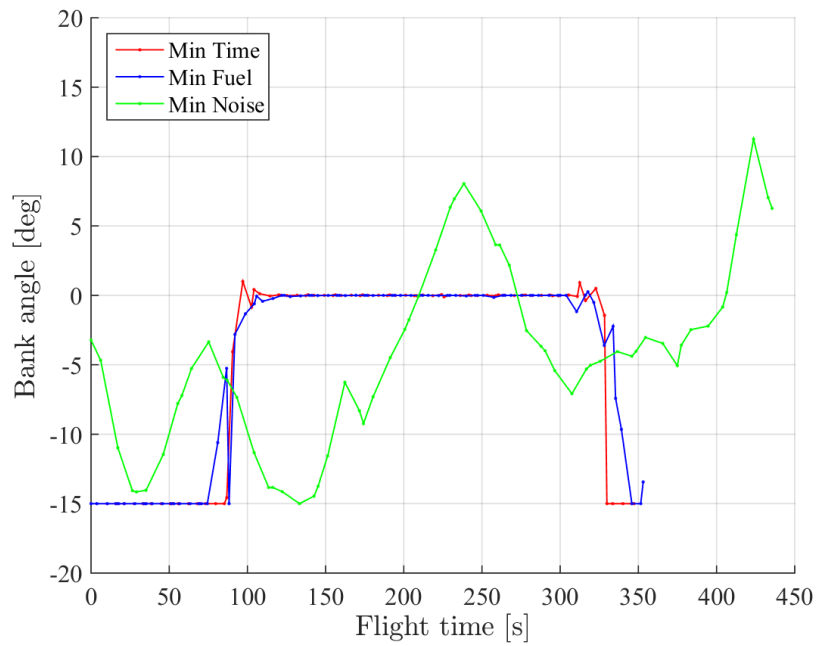


FIGURE 6.27: Bank angle profile - 4D Departure segment - Heathrow-Schiphol

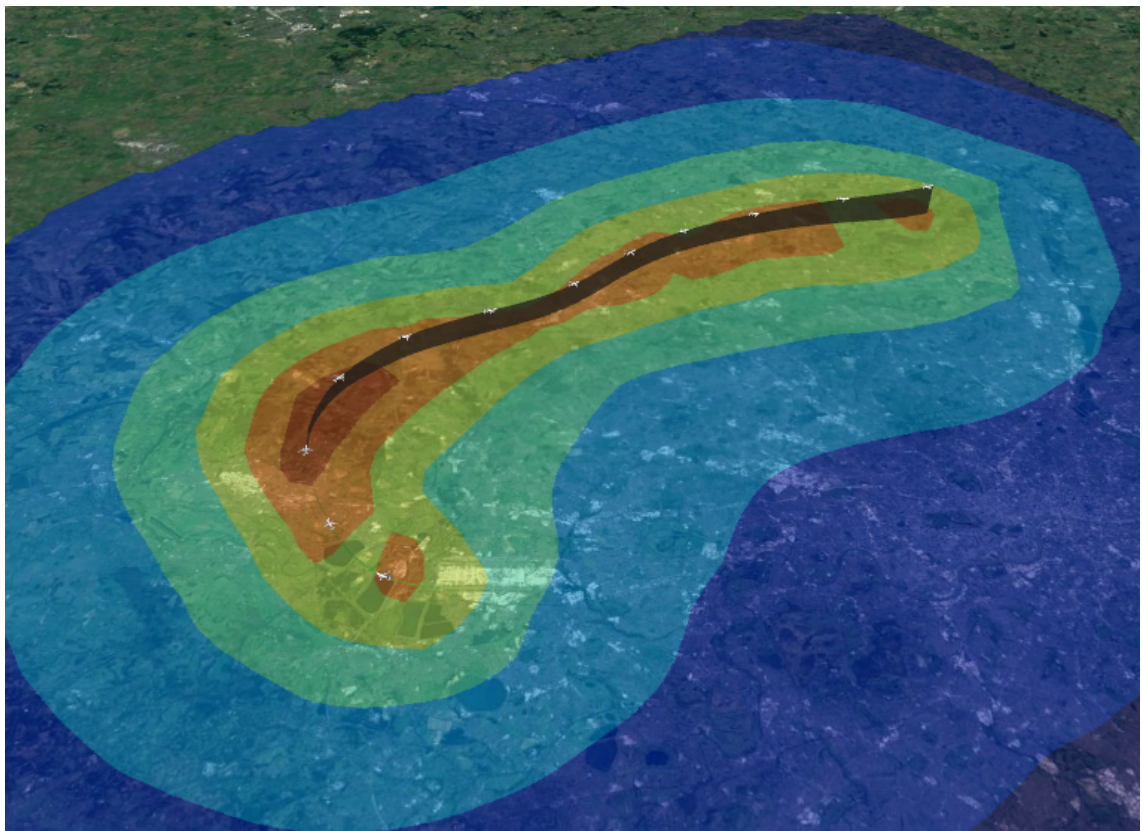


FIGURE 6.28: Noise SEL contours for minimum noise objective function

## 6.2.5 En-Route Phase

### 6.2.5.1 Current Procedure

In this case, the en-route starts after the aircraft has reached BPK VOR waypoint. The en-route phase can be summarized by list of the following waypoints: BPK, DIGSU, SONDO, SULUT and SUGOL. SUGOL indicates the entry point to the Amsterdam FIR as well as the start of Schiphol selected STAR procedure.

During the cruise, a minimum altitude of FL60 ft and a maximum altitude of FL450 are used. This band gives a freedom to the optimiser to choose an optimum flight level within both upper and lower airspaces. Similar to the first case, the airspeeds during cruise are limited by  $1.2 V_{stall}$  for the lower boundary and by the maximum operating Mach number ( $M = 0.82$ ) for the upper boundary. In addition the upper boundary is also limited to 350 KCAS. These settings should provide a freedom for the optimiser to exploit lower airspace which is common airspace used for the EGLL-EHAM route.

To maximise the optimisation process, the en-route phase has also been extended to SUGOL, the initial approach fix (IAF) point for Schiphol airport, in which the Instrument Approach starts. At this point, the altitude is constrained to between FL100 and FL70 whilst the speed is restricted to a maximum of 250 KIAS. This extension is based on that the IAF point is still above the North Sea area (uninhabited region) with altitude is still sufficiently high to disregard the noise impact of the arrival. During approach transition, further descent below FL70 will need an ATC clearance and the instruction to reduce speed below 250 KIAS. Therefore, the altitude is set to FL100 which will allow more detail of arrival phase optimisation where the impact on the en-route phase is considered negligible.

### 6.2.5.2 Problem definition

The problem is considered to be composed by 4 phases. The initial and final conditions for the variables describing the problem are summarized in the following table:

Variable name	Initial condition	Final condition	Min. boundary	Max. boundary
Altitude	6,000 ft	10,000 ft	6,000 ft	45,000 ft
FPA	0	0	-25 deg	25 deg
Heading	66 deg	90 deg	0 deg	360 deg
CAS	250 kts	250 kts	-	-
Latitude	51 44 59.00 N	52 31.53066 N	51 00 00.00 N	53 00 00.00 N
Longitude	000 06 24.00 W	003 58.04100 E	001 00 00.00 W	004 00 00.00 E
Mass	66,000 kg	-	60,000 kg	66,000 kg
Throttle	-	-	0.0	1.0
Vertical Load factor	-	-	0.0	2.0
Bank angle	-	-	-15 deg	+15 deg

TABLE 6.5: Problem setup for departure phase

The aircraft final mass is not specified because it is going to be determined along the optimisation. The aircraft minimum boundary for the departure phase was set to 60,000 kg even though a less fuel consumption is expected.

The list of the phases with start and end points and restrictions for the considered phase are summarised in the following table:

Phase	Start at	End at	Restrictions
P1	BPK	DIGSU	Aircraft can not exceed 250 KCAS below 10,000 ft. Aircraft can not exceed 0.82 M Aircraft can not exceed 350 KCAS Aircraft can not descend
P2	DIGSU	SONDO	Aircraft can not exceed 250 KCAS below 10,000 ft. Aircraft can not exceed 0.82 M Aircraft can not exceed 350 KCAS
P3	SONDO	SULUT	Aircraft can not exceed 250 KCAS below 10,000 ft. Aircraft can not exceed 0.82 M Aircraft can not exceed 350 KCAS
P4	SULUT	SUGOL	Aircraft needs to fly over SUGOL at 7,000 ft Aircraft can not exceed 250 KCAS below 10,000 ft. Aircraft can not exceed 0.82 M Aircraft can not exceed 350 KCAS Aircraft can not climb

TABLE 6.6: Phases definition for en-route phase

The first and last phase of the en-route are discretised by 10 intervals with 4 nodes per interval for a total of 40 nodes per phase. The two phases in between

are discretised by 20 intervals each and all using 4 nodes per interval for a total of 80 nodes per phase. The overall problem uses a total of 240 nodes.

The transcribed problem to be solved has 3168 objective variables and 2990 constraints. The total constraints contains also the linkage between the phases. The results are shown in the next section.

### 6.2.5.3 Results

Figure 6.29 shows the Pareto front obtained at the end of the MMO optimisation for the en-route segment using flight time and fuel consumption as objective functions. It is possible to notice a smooth continuous pattern of the Pareto front, without presence of non-convex regions. Figure 6.30 shows the Pareto front obtained at the end of the MMO optimisation for the en-route segment using flight time and fuel consumption as objective functions. It is possible to notice in this Pareto front, that adjacent to the minimum emission of NOx due to the flight, the fuel consumption increases rapidly without really obtaining a reduction of NOx. This is probably due to reaching the limit, where the low turbine temperature, which is connected to generation of NOx, results in a very low thrust produces which results in obtaining an overall flight time and therefore fuel consumption very high. There is although a presence of a straight line in the middle of the Pareto, which shows a proportional relation between fuel consumption and NOx generated during en-route.

If the extreme point of both Pareto fronts are considered (minimum time, minimum fuel consumption and minimum NOx cases), the trajectories are plotted in the next figures.

Figure 6.31 shows the ground footprint of the en-route trajectories. It is possible to see that all the trajectories follow the same path from initial waypoint to the last waypoint. The only minor differences are in the turning radius applied at each waypoint that is due to the different speed used along the flight.

Figures 6.32-fig:ResultsShortHaulEnRoute-CalibratedAirspeedProfile show the altitude, true and calibrated airspeed profile for the three different trajectories. It is possible to see that the minimum time trajectory accelerates to the maximum airspeed allowed, which is 350 KCAS, and maintains it till almost the end of the segment, where it is forced to meet the final condition of 250 KCAS. In addition,

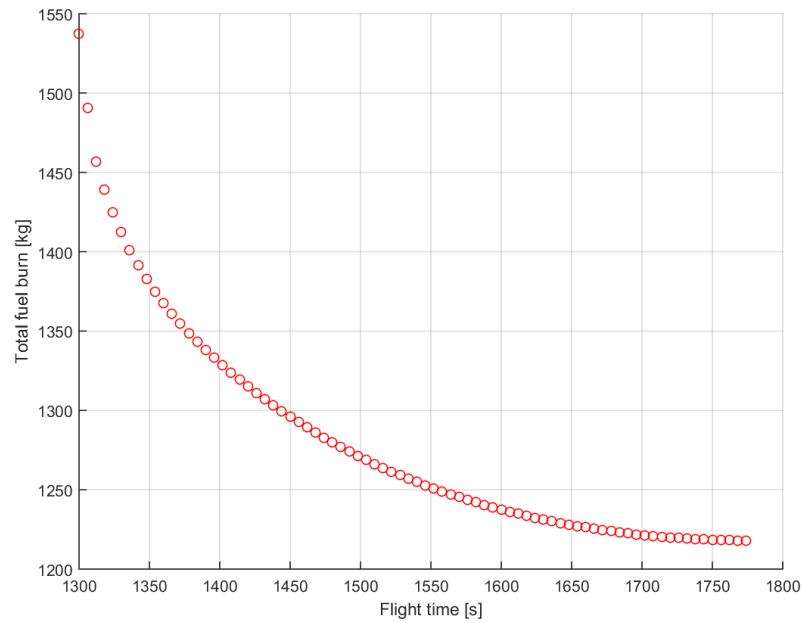


FIGURE 6.29: Pareto front fuel consumption vs flight time - EnRoute segment - Heathrow-Schiphol

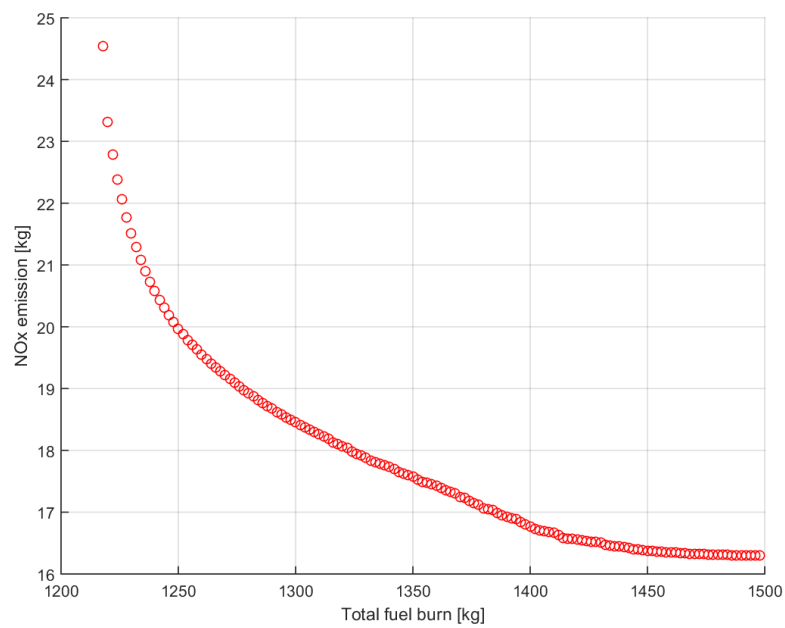


FIGURE 6.30: Pareto front fuel - NOx - EnRoute segment - Heathrow-Schiphol

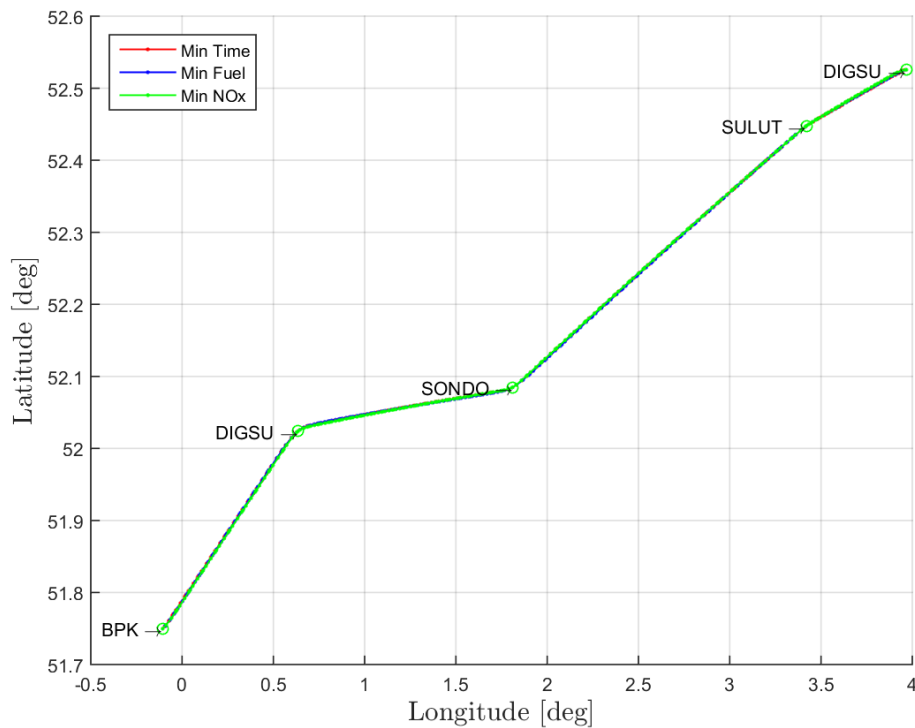


FIGURE 6.31: Latitude Longitude profile - EnRoute segment - Heathrow-Schiphol

the aircraft climbs to a lower flight level, around FL220, and maintains it till reaching Top Of Descent (TOD) at which starts to descend to meet the final altitude condition and maintain a level flight while decelerating to 250 KCAS.

The minimum fuel trajectory, instead, climbs with a slow increase of true airspeed, resulting in decreasing calibrated airspeed along the climb phase. The aircraft reaches Top Of Climb (TOC) at around FL310. The cruise level flight is very short, less than 100 s; the aircraft starts descending at low calibrated airspeed and maintain the engine in idle as flying the aircraft almost as a glider and decreasing the descent rate when almost reaching the 10,000 ft to allow the acceleration needed to meet the speed final condition.

The minimum NOx emission trajectory is a more simple solution. The aircraft never climbs above FL140 and maintain a calibrated airspeed of 200 KCAS. This allows to maintain a very low engine turbine temperature and therefore produce low amount of NOx emission, however this increase the overall fuel consumption as it will be shown later on.

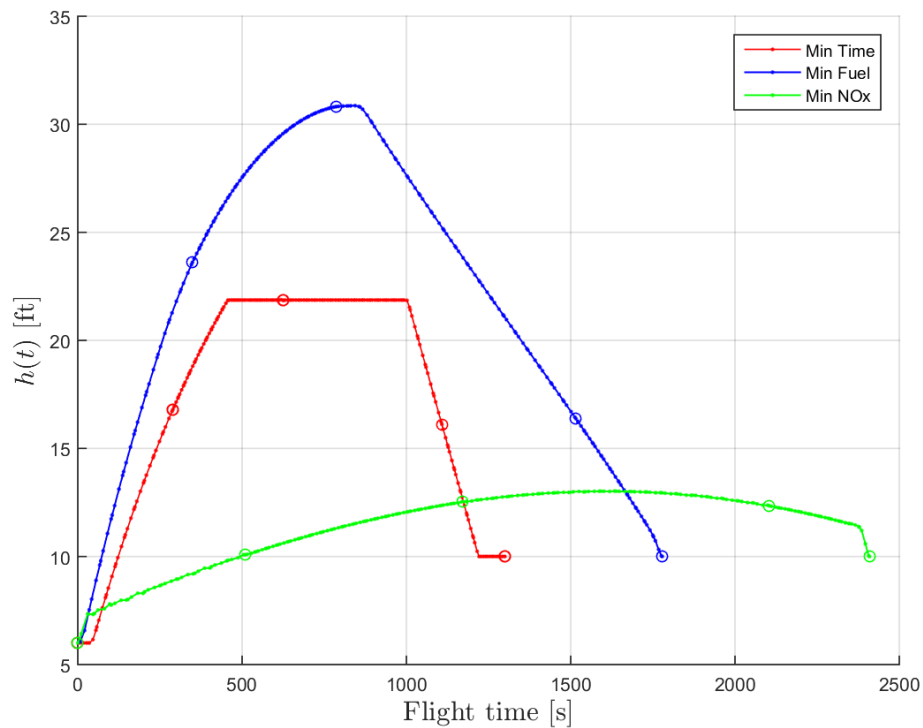


FIGURE 6.32: Altitude profile - EnRoute segment - Heathrow-Schiphol

Figures 6.35-6.36 show the flight path angle and heading angle for the three ultimate trajectories. Figure 6.37 shows the aircraft mass profile for the three selected trajectories. It is possible to see the minimum time trajectory resulting in consuming more fuel, hence reaching the final condition at overall lower mass. The minimum fuel trajectory is the one which ends up at the higher value of aircraft mass at the final condition. It is possible to see how the difference in aircraft mass increases during the half part of the flight, which is the descend phase. The minimum NOx trajectory instead, maintains a lower consumption rate but as stated before this results in having low thrust per each engine and therefore low airspeed, resulting in a high flight time and the final fuel consumption is close to the one obtained with minimum flight time, however the flight time resulted in almost half of the one obtained by minimum NOx trajectory.



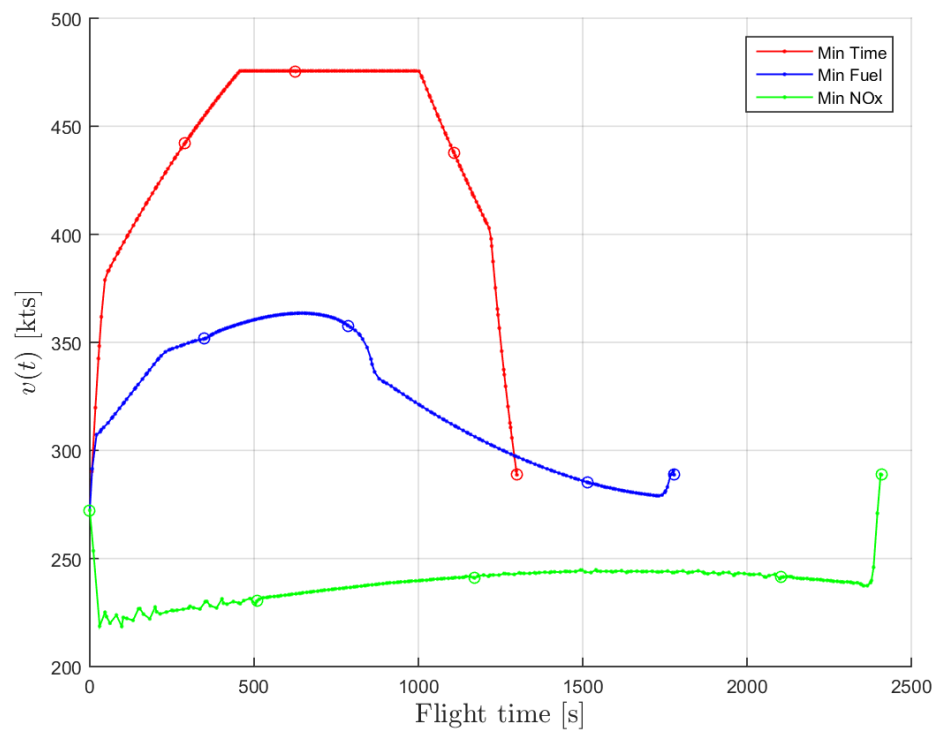


FIGURE 6.33: True airspeed profile - EnRoute segment - Heathrow-Schiphol

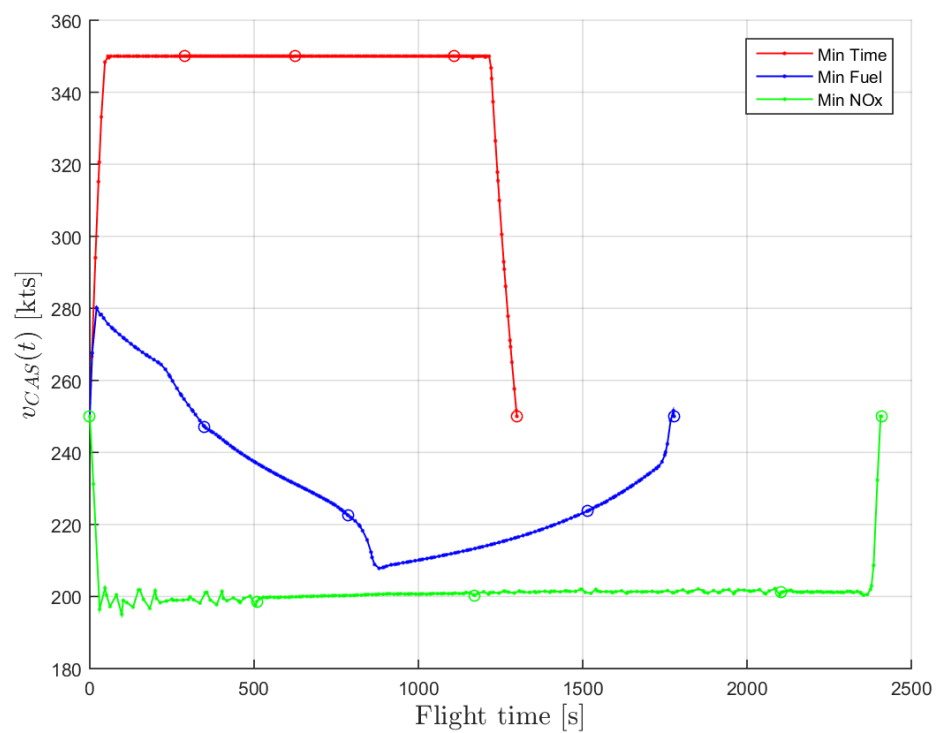


FIGURE 6.34: Calibrated airspeed profile - EnRoute segment - Heathrow-Schiphol

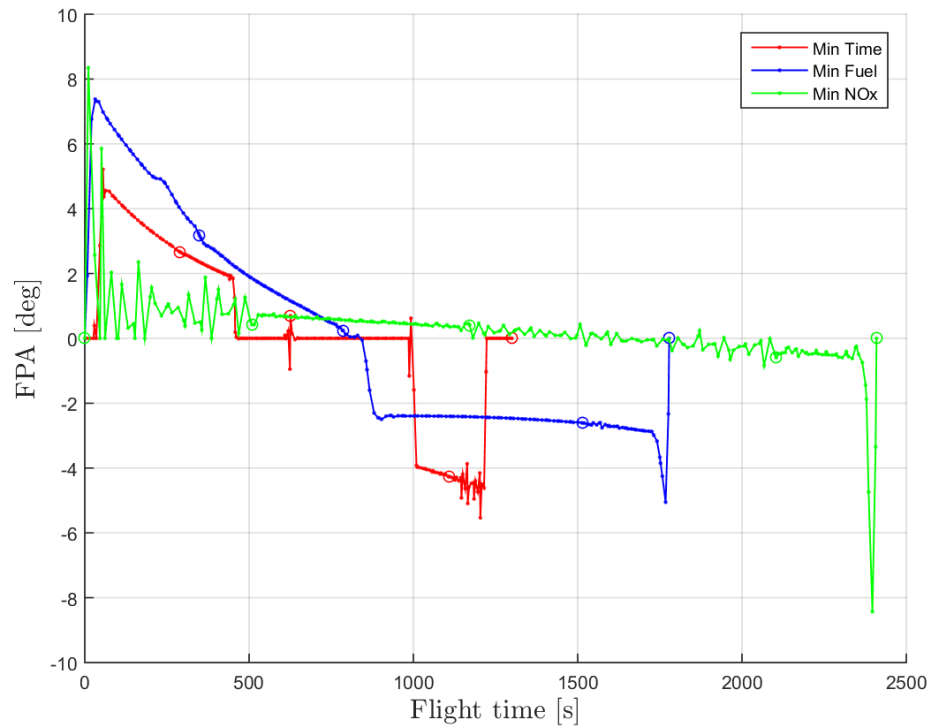


FIGURE 6.35: FPA profile - EnRoute segment - Heathrow-Schiphol

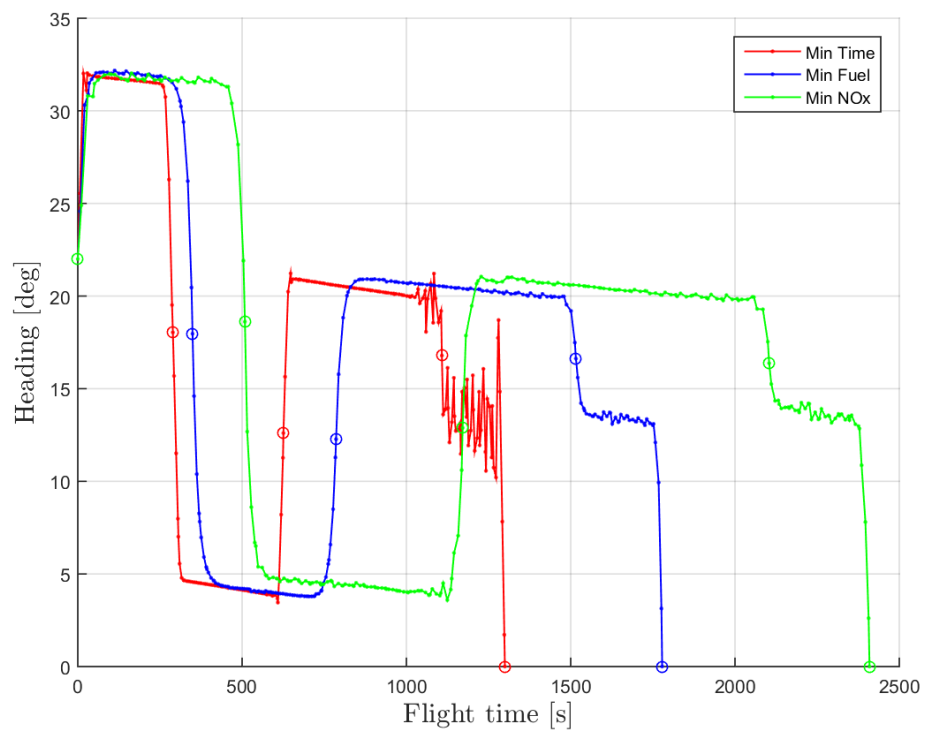


FIGURE 6.36: Heading profile - EnRoute segment - Heathrow-Schiphol

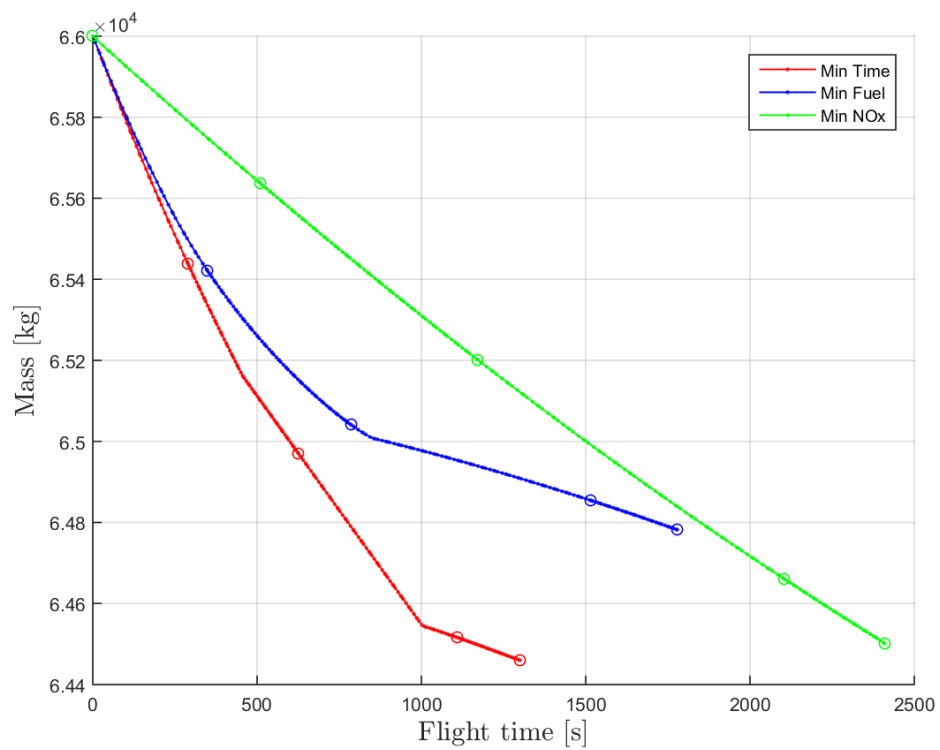
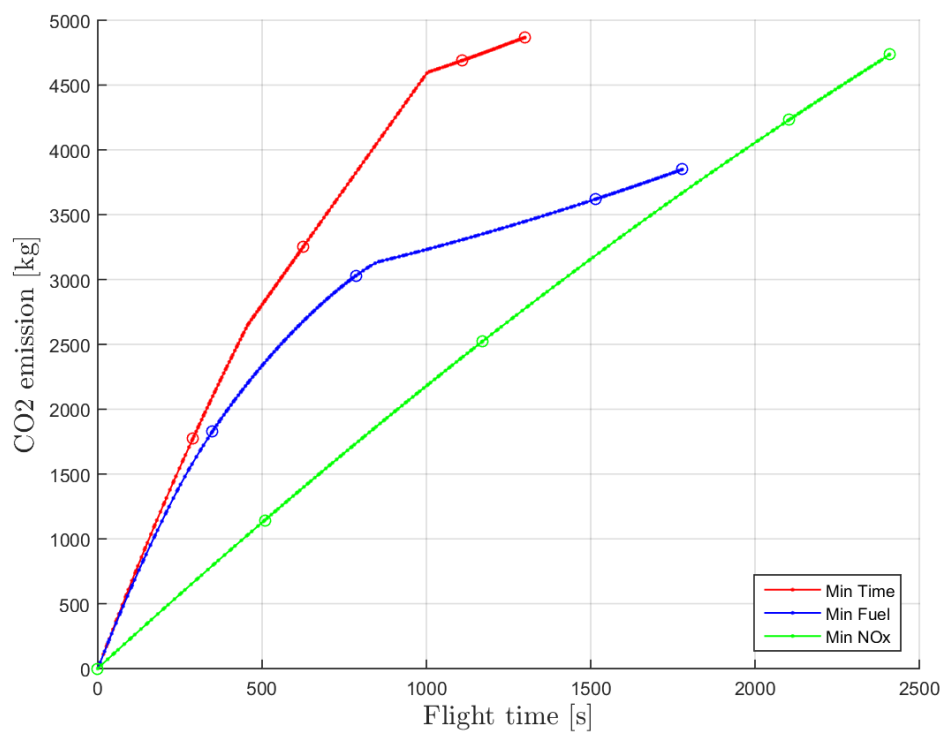


FIGURE 6.37: Aircraft mass profile - EnRoute segment - Heathrow-Schiphol

FIGURE 6.38: Aircraft  $CO_2$  emission profile - EnRoute segment - Heathrow-Schiphol

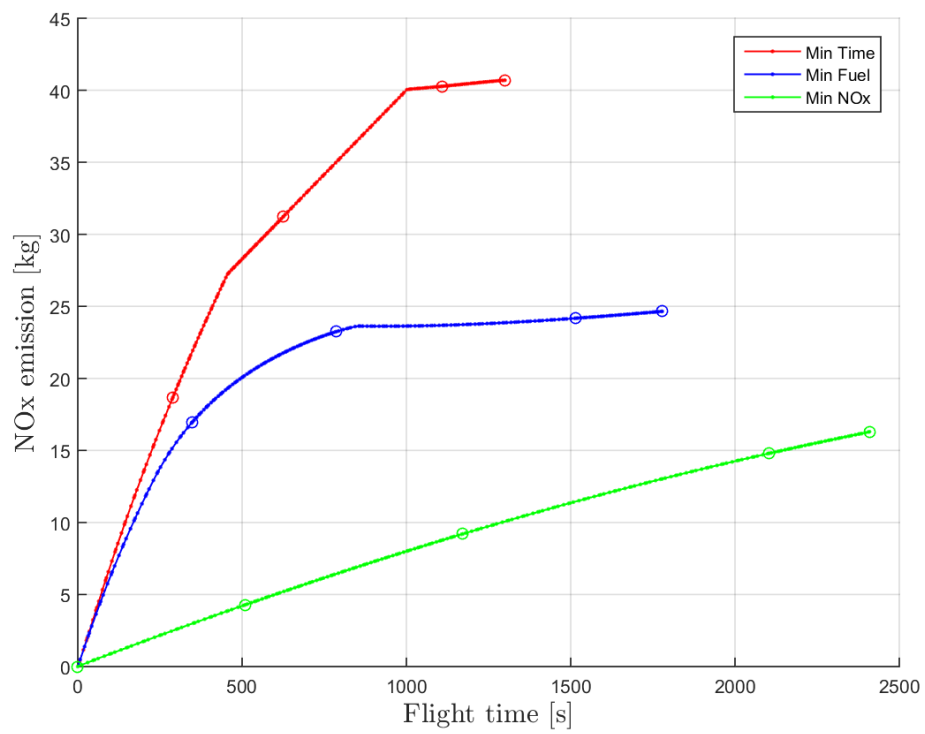


FIGURE 6.39: Aircraft  $NO_x$  emission profile - EnRoute segment - Heathrow-Schiphol



### 6.2.6.1 Problem definition

In order to provide full freedom to the optimiser, a free-flight is set-up whilst keeping the initial and final conditions as they are in the procedure. However, several constraints need to be imposed, for examples, the final ILS segment impose a descend gradient of 3 degrees, therefore a maximum flight path angle of  $-3$  degrees is imposed for altitude below 2,000 ft approach segments starting at SOKSI waypoint where minimum or exact altitudes and speeds need to be constrained. The arrival flight phase is considered to be composed by one phase which is described in Table 6.7.

Phase	Start at	End at	Restrictions
P1	SUGOL	RWY 06	Aircraft can not exceed 250 KCAS below 10,000 ft. Aircraft can not exceed 0.82 M Aircraft can not exceed 350 KCAS Aircraft can not climb Aircraft FPA can not exceed -3 deg below 2,000 ft

TABLE 6.7: Phases definition for arrival phase

The 4D arrival is discretized by 20 intervals with 4 nodes per interval for a total of 80 nodes. The overall states and control with initial and final boundaries conditions are listed in the following Table 6.8.

Variable name	Initial condition	Final condition	Min. boundary	Max. boundary
Altitude	10,000 ft	0 ft	0 ft	10,000 ft
FPA	0	0	-25 deg	0 deg
Heading	113 deg	58 deg	0 deg	360 deg
CAS	250 kts	150 kts	-	-
Latitude	52 31.53066 N	52 17 20.58 N	51 00 00.00 N	53 00 00.00 N
Longitude	003 58.04100 E	004 44 14.20 E	003 00 00.00 E	005 00 00.00 E
Mass	66,000 kg	-	60,000 kg	66,000 kg
Throttle	-	-	0.0	1.0
Vertical Load factor	-	-	0.0	2.0
Bank angle	-	-	-15 deg	+15 deg

TABLE 6.8: Problem setup for arrival phase

The transcribed problem obtained from optimisation tool has 809 objective variables and 640 constraints. The obtained results are shown in the next section.

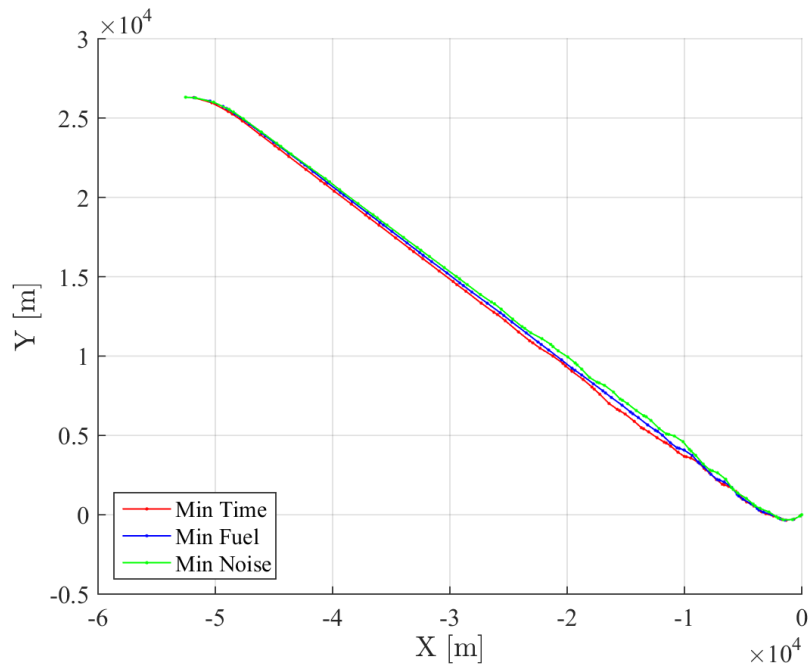


FIGURE 6.41: Footprint - 4D Departure segment - Heathrow-Schiphol

### 6.2.6.2 Results

From Figures 6.42-6.44 it is possible to see the different approach in the vertical and airspeed profiles. The minimum time solution climbs with the maximum climb rate allowed by the performance, reducing the climb rate only to accelerate but maintaining the minimum climb gradient constraint and then continues climbing till reaching the final altitude. The minimum fuel solution, instead, climbs with the minimum climb gradient allowed till the maximum calibrated airspeed allowed is achieved (i.e. 250 KCAS) and then continues climbing with a less rate of climb than the minimum time solution, to save fuel. The minimum noise solution initially follows the same pattern than the minimum fuel, it continues climbing with a slightly less and not constant airspeed, then it levels off while reduces the airspeed, to lower the number of people awakened by passing over their populated areas. Once the most populated areas are passed, the aircraft accelerates again and continues climbing again to reach the phase final conditions.

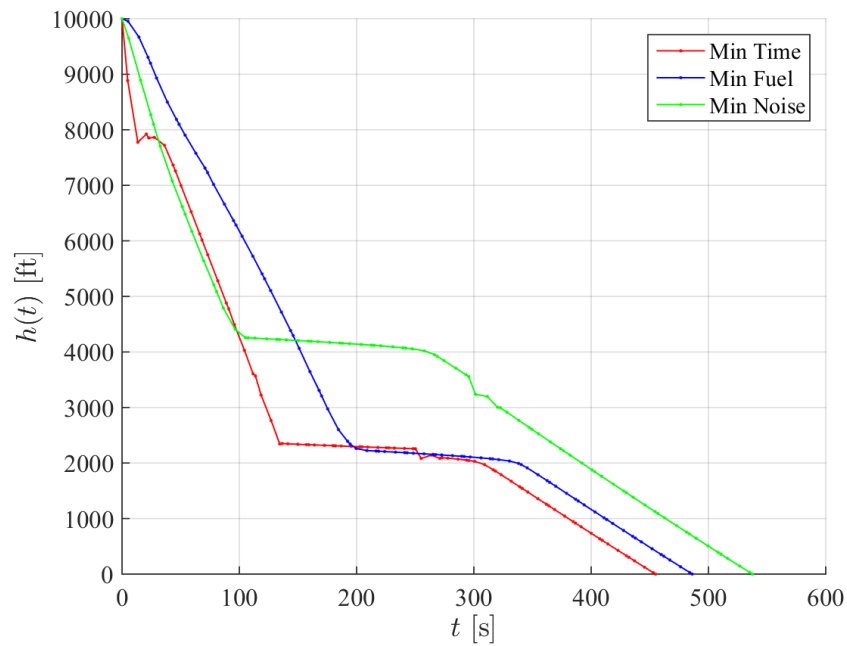


FIGURE 6.42: Altitude profile - 4D Arrival segment - Heathrow-Schiphol

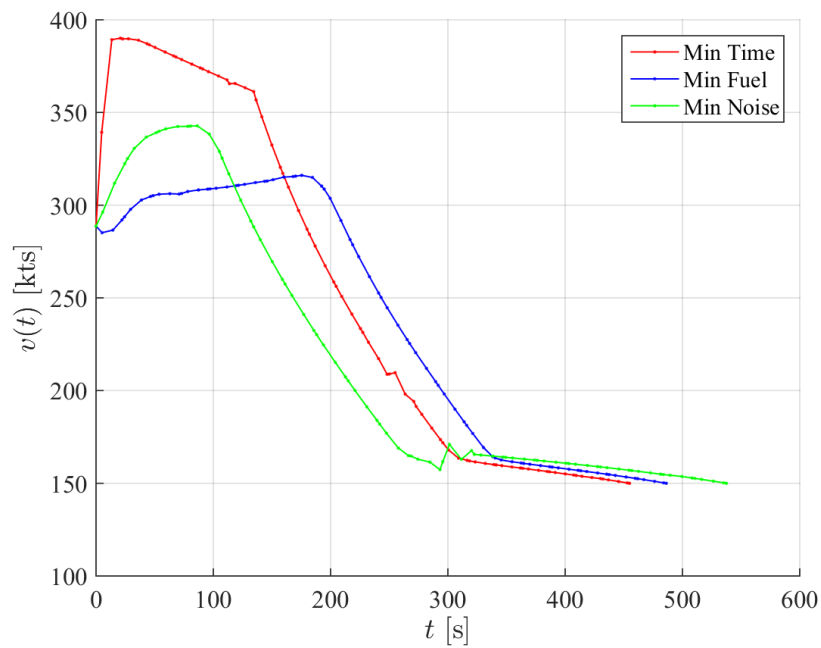


FIGURE 6.43: True airspeed profile - 4D Arrival segment - Heathrow-Schiphol



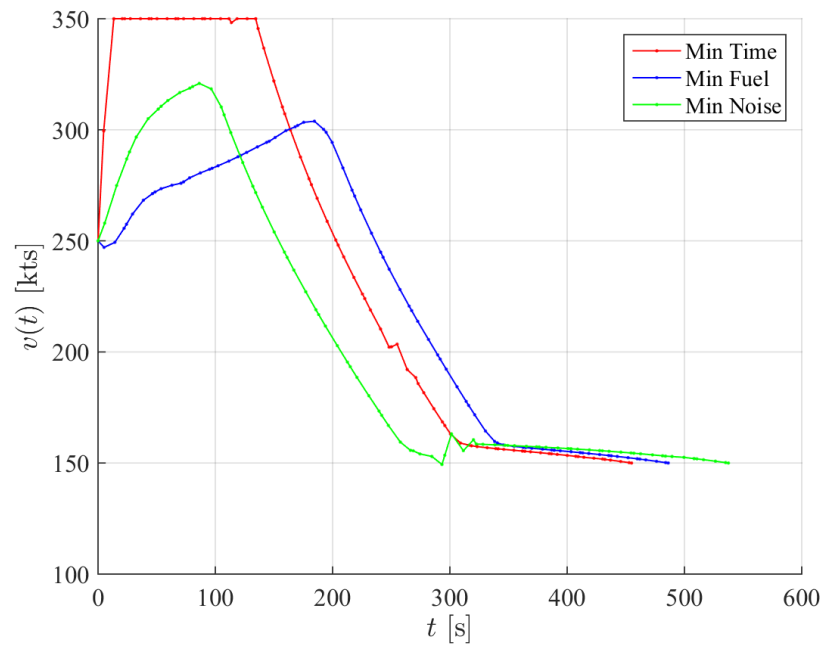


FIGURE 6.44: Calibrated airspeed profile - 4D Arrival segment - Heathrow-Schiphol

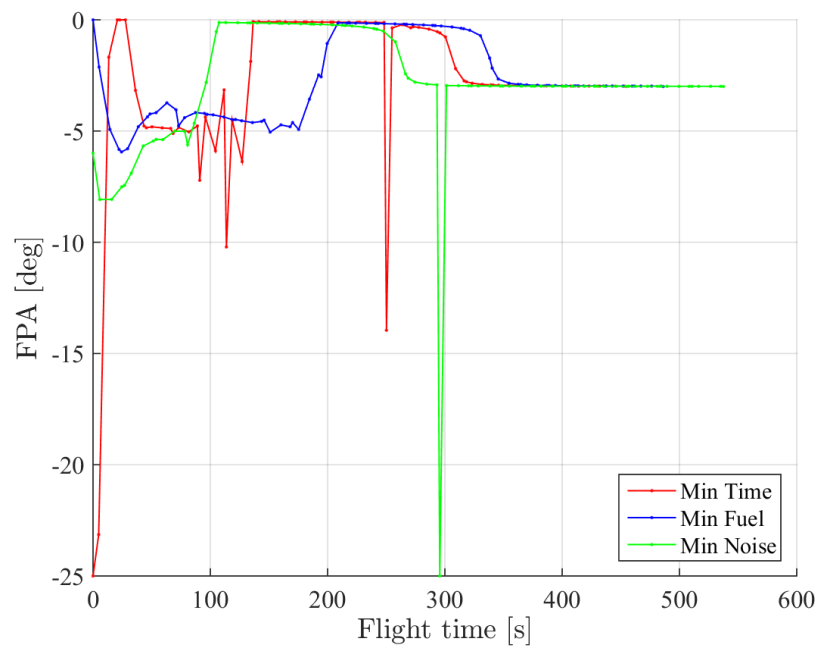


FIGURE 6.45: Flight path angle profile - 4D Arrival segment - Heathrow-Schiphol

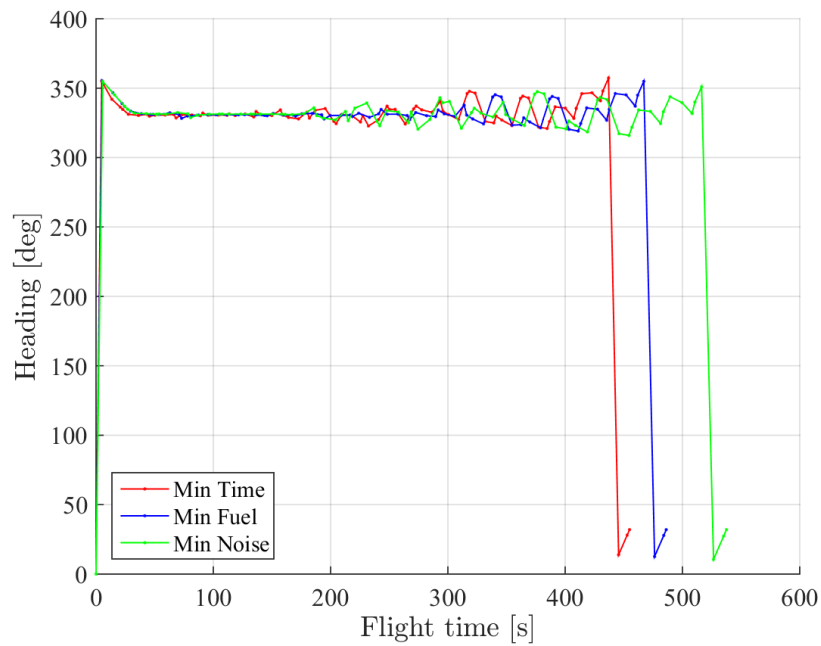


FIGURE 6.46: Heading profile - 4D Arrival segment - Heathrow-Schiphol

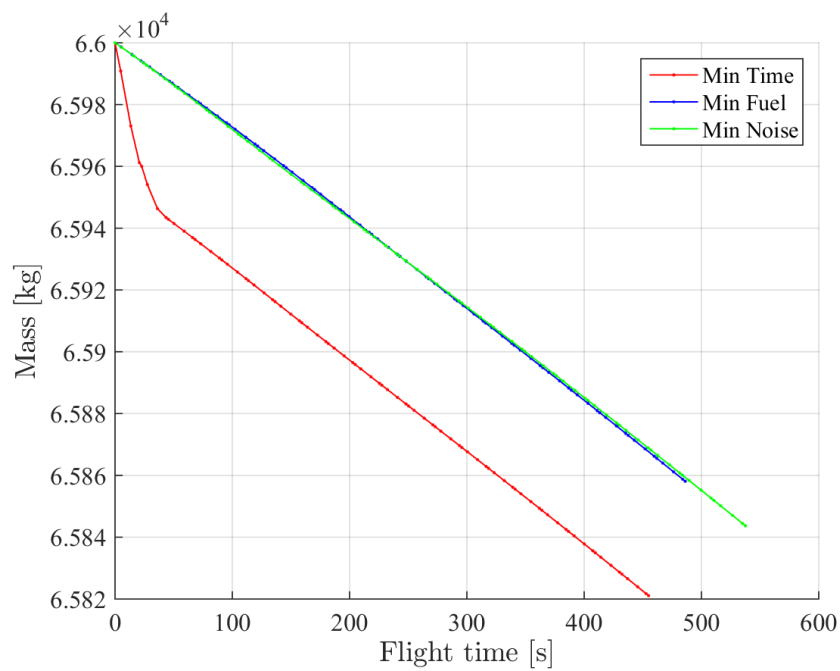


FIGURE 6.47: Mass profile - 4D Arrival segment - Heathrow-Schiphol

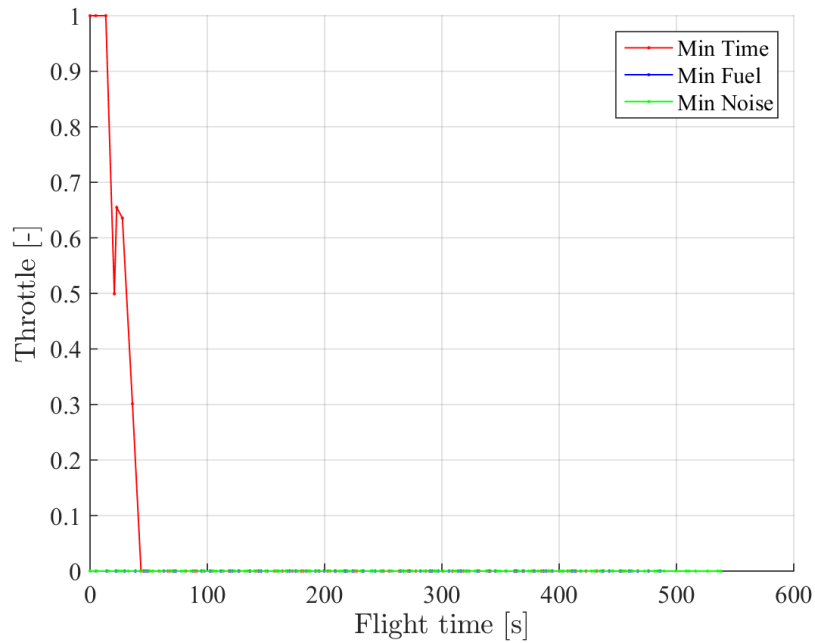


FIGURE 6.48: Throttle profile - 4D Arrival segment - Heathrow-Schiphol

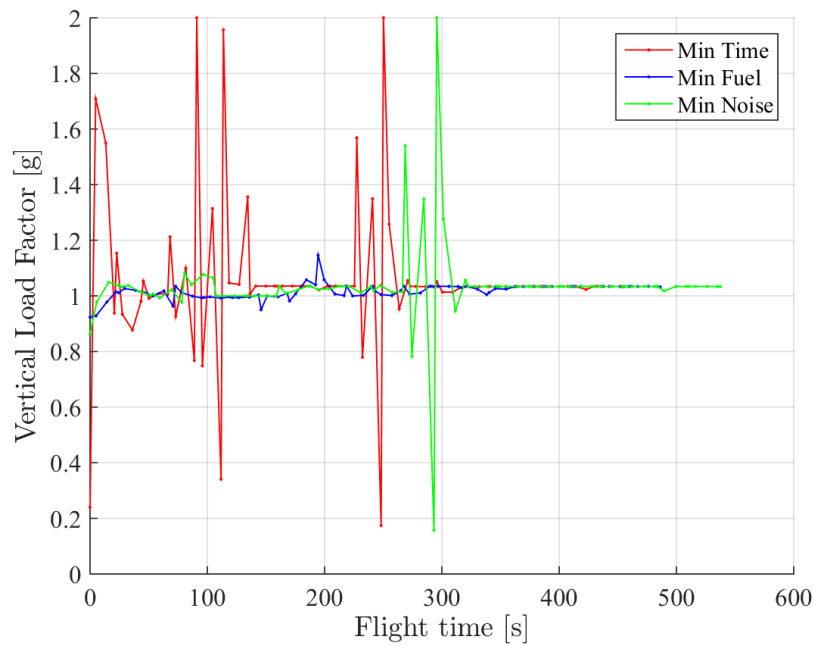


FIGURE 6.49: Vertical load factor profile - 4D Arrival segment - Heathrow-Schiphol

# Chapter 7

## Conclusions and Future Work

### 7.1 Conclusions

This research work reviewed the evolution of trajectory optimisation techniques applied to aircraft performance and commercial aircraft planning. Focus was towards the work done to optimised the overall commercial mission and in particular towards the work which took into consideration the generated noise and engine emissions during the flight. It was concluded that most of the work done was secluded in the old idea of portion of flights which was resulting in using the natural translation of constant aircraft states into a model which was fitting for parametric optimisation. With the introduction of the new ATM paradigm and the TBO concept aim to increase the safety and capability of air traffic, this was no longer acceptable. This established the need to release constraints in the commercial aircraft modelling to obtain more efficient trajectories which reduce overall pollutants (perceived noise, engine pollutants, contrails formation, etc.) which are due to the air traffic activity.

Consequently an optimisation tool was developed and implemented using the latest optimisation techniques available to be able to optimise the trajectory of a commercial aircraft during city pair mission and achieve more greener trajectories. To fulfil the aim of the study, aircraft had to be represented satisfactorily. The aircraft aerodynamic performance were obtained using preliminary design state methods which allowed to predict the aerodynamic characteristics for the overall flight envelope. The engine performance data were obtained using a thoroughly validated aircraft engine model on TURBOMATCH provided numerical solution

to predict engine performance characteristics such as net thrust, fuel consumption and turbine pressure and temperatures profiles also for the overall flight envelope. The engine performance characteristics, such as SFC and turbine characteristics allowed the use of enhanced emission models. Noise generation modelling was available from the literature but needed to be adapted to allow the use within the optimisation tool.

The optimisation tool was then configured for one case study aircraft. To test the overall functionalities, a real trajectory between London Heathrow and Amsterdam Schiphol, which is typically flown by Airbus A320 series, was simulated.

The ultimate trajectories are used as greener procedures and have to respect the new requirements requested by future generation air traffic rules. The methodology was successfully validated at many levels.

## 7.2 Contribution to knowledge

This thesis covers the development of enhanced technique for optimal trajectory planning considering at the reduction of direct operating cost as well as environmental pollutants and noise perceived in the terminal area. The use of the technique developed in this thesis allows to minimise multi-objectives considered in the flight and the application of the ultimate trajectories to on-board systems can produce benefits in the overall flight time, consumption and pollutants generation. The simulation of optimised trajectories in high-fidelity on-board systems can also be used as feedback in the design of on-board systems such as FMS and FCS. The major contributions made during this PhD study are summarised as follows:

- A modelling methodology to develop models for tackling constrained trajectory problem using optimal control techniques to obtain greener trajectories. The trajectory problem required the development of aircraft dynamic equations and aerodynamic and engine performance and atmospheric models were also developed. The engine pollutants model was developed and integrated with the engine performance model to obtain a direct dependency between engine control and pollutants. The noise annoyance model was also developed and integrated in the optimisation loop and instabilities in minimum

noise results were tabled to obtain a numerical-noise-free ultimate trajectories.

- A multi-objective methodology was developed using e-constraint to overcome non-convex regions in the Pareto front of the obtained trajectories. The methodology used multi-phase pseudospectral algorithm to convert the optimal control problem into a non-linear problem. The resulting non-linear problem has been solved using the SNOPT solver. This approach overcomes several above mentioned drawbacks and was successfully applied to real case city pair mission. New procedures were obtained considering multi-objectives such as time, fuel consumption and noise annoyance on the terminal area. In en-route phase the engine emissions were taken into consideration and pareto of trajectories were obtained to minimise fuel consumed, NOx pollutants and flight time. The ultimate greener trajectories allow the on-board systems to follow them without introducing any translation or manipulation which would result in non-optimal flown trajectory. Results from the city pair optimisation shows that the efficiency of current AIP flight plans could be improved by taking also into account pollutants and noise annoyance in the terminal area.
- A Simulation environment was developed. The simulation environment allowed to test and evaluate the obtained greener trajectories with a 6-DOF aircraft dynamic and on-board systems. This is a big step in the research of future on-board systems and allows also other researchers to develop their on-board systems and have feedbacks achieving greener trajectories. This contribution creates a bridge between the optimal trajectory and the trajectory which is actually flow by the aircraft with all the systems included in the loop.

### 7.3 Milestones achieved

- Modelled aircraft aerodynamic and engine performance characteristics at the conceptual and preliminary design stage.
- Enhanced the aircraft modelling with all the necessary components to model engine emissions, noise impact and contrails generation.

- Development of a optimisation tool to optimise commercial aircraft trajectories considering well known cost index and also engine pollutants, aircraft noise generation and perceived on the ground.
- Designed more efficient trajectories for real city pair mission.
- Established the impact that the more efficient trajectory have on aircraft on-board systems and its design.

## 7.4 Proposed Future Work

During this work new questions and research ideas arose. The following points are proposed for the future:

- The noise calculation procedures present in the literature do not take into account the wind vector and assume isotropic atmosphere. This assumption introduce errors in real life. The noise perceived at ground level is affected by shadow zones and wind refractions which results different from the generated noise. Therefore, if the noise model would be further improved by considering non standardised weather conditions, a further study to enhance the optimised trajectories would be carried out.
- The optimisation algorithms present in the literature are improving fast especially with the exponential power available in a medium-performance computer. Pseudospectral methods could be improved in the following years and the introduction of nodes will not penalise the stability of the overall trajectory. Testing different optimisation algorithms could be therefore carried out.
- The multi-objective optimised trajectories obtained did not show any non-convex regions in the Pareto front. Other multi-objective resolution techniques could be however considered to create benchmark results.
- The introduction of TBO into the ATC world is still at the beginning. More complex set of restrictions could be introduced into the optimisation problem. For example, when in the future several aircraft are flying their optimal trajectories, the on-board systems necessary have to take these 4D optimal trajectories as constraints into the overall optimisation context.

- The aircraft performance model used in trajectory optimisation techniques is lacking in describing the moving of Central of Gravity (CG) along the city pair mission. In addition the trim drag applied by the tail elevators along the mission is also not considered yet into the optimisation loop. For long-haul flights this can not be neglectable and both dynamic effect change the aircraft response to known commands, therefore the FMS has to take into consideration these components to maintain the ultimate trajectory between required performance navigation rules.



# Appendix A

## Flight Mechanics

This Appendix provides background description to obtain the equations of motion of a commercial aircraft modelled as rigid body and flying in an atmospheric environment which is needed in the problem described in this thesis.

### A.1 Reference Frames

There are five different coordinate systems which are of interest in this work: the Earth axes system  $E_{x_e y_e z_e}$ , the curvilinear ground system  $E_{XYZ}$ , the local horizon system  $O_{x_h y_h z_h}$ , the wind axes system  $O_{x_w y_w z_w}$  and the body axes system  $O_{x_b y_b z_b}$ .

The Earth axes system  $E_{x_e y_e z_e}$  is a Cartesian reference frame which is rigidly attached to the Earth. Its origin  $E$  is a point on the Earth's surface; the  $z_e$ -axis is vertical and positive downward; the  $x_e$ -axis and the  $y_e$ -axis are tangent to the Earth's surface and are directed in such a way that the trihedral  $E_{x_e y_e z_e}$  is the right-handed. Incidentally, the great circle tangents to the  $x_e$ -axis is called the fundamental parallel, while the great circle tangent to the  $y_e$ -axis, is called the fundamental meridian. Furthermore, a meridian is the intersection of the surface of the Earth and a plane perpendicular to the fundamental parallel, and a parallel is the intersection of the Earth's surface with a plane parallel to the fundamental parallel.

The curvilinear ground system  $E_{XYZ}$  is an orthogonal reference frame which is fixed to the Earth. Its origin  $E$  is a point on the Earth's surface; the  $X$ -coordinate is measured from  $E$  on the fundamental parallel; the  $Y$ -coordinate is measured

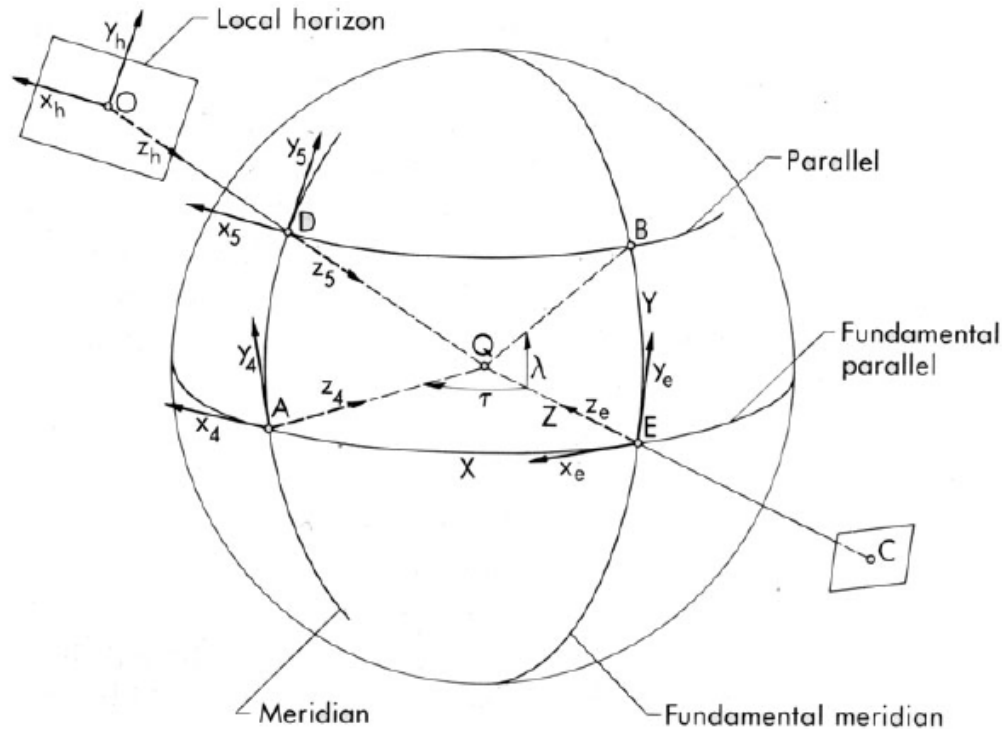


FIGURE A.1: Coordinate systems for flight over spheric Earth [13].

from  $E$  on the fundamental meridian; and the  $Z$ -coordinate is measured radially from  $E$ . Denote by  $O$  the instantaneous position of the aircraft and by  $D$  the instantaneous of the radial line passing through  $O$  with the Earth's surface. Indicate by  $A$  the intersection of the meridian passing through  $D$  with the fundamental parallel and by  $B$  the intersection of the parallel through  $D$  with the fundamental meridian, and by  $C$  the point where the spherical surface passing through the aircraft intersects the radial line passing through  $E$ . If the aircraft moves with respect to the Earth, its projections  $A, B, C$  simultaneously move; consequently, the three coordinates  $X, Y, Z$  suffice to determine the position of point  $O$  with respect to the Earth. Furthermore, the positive senses for  $X, Y, Z$  are consistent with the positive senses for the Earth axes.

The local horizon system  $O_{x_h y_h z_h}$  is a Cartesian reference frame having the following properties: its origin  $O$  is identical with the instantaneous position of the aircraft; the  $Z_h$ -axis is vertical and positive downward; the  $X_h$ -axis and  $Y_h$ -axis are contained in the plane tangent to the spherical surface passing through the aircraft and are such that trihedral  $OX_h Y_h Z_h$  is right-handed, in particular, the  $X_h$ -axis is parallel to the tangent to the parallel passing through  $D$ , while the  $Y_h$ -axis is parallel to the tangent to the median passing through  $D$ . The orientation

of the local horizon with respect to the Earth axes can be described in terms of two angular parameters, the longitude  $\tau$  and the latitude  $\lambda$ .

The wind axes system  $O_{x_w y_w z_w}$  is a Cartesian reference frame; its origin  $O$  is identical with the instantaneous position of the aircraft's centre of gravity (CG); its  $x_w$ -axis is tangent to the flight path and is positive forward; its  $z_w$ -axis is perpendicular to the  $x_w$ -axis, contained in the plane of symmetry and positive downward; its  $y_w$ -axis is perpendicular to the  $x_w z_w$ -plane and is directed in such a way that the trihedral is right-handed.

The body axes system  $O_{x_b y_b z_b}$  is a Cartesian reference frame; its origin  $O$  is the same as for the wind axes system; its  $x_b$ -axis is contained in the plane of symmetry and is positive forward; the  $z_b$ -axis is perpendicular to the  $x_b$ -axis, contained in the plane of symmetry and positive downward; the  $y_b$ -axis is perpendicular to the plane of symmetry and is directed in such a way that the trihedral is right-handed.

## A.2 Angular relationships

Angular relationships between the reference frames are needed to be able to convert from one reference system to another and vice versa.

The rotations necessary to perform the transformation from one system to another are easily understood if are used two intermediate coordinate: the system  $A_{x_4 y_4 z_4}$  is obtained from the Earth axes by means of the rotation  $\tau$  around the  $y_e$ -axis plus a translation; the system  $D_{x_5 y_5 z_5}$  is obtained from  $A_{x_4 y_4 z_4}$  by means of a rotation  $\lambda$  around the  $x_4$ -axis plus translation. Finally, the local horizon system is such that its axes and the corresponding axes of the system  $D_{x_5 y_5 z_5}$  are parallel and have the same positive sense. Following are given all relationship between the different frames with reference the Figure A.1.

$$\begin{bmatrix} i_4 \\ j_4 \\ k_4 \end{bmatrix} = \begin{bmatrix} \cos \tau & 0 & \sin \tau \\ 0 & 1 & 0 \\ -\sin \tau & 0 & \cos \tau \end{bmatrix} \times \begin{bmatrix} i_e \\ j_e \\ k_e \end{bmatrix} \quad (\text{A.1})$$

$$\begin{bmatrix} i_5 \\ j_5 \\ k_5 \end{bmatrix} = \begin{bmatrix} 1 & 0 & 0 \\ 0 & \cos \lambda & \sin \lambda \\ 0 & -\sin \lambda & \cos \lambda \end{bmatrix} \times \begin{bmatrix} i_4 \\ j_4 \\ k_4 \end{bmatrix} \quad (\text{A.2})$$

$$\begin{bmatrix} i_h \\ j_h \\ k_h \end{bmatrix} = \begin{bmatrix} i_5 \\ j_5 \\ k_5 \end{bmatrix} \quad (\text{A.3})$$

The curvilinear coordinates and the angles of rotation are related by

$$\begin{aligned} X &= r_0 \tau \\ Y &= r_0 \lambda \end{aligned} \quad (\text{A.4})$$

Where  $r_0$  is the Earth's radius. The final rotation is:

$$\begin{bmatrix} i_h \\ j_h \\ k_h \end{bmatrix} = \begin{bmatrix} \cos \tau & 0 & \sin \tau \\ -\sin \tau \sin \lambda & \cos \lambda & \cos \tau \sin \lambda \\ -\sin \tau \cos \lambda & -\sin \lambda & \cos \tau \cos \lambda \end{bmatrix} \times \begin{bmatrix} i_e \\ j_e \\ k_e \end{bmatrix} \quad (\text{A.5})$$

The orientation of the wind axes with respect to the local horizon can be described in terms of the heading angle  $\chi$ , flight path angle  $\gamma$ , and the bank angle  $\mu$ . The relationship between the wind axes and the horizon is given by:

$$\begin{bmatrix} i_w \\ j_w \\ k_w \end{bmatrix} = \begin{bmatrix} \cos \gamma \cos \chi & \cos \gamma \sin \chi & -\sin \gamma \\ \sin \mu \sin \gamma \cos \chi - \cos \mu \sin \chi & \sin \mu \sin \gamma \sin \chi + \cos \mu \cos \chi & \sin \mu \cos \gamma \\ \cos \mu \sin \gamma \cos \chi + \sin \mu \sin \chi & \cos \mu \sin \gamma \sin \chi - \sin \mu \cos \chi & \cos \mu \cos \gamma \end{bmatrix} \times \begin{bmatrix} i_h \\ j_h \\ k_h \end{bmatrix} \quad (\text{A.6})$$

The orientation of the local horizon with respect to the Earth axes can be described in terms of two angular parameters, the longitude  $\tau$  and the latitude  $\lambda$ . With reference to the Figure A.1 it is possible to see that

### A.3 Angular Velocity

Angular velocity of one reference system respect to another is shown.

### A.3.1 Local horizon-Earth axes

The rotations necessary to convert from the Earth axes to the local horizon occur around the  $y_e$ -axis and the  $x_4$ -axis. The infinitesimal angular displacement is therefore given by

$$d\boldsymbol{\Omega}_h = d\lambda\mathbf{i}_4 - d\tau\mathbf{j}_e \quad (\text{A.7})$$

And the angular velocity is given by

$$\boldsymbol{\omega}_h = \frac{d\boldsymbol{\Omega}_h}{dt} = \dot{\lambda}\mathbf{i}_4 - \dot{\tau}\mathbf{j}_e \quad (\text{A.8})$$

which can be rewritten using transformation matrices in the form

$$\boldsymbol{\omega}_h = \frac{\dot{Y}}{r_O}\mathbf{i}_h - \frac{\dot{X}}{r_O}\cos\left(\frac{Y}{r_O}\right)\mathbf{j}_h + \frac{\dot{X}}{r_O}\sin\left(\frac{Y}{r_O}\right)\mathbf{k}_h \quad (\text{A.9})$$

## A.4 Kinematic Relationships

The scalar relationships corresponding to the vectorial equation (A.6) are derived. Because the velocity is collinear with the  $x_w$ -axis, the velocity can be written as:

$$\mathbf{V} = V\mathbf{i}_w = V(\cos\gamma\cos\chi\mathbf{i}_h + \cos\gamma\sin\chi\mathbf{j}_h - \sin\gamma\mathbf{k}_h) \quad (\text{A.10})$$

after using the transformation matrix in Eq. (4). We can then rewrite the vector joining the origin of the Earth axes system with the aircraft as

$$\mathbf{EO} = \mathbf{EQ} - (r_0 + h)\mathbf{k}_h \quad (\text{A.11})$$

where  $\mathbf{EQ}$  is a vector rigidly attached to the Earth and  $h$  is the altitude of the rocket above sea level as shown in Figure 1. If we then take the time derivative of this equation as is required for Eq. (2) we get

$$\frac{d\mathbf{EO}}{dt} = -\dot{h}\mathbf{k}_h - (r_0 + h)\frac{d\mathbf{k}_h}{dt} \quad (\text{A.12})$$

where, because of Poissons formulas, the time derivative of the unit vector perpendicular to the local horizon is given by

$$\frac{d\mathbf{k}_h}{dt} = \boldsymbol{\omega}_h \times \mathbf{k}_h = -\frac{\dot{X}}{r_0}\cos\lambda\mathbf{i}_h - \frac{\dot{Y}}{r_0}\mathbf{j}_h \quad (\text{A.13})$$

As a final step, we combine Eqs. (2), (7), (8), and (9) to get the following kinematic relationships:

$$\begin{aligned}\dot{X} &= V \frac{r_0}{r_0+h} \frac{\cos \gamma \cos \chi}{\cos \lambda} \\ \dot{Y} &= V \frac{r_0}{r_0+h} \cos \gamma \cos \chi \\ \dot{h} &= V \sin \gamma\end{aligned}\tag{A.14}$$

## A.5 Equations of Motion

Finally it is possible to summarize the translational motion of an aircraft having variable mass and operating in a three-dimensional space over a spherical earth resulting in having 13 equations (). It is possible to add 5 functions contained in the equations which are dependant the characteristics of the aircraft and the installed engine (drag, lift, thrust, specific engine consumption). Assuming there is only one independent variable (e.i. the time) and 19 dependent variables which include the 8 derived variables (X, Y, h, V, chi, gamma, mu, mass ) and the 11 non derived variables ().

The resulting degrees of freedom of the system is  $n = 19 - 13 = 6$  which is logical in the view of the possibility to control the aircraft by time history of rudder deflection, elevator deflection, aileron deflection, thrust control, thrust sideslip angle and thrust angle of attack. The last two are normally constant since the engine is fixed with respect to the aircraft. Therefore the degrees of freedom reduces to 4.

# Appendix B

## Aeronautical Information Publication (AIP) Charts

This Appendix provides a collection of AIPs charts used in this work. The following charts have been used:

- London Heathrow - EGLL - BPK SID - FIGURE B.1
- Amsterdam Schiphol - EHAM - STAR - FIGURE B.2

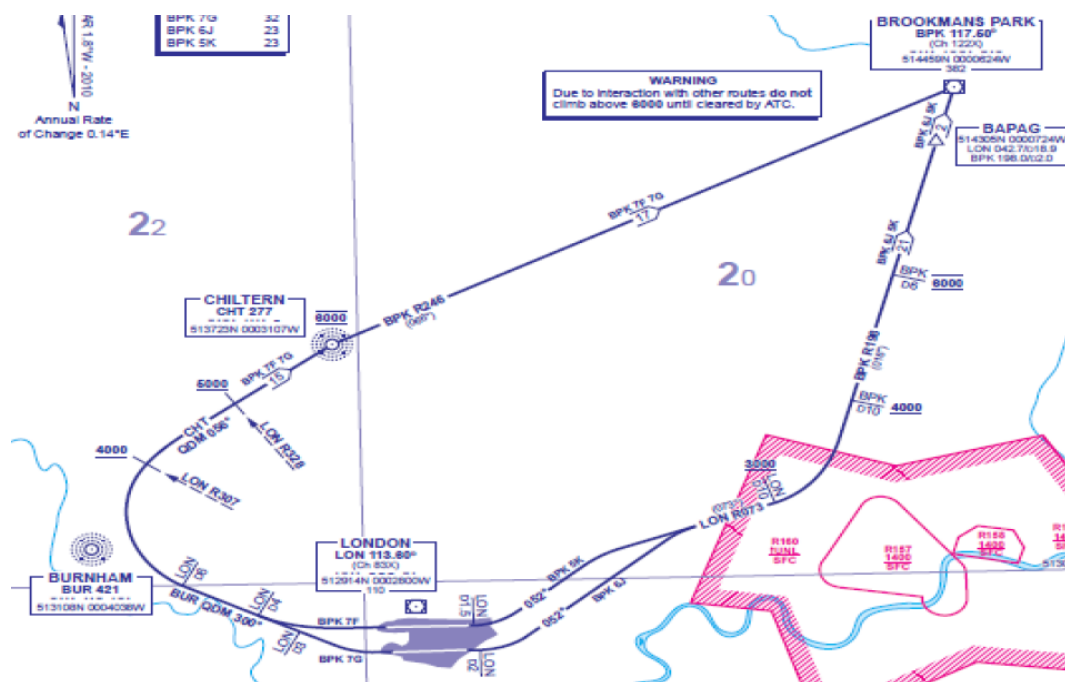


FIGURE B.1: London Heathrow (EGLL) - BPK SIDs

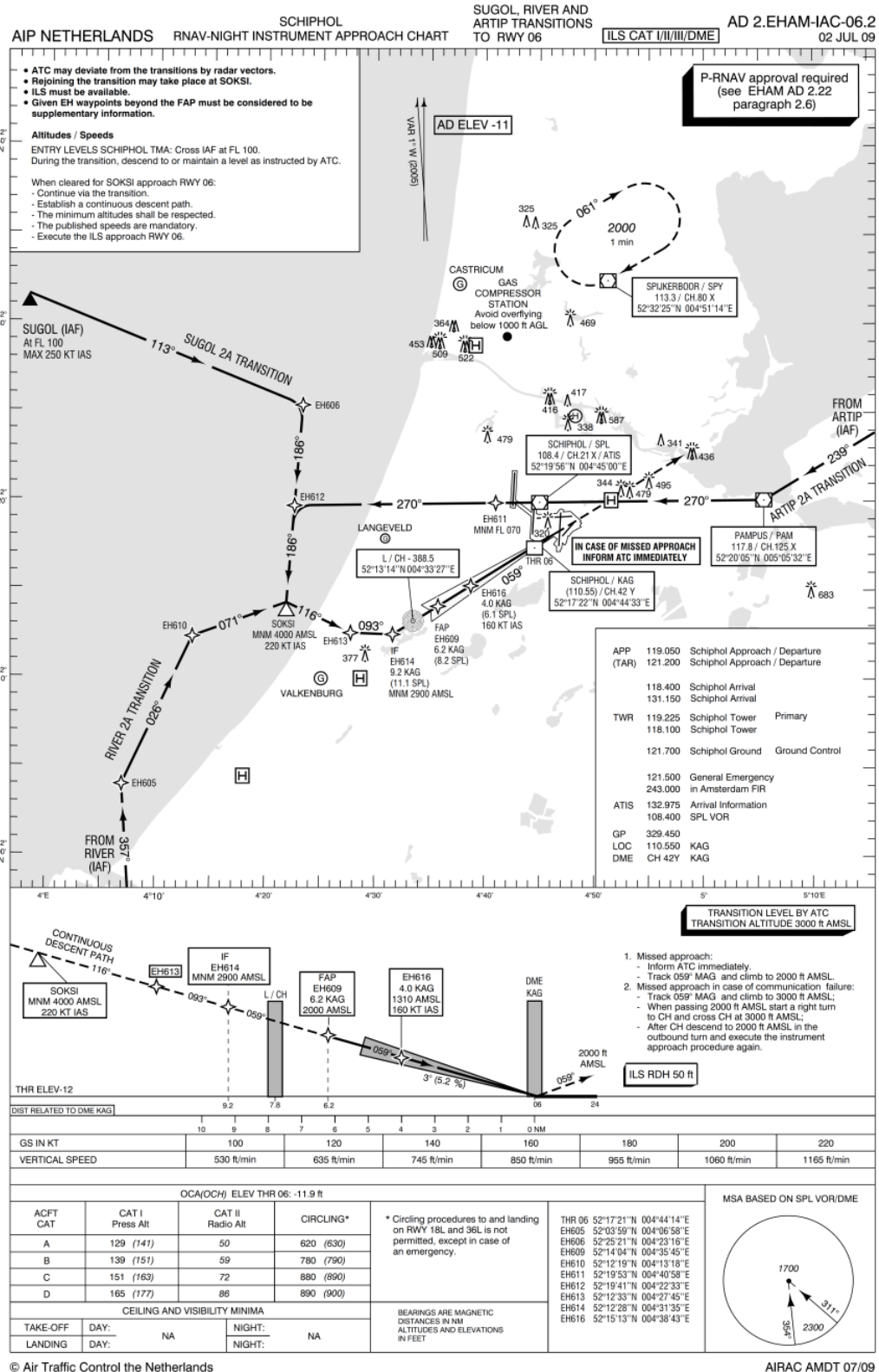


FIGURE B.2: Amsterdam Schiphol (EHAM) - RNAV Approach Chart



# Bibliography

- [1] 2013 icao air transport results confirm robust passenger demand, sluggish cargo market, 12 2013. URL <http://www.icao.int/Newsroom/Pages/2013-ICAO-AIR-TRANSPORT-RESULTS-CONFIRM-ROBUST-PASSENGER-DEMAND,-SLUGGISH-CARGO-MARKET.aspx>.
- [2] Faa aerospace forecast fiscal years 2013-2033, 2013.
- [3] Eurocontrol seven-year forecast. flight movements and service units 2013 - 2019.
- [4] Challenges of growth 2013. task 4: European air traffic in 2035, 2013.
- [5] 2008 addendum to the strategic research agenda, 2008. URL <http://www.acare4europe.com/documents/archive/acare-2008-addendum-strategic-research-agenda>.
- [6] Sesar joint undertaking. URL <http://www.sesarju.eu>.
- [7] Clean sky programme. URL <http://www.cleansky.eu>.
- [8] Efficiency trends for new commercial jet aircraft 1960 to 2008, 2009.
- [9] Air Travel Greener by Design. Mitigating the environmental impact of aviation: Opportunities and priorities, 07 2005.
- [10] Report on the progress in noise reduction submitted to icao., 2005.
- [11] European atm master plan 2012, 2012.
- [12] D. De Smedt and G. Berz. Study of the required time of arrival function of current fms in an atm context. In *Digital Avionics Systems Conference, 2007. DASC '07. IEEE/AIAA 26th*, pages 1.D.5–1–1.D.5–10, Oct 2007. doi: 10.1109/DASC.2007.4391837.

- [13] A. Miele, M. W. Weeks, and M. Ciarci. Optimal trajectories for spacecraft rendezvous. *Journal of Optimization Theory and Applications*, Volume 132 (Issue 3):pp 353–376, March 2007.
- [14] K. F. Graham and A. V. Rao. Minimum-time trajectory optimisation of multiple revolution low-thrust earth-orbit transfers.
- [15] D. F. Bender and A. L. Blackford. *Guidance, Flight Mechanics and Trajectory Optimization Volume XII - Relative Motion, Guidance Equations for Terminal Rendezvous*. NASA, 1968.
- [16] A. E. Bryson, M. N. Desai, and W. C. Hoffman. Energy-state approximation in performance optimization of supersonic aircraft. *Journal of Aircraft*, Vol. 6(No. 6):pp. 481–488, 1969. doi: 10.2514/3.44093.
- [17] A. V. Rao and D. Benson. *User's Manual for GPOPS Version 4.x: A MATLAB Software for Solving Multi-phase Optimal Control Problems using hp-adaptive Pseudospectral Methods*, 2011.
- [18] David G. Hull. *Optimal Control Theory for Applications*. Springer, 2003.
- [19] F. J. Vormer, M. Mulder, M. M. Van Paassen, and J. A. Mulder. Optimization of flexible approach trajectories using a genetic algorithm. 2006.
- [20] Di Wu and Yiyuan J. Zhao. Performances and sensitivities of optimal trajectory generation for air traffic control automation. 2009.
- [21] Rosa Torres, Jrme Chaptal, Christian Bes, and Jean-Baptiste Hiriart-Urruty. Multi-objective clean take-off flight paths for civil aircraft. In *Aviation Technology, Integration, and Operations (ATIO) Conferences*, pages –. American Institute of Aeronautics and Astronautics, September 2009. doi: 10.2514/6.2009-6931. URL <http://dx.doi.org/10.2514/6.2009-6931>.
- [22] Sai Vaddi, G. D. Sweriduk, and Monish Tandale. 4d green trajectory design for terminal area operations using nonlinear optimization techniques. In *AIAA Guidance, Navigation, and Control Conference 13 - 16 August 2012, Minneapolis, Minnesota*, 2012.
- [23] Anil V. Rao. Trajectory optimization. *Encyclopedia of Aerospace Engineering*, 2010.

- [24] J. V. Breakwell and H. Shoe. Minimum fuel flight paths for given range. In *Guidance, Navigation, and Control and Co-located Conferences*, 1980.
- [25] John T. Betts and Evin J. Cramer. Application of direct transcription to commercial aircraft trajectory optimization. *Journal of Guidance, Control, and Dynamics*, 18(1):151–159, January 1995. ISSN 0731-5090. doi: 10.2514/3.56670. URL <http://dx.doi.org/10.2514/3.56670>.
- [26] M. Soler, A. Olivares, and E. Staffetti. Hybrid optimal approach to commercial aircraft trajectory planning. 33(3):985–991, 2010.
- [27] Sander Hartjes, Hendrikus G. Visser, and Sander J. Hebly. Optimization of rnav noise and emission abatement departure procedures. In *Aviation Technology, Integration, and Operations (ATIO) Conferences*, pages –. American Institute of Aeronautics and Astronautics, September 2009. doi: 10.2514/6.2009-6953. URL <http://dx.doi.org/10.2514/6.2009-6953>.
- [28] M. Houacine and S. Khardi. Gauss pseudospectral method for less noise and fuel consumption of aircraft operations. *Journal of Aircraft*, 47(6):2152–2158, November 2010. ISSN 0021-8669. doi: 10.2514/1.C031007. URL <http://arc.aiaa.org/doi/abs/10.2514/1.C031007>.
- [29] Rafael Fernandes de Oliveira and Christof Bskens. On-board trajectory optimization of rnav departure and arrival procedures concerning emissions and population annoyance. In *SAE Technical Paper*. SAE International, 2011. doi: 10.4271/2011-01-2595. URL <http://papers.sae.org/2011-01-2595/>.
- [30] Banavar Sridhar, Hok Ng, and Neil Chen. Aircraft trajectory optimization and contrails avoidance in the presence of winds. *Journal of Guidance, Control, and Dynamics*, 34(5):1577–1584, September 2011. ISSN 0731-5090. doi: 10.2514/1.53378. URL <http://dx.doi.org/10.2514/1.53378>.
- [31] Antonio Franco and D. Rivas. Minimum-cost cruise at constant altitude of commercial aircraft including wind effects. 34(4):1253–1260, 2011.
- [32] R. Weinstock. *Calculus of variations*. 1974.
- [33] John T. Betts. Survey of numerical methods for trajectory optimization. *Journal of Guidance, Control, and Dynamics*, 21(2):193–207, March 1998.

- ISSN 0731-5090. doi: 10.2514/2.4231. URL <http://dx.doi.org/10.2514/2.4231>.
- [34] A. E. Bryson and Y.-C. Ho. *Applied Optimal Control: Optimization, Estimation and Control*. Taylor & Francis, 1975.
- [35] S. A. Orszag. Comparison of pseudospectral and spectral approximations. 51(3):253–259, 1972.
- [36] J. Vlassenbroeck and R. V. Dooren. A chebyshev technique for solving nonlinear optimal control problems. 33:333–340, 1988.
- [37] D. Schomisch H. Mhlenbein and J. Born. The parallel genetic algorithm as function optimizer. 1991.
- [38] A. V. Rao. A survey of numerical methods for optimal control (aas 09-334). 2009.
- [39] Q. McEnteggart and J. Whidborne. A multiobjective trajectory optimisation method for planning environmentally efficient trajectories. In *Control (CONTROL), 2012 UKACC International Conference on*, pages 128–135, 2012. doi: 10.1109/CONTROL.2012.6334618.
- [40] William B. T. Mock. *Pareto Optimality*, pages 808–809. Springer Netherlands, Dordrecht, 2011. ISBN 978-1-4020-9160-5. doi: 10.1007/978-1-4020-9160-5\_341. URL [https://doi.org/10.1007/978-1-4020-9160-5\\_341](https://doi.org/10.1007/978-1-4020-9160-5_341).
- [41] K. Deb E. Zitzler and L. Thiele. Comparison of multiobjective evolutionary algorithms: Empirical results. 2000.
- [42] R. T. Marler and J. S. Arora. Survey of multi-objective optimization methods for engineering. 2004.
- [43] Johan Andersson. A survey of multiobjective optimization in engineering design, 2000.
- [44] K. Deb. *Multi-Objective Optimisation using Evolutionary Algorithms*. 2001.
- [45] ICAO. Noise data bank, 2001. URL <http://noisedb.stac.aviation-civile.gouv.fr/>.

- [46] S. Fidell, J. Mills, S. Teffeteller, and K. Pearsons. Community response to three noise abatement departure procedures at john wayne airport, 1982.
- [47] ESDU International. Airframe noise prediction - esdu 90023, 1990.
- [48] ESDU International. Prediction of combustor noise from gas turbine engine - esdu 05001, 2005.
- [49] ESDU International. An introduction to aircraft noise - esdu 02020, 2002.
- [50] A. B. David and H. H. Colin. *Engineering Noise Control Theory - 3rd ed.* 2003.
- [51] Eric R. Boeker and Eric Dinges. *Integrated Noise Model (INM) Version 7.0 Technical Manual*, 2008.
- [52] EUROPEAN CIVIL AVIATION CONFERENCE (ECAC). Report on standard method of computing noise contours around civil airports, 2016.
- [53] Federal Interagency Committee on Aviation Noise (FICAN). Effects of aviation noise on awakenings from sleep. 1997.
- [54] SAE International. Procedure for the calculation of aircraft emissions - air5715, 2009.
- [55] Patrick Minnis, J. Kirk Ayers, Rabindra Palikonda, and Dung Phan. Contrails, cirrus trends, and climate. 2004.
- [56] U. Schumann. Aircraft emissions volume 3. 2002.
- [57] ICAO. Annex 16 - volume ii aircraft engine emissions. 2008.
- [58] Kouamana Bousson and Paulo Machodo. 4d flight trajectory optimization based on pseudospectral methods. *World Academy of Science, Engineering & Technology*, Sep1020, Issue 45:551, 210.
- [59] Damin Rivas, Alfonso Valenzuela, and Jos L de Augusto. Computation of global trajectories of commercial transport aircraft. *Proceedings of the Institution of Mechanical Engineers, Part G: Journal of Aerospace Engineering*, 2012. doi: 10.1177/0954410011427107. URL <http://pig.sagepub.com/content/early/2012/01/11/0954410011427107.abstract>.

- [60] Rafael Fernandes de Oliveira and Dr.Christof Bskens. Benefits of optimal flight planning on noise and emissions abatement at the frankfurt airport. In *Guidance, Navigation, and Control and Co-located Conferences*, pages – . American Institute of Aeronautics and Astronautics, August 2012. doi: 10.2514/6.2012-4482. URL <http://dx.doi.org/10.2514/6.2012-4482>.
- [61] R.A. Paielli and H. Erzberger. Conflict probability estimation for free flight. 1996.
- [62] A. Miele. *Flight Mechanics: Theory of Flight Pahts*. 2016.
- [63] M. Soler. *Commercial Aircraft Trajectory Planning based on Multiphase Mixed-Integer Optimal Control*. PhD thesis, 2013.
- [64] Kelly Klima. Assessment of a global contrail modeling method and operational strategies for contrail mitigation. Master’s thesis, 2005.
- [65] Nuic A. User manual for the base of aircraft data (bada) revision 3.12, 2014.
- [66] S. Hartjes and H. G. Visser. Optimization of rnav noise and emission abatement departure procedures. In *AIAA Aviation Technology, Integration and Operations Conference (ATIO)*, 2009.
- [67] ICAO. Procedures for air navigation sservice - aircraft operations (pans-ops) - volume i, flight procedures. 5th ed., 2006. URL [http://www.chcheli.com/sites/default/files/icao\\_doc\\_8168\\_vol\\_1.pdf](http://www.chcheli.com/sites/default/files/icao_doc_8168_vol_1.pdf).
- [68] Doug DuBois and Gerald Paynter. ”fuel flow method2” for estimating aircraft emissions. 2006.
- [69] Frank Jelinek, Sandrine Carlier, and James Smith. Advanced emission model (aem3) - eec report eec/see/2004/004, 2004.
- [70] P. D. Norman. Development of the technical basis for a new emissions parameter covering the whole aircraft operation. 2003. Final Technical Report; NEPAIR/WP4/WPR/01. EC Contract Number G4RD-CT-2000-00182.
- [71] ICAO. Icao engine exhaust emissions databank - doc 9646-an/943, 1995. URL <https://www.easa.europa.eu/document-library/icao-aircraft-engine-emissions-databank>.

- [72] H. G. Visser and R. A. A. Wijnen. Optimisation of noise abatement arrival trajectories. 2003.
- [73] Xavier Prats Menndez. *Contributions to the optimisation of aircraft noise abatement procedures*. PhD thesis, 2010.
- [74] P. E. Gill, W. Murray, and M. A. Saunders. *User's Guide for SNOPT Version 7*, 2008.
- [75] S. Rump. Intlab - interval laboratory, 2011. URL <http://www.ti3.tu-harburg.de/rump/intlab/>.
- [76] W. C. Gear. *Numerical Initial-Value Problems in Ordinary Differential Equations*. 1971.
- [77] S. H. Crandall. *Engineering Analysis*. 1956.
- [78] C. d. Boor and B. Schwartz. Collocation at gaussian points. Vol. 10:pp. 582606, 1973.
- [79] F. Topputo and C. Zhang. Survey of direct transcription for low-thrust space trajectory optimization with applications. 2014.
- [80] D. Garg, W. W. Hager, and A. V. Rao. Pseudospectral methods for solving infinite-horizon optimal control problems. 2011.
- [81] M. A. Patterson and A. V. Rao. Gpops-ii: A matlab software for solving multiple-phase optimal control problems using hp-adaptive gaussian quadrature collocation methods and sparse nonlinear programming. 2014.
- [82] Michael Anthony Cooper. *SIMULATING ACTUATOR ENERGY DEMANDS OF AN AIRCRAFT IN FLIGHT*. PhD thesis, 2014.
- [83] D. J. Allerton. *Principles of Flight Simulation*. 2009.
- [84] R. D. Finck. Usaf stability and control datcom, 1977.
- [85] M. Drela and H. Youngreen. Athena vortice lattice, 2004. URL <http://web.mit.edu/drela/Public/web/avl/>.
- [86] B. Galbraith. Dmodel+ predicted aerodynamic model, 2004. URL [www.holycows.net](http://www.holycows.net).

- [87] W. B. Blake. Prediction of fighter aircraft dynamic derivatives using digital datcom. 1985.
- [88] Johannes von Helldor. Design study of short and medium. Master's thesis, 2010.
- [89] A. A. Lambregts. Functional integration of vertical ight path and speed control using energy principles. 1983.
- [90] M. H. J. Amelink. *Ecological Automation Design, Extending Work Domain Analysis*. PhD thesis, 2010.
- [91] K. R. Bruce. Integrated autopilot/autothrottle for the nasa tsrv b-737 aircraft: design and verification by nonlinear simulation. Technical report, Tech. Rep. NASA CR-4217, 1989.
- [92] K. R. Bruce, J. R. Kelly, and L. H. Person. Nasa b737 ight test results of the total energy control system. Technical report, Tech. Rep. NASA-CR-178285, 1987.
- [93] P. Chudy and P. Rzucidlo. Tecs/thcs based ight control system for general aviation. In *AIAA Modeling and Simulation Technologies Conference*, 2009.
- [94] M. Eladl, K. Eltohamy, B. Hill, T. Horne, B. Krasnovskiy, K. Leiphon, and S. Taylor. Advanced guidance and control - operational and safety benefits. Technical report, Federal Aviation Administration (FAA), 2008.
- [95] M. A. Bruzzini. *Development of a TECS Control Law for the Lateral Directional Axis of the McDonnell Douglas F-15 Eagle*. PhD thesis, 1994.
- [96] A. A. Lambregts. Automatic flight controls, tech. rep. knvlpap6, 1998. URL <https://faaco.faa.gov/index.cfm/attachment/download/10304>.
- [97] J. Herzog. A320 enhanced (a320e) prototype (fwwiq) with sharklets at ilar berlin air show 2012., (2012). URL <http://commons.wikimedia.org/wiki/File:F-WWIQAirbusA320sharkletILA201207.jpg>.
- [98] British Airways Flight (BA440). Egll-eham flight tracker. flightflight - live flight tracker, 2014. URL <https://uk.flightaware.com>.
- [99] Civil Aviation Authority. Ered report 1001 - noise exposure contours for heathrow airport 2009, 2010. URL <http://webarchive>.



[nationalarchives.gov.uk/20120606191521/http://assets.dft.gov.uk/publications/noise-exposure-contours/noiseheathrow09.pdf](http://nationalarchives.gov.uk/20120606191521/http://assets.dft.gov.uk/publications/noise-exposure-contours/noiseheathrow09.pdf).

- [100] Civil Aviation Authority (CAA). Uk aip ad 2-egll-6-3: London heathrow, 2014. URL [http://www.ead.eurocontrol.int/eadbasic/pamslight-81F4C0B9B0B02FF693C780739DC4DF83/7FE5QZZF3FXUS/EN/Charts/AD/AIRAC/EG\\_AD\\_2\\_EGLL\\_6-3\\_en\\_2014-10-16.pdf](http://www.ead.eurocontrol.int/eadbasic/pamslight-81F4C0B9B0B02FF693C780739DC4DF83/7FE5QZZF3FXUS/EN/Charts/AD/AIRAC/EG_AD_2_EGLL_6-3_en_2014-10-16.pdf).